UNIVERSITY OF SOUTHAMPTON

Development, Evaluation & Application of a Geomagnetic Reference Field Model for Attitude Determination of Small Satellites

George Michalareas

Doctor of Philosophy

Astronautics Research Group
School of Engineering Sciences

August 2003

UNIVERSITY OF SOUTHAMPTON

ABSTRACT

FACULTY OF ENGINEERING

AERONAUTICS & ASTRONAUTICS

Doctor of Philosophy

DEVELOPMENT, EVALUATION & APPLICATION OF A GEOMAGNETIC FIELD MODEL FOR ATTITUDE DETERMINATION OF SMALL SATELLITES

The subject of this thesis is the development, evaluation and application of a new model of the geomagnetic field for the purpose of attitude determination for near-earth spacecraft. Although high accuracy magnetometers have been included in numerous missions, the accuracy in attitude determination has been moderate. The reason for this is the inaccuracy of the models used as the reference to the acquired measurements. The most widely used model is the International Geomagnetic Reference Field (IGRF).

The first important limitation of this model is the wide coverage it provides for all latitudes and longitudes. The second main limitation of the IGRF is that one of its components, the most dynamic, cannot be used onboard a satellite as it dependents on D_{st}, an index evaluated on earth observatories and impractical to upload to a satellite. This part describes the effect of the magnetospheric ring current.

To overcome these limitations two solutions are proposed. Firstly the inaccuracy due to wide coverage was treated by performing the exact opposite operation, the segmentation of the field in different parts. Seven different segments were investigated and a different model was developed for each one. The second limitation, arising from the D_{st}, was treated by the development of a magnetic activity index by measurements on board the spacecraft, in real time. This index was first evaluated for its consistency by comparison to the original D_{st} index. Then 16 different models were developed, each one for a different level of disturbance and a different condition of use.

After the derivation of these models, the last part investigates the accuracy that can be achieved in an attitude determination system by the use of these models. For this purpose a conceptual design was performed and simulation established that the use of the dynamic part reduced, for this particular system, the error by a significant amount.

All the results from the above research showed that the developed solutions indeed lead to higher accuracy in attitude determination.

Contents

List of Figures

List of Tables

Acknowledgments

I would like to thank my two supervisors Dr. Gabriel and Professor Rogers for giving me the opportunity, the assistance and the motivation to carry through this research.

Special thanks to the Oersted Science Team for providing all the information that made this work possible.

Most of all I would like to thank my parents , Ilia and Athena and my brother Thodori for their love and support.

Many thanks I own to Mr Fotis Papatheodorou for being a real friend when it was mostly appropriate.

I would like also to thank Mr Ismat Rudwan for the inspiring conversations, Mr Leonida Doko for his unique advice and Mr Thanos Mourikis for just being my best friend.

Finally I would like to thank all these people who have provided me with strength and inspiration.

Concluding I would like to give special thanks to my supervisor Dr Gabriel for his understanding and his support in difficult times.

Abbreviations

AD	Attitude Determination
BMS	Body Mounted Horizon Sensor
BSS	Boeing Satellite Systems
CHAMP	Challenging Minisatellite Payload
CM	Centre of Mass
CMOS	Complementary Metal-Oxide Semiconductor
CP	Centre of Pressure
FOAM	Fast Optimal Matrix Algorithm
FOV	Field of View
GPS	Global Positioning System
IAGA	International Association of Geomagnetism and Auronomy
IGRF	International Geomagnetic Reference Field
ION-F	Ionospheric Observation Nanosatellite Formation
IMF	Interplanetary Magnetic Field
IRLS	Iterated Least Squares
JPL	Jet Propulsion Laboratory
LEO	Low Earth Orbit
MEME	Mean Equatorial Magnitude Error
NASA	National Aeronautics and Space Administration
PAS	Panoramic Attitude Sensor
POGS	Polar Orbiting Geomagnetic Satellite
QUEST	Quaternion Estimator
RG	Rate Gyro
RIG	Rate Integrating Gyro
SAMPEX	Solar Anomalous and Magnetospheric Particles Explorer

SMART-1	Small Missions for Advanced Research in Technology
SNAP	Surrey Nanosatellite Applications Platform
SSTL	Surrey Satellite Technology Limited
TRIAD	Triaxial Attitude Determination

Nomenclature

q_n^m, s^m Gaussian coefficients describing external sources, page 51

(x, y, z) Cartesian Coordinates, page 29

α Right Ascension, page 40

α,β,γ constants, page 30

α_G Right Ascension of the Greenwich Meridian, page 40

χ_i merit function, page 42

δ Latitude, page 40

ϵ_0 permittivity of vacuum, page 27

$\epsilon_{k,i}$ normalised residual of the kth data point in the ith iteration, page 57

$\hat{\mathbf{n}}$ is the normal vector outward of the surface element, page 276

$\hat{\mathbf{v}}_b$) unit vector in the direction of the orbital velocity in the body coordinate system, page 276

$\hat{e}$ Euler axis, page 258

λ Step of Marquardt method, page 47

λ eigenvalue, page 272

λ_{opt} eigenvalue, page 273

$\mathbf{I}$ Moment of inertia matrix, page 263

$\mathbf{L}$ Angular Momentum, page 263

μ Earth Gravitational constant, page 275

μ permeability, page 314

μ_0 permeability of vacuum, page 27

Ω Loss function for attitude determination, page 273

Ω Skew symmetric matric containing that components of the spacecraft angular velocity, page 269

ω angular velocity of satellite in body coordinate system, page 261

$\omega_{1m}, \omega_{2m}, \omega_{3m}$ Maximum values of angular velocity components, page 263

$\omega_1, \omega_2, \omega_3$ angular velocity components, page 262

ω_p Nutation rate, page 263

Φ Angle of rotation around the Euler axis, page 258

ϕ Longtitude, page 40

ρ Atmospheric density, page 276

ρ charge density, page 27

σ_i standard deviation of data point, page 42

$\mathbf{g}$ Control Torque, page 261

$\mathbf{n}_b$ unit direction vector in the body coordinates from the center of the mass to the center of the Earth, page 275

$\mathbf{q}$ quaternion, page 260

$\mathbf{w}_n$ Disturbance Torque, page 261

$\tilde{q}_1^0, \tilde{q}_1^1, \tilde{s}_1^1$ Gaussian coefficients accounting for the variability of contributions of $\widetilde{RC}$, page 51

$\widetilde{RC}$ traditionally the D_{st} index, page 51

A Loop Area, page 313

A Transformation Matrix, page 257

A Vector Field, page 27

a mean radius of Earth, page 51

$A(x), B(y), C(z)$ Independent functions, page 29

a_i model fitting parameter, page 43

a_i, b_i Spherical Coordinates, page 34

AE AuroralElectrojetIndices, page 24

AL Auroral Electrojet Index - Lower Envelope, page 24

AO Auroral Electrojet Index - Zonal Current, page 24

AU Auroral Electrojet Index -Upper Envelope, page 24

B magnetic field, page 27

B_r, B_θ, B_ϕ Magnetic Field components in spherical coordinate system, page 39

B_x, B_y, B_z Magnetic Field components in Geocentric Coordinate system, page 40

C Variance Covariance Matrix, page 44

c constant, page 57

C_D Drag coefficient, page 276

cn, sn, dn Jacobi elliptic functions, page 262

D_{ij} derivative of calculated data point i for model parameter j , page 43

D_{st} Distutbance Field Index, page 24

D_{st} Planetarische Kennziffer (planetary index), page 24

dA Spacecraft surface element, page 276

E Skew Symmetric axis containing euler axis components, page 259

E electric field, page 27

E_i difference of data point and current calculated data point, page 43

E_k Angular kinetic energy, page 263

F Field, page 26

$f(x), g(x)$ Orthogonal functions, page 48

$f(x, y, z)$ Continuous function - Solution of the Laplace Equation, page 34

f_{aero} Atmospheric force, page 276

f_{int}, f_{ext} Spherical harmonic functions describing a field inside and outside the generating sphere respectively, page 38

f_{mean} Mean Value of Solution of Laplace's Equation over a sphere, page 35

g_{ij} Metric Tensor, page 31

g_i calculated data point, page 42

g_n^m, h_n^m Gaussian coefficients of degree n and order m, page 38

h_i Square Root of Metric Tensor Diagonal Element i, page 31

I current, page 313

I_m Moment of Inertia, page 261

Ih High moment of inertia of nanosatellite, page 300

Il Low moment of inertia of nanosatellite, page 300

J current density, page 27

M_j Magnetic moment of element j, page 315

N Number of turns, page 313

n, m Degree and Order of Associated Legenfre Functions, page 37

$P_{n,m}$ Associated Legendre Functions, page 37

P_n Legendre Polynomials, page 33

P_n Legenfre Polynomials, page 27

Q Skew symmetric matric containing the vector components of quaternion, page 260

q_n^0, h_n^0 Gaussian coefficients describing the seasonal dependence of the ambient external field, page 54

R Radius of Sphere of Laplace's equation solution, page 35

r geocentric distance, page 275

r,θ,ϕ Sperical Coordinates, page 32

s Roots of the characteristic polynomial of Laplace's equation, page 30

V Scalar Field, page 27

V_{ext} Ambient External Field Potential, page 53

V_{int} Potential of External Field Described by D_{st}, page 53

V_{int} Static Internal Field Potential, page 52

V_{sec} Potential for Internal Field's Secular Variation, page 52

w weight of Huber distribution, page 57

W_i weighting matrix, page 43

y_i data point, page 42

Chapter 1

Introduction

This thesis describes the development of a model of the geomagnetic field targeted for the use on board satellites in Low Earth Orbit for the purpose of Attitude Determination. Magnetometers are inexpensive and light weight sensors and for this reason have been used in the majority of near Earth missions. The accuracy they provide is low not due to error in their design but due that in the reference they use. This is the model of the geomagnetic field.

1.1 Geomagnetic Field

The Earth's magnetic field, as measured by a magnetic sensor above its surface, is composed of several magnetic fields generated by a variety of sources. These fields are superimposed on to each other and through inductive processes interact with each other.

The most important of these sources are:

- the earth's conductive fluid core
- the earth's crust and upper mantle
- the ionosphere
- the magnetosphere

The earth's outer core generates more than 95 percent of the geomagnetic field. This portion of the geomagnetic field is represented by the 2000 International Geomagnetic Reference Field (IGRF) charts [1]. The IGRF model and its secular variation (annual change) consist of a spherical harmonic equation of degree 10 and order 10. This equation is based

on several proposed geomagnetic models, which are weighted according to their determined validity. The IGRF model and its secular variation are updated every five years. Each model is assumed to be valid from its base year through the next five years.

In addition to the static part describing the internal main field, the IGRF also includes two dynamic components. One of them describes the secular variation of the field in time and the other the effect of the magnetosphere. The magnetosphere is the area of space within which the magnetic field of the earth is confined.

Many current systems exist in the magnetosphere, most of which are of an irregular nature. The only current system that shows a consistent shape and is always present is that caused by the so called "ring current". Its name is derived from the fact that it runs on a ring engulfing the Earth in the center. The effect of this current is the creation of a magnetic field of dipole shape. The intensity of the current and the dipole is not constant but depends on the amount of charged particles arriving from the sun. This flow of particles is also known as "solar wind". When the strength of the solar wind increases, the intensity of the dipole increases. This creates the known "magnetic storms" and most of the "magnetic substorms". This activity is measured by various indices based on the use of earth observatories.

The International Geomagnetic Reference Field (IGRF) employs one of these indices, known as D_{st}. This index is derived from 4 observatories distributed around the earth and located close to the equator where the effect of the disturbance is easier to identify. The deviation is measured, then averaged and it becomes available to public one hour after the measurement. The IGRF employs this index to derive a model that describes the effect of the dipole created by the ring current.

1.2 The Geomagnetic Field as a Reference vector

The attitude of a spacecraft is its orientation in space relative to a reference coordinate system. As knowledge of its orientation is necessary for any spacecraft operation, sensors are employed for this purpose which are categorized mainly by the reference they measure in order to provide orientation information. Sensors that provide highly accurate information are usually heavy, power consuming and, critically, expensive. Additionally they cannot operate under any orientation of the spacecraft. For example, star sensors, the most accurate, must be pointed in space in order to operate.

The main sensors that do not require any specific orientation for measurement of their reference are inertial sensors and magnetometers. Inertial sensors measure the deviation

from the inertial position and thus it is more appropriate to categorize them as angular rate rather than attitude sensors. Conversely, magnetometers on the other hand are relatively simple devices that measure through various techniques the magnetic field. Magnetometers of various accuracies are available and can be constructed to be extremely accurate. At the same time their weight and mass are relatively small in comparison to most of the other sensors.

In order that orientation information is available to the spacecraft, the measured magnetic field is compared with a produced value from a model. This model in most cases is the IGRF. Provided that the magnetometer has a high accuracy, the consistency of the provided information about the orientation of the spacecraft depends solely on the accuracy of the model.

Almost every satellite that uses magnetometers for attitude information, uses as a model the IGRF. The parts of the IGRF that can be used on board a spacecraft are the static part describing the main field and the dynamic part that describes its secular variation. The dynamic part that describes the effect of the ring current cannot be used due to the fact that depends on the D_{st} index. Transmitting the index to a satellite is a completely impractical idea and the exclusion of this part introduces a significant source of error in the on board model. This is mainly due to fact that variations occur very often in the ring current which result in variations in the observed field by the satellite. The errors that occur in the measurements are directly imposed on the accuracy of the attitude information as the satellite has no mechanism of knowing if the activity is high or low. This is one of the reasons why magnetometers are classified as moderate accuracy sensors.

Another source of error arises from the fact that the field model is developed using a very large number of measurements from different sources, such as satellites or observatories, and from all latitudes and longitudes, in order to tune correctly the model parameters. The methodologies employed for the derivation of the model minimize the error between the resulting model and the entire pool of measurements used. This creates a fitting of the overall shape of the field and smooths out local characteristics of the field and is perceived as a second source of error.

The analytical methodology for deriving such a solution is the theory of spherical harmonics developed by Gauss. The data used for the implementation of the models developed in this thesis was acquired from Oersted, a Danish satellite that was launched in 1999 [2], with a mission objective to measure the near-earth magnetic field. The measurements acquired

are of the highest quality to date and have boosted many areas of research in geophysics.

1.2.1 Use of the Magnetic field model for Attitude Determination

Traditionally, magnetometers have been used with sun sensors in order to provide attitude measurement. They can also be used with any other type sensor to provide attitude. The advent during the last 20 years of small satellites in the scale of 10 kilograms, called nanosatellites has made the magnetometers the most suitable sensors for such small spacecraft due to their low mass and power requirements. Additionally, it offers attitude information irrespective of the orientation of the spacecraft.

This great demand for magnetometer based systems has created an entire area of research focusing on attitude determination systems based only on magnetometer measurements. Oersted itself utilized such a system. Another spacecraft, SNAP developed by the Surrey Satellite Space Center has used such a system as its only attitude determination method. These methodologies employ estimation filters that require time to converge to a solution but the techniques have not yet managed to offer an attitude determination lower than 0.9^o at best. As an alternative, we examine the accuracy of using a magnetometer with a miniature solid state gyroscope. Miniature gyros have been developed based on silicon devices which can offer performance comparable to much heavier units.

1.2.2 Objectives and Contributions

A major objective of this research was the elimination of the error of the geomagnetic field model due to the exclusion of the D_{st} dependent part and the smoothing error resulting from the entire field representation. The other major objective was to identify a system that could be used on board a nanosatellite and take advantage of the improved accuracy.

The main contributions are:

- The development of seven different models for different segments of the geomagnetic field. Additionally, the errors associated with the models is treated in terms of the angle of deviation in order to get a better insight on a corresponding inaccuracy in an attitude determination system.

- The development of a magnetic activity indicator - Mean Equatorial Magnitude Error (MEME)- for the ring current based on measurements of the spacecraft over the equatorial region. No attitude information is required. The validity of the new index is confirmed by the identification of the ring current activity.

- The development of the models for the representation of the ring current effect based on the MEME index. In order to provide adaptation to the character of the disturbance 16 models are developed, each for a different category of disturbance and a different scenario of side of measurement and side of use.
- Evaluation of the performance of the new models and the MEME dependent model on a conceptual attitude determination system design.

1.3 Thesis Layout

The thesis is organized as follows:

- **CHAPTER 2 - The Geomagnetic Field and its Modelling** First a qualitative description of geomagnetic field and the magnetospheric phenomena is presented. This is followed by the theory behind the quantitative modelling of the geomagnetic field. A review of the latest model is presented and the problems and limitations are identified.
- **CHAPTER 3 - Field Segmentation and a New Index - MEME** The limitations and problems are analysed and the proposed solutions are formed. The segmentation methodology is devised and the method for the derivation of the MEME index and its use for the derivation of the corresponding models is also presented. Finally the data selection is presented together with extra statistical measures of the error.
- **CHAPTER 4 - Results - Segmentation, MEME** In this chapter results and associated discussion for the segmented modelling are first given. Then the results from the evaluation of MEME as a consistent indicator of the ring current activity is given. Finally the results from the derivation of the MEME dependent models are presented.
- **CHAPTER 5 - The Model in an Attitude Determination System** The general theory of spacecraft dynamics and kinematics is presented, followed by an examination of suitable attitude determination components for a nanosatellite and their feasibility. This is followed by a choice of methodology for attitude determination and the choice of the components that will be considered in the conceptual design. Finally a nanosatellite conceptual design is derived for testing and the expected disturbances are evaluated.
- **CHAPTER 6 - Testing and Results for Attitude Determination** This chapter presents the testing and the results for the chosen configuration of sensors. First the

system is evaluated for a set of magnetically quiet days for different sampling rates, angular velocities and segments. Then it is evaluated for a set of magnetically disturbed days and the errors are compared with and without the MEME dependent part.

- **CHAPTER 7 - Conclusions and Recommendations** Conclusions are drawn from all parts of the work reported here. Also recommendations for future work are given.

Chapter 2

The Geomagnetic Field and its Modelling

2.1 Qualitative Description of the Geomagnetic Field

2.1.1 Introduction

The science of geomagnetism is the oldest branch of geophysics, and possibly even one of the oldest branches of scientific study in general. The magnetic compass was probably in use in China before the birth of Christ, and the records exist in Europe of scientific study of the geomagnetic field from around 1200 onwards, culminating in the book De Magnete by William Gilbert, published in 1600, arguably the first truly modern scientific text.

He demonstrated that the Earth behaved "like a giant magnet", as if the Earth were a uniformly magnetized iron sphere. Although this was an astonishing insight, unsurprisingly the real situation is more complicated. The geomagnetic field can be broadly divided into three parts, all of which are the subject of major scientific study. The dominant component is the so-called *"main field"*, with strength between $20000nT$ and $70000nT$ at the Earth's surface. The field is generated by a hydrodynamic dynamo operating in the earth's fluid core. This is the one that gives the basic dipole structure of the field, allowing the simple use of the compass for navigation. It varies, although slowly. The strength of the dipole field is currently decaying by about 1% every 10 years. Using this variation, we can probe the nature of the earth's core and its interaction with the rest of the earth. In particular, we can construct models of the fluid flow at the core surface, and investigate the effect of changes in core flow on earth rotation.

The second contribution comes from the earth's lithosphere, from magnetized rocks, of

typical magnitude hundreds of nanoTesla. This part of the field is much used in geophysical prospecting, and was an important foundation (through sea-floor magnetic anomalies) for the theory of plate tectonics. New maps of the long wavelength magnetic field promise new insights into the earth's structure and tectonics on continental scales.

The third contribution comes from outside the earth, and, in particular, from current systems in the ionosphere and magnetosphere. This part of the field can vary rapidly, depending in particular on solar activity. In quiet times it has magnitude of about $20nT$. During a magnetic storm this can increase more than ten-fold. External magnetic fields can pose a significant natural hazard, causing damage to, for example, power grids, telecommunications systems and oil pipe lines. The understanding and mitigation of this hazard, generally known as space weather, rests on the foundations of a detailed knowledge of the near-earth magnetic environment.

The fundamental requirement for understanding the magnetic field is detailed measurement. To understand the detailed temporal behavior of the field on time scales of seconds to decades requires detailed stable measurements at a single location. This is the role played by the worldwide network of magnetic observatories. However, these measurements do not provide the truly global distribution of data required for accurate field modelling for both scientific and practical applications. This can only be achieved by measurement from satellites, in our case Oersted [3], which is providing data of unrivaled sensitivity and quality.

2.1.2 Internal Field

The earth's magnetic field near to its surface can be approximately described as that of a dipole or of a uniformly magnetized sphere. In reality however, there is a significant deviation from this idealized assumption. One deviation is due to the fact that the axis of the dipole does not coincide with the geographic axis passing through the north and south geographic poles. Additionally, the magnetic field lines do not form great circles and the antipodal symmetry of a dipole is highly corrupted in the case of the geomagnetic field. Over specific regions of the planet the deviation from a dipole is very significant and has a constant character. Such areas are middle Asia, South Africa, the surrounding oceans and northern Canada.

These anomalies are called *regional* and they are the main sources of distortion of the dipole. Superposed on the regional anomalies, are the *local anomalies* which occur in a much smaller spatial scale and their effects on the dipole are much smaller than the regional.

Such local anomalies appear in many places on the planet such as Kursk in Russia, Lapland, Finland,and East Prussia. These local anomalies tend to appear as small local dipoles which are both distinct and separated from the magnetic field lines of the main field. In addition to the spatial anomalies, the geomagnetic field also exhibits a temporal variation. This temporal variation appears both in the average magnitude of the field as well as the direction of the dipole axis relative to the geographic axis of rotation. The internal field has two components:

- the crustal field.
- the core field.

2.1.2.1 The crustal field

The spatial attenuation of the field by the inverse square of distance means that the short wavelength variations at the earths surface must have a shallow source. It cannot be much deeper than mid crust, since otherwise the temperatures would be too high. More is known about the crustal field than about the core field since we know more about the composition and physical parameters such as temperature and pressure and about the types of magnetization.

There are two important types of magnetization. The first is called *remanent magnetization* (there is a field even in absence of an ambient field). If this persists over time scales of 10^8 years, it is called *permanent magnetization.* Rocks can acquire permanent magnetization when they cool beneath the Curie temperature (about $500 - 600^oC$ for most relevant minerals). The ambient field then gets frozen in, which is very useful for paleomagnetism. The second type is called *induced magnetization* (no field, unless induced by an ambient field). No magnetic field exists on the mantle. The reason for this is firstly because the mantle consists mainly of silicates and the average conductivity is very low. Secondly, fields in a low conductivity medium decay very rapidly unless sustained by rapid motion, but convection in the mantle is too slow for this to happen. Thirdly, permanent magnetization is not possible since mantle temperatures are too high (higher than the Curie temperature in most of the mantle).

2.1.2.2 The core field

In the earth's core the temperatures are too high for permanent magnetization. The field is caused by rapid (and complex) electric currents in the liquid outer core, which consists

mainly of metallic iron. Convection in the core is much more vigorous than in the mantle: about 10 times faster than mantle convection (i.e, of the order of about $10km/yr$).

The core field has the following characteristics:

- 90% of the field at the earths surface can be described by a dipole inclined at about 11^oC to the earths spin axis. The axis of the dipole intersects the earths surface at the so called geomagnetic poles at about (78.5^o N, 70^oW) (West Greenland) and (75.5^o S, 110^o E).

- The remaining 10% is known as the non-dipole field and consists of a quadrupole and an octopole, etc. At the core-mantle-boundary the relative contribution of these higher degree components is much larger. This relative contribution 90% to 10% can change over time as part of the secular variation.

- The strength of the earths magnetic field varies from about $60,000nT$ at the magnetic pole to about $25,000nT$ at the magnetic equator on earth's surface.

2.1.3 Secular variation

The westward drift and changes in the strength of the dipole field are very important factors. Secular variation is loosely used to indicate slow changes with time of the geomagnetic field (declination, inclination, and intensity) that are (probably) due to the changing pattern of core flow. The term *secular variation* is commonly used for variations over time scales of 1 year and longer. This means that there is some overlap with the temporal effects of the external field, but in general the variations in the external field are much more rapid and much smaller in amplitude so that the correlation is, in fact, small. There are at least three important phenomena:

- Change in the strength of the dipole. The relaxation time of the dipole is about 1000 years; in other words, the current rate of change of the strength of the dipole field is about 8% per $100yrs$. Note that this represents a snapshot of a possibly complex process, and it does not necessarily mean that we are headed for a field reversal within 1000 years.

- Change in orientation of the main field. The orientation of the best fitting dipole appears to change with time, but on average, say over intervals of several tens of thousands of years, it can be represented by the field of an axial dipole. For London,

over the last 400 years, the change in declination and inclination describe a clockwise, cyclic motion which is consistent with a westward drift of the field.

- Westward drift of the field. The westward drift is about $0.2^o/yr$ in some regions. Although it forms an obvious component of the secular variation in the past $300-400$ years, it may not be a fundamental aspect of secular variation for longer periods of time. Also there is a strong regional dependence. It is not observed on the Pacific realm, and it is mainly confined to the region between Indonesia and the Americas.

The slow variation of the field with time is most likely due to the reorganization of the lines of force in the core, and not to the creation or destruction of field lines. The variation of the strength and direction of the dipole field probably reflect oscillations in core flow. The westward drift has been attributed to one of two mechanisms:

- Differential rotation between core and the mantle
- Hydromagnetic wave motion: standing waves in the core that slowly migrate westward, but without differential motion of material. Like many issues in this scientific field, this problem has not been resolved and the cause of the secular variations are still under debate.

2.1.4 Magnetospheric topology

The field lines of the geomagnetic field extend upward through the neutral atmosphere. In the ionosphere the effect of the magnetic field is quite considerable. An important component of the ionosphere are ionized particles, which are affected greatly by magnetic fields. The earth's magnetic field thus greatly influences the electrical currents owing in the ionosphere. At yet larger altitudes, the effects of the magnetic field become even more critical. Above the ionosphere, the effects are so important that this region is termed the **magnetosphere** for the strong control that the magnetic field exerts in this region.

The effects of the earth's magnetic field on the space environment only extend over a limited distance. The sun is also a source of a magnetic field which interacts with that of the earth. In addition, a constant outpouring of plasma from the sun creates a continuous supersonic wind - the solar wind - of particles. As the plasma is ejected from the solar surface its force exceeds that of the magnetic field, and the magnetic field is dragged along with the plasma. As the magnetized solar wind flows past the earth's magnetosphere a collisionless

shock is formed as the flow diverts around the magnetic obstacle and a boundary surface is created between the solar wind and the magnetospheric cavity.

The location of these boundaries are dictated by the pressure equilibrium that must be maintained between the plasma and magnetic field of the magnetospheric cavity, and the dynamic pressure of the plasma and magnetic field of the solar wind. Depending on the properties of the solar wind, the magnetopause may either allow leakage of plasma and energy across into the magnetosphere, or completely shut out the solar wind. This leakage may give rise to major dynamical modes of the magnetosphere, such as geomagnetic storms and substorms. Inside the magnetospheric cavity there exist different regions of the magnetosphere, with a wide variety of properties. These properties depend largely on the locations of the regions, the shape and strength of the magnetic field in the regions, and how the magnetic field lines that flow through those regions connect to other regions of space.

Figure 2.1 is a schematic of the current understanding of the configuration of the average static magnetosphere. The magnetopause, which is represented by the lightly dotted surface

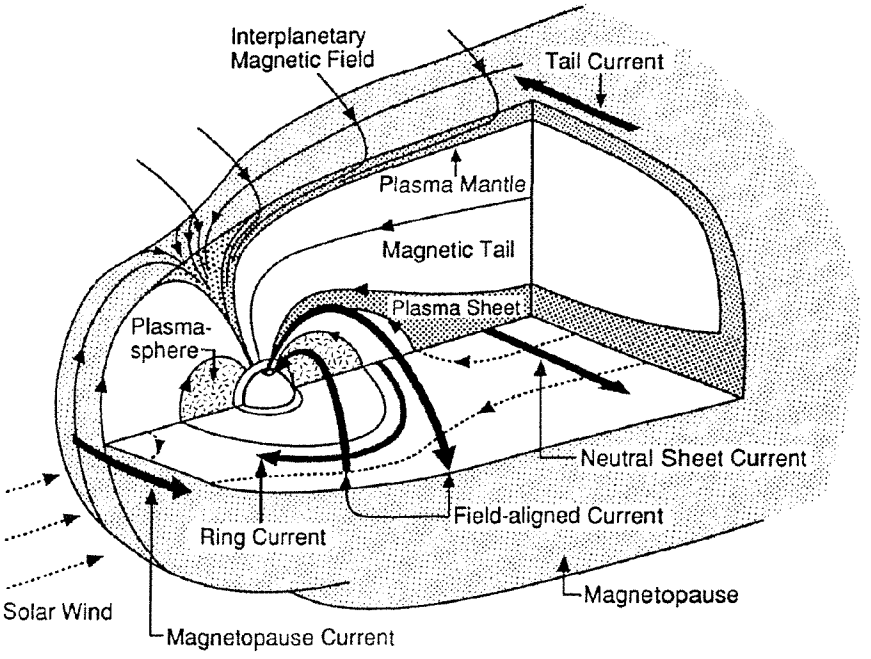

Figure 2.1: Magnetospheric Topology and Current Systems

in Figure 2.1 is the boundary surface between the shocked solar wind and the magnetosphere. In order to maintain the magnetic field configuration of the magnetosphere, a current flows

along the magnetopause. A reverse current flows inside the magnetosphere from its dawn side to its dusk across the length of its tail. This is the plasma sheet current or neutral sheet current. The plasma sheet consists of relatively dense and hot plasma confined on closed but severely stretched field lines connecting to the high-latitude regions of the nightside of the earth. The plasma in the plasma sheet consists mainly of ionospheric particles that have drifted out of the ionosphere. On either side of the plasma sheet can be found the magnetotail lobes. The lobes are almost completely free of plasma. They are thought to connect to the high-latitude polar cap region of the earth at one end, and into the solar wind at the other end. Consequently plasma that escapes the ionosphere on a lobe field line will likely either escape the magnetosphere or drift into the plasma sheet. Close to the earth, the plasma sheet particle population merges with the energetic ring current particle population. In this thesis particular attention will focus on the region closer to the earth than the plasma sheet, typically within 2 earth radii (RE) of the center of the earth. This is the region in which the largest spatial variations can be seen.

Particles fluxes can vary by many orders of magnitude yet there is a certain overall structure to this region. A good fundamental understanding of the average configuration of the inner magnetosphere is very useful for studying dynamical processes. These can then be treated as perturbations to the average configuration. Extensive work has already been done on this for the magnetic field, but with significant room still left for improvement. For example, there is not yet an "average" global substorm evolution model. Over the past twenty years, significant improvement has been made in the representation of the magnetic field. A good summary of early work can be found in Walker [4]. Some of the most popular models are due to Tsyganenko and Usmanov [5], and Tsyganenko [6], [7]. These magnetic field models are today used exactly as background frameworks for studies. Perturbations are applied to them in order to model real dynamical phenomena, or they are used as a proxy for tracing the connection between different regions of the magnetosphere.

Sugiura et al. [8] created the first comprehensive map of magnetic field magnitude variations in near earth space. They found significant variations from the dipole magnetic field which were observed even deep in the inner magnetosphere, inside of 2RE. This variation exists even during quiet periods, and varies with geomagnetic activity, as measured by the ground magnetic index K_p, suggesting that a significant ring current is present even during quiet conditions. They further suggested that the storm time ring current is then merely an intensification of the quiet ring current. Lui et al. [9] studied the ring current particle popu-

lation during two geomagnetic storms using single passes of the high altitude AMPTE/CCE satellite on the afternoon side. From measurements made near the magnetic equator, they observed a pressure profile first increasing towards the earth until near 3RE, and then a sharp inward drop in pressure. The derived electric current profiles resulted in an eastward current inside of 3RE, and a westward ring current outside of 3RE.

Ijima et al. [10] analyzed the large scale properties of the currents in the inner magnetosphere using AMPTE/CCE measurements in the region 4 to $8RE$. They found that the equatorial currents in that region flow predominantly westward. Also they observed a strong noon-midnight asymmetry in the total current, with the current on the nightside being 2 to 3 times larger than the dayside currents. Lui and Hamilton [11] produced radial profiles of the quiet time (as characterized by the ground magnetic index D_{st}) magnetospheric parameters along single orbits. They observed a pressure peak in the near midnight region just inside of 3RE. In the limit of MHD equilibrium, this pressure peak corresponds to an eastward current inside of this region, and a westward current outside this region.

De Michelis et al. [12] derived the average terrestrial ring current from measurements made by the AMPTE/CCE/CHEM experiment. They found both the inner eastward and outer westward ring current from pressure measurements. They also found that the total current in the inner ring current is slightly smaller than that in the outer ring current, resulting in a net westward ring current. Furthermore, they found that for a fixed magnetic local time (MLT), the ring current is a function of geomagnetic activity (they used AL as their indicator of geomagnetic activity), and that for a fixed geomagnetic activity level, the ring current is a function of MLT, with peak current at around $23MLT$, $2-3$ times stronger than the current on the dayside.

A recent study of the magnetic field in the region $2RE-5RE$ was performed by Nakabe et al. [13]. They used magnetometer data from the DE-1 spacecraft, which sampled out to $5RE$ at all latitudes. They grouped the magnetic field measurements according to location and activity to create plots of field deviation, which were then used to calculate currents. They did not find any eastward current on the nightside, and found a very strong eastward current on the dayside, which was independent of activity as measured by D_{st}. The result of seeing no eastward current at midnight is in contrast to all of the results referred to above.

A similar study by Nakai et al. [14] calculated the average configuration of the magnetotail current using the ISEE-1 data for 1978 to 1987. This was done both for "disturbed" and "quiet" periods as measured by the AL index. A variation of the cross-tail current was

found, but no significant signature of a "current disruption" in the inner magnetosphere was found. There appears to be a general agreement in the literature concerning the existence of an asymmetric ring current. There is, however, no good agreement as to whether this asymmetric component exists on the dusk side, or on the nightside of the magnetosphere, nor if it exists at all times, or only during the main phase and early recovery phase of geomagnetic storms.

2.1.5 Indices of magnetic Activity

In space physics, the use of geomagnetic indices is often used to characterize magnetospheric phenomena. An index is essentially a single number on a scale that determines the magnitude (or some other quantity) of a magnetospheric phenomenon. In this thesis, use will be made of three such measures of activity: the AE family of indices, the D_{st} index, and the K_p index. All of these indices are derived from ground magnetometer measurements; details of their derivation may be found in Mayaud [15]. In each instance, these indices provide a simple measure of the three-dimensional dynamic electrical currents existing in geospace. These changing currents are driven by the dynamics of the solar wind-magnetosphere interaction, and conveniently, their gross, collective effects can be recorded at the surface of the earth.

The K_p index is calculated on a 3-hour time scale, and is therefore only useful for looking at very long trends of activity, such as storms. The procedure used to derive the K_p index is quite complex. It is composed of individual K indices measured at stations distributed in Europe, North America, and New Zealand. The K indices measure the range of magnetic variations during the 3-hour period the index is measured over, and the planetary K_p is the arithmetic average of the individual station K's. The K_p index is mainly useful for measuring a global level of magnetospheric disturbance.

To measure the ring current intensity, the D_{st} index is used. This index is calculated as the average detection from the average quiet value of a set of magnetic observatories placed around the geomagnetic equator. This is in principle a very simple index to calculate. In practice, however, there are many secular variations to consider and which must be subtracted from it. Since this index measures an "absolute" deviation from a "quiet" level, and the secular variations can be as large or even larger than the external variations, proper subtraction is vitally important. The D_{st} index is calculated at a resolution of 2.5 minutes, but in practice most available D_{st} index data is available at a resolution of 1 hour. While the D_{st} index is excellent at measuring the ring current strength, it has virtually no response

to auroral variations. This is because it measures only field variations that are detectable at low latitudes.

The AE index family measures the maximum global variation of the magnetic field in the auroral zone and is therefore appropriate for substorm studies. A number of magnetic field stations are located in the auroral zone. These are subject to similar secular variations to the D_{st} index stations, and similar corrections need to be performed, since this index also measures the absolute deviation from a "quiet" level. From these data four indices are derived. The Auroral Lower (AL) index is at any given time the lowest value of the deviation from the quiet levels of any stations horizontal component. The Auroral Upper (AU) index is the highest deviation from quiet level of any station. The Auroral Envelope (AE) is defined as $AE = AU - AL$, and AO is defined by $AO = AU + AL$. With these definitions, the indices will always satisfy the following inequality: $AE \geq AU \geq AO \geq AL$.

2.1.6 Magnetic Storms and Substorms

The two most important large-scale phenomena in the earth's magnetosphere are storms and substorms. A geomagnetic storm develops when the geomagnetic coupling between the solar wind and the earth's magnetosphere becomes strong and prolonged. Magnetic storms have been studied with increasing sophistication using better data and theory since the first thorough treatment by Chapman and Ferraro [16], [17], [18]. The beginning of the magnetic storm is often marked by a sudden increase in the D_{st} index. This is caused by the earthward motion of the magnetopause with increased solar wind pressure. This sudden decrease is followed by a period, which can last between several hours up to a day, in which the D_{st} index decreases sharply. This period is caused mainly by injection of energetic ions into the inner magnetosphere. These energetic ions will drift westward around the earth, and form or enhance the ring current. The ring current magnetic field is directed in such a way that it opposes the surface magnetic field of the earth. This decrease in the surface magnetic field is then a measure of the strength of the ring current, and the severity of the storm. This is the main phase of the storm.

The main phase is followed by the recovery phase. During the recovery phase of the storm, the enhanced ring current decays. Substorms are much more frequent than storms. The auroral substorm was first described fully by Akasofu [19] from the ground-based view and the magnetospheric substorm by Russell and McPherron [20], and McPherron [21]. On average, several substorms occur each day, while typically large storms only occur once per

month.

Conversely, a substorm is a much milder perturbation of the inner magnetosphere than the storm, and decays away in a few hours whereas the storm takes several days to decay fully. The substorm is the sequence of events that occur when the IMF turns southward, resulting in energy being loaded into the magnetosphere. During the substorm, previously quiet and dim auroral arcs suddenly brighten, and go through a sequence of evolutions. The auroral brightenings are the results of precipitation from the magnetosphere as well as horizontal currents owing to the ionosphere in a circuit closed in the magnetosphere.These currents serve to reconfigure the earth's magnetic field from the highly stressed configuration that was induced by the solar wind's driving of the magnetosphere into a relaxed configuration.

Although both storms and substorms are global phenomena, they include localized complex variations that often have amplitudes as large the local measurement of the global properties of the storm or substorm. For this reason, studying storms and substorms from single point measurements give rise to ambiguities which have hampered the study of both fields. In recent years, multi-point measurements, including many space-based and ground based observatories have somewhat alleviated this situation.

2.2 Quantitative modelling of the geomagnetic field

2.2.1 Laplace's Equation

Helmholtz's theorem states: "If a vector field F defined in the Eucledian space(R^3), which is continuously differentiable in all this space except across certain surfaces of jump discontinuities, approaches zero at infinity then it is uniquely defined by its divergence, curl and jump discontinuities" [22]. This is translated by expressing a field F in terms of two parts, the divergence and the curl:

$$F = -\nabla V + \nabla \times A \tag{2.1}$$

The two potentials V and A are different in nature. In particular V is a scalar and A is a vector field. These definitions of the divergence and curl of the vector field F are justified by the following integral expressions:

$$V(r) = \frac{1}{4\pi} \int d^3s \frac{\nabla \cdot F(s)}{\mid r - s \mid} \tag{2.2}$$

$$A(r) = \frac{1}{4\pi} \int d^3s \frac{\nabla \times F(s)}{\mid r - s \mid} \tag{2.3}$$

It is important to note here Maxwell's equations and the applicability of this theorem in solving them:

$$\nabla \times E = -\vartheta_t B \tag{2.4}$$

$$\nabla \cdot E = \frac{\rho}{\epsilon_0} \tag{2.5}$$

$$\nabla \times B = \mu_0(J + \epsilon_0 \vartheta_t E) \tag{2.6}$$

$$\nabla \cdot B = 0 \tag{2.7}$$

where ρ is the charge density, J is the current density, μ_0 is the permeability of vacuum, ϵ_0 is the permittivity of vacuum, E: electric field, B is the magnetic field. For simplicity at this early stage of analysis, static conditions are assumed. This means that only static charges and steady current flows exist. Under these conditions, $\vartheta_t E = 0$ and consequently $\nabla \times B = \mu_0 J$ or $J = \nabla \times \frac{B}{\mu_0}$. Taking the divergence of the last equation leads to

$$\nabla \cdot J = 0 \tag{2.8}$$

This obviously leads to $\nabla \cdot A = 0$.

The analysis here is targeted at examining the behavior of a field with the above characteristics and which emanates from within a sphere of radius α, such as earth in the case of the geomagnetic field. The earth can be represented to a first abstract approximation by a sphere of radius a. The electric charges are assumed static and the electric currents are assumed to have a constant flow rate. Both charges and currents are confined within the sphere. The electric field E and the magnetic field B produced from these charges and currents respectively are extended to infinity according to inverse square law of distance [23]. If the ball is denoted by $Ball(a)$, then its boundary is represented by $\vartheta Ball(a)$. Due to the assumption that no electric charges or currents exist outside the sphere, the charge density ρ and the current density J should vanish on the boundary $\vartheta Ball(a)$ and for $r \geq a$. Then(2.7) states that $\nabla \cdot B = 0$ which means that the divergence of the magnetic field is zero. Substituting in (2.2) whose divergence is one of the descriptive elements of B we have that

$$V(r) = \frac{1}{4\pi} \int d^3 s \frac{\nabla \cdot B(s)}{\mid r - s \mid} = 0 \tag{2.9}$$

Consequently $B = \nabla \times A$. The vector field A is called the *magnetic vector potential.* It has been also shown that because all the charges are assumed to be in the steady state $\nabla \times B = \mu_0 J$. Now looking at the general expression for the vector potential in the Helmoltz

equation (2.3) we have that:

$$A(r) = \frac{1}{4\pi}\int d^3s \frac{\nabla \times B(s)}{\mid r - s \mid} \leftrightarrow A(r) = \frac{1}{4\pi}\int d^3s \frac{J(s)}{\mid r - s \mid} \tag{2.10}$$

and it follows that the vector potential $A(r)$ vanishes in regions free of currents. In such areas, the resulting field is expressed as the gradient of a scalar function.

$$F = -\nabla V \tag{2.11}$$

In the case of the magnetic field this can be written as:

$$B = -\nabla V \tag{2.12}$$

and substituting this expression for B into the fourth Maxwell equation (2.7) we obtain:

$$\nabla^2 V = 0 \tag{2.13}$$

This is the well known *Laplace equation.* Steady state magnetic fields obey this equation when there are no charges or current present. The operator

$$(\nabla \cdot \nabla) = \nabla^2 = \frac{\vartheta}{\vartheta x} + \frac{\vartheta}{\vartheta y} + \frac{\vartheta}{\vartheta z} \tag{2.14}$$

is termed the *Laplacian* in Cartesian coordinates.

2.2.2 Harmonic functions

The three vector components of the geomagnetic field can be described as the gradient of a scalar potential function (Maxwell equations) in the Cartesian coordinate system. The three components satisfy then *Laplace*'s equation. If f is a scalar function, then the Laplace equation in Cartesian coordinates is:

$$\frac{\vartheta^2 f}{\vartheta x^2} + \frac{\vartheta^2 f}{\vartheta y^2} + \frac{\vartheta^2 f}{\vartheta z^2} = 0 \tag{2.15}$$

Two important comments have to be made here:

- A solution of the Laplace's equation is termed a "harmonic function".
- Since the Laplace equation is linear, the sum of two or more individual solutions is also a solution.

The most common method of solving the Laplace equation is to seek a "separable solution' given by the product of the independent functions of x, y, z as follows:

$$f(x, y, z) = A(x)B(y)C(z) \tag{2.16}$$

Every solution can be expressed as a sum of solutions of this form. Substituting the solution of (2.16) into the Laplace equation and evaluating the derivatives gives:

$$\frac{d^2A(x)}{dx^2}B(y)C(z) + A(x)\frac{d^2B(y)}{dy^2}C(z) + A(x)B(y)\frac{d^2C(x)}{dz^2} = 0 \tag{2.17}$$

Dividing by the product $A(x)B(y)C(z)$ now results in:

$$\frac{1}{A(x)}\frac{d^2A(x)}{dx^2} + \frac{1}{B(y)}\frac{d^2B(y)}{dy^2} + \frac{1}{C(z)}\frac{d^2C(x)}{dz^2} = 0 \tag{2.18}$$

Since x, y, z are independent (they can be varied independently), this equation can only be identically satisfied if each one of the three terms is a constant and these three constants sum to zero. As the equation involves the second partial derivatives it is convenient to represent the three constants as α^2, β^2 and γ^2 respectively. This results in three independent ordinary differential equations:

$$\frac{1}{A(x)}\frac{d^2A(x)}{dx^2} = \alpha^2 \qquad \frac{1}{B(y)}\frac{d^2B(y)}{dy^2} = \beta^2 \qquad \frac{1}{C(z)}\frac{d^2C(x)}{dz^2} = \gamma^2 \tag{2.19}$$

with the condition $\alpha^2 + \beta^2 + \gamma^2 = 0$.

Taking the first of these equations and rearranging gives:

$$\frac{d^2A(x)}{dx^2} - \alpha^2 A(x) = 0 \tag{2.20}$$

which is the equation of harmonic motion and hence the characteristic polynomial is:

$$s^2 - \alpha^2 = 0 \tag{2.21}$$

with roots $s = \pm\alpha$. The general solution of the differential equation here is:

$$A(x) = a_1 e^{\alpha x} + a_2 e^{-\alpha x} \tag{2.22}$$

for constants a_1 and a_2. The same procedure and form of solutions hold for $B(y)$ and $C(z)$. Hence the overall solution to Laplace's equation is of the form:

$$f(x, y, z) = (a_1 e^{\alpha x} + a_2 e^{-\alpha x})(b_1 e^{\beta y} + b_2 e^{-\beta y})(c_1 e^{\gamma z} + c_2 e^{-\gamma z}) \tag{2.23}$$

where a_i, b_i and c_i are arbitrary constants and α,β and γ are any complex constants such that $|\alpha|^2 + |\beta|^2 + |\gamma|^2 = 0$. By summing terms of this general form using the techniques of Fourier analysis we can determine the values of these constants necessary to match any given boundary conditions.

The above analysis is useful when the boundary conditions are easily expressible in terms of Cartesian coordinates. However, in cases such as the modelling of the geomagnetic field,

the boundary conditions are better expressed in curvilinear coordinate systems. The general form of the Laplacian operator for an arbitrary(differentiable) coordinate system x^k, $k = 1, 2, 3$ with the metric tensor g_{ij} is:

$$\nabla^2 f = \frac{1}{\sqrt{g}} \sum_{m=1}^{3} \sum_{n=1}^{3} \frac{\vartheta}{\vartheta x^m} \left(\sqrt{g} g^{mn} \frac{\vartheta f}{\vartheta x^n} \right) \tag{2.24}$$

where g is the determinant of the covariant metric tensor. If the basis vectors of the coordinate system are mutually orthogonal at each point, then the fundamental line element has the diagonal form:

$$(ds)^2 = (h_1 dx^1)^2 + (h_2 dx^2)^2 + (h_3 dx^3)^2 \tag{2.25}$$

where $h_i = \sqrt{g_{ii}}$. In this case we have $\sqrt{g} = h_1 h_2 h_3$ and $g_{ij} = 0$ for all $i \neq j$. Also the non-zero components of the contravariant metric are $g^{ii} = \frac{1}{g_{ii}}$, so the Laplacian in terms of orthogonal coordinates has the form:

$$\nabla^2 f = \frac{1}{h_1 h_2 h_3} \left[\frac{\vartheta}{\vartheta x^1} \left(\frac{h_2 h_3}{h_1} \frac{\vartheta f}{\vartheta x^1} \right) + \frac{\vartheta}{\vartheta x^2} \left(\frac{h_1 h_3}{h_2} \frac{\vartheta f}{\vartheta x^2} \right) + \frac{\vartheta}{\vartheta x^3} \left(\frac{h_1 h_2}{h_3} \frac{\vartheta f}{\vartheta x^3} \right) \right] \tag{2.26}$$

This general expression is useful when a change of coordinates is necessary. If the desired coordinate system is spherical coordinates r, θ, ϕ then the expressions for the Cartesian coordinates are:

$$x = r \sin(\theta) \cos(\phi) \qquad y = r \sin(\theta) \cos(\phi) \qquad z = r \cos(\theta) \tag{2.27}$$

The spherical coordinate basis vectors in the r,θ and ϕ directions are mutually orthogonal at each point. So we can express the Laplacian in terms of the spherical coordinates by means of (2.26). The line element for spherical coordinates is found by simply evaluating the derivatives $\frac{ds}{dr}$, $\frac{ds}{d\theta}$, $\frac{ds}{d\phi}$ along the coordinate axes to give:

$$(ds)^2 = (dr)^2 + r^2 (d\theta)^2 + r^2 \sin^2(\theta) (d\phi)^2 \tag{2.28}$$

and we have $h_r = 1$, $h_\theta = r$, $h_\phi = r \sin(\theta)$.

As in the case of Cartesian coordinates, we can focus on separable solutions, i.e. solutions of the form:

$$f(r, \theta) = A(r) B(\theta) \tag{2.29}$$

Evaluating the Laplacian, equating this to zero, and dividing by $A(r)B(\theta)$ gives:

$$r^2 \frac{\ddot{A}(r)}{A(r)} + 2r \frac{\dot{A}(r)}{A(r)} + \frac{\ddot{B}(\theta)}{B(\theta)} + \frac{\cos(\theta)}{\sin(\theta)} \frac{\dot{B}(\theta)}{B(\theta)} = 0 \tag{2.30}$$

where dots denote derivatives of the function with respect to the argument. Since r and θ are independent variables, this equation can be identically satisfied only if the sum of the first two terms is constant and the sum of the last two terms is constant. Denoting these constants by μ, v we have two separate ordinary linear differential equations:

$$r^2\ddot{A}(r) + 2r\dot{A}(r) - \mu A(r) = 0 \tag{2.31}$$

$$\sin(\theta)\ddot{B}(\theta) + \cos(\theta)\dot{B}(\theta) - v\sin(\theta)B(\theta) = 0 \tag{2.32}$$

subject to $\mu + v = 0$. We could solve these explicitly, but notice that the first one is satisfied by setting $A(r) = r^n$ provided we set $\mu = n(n+1)$. Also if we set $B(\theta) = \cos(\theta)$, the second equation is satisfied with $v = 0$. Hence the function $f(r,\theta) = r^n\cos(\theta)$ is a solution of Laplace's equation provided $n(n+1) = 0$, which implies that $n = 0$ or $n = -1$. More generally, we can consider solutions which are linear combinations of functions of the form:

$$f(r,\theta) = r^n P_n(\cos(\theta)) \tag{2.33}$$

where $P_n(x)$ is a polynomial. Substitution in the axially symmetric form of Laplace's equation(2.26) now gives:

$$n(n+1)r^n\left(P_n(\cos(\theta)) + r^n(\sin^2(\theta))\ddot{P}_n(\cos(\theta)) - 2\cos(\theta)\ddot{P}(\cos(\theta))\right) \tag{2.34}$$

where the notes denote derivatives of $P_n(x)$ with respect to x. Dividing through by r^n, replacing $\cos(\theta)$ with x, and using $\sin^2(\theta) = 1 - \cos^2(\theta)$, now gives:

$$(1-x^2)\ddot{P}_n(x) - 2x\dot{P}_n(x) + n(n+1)P_n(x) = 0 \tag{2.35}$$

There is a unique (up to a constant factor) polynomial P_n for each value of $n(n+1) = k$, which implies that each polynomial here is compatible with two distinct values of n, i.e., the two roots $\hat{n}$ and $\acute{n}$ of $n^2 + n = k$. Of course, n need not to be an integer, but if it is, we can easily determine the polynomial $P_n(x)$ that satisfies the above equation, by simply inserting a polynomial with undetermined coefficients into the equation and solving for the coefficients. The results for the first few values of n are as shown in Table 2.1.

The general formula for evaluation of the Legendre function is:

$$P_n(x) = \frac{1}{n!2^n}\frac{d^n}{dx^n}(x^2-1)^n \tag{2.36}$$

Up to a scale factor these are the Legendre polynomials (discussed next). We can express an axially symmetrical solution of the Laplace equation as a linear combination of these individual solutions as follows:

$$f(r,\theta) = \left(a_0 + b_0\frac{1}{r}\right) + \left(a_1 r + b_1\frac{1}{r^2}\right)\cos(\theta) + \left(a_2 r^2 + b_2\frac{1}{r^3}\right)\left(3\cos^2(\theta) - 1\right) + \cdots \tag{2.37}$$

n	$\acute{n}$	k	$P(x)$
0	-1	0	1
1	-2	2	x
2	-3	6	$3x^2 - 1$
3	-4	12	$5x^3 - 3x$
4	-5	20	$35x^4 - 30x^2 + 3$

Table 2.1: Legendre Polynomials

where the a_i and b_i are arbitrary constants. The factors of the form $P_n(\cos(\theta))$ in this expansion are called **zonal harmonics** and note that if a continuous function $f(x, y, z)$ is a solution of Laplace's equation then the mean value of f on any sphere centered on the point p is equal to the value $f(p)$ at this point. The proof of this is trivial consequence of the *Divergence Theorem*. Another way to see this is to shift p to the origin (this can be done with no loss of generality) and then expand about the origin in this new co-ordinate system to yield:

$$f(x, y, z) = c_0 + c_1 x + c_2 y + c_3 z + c_4 xy + c_5 xz + c_6 yz + c_7 x^2 + c_8 y^2 + c_9 z^2 + \cdots \quad (2.38)$$

Recall that if θ denotes the geographical latitude (zero at the equator) and ϕ the longtitude, then the mean value of a function $f(\theta, \phi)$ over the surface of a sphere of radius R is given by the double integral:

$$f_{mean} = \frac{1}{4\pi} \int_{-pi}^{\pi} \int_{-\pi/2}^{\pi/2} f(\theta, \phi) \cos(\theta) d\theta d\phi \quad (2.39)$$

Substituting $x = R\cos(\phi)\cos(\theta)$, $y = R\sin(\phi)\cos(\theta)$, $z = R\sin(\theta)$ into this last expression for f and evaluating the mean value over this sphere gives:

$$f_{mean} = c_0 + \frac{1}{3}(c_7 + c_8 + c_9)R^2 \quad (2.40)$$

Since we have placed the point p at the origin, the value of f at p is just c_0, whereas this last analysis shows that the average value of f on the sphere (up to second order) has an additional term equal to the average of the three coefficients of the squared coordinates times the square of the radius. But if we substitute our expansion for $f(x, y, z)$ into Laplace's equation we find that $c_7 + c_8 + c_9 = 0$, and therefore $f_{mean} = f(x_p, y_p, z_p)$.

Several useful facts now follow directly. For example, it's clear that a continuous differentiable harmonic function f (i.e., a solution of Laplace's equation) cannot contain a local

maximum or minimum, because by definition such points have values of f greater than (resp. less than) the values of f for all surrounding points, which would make it impossible for the average on the surface of a sphere surrounding the point to equal the value of f at that point. From this it follows that if the value of a harmonic function f has the constant value c over an entire surface that completely encloses a region of space, then the value of f must be c throughout that region. This is because if the value was anything other than c at any point in the interior of the region, then the region must contain a local maximum or minimum, which is already ruled out.

Having established this last fact, we can also see that the solution of Laplace's equation satisfying a complete set of boundary conditions is unique. To show this, suppose two distinct harmonic functions f_1 and f_2 have the same values on a closed surface, but have different values in the interior of the enclosed region. Then we know that harmonic functions are additive, so $f_1 - f_2$ is also a harmonic function, and it's value is zero over the closed surface. This, in turn, implies that the difference is zero throughout the interior region enclosed by the surface (by the above discussion), so f_1 and f_2 are identical throughout the region. The number n in (2.36) is called the *degree* of each harmonic solution.

The Legendre functions were evaluated for each degree from the radial solution of the Laplacian. The zonal harmonics however are independent of longitude. The dependence on longitude can be incorporated by the same methodology. Because the longitude has a period of 2π in spherical harmonics, a trivial solution is its approximation by a trigonometric series. After this decision, a set of functions can be evaluated similar to the Legendre functions which together with the selected function will satisfy Laplace's equation for all members of the series. The form of the overall function will be:

$$f(\theta,\phi) = \sum_{m=0}^{\inf} (a_m(\theta)\cos(m\phi) + b_m(\theta)\sin(m\phi))P_m(\theta) \tag{2.41}$$

The resulting functions must also include the Legendre functions as the zonal harmonics must also satisfy Laplace's equation. As they are dependent on both the degree n and the order of the trigonometric series m, they are more appropriately denoted by $P_{n,m}$. They are termed *associated Legendre functions* and they are derived from the zonal harmonics and the order m using the following equation:

$$P_{n,m}(x) = (1-x^2)^{\frac{1}{2}m}\frac{d^m P_n(x)}{dx^n} \tag{2.42}$$

From this last equation it is obvious that when $m > 0$ then $P_{n,m}(x) = 0$. Additionally the zonal harmonics P_n can be written as $P_{n,0}$. By repeated partial integration using (2.42) and

substituting from equation (2.36), we have that:

$$\int_{-1}^{1} P_{n,m}(x)P_{n',m}(x)dx = \frac{2}{2n+1}\frac{(n+m)!}{(n-m)!} \qquad \text{for} \qquad n = n' \tag{2.43}$$

and 0 otherwise. This result shows that the functions $P_{n,m}$ are of very diverse orders of magnitude. For example the mean values of $P_{4,1}$ and $P_{4,4}$ are in the ratio 1:2016. To eliminate this effect, Schmidt [24] defined new orthogonal functions $P_n^m(\theta)$, which are numerical multiples of $P_{n,m}(\theta)$, as follows:

$$P_n^m(\theta) = P_{n,m}(\theta) \qquad \text{when} \qquad m = 0 \tag{2.44}$$

and

$$P_n^m(\theta) = \left\{2\frac{(n-m)!}{(n+m)!}\right\}^{\frac{1}{2}} P_{n,m}(\theta) \qquad \text{when} \qquad m > 0 \tag{2.45}$$

Although not completely normalized, these have the advantage that the associated Legendre functions of higher degrees will have similar orders of magnitude to the zonal functions. The complete function which satisfies Laplace's equation is then of the following form.

$$f_{int}(r,\theta,\phi) = a\sum_{n=1}^{\text{inf}}\left(\frac{a}{r}\right)^{(n+1)}\sum_{m=0}^{n}\left(g_n^m\cos(m\phi) + h_n^m\sin(m\phi)\right)P_n^m(\theta) \tag{2.46}$$

and

$$f_{ext}(r,\theta,\phi) = a\sum_{n=1}^{\text{inf}}\left(\frac{r}{a}\right)^{n}\sum_{m=0}^{n}\left(g_n^m\cos(m\phi) + h_n^m\sin(m\phi)\right)P_n^m(\theta) \tag{2.47}$$

If we assume that the field is created by a hollow magnetized sphere then f_{int} is valid for the description of a magnetic field outside the generating sphere and f_{ext} describes the field inside the sphere, with the condition that no generating sources are located there.

The variables g_n^m, h_n^m are called *Gaussian coefficients* and are the factors that are modified to fit the geomagnetic field model to a specific pool of measurements. The variable a is the mean radius of the earth. The zonal functions are not the only orthogonal system of functions of x in the interval $-1 < x < 1$. The equations of the geomagnetic field are polynomials with coefficients derived by the least square fit algorithm from a pool of observed data.

As the magnetic scalar potential is expressed in spherical coordinates, the geomagnetic field vector can be decomposed into three components in a coordinate system parallel to the unit vectors of the spherical coordinate system. These are:

$$B_r = -\frac{\vartheta V}{\vartheta r} \tag{2.48}$$

$$B_\theta = -\frac{1}{r}\frac{\vartheta V}{\vartheta \theta} \tag{2.49}$$

$$B_\phi = -\frac{1}{\sin\theta}\frac{\vartheta V}{\vartheta \phi} \tag{2.50}$$

Hence we have that:

$$B_r = \sum_{n=1}^{k} \left(\frac{a}{r}\right)^{n+2} (n+1) \sum_{m=0}^{n} (g_n^m \cos m\psi + h_n^m \sin m\psi) P_n^m(\theta) \tag{2.51}$$

$$B_\theta = -\sum_{n=1}^{k} \left(\frac{a}{r}\right)^{n+2} \sum_{m=0}^{n} (g_n^m \cos m\psi + h_n^m \sin m\psi) \frac{\partial P_n^m(\theta)}{\partial \theta} \tag{2.52}$$

$$B_\psi = -\frac{1}{\sin\theta} \sum_{n=1}^{k} \left(\frac{a}{r}\right)^{n+2} \cdot \sum_{m=0}^{n} m(-g_n^m \sin m\psi + h_n^m \cos m\psi) P_n^m(\theta) \tag{2.53}$$

The number of terms in each of these equations depends on the degree. For a given degree N, the total number of Gaussian coefficients are :

$$N_{total} = 2 \cdot \left(\sum_{t=1}^{N+1} t \right) - N \tag{2.54}$$

For given spherical coordinates, the associated Legendre functions must be evaluated for every degree n and order m. To avoid this calculation for every n and m, the following relationships hold [25]:

$$P^{0,0} = 1 \tag{2.55}$$

$$P^{n,n} = \sin\theta P^{n-1,n-1} \tag{2.56}$$

$$P^{n,n} = \cos\theta P^{n-1,n-1} - K^{n,m} P^{n-2,m} \tag{2.57}$$

where

$$K^{n,m} = \frac{(n-1)^2 - m^2}{(2n-1)(2n-3)} \quad \text{for} \quad n > 1 \tag{2.58}$$

$$K^{n,m} = 0 \quad \text{for} \quad n = 1 \tag{2.59}$$

Similarly

$$\frac{\partial P^{0,0}}{\partial \theta} = 0 \tag{2.60}$$

$$\frac{\partial P^{n,n}}{\partial \theta} = (\sin\theta) \frac{\partial P^{n-1,n-1}}{\partial \theta} + (\cos\theta) P^{n-1,n-1} \tag{2.61}$$

$$\frac{\partial P^{n,m}}{\partial \theta} = (\cos\theta) \frac{\partial P^{n-1,m}}{\partial \theta} - (\sin\theta) P^{n-1,m} - K^{n,m} \frac{\partial P^{n-2,m}}{\partial \theta} \tag{2.62}$$

The normalized associated Legendre functions are then evaluated as:

$$P_n^m = S_{n,m} P_{n,m} \tag{2.63}$$

where

$$S_{n,0} = S_{n-1,0} \left[\frac{2n-1}{n} \right] \tag{2.64}$$

$$S_{n,m} = S_{n-1,m} \frac{2n-1}{n} \tag{2.65}$$

$$S_{n,m} = S_{n-1,m} \sqrt{\frac{(n-m+1)(\delta_m^1 + 1)}{n+m}} \tag{2.66}$$

where the Kronecker delta is defined as $\delta_j^i = 1$ if $i = j$ and 0 otherwise. Finally the geocentric inertial components are:

$$B_x = (B_r \cos(\delta) + B_\theta \sin(\delta)) \cos a - B_\phi \sin a \quad (2.67)$$

$$B_y = (B_r \cos(\delta) + B_\theta \sin(\delta)) \sin a + B_\phi \cos a \quad (2.68)$$

$$B_z = (B_r \sin(\delta) + B_\theta \cos(\delta)) \quad (2.69)$$

where

$$\delta = 90^o - \theta \quad (2.70)$$

and a is the right ascension linked to the longtitude ϕ by the following relationship:

$$\phi = a - a_G \quad (2.71)$$

where a_G is the right ascension of the Greenwich meridian or the sidereal time at Greenwich.

2.2.3 Fitting algorithms for non-Gaussian Distributions

The representation of the geomagnetic field by spherical harmonics includes terms dependent on spherical coordinates and the Gaussian coefficients which are determined by fitting the model to a pool of measurements. The equations for all three components must be satisfied in order for the model to adapt not only to the magnitude of the measured field but also to its orientation.

Satellites, such as Oersted [3], provide measurements of all the three components of the geomagnetic field accompanied by the corresponding spherical coordinates for the location of each measurement. Then the Gaussian coefficients are evaluated so that the resulting model describes as closely as possible the measured field. The concept *"as close as possible"* is translated into the least squared error between the model and the corresponding measurements.

Many researchers have established that the modelling of the geomagnetic field lies in the category of non-linear fitting problems. Cain et al. [26] showed that the error in geomagnetic field data is not Gaussian and used a non-linear iterative least-square technique. This method was used for the following years and Langel et al. [27] included higher temporal derivatives. Walker and Jackson [28] investigated the effect of assuming different distribution functions a priori of the modelling process and used the maximum likelihood linear approach. They compared Gaussian and Laplacian distributions and concluded that none describes the field

entirely and highlighted the importance of the effect of data rejection above the three standard deviation boundary. Whaler et al. [29] applied a linear inverse technique for modelling of the geomagnetic field and concluded that the maximum likelihood least squares methodology was not suitable for this task. Finally Olsen [1] using data from Oersted satellite showed that the error followed a Huber distribution (Gaussian at the center and Laplacian at the tails [30]). All of this research agrees on the fact that the geomagnetic field modelling problem should be solved as a non-linear problem. Data with a non-Gaussian distribution can be treated by two different methods, the iterative least squares method and the steepest descent Marquardt method. Both are summarized next.

2.2.3.1 Iterative least squares algorithm

General non-linear least squares fitting of the sort required for most magnetometer data, relies on some understanding of statistical distributions, estimation of functions and solving a set of equations (matrix inversion).

Suppose that our data are y_i,$i = 1, ..., N$ at points x_i. Let the parameters in the model be denoted by a_j, $j = 1, ..., M$. Calculated data points are $g_i = f(x_i, a_1, a_2, \ldots a_M)$. Define a merit function

$$\chi^2 = \sum_{i=1}^{N} \left(\frac{y_i - g_i}{\sigma_i} \right)^2 \tag{2.72}$$

Then if the errors (standard deviations) σ_i on data are independent and have a normal (*Gaussian*) distribution then the minimum value of χ^2 is the *most likely* solution and is expected that $\frac{\chi^2}{(N-M)} \approx 1$.

A normal distribution is within $\pm 2\sigma$, 68% of the time, $\pm 3\sigma$, 95% of the time. The Poisson distribution has a broader tail for small counts (Freedman et al. [31]). Since the merit function is then not quite correct, outliers can be a problem, hence their weights W_i is set to zero (Linnik [32]). At the minimum value of χ^2, its derivative with respect to each of the parameters a_j will be zero:

$$\frac{\vartheta(\chi^2)}{\vartheta a_j} = 0 \Leftrightarrow \sum_i W_i (y_i - g_i) \frac{\vartheta g_i}{\vartheta a_j} = 0 \tag{2.73}$$

where

$$W_i = \frac{1}{\sigma^2} \tag{2.74}$$

For the simplest case, the model is *linear* in its parameters, each of which is just a scale

factor times some mathematical function (which itself may be very nonlinear) so that:

$$g_i = \sum_{k=1}^{M} a_k f_k(x_i) = \sum_{k=1}^{M} a_k D_{ik} \tag{2.75}$$

Note that each *basis function* is actually just the derivative D_{ij} of the calculated model for that parameter:

$$D_{ij} = \frac{\vartheta g_i}{\vartheta a_j} = f_j(x_i) \tag{2.76}$$

In the linear case the set of equations (2.73) can be solved exactly to give the parameter values a_j. In the nonlinear case, where an exact solution is not immediately available, iterations are employed until the error reaches a minimum value. Assume that the present parameters a_j^p give g_i^p with differences $E_i = (y_i - g_i^p)$ We need to shift the parameters to $a_j = a_j^p + \Delta a_j$ to give the best (or at least a smaller) value of χ^2. Since the problem is linear, we can use (2.76) to write

$$g_i = g_i^p + \sum_k \Delta a_k D_{ik} \tag{2.77}$$

which is substituted into (2.73) to give a set of M equations:

$$\sum_i W_i \left(E_i - \sum_k \Delta a_k D_{ik} \right) D_{ij} \tag{2.78}$$

The equations are easier to manipulate when written in matrix form as:

$$\Delta a(D^T W D) - D^T W E = 0 \tag{2.79}$$

which may be rearranged to give the desired a column of parameter shifts Δa as a product of a square *least squares matrix* and a column matrix :

$$\Delta a = (D^T W D)^{-1}(D^T W E) \tag{2.80}$$

Δa is an $M \times 1$ column vector, the derivative matrix D has N rows and M columns, the weights W_{ii} form a diagonal $N \times N$ matrix W, and the differences E is a $N \times 1$ column vector. The superscript T denotes transpose (i.e.$D_{ij}^T = D_{ji}$) and -1 denotes the matrix inverse. In the linear case (such as a polynomial or straight line fit) Δa gives an immediate and exact solution, even with zero starting parameters. For a non-linear case (such as geomagnetic field data) (2.78) to (2.80) are only approximately true, so the solution must be iterated. Fortunately it can be shown that ignoring the second derivatives in (2.78) is not detrimental, since they are usually small and statistically they should cancel out when summed over the

data (Kashyap et al. [33]). Nor does this have an effect on the location of the χ^2 minimum, only on the route taken to reach it. The $M \times M$ matrix

$$C = (D^T W D)^{-1} \tag{2.81}$$

is the variance-covariance matrix. Its diagonal elements are $C_{jj} = \sigma_j^2$, the square of the statisitical standard deviation for each parameter a_j - assuming the conditions imposed above on σ_i for the data are valid. Off-diagonal elements C_{ij} give the correlation coefficients between parameters, which are helpful in identifying poor parameterization of a model. In some applications, it may be useful to include off-diagonal elements in the weight matrix W to allow for correlation between data points. This can help to give more realistic error estimates. All that is needed for least squares fits are:

a. routines to calculate the model and its derivatives for a given set of parameters and x values.

b. a routine to invert a symmetric matrix (i.e. to solve a set of equations) (Hildebrand [34]).

The non-linear nature of geomagnetic field modelling requires that the least squares solutions are iterated (Lowes et al. [35]). In a well behaved system, each iteration gets closer to the χ^2 minimum and when $\chi 2$ ceases to improve further the fit has converged.

2.2.3.2 Steepest Descent and the Marquardt method

If the χ^2 merit function (2.72) is not well approximated by a quadratic near its minimum then the iterative least squares solution may not work. Some oscillatory behavior of given Δa_j between iterations may be damped down by applying only a fraction of the calculated shifts. Worse behavior might require some time consuming trial and error on key parameters. Following the *steepest descent* gradient of the χ^2 surface may be an alternative route to the desired minimum. Least squares algorithms tend to spiral down at right angles to the steepest descent of the χ^2 surface, thereby exploring more parameter space and being less likely to become stuck in a local minimum, but often in badly behaved cases it will "blow up".

Marquardt (using an idea of *Levenberg*-Bjorck, A. [36]) noted a simple connection between the least squares and steepest descent routes. Replacing $(D^T W D)$ in (2.80) by a constant diagonal matrix gives the steepest descent route. By multiplying the diagonal elements of $(D^T W D)$ by $(1 + \lambda)$ where λ is "*small*" for least squares or "*large*" for steepest descent gives a route that varies between the two extremes. There are four main probable types of behavior in least squares process (Dennis et al. [37]).

- A. Well behaved least squares, explores reasonable parameter space.
- B. Least squares "blows up" as shifts are too large (could be damped down).
- C. Steepest descent from a new starting point finds the best fit.
- D. Steepest descent finds a local minimum.

The Marquardt method would steer between B and D, but still might be trapped into the local minimum. The Marquardt method implementation is applied by the following steps:

- Start with a *modest* $\lambda \approx 1$.
- Compute D and χ^2.
- Calculate the parameter shifts using (2.80) with diagonal elements of $(D^T W D)$ multiplied by $(1 + \lambda)$.
- Computes new parameters and their χ^2.
- If the fit has converged, or too many iterations have elapsed, then stop.
- If the fit improves, keep the new parameters, divide λ by 10 and return to (ii).
- If the fit worsens, multiply λ by 10, return to 3 (no new computation of D)

In order to obtain the proper error estimates σ_j on parameters a_j, it sets $\lambda = 0$ for a final calculation. The fit is guaranteed to improve, if only slowly, but not (in poorly behaved cases) to find a global minimum for χ^2 as the steepest descent route can become stuck in a local minimum. It may be important, as with ordinary least squares, to try to find the solution again from slightly different starting points.

2.2.3.3 Choice of fitting algorithm

The *Steepest Descent* method has the great disadvantage that even if the algorithm converges, it is not guaranteed that the resulting error will be the global minimum. Additionally the fact that according to performance λ has to be reweighted provides an additional disadvantage. Iterative least squares is a better option as if it provides a converged solution then it is guaranteed to be the global minimum.

2.2.4 Orthogonality of spherical harmonics

One of the most important properties of the spherical harmonics is their orthogonality. Two functions $f(x)$ and $g(x)$ are orthogonal on the interval $a < x < b$ if

$$\int_a^b f(x)g(x)dx = 0 \tag{2.82}$$

In the context of the spherical harmonics, both the trigonometric series and the associated Legendre functions satisfy this condition. The associated Legendre functions satisfy the following condition:

$$\int_{-1}^{1} P_n^m(x)P_{n'}^m(x)dx = 0 \qquad \text{for} \qquad n \neq n' \tag{2.83}$$

The variable x is replaced by $\cos\theta$. The colatitude θ varies between 0^o to 180^o. The trigonometric series representing the dependence of the model on longitude are also orthogonal. As in spherical coordinates the longitude has a period of 0 to 2π radians, and the trigonometric functions have to satisfy the orthogonality criterion over this region. This can be seen from the following relations:

$$\int_0^{2\pi} \sin mt \sin ntdt = 0 \tag{2.84}$$

$$\int_0^{2\pi} \sin mt \cos ntdt = 0 \tag{2.85}$$

$$\int_0^{2\pi} \cos mt \cos ntdt = 0 \qquad \text{for} \qquad n \neq m \tag{2.86}$$

The significance of orthogonality can be seen in (2.80) of the iterative least squares algorithm.

$$\Delta a = (D^T W D)^{-1}(D^T W E) \tag{2.87}$$

The inverse of $D^T W D$ must exist in order for the model to have a converged solution. Each row of the matrix D corresponds to one measurement and contains the factors of the Gaussian coefficients calculated from the model for the geomagnetic field and the spherical coordinates for each data point. The matrix product creates a matrix where in the diagonal each element is the sum of the squares of a harmonic component for all measurements. Each off-diagonal component is the sum of the weighted product between two different harmonic terms for all measurements. If the measurements are well distributed in interval of periodicity then the sum of the product between two different harmonics will be 0. Thus the resulting matrix will be a diagonal matrix with non zero components on the diagonal, for which the inverse exists.

For a specific longitude, if we take measurers from the entire range of latitudes then all products involving two different Legendre functions will be eliminated as they are off diagonal components.

For a specific longitude if we take measurements from the entire range of longitudes then all the components which are the sum of products of trigonometric functions of different orders will be eliminated after summing over the entire range from 0 to 2π.

The orthogonality property of both the associated Legendre functions and the trigonometric functions ensures that the off-diagonal components of the resulting matrix are near 0 and that the diagonal components are all positive.

2.3 International Geomagnetic Reference Field

The International Association of Geomagnetism and Aeronomy (IAGA) is responsible for assigning to a scientific working group the derivation of a quantitative geomagnetic field model every 5 years. This period of time was decided so that adequate data can be acquired for determination of the changes in the geomagnetic field. Until the end of the 1970's these models were of low accuracy due to bad data quality. Most of the data was collected from various satellites, not specifically assigned for this task, and earth observatories.

The launch of Magsat satellite in October 1979 was targeted at the collection of high quality geomagnetic field vector data. As early as the beginning of 1980, data from MAGSAT was used for the derivation of the IGRF1980 (Langel et al [27]). A more updated version with more data from Oersted was derived by Langel et al. [38]. In 1990, the POGS satellite was launched with the same objective, with the main difference being that it only carried a scalar magnetometer. A quantitative model based on POGS data was developed by Quinn et al. [39].

The Oersted satellite was launched in 23rd of February 1999 and was placed in a near polar orbit with inclination 96.5^o. Its primary objective was to measure the near earth geomagnetic field and two instruments were used for this purpose. One 3-axis flux magnetometer and one Overhauser magnetometer measuring only the magnitude. Soon after each launch Mandea et al. [40] used scalar data (only scalar data was available at the time) to derive a model for epoch 2000. At the same time Langlais et al. [41] and Golovkov et al. [42] derived models for the main field and most importantly the secular variation from data acquired on earth and from the POGS satellite and compared these against the Oersted data.

These results were presented in July of the same year to an IAGA meeting which included

submission of different candidate IGRF models from different working groups [43]. After evaluation of the different models [44] IAGA decided to assign the derivation of IGRF 2000 to a group led by Olsen and the model was released in October of the same year [45]. Due to the limited data available, the model was not considered to be of adequate accuracy and after that date further modelling efforts were published. The latest version of the IGRF2000 model was developed by Olsen and was published in 2002 [1]. This latest version of IGRF2000 is referred as the **Olsen2000** model for the rest of this thesis, and was tested with data from CHAMP satellite. CHAMP was launched at the beginning of 2000 carrying instruments similar to those of Oersted for measuring the geomagnetic field.

The modelling methodology was based on spherical harmonic functions and the overall scalar potential function describing the geomagnetic field was:

$$\begin{aligned} V &= a\Big\{ \sum_{n=0}^{N_{MF}} \sum_{m=0}^{n} (g_n^m \cos m\phi + h_n^m \sin m\phi)) \cdot \left(\frac{a}{r}\right)^{n+1} P_n^m(\cos\theta) \\ &+ \sum_{n=0}^{N_{SV}} \sum_{m=0}^{n} (\dot{g}_n^m \cos m\phi + \dot{h}_n^m \sin m\phi))(t - t_0) \cdot \left(\frac{a}{r}\right)^{n+1} P_n^m(\cos\theta) \\ &+ \sum_{m=0}^{1} (q_n^m \cos m\phi + s_n^m \sin m\phi) \cdot \left(\frac{r}{a}\right)^{n+1} P_n^m(\cos\theta) \Big\} \\ &+ \widetilde{RC} \cdot \left[\left(\frac{r}{a}\right) + Q_1 \left(\frac{r}{a}\right)^2 \right] \times \left[\tilde{q}_1^0 P_1^0(\cos\theta) + \left(\tilde{q}_1^1 \cos\phi + \tilde{s}_1^1 \sin\phi\right) P_1^1(\cos\theta) \right] \Big\} \end{aligned} \tag{2.88}$$

where

$a = 6371.2km$: mean radius of the earth

(r, θ, ϕ): geographical coordinates

P_n^m: associated *Schmidt* semi-normalized *Legendre functions*

g_m^n, h_m^n: *Gauss* coefficients describing internal sources

$\dot{g}_m^n, \dot{h}_m^n$: *Gauss* coefficients describing linear secular variation of internal sources

q_m^n, s_m^n: *Gauss* coefficients describing external sources

$\widetilde{RC}$: traditionally the D_{st} index used to measure the magnetospheric ring current

$\tilde{q}_1^0, \tilde{q}_1^1, \tilde{s}_1^1$: *Gauss* coefficients accounting for the variability of contributions of $\widetilde{RC}$

The above equation for the scalar potential describing the geomagnetic field includes the effect of the following sources.

2.3.0.1 Static Internal Field

This is the main field and it obeys only spatial variation. This spatial variation is represented by the spherical coordinates.

$$V_{int} = a\sum_{n=1}^{N_{MF}}\sum_{m=0}^{n}(\frac{a}{r})^{n+1}(g^{n,m}\cos m\psi + h^{n,m}\sin m\psi)P^{n,m}(\theta) \tag{2.89}$$

where $N_{MF} = 29$.

2.3.0.2 Secular Variation

This potential describes the variation of the internal field with time due to its dynamic temporal character. The time t_0 for the Olsen2000 model is set as the year 2000, as the model was calculated for this epoch. The time t is that elapsed since that date. Additionally, in order to represent the spatial diversity of this temporal variation, the model also depends on the geographic spherical coordinates.

$$V_{sec} = a\sum_{n=1}^{N_{SV}}\sum_{m=0}^{n}(\frac{a}{r})^{n+1}(t-t_0)(\dot{g}^{n,m}\cos m\psi + \dot{h}^{n,m}\sin m\psi)P^{n,m}(\theta) \tag{2.90}$$

where $N_{SV} = 13$.

2.3.0.3 The effects of Ring Current

This part represents the external field created by the ring current. It is dependent on the geographic coordinates in order to model the different effect of this external field on different areas of the geomagnetic field. The most important characteristic of this potential function is its proportional dependence on the magnetic index D_{st} describing the deviation of the main field due to the effect of the ring current.

$$V_{dist} = aD_{st}[(\frac{r}{a}) + Q_1(\frac{a}{r})^2] \times [\tilde{q}_1^0 P_1^0(\cos\theta) + (\tilde{q}_1^1\cos\phi + \tilde{s}_1^1\sin\phi)P_1^1(\cos\theta)] \tag{2.91}$$

The above equation contains the effect of two fields, one arising directly from the ring current which appears external to the satellite and one which appears internal to it and is used to model the currents within the earth, which are induced by the effect of the ring current. The level of dependency between the induced currents and the ring current is represented by the factor $Q_1 = 0.27$, due to Langel and Estes [38].

2.3.0.4 External Field

This is the ambient external magnetic field which is always present irrespective of the external magnetic activity. It is dependent only on the geographic location:

$$V_{ext} = a \sum_{n=1}^{N_{EXT}} \sum_{m=0}^{n} (\frac{r}{a})^n (q^{n,m} \cos m\psi + s^{n,m} \sin m\psi) P^{n,m}(\theta) \tag{2.92}$$

where $N_{EXT} = 2$.

2.3.0.5 Seasonal Dependence of External Field Contributions

Earlier versions of the IGRF have shown that there is a seasonal dependence on the contribution of the external ambient field. This dependence has been identified to occur in the zonal harmonics, for which the effect is the same for all longtitudes and varies only with latitude. Olsen [1] in his model included this seasonal dependence by adding a harmonic function for the coefficients of the external ambient field of degrees 1 and 2, relative to the season.

$$q_n^0(\tau) = q_{n,0}^0 + \left(q_{n,1c}^0 \cos(\tau) + q_{n,1s}^0 \sin(\tau)\right) + \left(q_{n,2c}^0 \cos(2\tau) + q_{n,2s}^0 \sin(2\tau)\right) \tag{2.93}$$

$$h_n^0(\tau) = h_{n,0}^0 + \left(h_{n,1c}^0 \cos(\tau) + h_{n,1s}^0 \sin(\tau)\right) + \left(h_{n,2c}^0 \cos(2\tau) + h_{n,2s}^0 \sin(2\tau)\right) \tag{2.94}$$

for $n = 1, 2$ where τ is the season in radians starting from January 1 2000. This model varies with annual and semi-annual period.

Olsen2000 does not include any potential functions representing ionospheric currents. This exclusion can be easily justified especially for the polar ionospheric currents. They possess a highly irregular character and their behavior is unpredictable in any time scale. This is also reflected in two facts. First, in the released data files by the OERSTED team, a very small number of measurements is available for colatitudes $20^o < \theta$ and $\theta > 160^o$. Secondly, the satellite data used for the derivation of Olsen2000 is collected only for colatitudes $40^o > \theta > 140^o$.

The exclusion of the ionospheric equatorial electrojet is based on less obvious reasons. The main reason is probably the fact that at the time of the derivation of the Olsen2000, the available data was not adequately spanning in time in order to reveal the seasonal dependence of the equatorial electrojet. The exclusion of this source of geomagnetic anomaly is also reflected in the fact that the data used for the modelling was only from the nightside of OERSTED orbits. This naturally provides a shielding against the effect of the equatorial electrojet and any other current systems owing to the higher conductivity of the dayside ionosphere.

In Olsen2000 [1], an alternative to the D_{st} index was used. The reason for this was that the D_{st} is calculated from data collected from 4 observatories close to the equator, located at both the dayside and nightside of the globe. Conversely the data used for the derivation of the refined Olsen2000 model was collected only from the nightside. As the ring current is believed to be asymmetric, being stronger in the nightside, the resulting perturbation in the data would not adequately be described by the D_{st} index. Instead, a modified index,$\widetilde{RC}$, estimated from corrected data of worldwide distributed observatories in the same local-time sector as the satellite data, was used.

2.3.1 Data selection for the Olsen2000 Model

The data used for the Olsen2000 model spanned two and a half years from March 1999 to September 2001. In order to minimize the effect of magnetic disturbances all the data points were chosen for time instances when the K_p index was smaller than 1+ for the time of observation and smaller than 2 for the past 3 hours. Additionally at the same time instances the D_{st} index was within $\pm 10nT$ and $|dD_{st}/dt| < 3nT/hr$. The effect of the auroral electrojet was minimized by selecting data only for time instances when the dawn-dusk component of the interplanetary magnetic field was $|B_y| < 3nT$.

In order to minimize the effect of ionospheric currents in middle and low latitudes, the data was selected only from the nightside. Vector data was used for dipole latitudes equatorward of $\pm 50^o$ and scalar data were used for latitudes poleward of $\pm 50^o$. This pool of data was used to evaluate the model for the internal field, the external ambient field and the part corresponding to the perturbation of the ring current. The part of the model representing the secular variation was not evaluated from satellite data but only from data obtained from earth observatories. This was mainly due to the fact that the observatories, fixed in specific locations, can provide more accurate information about the transformation of the dipole in time . Satellite measurements cannot be repeated in short intervals at the same point in space and thus the secular variation of the field cannot be accurately measured. Data spanning three years (1998-2000) was used. For 1998 data from 115 observatories was available, for 1999 from 106 and for 2000 from 94 observatories. In order to again minimize the effect of the ionospheric currents in middle and low latitudes, where most of the observatories are located, data was selected only from local midnight measurements.

2.3.2 Fitting Algorithm

The model was derived using the iterative least squares algorithm and here an important innovation was made. This was that the random error present in the measurements was not assumed to have a Gaussian distribution. First evidence of this fact was presented by Walker and Jackson [28] and Bloxham et al. [46] who demonstrated that the error in some magnetic data followed a Laplacian rather than a Gaussian distribution. Olsen [1] showed that it was better represented by a Huber distribution which is a combination of the two. This is a Gaussian distribution in the centre and a Laplacian at the tails Huber [30].

As the error in the data is not Gaussian, the maximum-likelihood least square approach could not be applied. The technique used in non-Gaussian cases in the iterative least squares method or, as mostly seen in literature, iteratively reweighted least squares (IRLS) method described in the previous section. The main difference in the IRLS is that the weights in each iteration are calculated as follows:

$$w_{k,i} = max\left(\frac{c}{\epsilon_{k,i}}, 1\right) \tag{2.95}$$

where $c = 1.5$ is a constant and $\epsilon_{k,i} = \frac{(d_{obs,k} - d^{(i)}_{mod,k})}{\sigma_k}$ is the normalized residual of the kth data point in the ith iteration. Constable [47] showed that if the data follows a Huber distribution, then the use of Huber weights in the IRLS results in the same fit as if the maximum likelihood method was used and the data was Gaussian. In his paper, Olsen [1] experimentally showed that the use of Huber weights resulted in a better fit.

2.3.3 Accuracy of Olsen2000

Table 2.2 gives the error figures for the latest model developed by Olsen [1] where F denotes the scalar magnitude data and B the vector data. The three vector components B_B, B and B_3 are the components in a coordinate system for which the error due to attitude inaccuracy in each component is uncorrelated. B_B is the component along the magnetic field vector, B is the component perpendicular to both the magnetic field vector and the unit vector along the boresight of the star imager of the satellite, and B_3 is the third component which completes a right hand coordinate system. The component B is the one with the highest rms error. This is natural as it is perpendicular to the axis of the star imager, which provides the most accurate information. N is the number of measurements, mean and rms are the error figures in nT, and n indicates how much the component contributes to the model.

Here it must be noted that due to the procedure above, the data acquired by Oersted

component	N	mean	rms	n
F_{polar}	14036	-0.36	4.76	20%
$F_{nonpolar} + B_B$	54412	0.02	2.89	51%
B	24585	0.13	6.40	8%
B_3	24585	0.15	3.25	19%
$\dot{B}_{r,obs}$	119	-1.26	5.09	0.666 %
$\dot{B}_{\theta,obs}$	119	2.9	5.77	0.666%
$\dot{B}_{\phi,obs}$	119	0.06	4.70	0.666%

Table 2.2: Accuracy of the latest IGRF Model [1]

component	N	mean	rms
$F_{CHAMP,polar}$	1571	0.99	5.36
$F_{CHAMP,nonpolar}$	4891	0.11	3.41

Table 2.3: Accuracy of the IGRF for CHAMP data

has been processed and the error due to attitude inaccuracy has been removed.The main framework for this study was developed by Holme [48]. This provides the highest possible quality of geomagnetic field measurements to date.

In order to verify the model for days that were not included in the derivation of the model, Olsen [1] used data from CHAMP. This data was selected with exactly the same criteria as the data from Oersted. The CHAMP satellite acquired only scalar magnitude measurements. Table 2.3 shows the error figures for this data. The low, mean and rms values of error confirmed the validity of the model.

2.3.4 Comments on the accuracy and applicability of the refined Olsen2000 model for use as an Attitude Determination reference of a satellite

2.3.4.1 Accuracy

The accuracy of the Olsen2000 model was very high. This accuracy though is not valid for the entire magnetic field and for the three vector components. The first fact that must be taken into consideration is that the data both from OERSTED satellite used for the modelling and CHAMP satellite used for validation of the model were taken from the nightside. This immediately implies that the accuracy of the model is valid only for the nightside of the

earth and not the dayside.

The second fact that must be taken into consideration is that the data used was taken from magnetically quiet days. The D_{st} index was selected to vary only within $\pm 10nT$. This raises questions about the validity of the model accuracy for days with higher magnetic disturbance from the ring current. The model is ,of course, proportional to the D_{st} index and once this index is known then the model should have a comparable level of accuracy, a feature which was not investigated in the paper of Olsen [1]. The same implications are drawn for the days when the auroral ionospheric currents are more active than the days used in the derivation and validation of the model.

Finally poleward of $\pm 50^o$ latitude, the data used was, in the main, scalar. This means that although the magnitude of the magnetic field vector might be known with the derived accuracy, its orientation is not necessarily modelled with the same accuracy.

2.3.4.2 Implications for use as an Attitude Determination Reference Vector

The questions summarized above need to be investigated if Olsen2000 is to be used in an attitude determination system with accuracy specifications close to the accuracy of this model. To understand the limitations of the use of this model for such a system, we consider a satellite with the same orbit as Oersted. This is nearly polar (96.5^o inclination) and circular at 640km altitude.

If the satellite was to use the Olsen2000 model for attitude determination, then in which cases the accuracy of the onboard model would as low as at its derivation and in which cases it would not? Here an important fact must be introduced concerning attitude determination. In this process, it is required to know both the magnitude and the orientation of the geomagnetic field vector. In fact for the case of attitude determination but not attitude control, the knowledge of orientation is much more important that magnitude. This is due to the fact that even if there is a mismatch in magnitude, the orientation can still provide the required attitude information for the satellite. Simply the model is required to satisfy the accuracy requirements for all the three vector components and not only for the magnitude.

The first part of the question is answered if all the conditions of data selection are satisfied at the time of a measurement. This means that the satellite must be at the nightside of the earth and the auroral ionospheric currents must have low activity. As all three vector components are required, the accuracy is only guaranteed for latitudes equatorward of $\pm 50^o$. Finally the constraints about the D_{st} index must all be satisfied. Here there is a crucial

question about the applicability of the refined Olsen2000 model for attitude determination. In particular, can the D_{st} index be available at the time of a measurement? The answer is simply no. Olsen in his paper about the refined Olsen2000 model [1] says in his concluding sentence:

"This indicates that one of the limiting factors in field modelling with data from high precision geomagnetic satellites like Oersted, CHAMP and Oersted-2/SAC-C is the availability of a suitable indicator of magnetospheric field contributions for the same time instant and geographic longtitude as the satellite data. "

The D_{st} index is provisionally available from the Kyoto World Center for Geomagnetism one hour after the measurements at the observatories. This time is enough for the magnetospheric conditions to be significantly altered. Secondly even if this time delay can be considered satisfactory, the uploading of the D_{st} index to a satellite in a polar orbit would require an enormous number of ground stations spread around the globe. Simply the satellite cannot have any information about the ring and ionospheric currents activity.

As the ring current is present even during quiet days, in which case the D_{st}index has values between $\pm 10nT$, the refined Olsen2000 model cannot guarantee its accuracy on board a satellite.

Chapter 3

Field Segmentation and a New Index - MEME

3.1 Specifications for an onboard Geomagnetic Field Model

The three main sources that disturb the quiet geomagnetic dipole are the auroral electrojet, the dayside ionospheric fields known as solar quiet field, (S_q), and the magnetospheric ring current. In the data provided from satellite measurements, the effects of all the different sources are superimposed. Careful selection of data is necessary to provide the highest possible degree of elimination of the effects of all the external sources whilst modelling as accurately as possible the internal geomagnetic field.

In previous modelling efforts, i.e. IGRF2000 [45], Olsen2000 [1], Thomson et.al. [49], Lui et al. [50], the data used was only from nightside measurements. This eliminated the effect of the solar quiet field. The data was collected from measurements taken for geographic latitudes poleward of $\pm 50^o$. This was intended to eliminate the effect of the auroral electrojet. At the same time the data was collected from days when the magnetic activity index K_p was smaller than 1+, in order to ensure that even at these latitudes the effect will be small. Finally the effect of the ring current was eliminated by incorporating the D_{st} index in the spherical harmonics model.

These efforts have produced models that describe the entire field. Although they produce a good overall accuracy, the problem that remains is that the error is not equally distributed throughout the field. This is mainly due to the fact that the auroral electrojet effect is still present, especially at mid latitudes, even after the elimination of data from high latitudes. The effect of the ionospheric dynamo is not expected to be significant as the data used in

only from nightside. If there would be a remaining effect, it would be stronger around the area of the equator where the ionospheric dynamo effect is higher. Finally the effect of the ring current has been incorporated in the field model and, as it follows a dipole configuration, it should not axhibit great variations at any latitude from a dipole.

Consequently the main remaining effect that distorts the dipole model is the auroral electrojet. This means that at higher latitude the error will have higher magnitude of oscillations around a mean.

This discussion is translated into the following three theoretical expectations.

1. The geomagnetic field around the equator is expected to be approximated well by a dipole as the effect of the auroral electrojet is minimum there.

2. The mean value of the error, in addition to the standard deviation is expected to increase as data from higher latitudes is included.

3. The effect of the ionospheric dynamo, if present at the nightside, should appear higher at the equator and lower for higher latitudes.

4. If the geomagnetic field is modelled in zonal latitude segments then, because of the narrower magnitude range and the narrower levels of disturbance, the fit is expected to be better than that for the entire field.

Now consider the main error in the geomagnetic field data, i.e the auroral electrojet. As its effect is lower for lower latitudes, we consider 3 zonal segments dividing the northern hemisphere into zones of 30^o latitude width. If the error in these segments is denoted by err_1, err_2 and err_3 respectively, then the following natural relationship is expected to hold true.

$$E\{err_1\} < E\{err_2\} < E\{err_3\} \tag{3.1}$$

where $E\{\}$ denotes the expectation operator. If data from the entire field is used, the least squares algorithm for the fitting of the model will calculate the correction at each iteration as:

$$\Delta a = (D^T W D)^{-1}(D^T W(Er + V_{err1} + V_{err2} + V_{err3})) \tag{3.2}$$

where V_{err1}, V_{err2}, V_{err3} are the matrices containing the errors for the three zonal segments respectively.

Due to (3.2), the resulting error will be maximum if data from the entire range of latitudes is used. If the data is collected only from locations in segment 1, the one adjacent to the geographic equator, the present error will by $err1$ and consequently the resulting Δa will be more accurate than the case when data from other segments is included.

In the case of the effect of the ionospheric dynamo in the nightside then the error relationship is reversed due to the physical configuration of the creating currents.

$$E\{err_1\} > E\{err_2\} > E\{err_3\} \tag{3.3}$$

The segmentation of the field would still provide a better fit if segment 3 is modelled separately with data only from the corresponding latitude range.

Although the relative strength of these two kinds of disturbances cannot be estimated analytically it can be examined experimentally. If the geomagnetic field is modelled in segments, and these disturbances are not present, the error should have the same mean and same standard deviation as in the case when the model is derived from the entire range of latitudes.

In the case when these disturbances are present, their relative strength will be revealed by comparing the mean and rms errors of the different segments. If the error is lower at the segment adjacent to the pole then the effect of the ionospheric dynamo disturbance will be higher. If the error is lower for the segment adjacent to the equator then the effect of the auroral electrojet would be higher.

A realistic conjecture is that the effect of the auroral electrojet will be the dominant disturbance because the entire data is collected in the nightside of the Earth and because the electrojet is located over the poles creating a symmetric disturbance. This is in contrast with the ionospheric dynamo configuration, which is symmetric around the noon meridian.

The quantitative segmentation of the field is not as a straightforward procedure as presented in the above qualitative discussion. There are two main constraints resulting from the use of spherical harmonics for the construction of the model. Both these result from the orthogonality constraints of the associated Legendre functions and the trigonometric functions.

Recalling the equations for the three components of the geomagnetic field we have:

$$
\begin{aligned}
B_r &= -\frac{\partial V}{\partial r} = \sum_{n=1}^{k}(\frac{a}{r})^{n+2}(n+1)\sum_{m=0}^{n}(g^{n,m}\cos m\psi + h^{n,m}\sin m\psi)P^{n,m}(\theta) \\
B_\theta &= -\frac{1}{r}\frac{\partial V}{\partial r} = -\sum_{n=1}^{k}(\frac{a}{r}^{n+2}\sum_{m=0}^{n}(g^{n,m}\cos m\psi + h^{n,m}\sin m\psi)\frac{\partial P^{n,m}(\theta)}{\partial \theta} \\
B_\psi &= -\frac{1}{r\sin\theta}\frac{\partial v}{\partial \psi} = -\frac{1}{\sin\theta}\sum_{n=1}^{k}(\frac{a}{r})^{n+2}\cdot\sum_{m=0}^{n}m(-g^{n,m}\sin m\psi + h^{n,m}\cos m\psi)P^{n,m}(\theta)
\end{aligned}
$$

These three equations provide the factors of the coefficients to be estimated by the least squares fitting procedure. Recall the algorithm for the least squares procedure from (2.80):

$$\Delta a = (D^T W D)^{-1}(D^T W E r) \tag{3.4}$$

where

$$D_{ij} = \frac{\vartheta g_i}{\vartheta a_j} \tag{3.5}$$

Each row of the D matrix corresponds to a different data point and each column corresponds to a different coefficient of distinct degree and order. The matrix inside the parenthesis in (3.4) has as diagonal components the weighted squares of each element D_{ii}.

$$
\begin{bmatrix}
D_{11} & D_{12} & D_{13} & \cdots & D_{1j} \\
D_{21} & D_{22} & D_{23} & \cdots & D_{2j} \\
D_{31} & D_{32} & D_{33} & \cdots & D_{3j} \\
\cdots & \cdots & \cdots & \cdots & \cdots \\
D_{i1} & D_{i2} & D_{i3} & \cdots & D_{ij}
\end{bmatrix}
\cdot
\begin{bmatrix}
W_1 & 0 & 0 & \cdots & 0 \\
0 & W_2 & 0 & \cdots & 0 \\
0 & 0 & W_3 & \cdots & 0 \\
\cdots & \cdots & \cdots & \cdots & \cdots \\
0 & 0 & 0 & \cdots & W_i
\end{bmatrix}
\cdot
\begin{bmatrix}
D_{11} & D_{21} & D_{31} & \cdots & D_{i1} \\
D_{12} & D_{22} & D_{32} & \cdots & D_{i2} \\
D_{13} & D_{23} & D_{33} & \cdots & D_{i3} \\
\cdots & \cdots & \cdots & \cdots & \cdots \\
D_{1j} & D_{2j} & D_{3j} & \cdots & D_{ij}
\end{bmatrix}
\tag{3.6}
$$

Each diagonal element in the resulting matrix is the sum of the weighted squares of the individual factors. The off-diagonal components are the sum of the products of different factors and the sum is performed over the entire range of data.

Legendre polynomials were chosen to represent the dependence on the latitude. Due to their orthogonality the sum of the products of different Legendre polynomials over the colatitude range 0^o to 180^o must be zero. Additionally the trigonometric functions *cosine* and *sine* are used to represent the dependence on the longitude. Again the sum of the products of these functions over the range 2π is zero. Following these characteristics of the spherical harmonics, the off-diagonal components in the above matrix should approach

values close to zero, as they are the sum of products over the entire range of latitude and longitude.

If, for example, a segment is selected with colatitude width of 0^o to 30^o then the Legendre polynomials will not cancel for the off-diagonal components as their values are symmetric about the 90^o colatitude. If, however, the segment is formed from both the polar areas, colatitudes 0^o to 30^o and 150^o to 180^o, then the products of different Legendre polynomials cancel out in the sum. Since the segments are zonal, the longitude range is still 0 to 2π radians so they satisfy the orthogonality criterion. This method of modelling in segments is simple because no changes in the model are required.

As the models are zonal they all satisfy Laplace equation. Each model is a different representation of the main field which provides a better fit within the segments from which it was developed. For the rest of latitudes, not included in its derivation, the model does not represent the field correctly and another model developed from these latitudes has to be used. The only requirement to be changed is the data used for the modelling as it needs to be separated into pools, each for different segments.

3.2 Segmentation of the field

The first part of the attempt to improve the accuracy of the magnetic field model is to derive different models for different segments of the geomagnetic field. The first decision concerning the segmentation of the field is to do so in latitude only and not in longitude. Secondly each segment contains areas with latitudes symmetric relative to the equator. This decision was made so that the spherical harmonic functions preserve their orthogonality property.

The latitude refers to the geographic spherical coordinates and not to the dipole ones. As such the zone containing the geographic equator must be wide enough in order to contain the magnetic dipole equator. According to the IGRF2000 model the dipole's northern pole was located at geographic latitude of 79.54^o. Thus the dipole is tilted by 10.46^o and hence the magnetic equator is located between latitudes of $0^o \pm 10.46^o$. Consequently it was decided that the segment containing the magnetic equator should extend also upward and downward by 10^o from the geographic equator. This led to the first segment which was used to include latitudes equatorward (geographic) of $\pm 20^o$. The rest of the field was divided into 3 more segments as shown in Figure 3.1. Segment 6, includes the poles, segments 1 and 2 include mid latitudes, and finally segment 3 includes the equator. Segment 6 is wider than the other single segments as it was decided to isolate the latitudes poleward of $\pm 60^o$ as this is the area

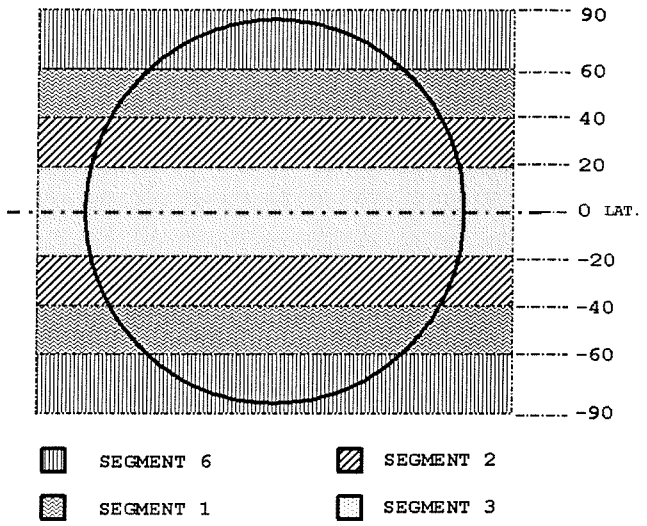

Figure 3.1: Segmentation of the field in zones symmetric around the equator

of the highest disturbance due to the auroral ionospheric currents.

This methodology of segmenting the field offers the opportunity to examine both the level of contamination of the data from auroral fields and the level of adaptability of the models to regional anomalies.

Another subject to be examined is the effect of contamination of the model from the inclusion of data from higher latitudes. To do this the field is divided into zones symmetric around the equator which include the entire latitude range equatorward. As segment 3 satisfies this symmetry, three more segments are added. This are the zones containing the equator and spanning to latitudes equatorward of $\pm 40^o$,$\pm 60^o$ and finally the entire field. They can be seen in Figure 3.2. and Table 3.1 shows the latitudes included in each segment. Another important fact that must be mentioned is that segment 7 includes data from the entire range of latitudes. The model developed from this data is similar to the IGRF model which has also been developed from data spanning the entire latitude range.

3.2.1 Modelling methodology and Data Selection

The modelling methodology followed is similar to that for Olsen2000. Since the part of the model representing the effect of the ring current cannot be used on board a satellite, the derived models will be compared with the Olsen2000 model with this part discarded.

The structure of the derived models for the main internal and external ambient field are derived from a combination of two scalar potentials similar to the Olsen2000 models. These

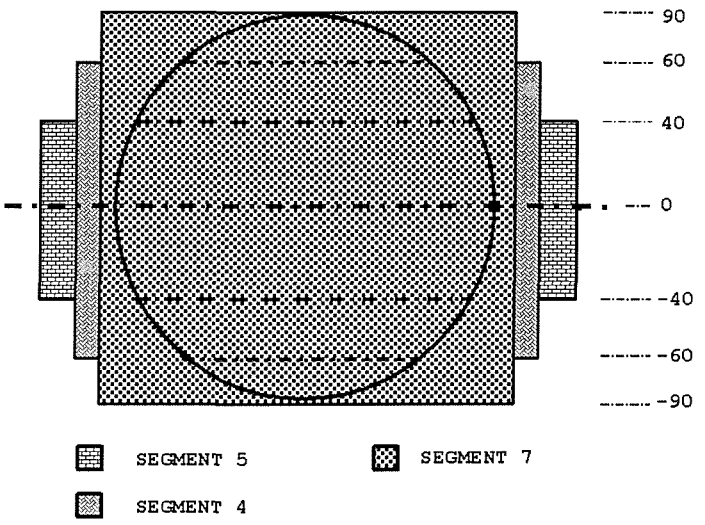

Figure 3.2: Segmentation of the field in zones symmetric around the equator/including the equator

are as follows:

3.2.1.1 Static Internal Field

This is the main field and only has spatial variation which is represented in spherical coordinates as:

$$V_{int} = a \sum_{n=1}^{N_{MF}} \sum_{m=0}^{n} (\frac{a}{r})^{n+1} (g^{n,m} \cos m\psi + h^{n,m} \sin m\psi) P^{n,m}(\theta) \tag{3.7}$$

The value of N_{MF} was set to 13.

3.2.1.2 External Ambient Field

This is the ambient external magnetic field and is always present irrespective of the external magnetic activity. It only depends on the geographic location.

$$V_{ext} = a \sum_{n=1}^{N_{MF}} \sum_{m=0}^{n} (\frac{r}{a})^{n} (q^{n,m} \cos m\psi + s^{n,m} \sin m\psi) P^{n,m}(\theta) \tag{3.8}$$

and here $N_{EXT} = 2$.

The coefficients of the above functions were fitted to the data selected, as detailed later in this section. An additional part for the secular variation was used. In particular, the model for the secular variation of the main field was taken to be the same as in Olsen2000. This decision was based on the fact that the model by Olsen [1] for the secular variation

Number of Segment	min north latitude	max north latitude	min south latitude	max south latitude
6	60^o	90^o	-90^o	-60^o
1	40^o	60^o	-60^o	-40^o
2	20^o	40^o	-40^o	-20^o
3	0^o	20^o	-20^o	0^o
4	0^o	40^o	-40^o	0^o
5	0^o	60^o	-60^o	0^o
7	0^o	90^o	-90^o	0^o

Table 3.1: Range of Latitudes and Indexing of Segments

was developed by a robust methodology from observatories' measurements. This was due to the fact that the observatories provide measurements at the same location (in contrast to satellites) and thus they offer a higher accuracy of the secular variation of the main field. As the data is corrected for local anomalies, it is of the highest possible quality and is considered more reliable than satellite data for the purpose of identifying the secular variation. For this reason the coefficients of the model for the secular variation are the same as those for the refined Olsen2000.

3.2.1.3 Secular Variation

This potential describes the variation of the internal field with time. It is dependent on time in order to include this dynamic temporal character. The time t_0 for the Olsen2000 model is set at year 2000 as the model was calculated for this epoch. The time t is that elapsed since that date. Additionally, in order to represent the spatial diversity of this temporal variation, the model depends on the geographic spherical coordinates.

$$V_{sec} = a\sum_{n=1}^{N_{SV}}\sum_{m=0}^{n}(\frac{a}{r})^{n+1}(t-t_0)(\dot{g}^{n,m}\cos m\psi + \dot{h}^{n,m}\sin m\psi)P^{n,m}(\theta) \tag{3.9}$$

Here $N_{SV} = 13$ is used.

In parallel to the development of the new models, the performance of the Olsen2000 was evaluated for the same pool of data for comparison. However the resulting Olsen2000 is not used as published. In particular, there are two main differences which both stem from the fact that the models are intended to be used onboard a satellite. Firstly the D_{st} dependent part is discarded as if it were used by a satellite in real time. Secondly in the original version

of Olsen2000 the spherical harmonics of the internal field were developed up to degree 29. This resulted in 899 coefficients and required the corresponding evaluation of trigonometric functions. As the model is intended for use on board a small satellite with tight power and computational requirements, this degree is considered excessive. Thus it was decided to eliminate the higher harmonic coefficients and keep only up to degree 13, the same as the degree of the secular variation.

The rational for this decision was also reinforced by the fact that the IGRF models which have been the most popular choice for satellite attitude control are also developed up to degree 13. These reasons also determined the degree of the models that were developed. The resulting number of coefficients is 195 for the internal field. The external field is expanded up to degree 2 which gives 8 more coefficients in a similar manner to Olsen2000.

The seasonal variation part of the Olsen2000 model was preserved. This dependence was not used in the new models as no D_{st} part was included in the initial phase and this fact creates a distortion of the external coefficients relative to those of Olsen2000. Consequently the derivation of the seasonal dependence would not be consistent. The coefficients for the seasonal variation correspond only to the Olsen2000 model.

The first main decision for data selection was dictated by the aim of attitude determination for which it is required that the resulting modelled field must be in as good agreement as possible with the real one in terms of orientation. The inclusion of scalar data would give a better magnitude fit but would distort the accuracy in orientation (Lowes [51]). To avoid this effect only vector data was used.

For the modelling of the internal and external ambient fields, it is necessary to ensure that any other magnetospheric sources of disturbance are minimal. The first measure towards this criterion is the selection of data from the nightside only, in order to eliminate the contamination from the equatorial electrojet and other dayside ionospheric currents . The other disturbance sources were eliminated based on the magnetic indices K_p and D_{st}. The Kyoto World Center for Geomagnetism has released the values for these two magnetic indices for the last two decades. It was decided to select data from days spanning within the interval between 2000 and 2001. The 35 most quiet (magnetically) days were selected with the following criteria. The K_p index must be smaller or equal to 2, and at the same time the D_{st} index must be less than or equal to $\pm 10nT$. Table 3.2 shows the dates selected and the corresponding K_p index and Table 3.3 shows the selected dates with the corresponding D_{st} index.

No.	Date	0-3	3-6	6-9	9-12	12-15	15-18	18-21	21-24	Sum
1	09-01-00	1+	1+	0	0	0+	0+	0+	2-	5+
2	21-01-00	1-	0	0	0+	1-	0+	0	0+	2+
3	04-03-00	0	0	0+	1-	2-	2	1-	1-	6
4	27-03-00	1	1+	1	1-	1+	1-	1-	1	8-
5	14-04-00	0	0+	0+	1-	0+	1-	1+	0+	4
6	03-11-00	0	0	0+	0+	1	1	2	2	7-
7	17-11-00	1+	0+	1-	1-	1-	1-	0+	0	5-
8	20-12-00	0	0	1-	1+	1-	1-	1+	1-	5+
9	31-12-00	1+	0	0+	1	1-	0	0	0+	4-
10	06-01-01	2	1	1	1-	1	1	0+	1	8
11	03-02-01	0+	0	0+	0+	1-	0+	0	0	2
12	04-02-01	0	0	0	0+	1	0+	1	0	2+
13	18-02-01	1	0+	0+	0+	1-	1-	1-	1-	5-
14	25-02-01	0	0+	1-	1-	0+	0+	1+	1-	4+
15	15-03-01	0	0+	1	0+	1-	0+	0+	1-	4-
16	16-03-01	0	0	0	0+	1-	1	0+	1+	4-
17	30-04-01	1-	0	0+	0	0	0	1	0+	2+
18	01-05-01	1	0+	1-	1-	1	0+	2-	1-	6+
19	05-05-01	0+	0+	1-	1-	0	1-	1	1	5-
20	30-05-01	0+	0+	0	0+	1+	11-	1+	1	5+
21	31-05-01	0+	0+	0	0+	1	1-	1-	1-	4
22	23-06-01	1+	1+	1	1	1+	1+	1+	1+	10
23	28-06-01	0	0+	0+	0+	0+	0+	0+	1-	3-
24	21-07-01	1	1+	1-	1	1+	1	1-	2-	9
25	16-08-01	1-	1	0+	1-	1-	1-	1-	1	6-
26	24-08-01	1-	1+	0+	1	1	1-	0+	0	5+
27	10-09-01	1+	1-	0+	0+	1-	1	1	1	6+
28	20-09-01	1	1+	1-	2-	1+	1-	1-	2	9+
29	18-10-01	1-	0	0+	0+	1	1+	29-	1-	6
30	13-11-01	1-	1	1-	0+	1-	2-	2-	1+	8
31	14-11-01	1-	1-	1+	1-	1-	0+	1-	0+	5+
32	29-11-01	1+	0+	1+	1	1-	0+	0+	0	5+
33	30-11-01	1-	0+	0	0+	0+	0+	1	1	4
34	09-12-01	0+	1-	0	1+	1-	0	0+	2-	5
35	10-12-01	0+	0+	1	1-	2-	1-	1-	1+	7-

Table 3.2: K_p index for days used for modelling

No.	Date	1	2	3	4	5	6	7	8	9	10	11	12	13	14	15	16	17	18	19	20	21	22	23	24
1	09-01-00	-7	-9	-10	-11	-8	-6	-4	-3	-5	-7	-8	-7	-7	-9	-7	-8	-5	-3	-1	2	3	4	4	3
2	21-01-00	-3	-1	1	-1	-4	-5	-6	-4	-1	0	1	4	4	4	5	5	5	5	5	2	0	3	4	2
3	04-03-00	-3	-1	-3	-3	-4	-4	-3	-3	-2	-1	1	3	1	0	1	-3	-7	-5	0	-2	1	3	4	9
4	27-03-00	-3	-4	-2	-2	-3	-2	-2	-1	0	0	-1	-2	-2	-1	0	2	1	2	5	9	12	14	9	6
5	14-04-00	-6	-9	-9	-8	-6	-6	-8	-8	-4	-2	-3	-3	-3	-3	-1	-4	-4	-1	2	2	10	9	8	6
6	03-11-00	-2	-2	-3	-3	-1	2	4	6	8	7	6	5	3	-2	-5	-6	-5	-3	2	9	6	4	1	3
7	17-11-00	-2	-4	-6	-7	-3	1	2	2	3	1	-1	2	0	2	3	1	1	0	-1	-1	-3	-1	2	2
8	20-12-00	-8	-10	-7	-3	-1	-1	-1	-1	1	3	2	4	6	5	3	-2	-9	-12	-10	-9	-11	-11	-13	-9
9	31-12-00	-2	-1	1	1	1	3	5	7	7	7	3	0	-2	-4	-2	2	2	4	6	7	6	8	9	8
10	06-01-01	-4	-4	-2	0	4	5	2	-1	-2	0	2	4	7	7	4	3	5	8	7	7	6	7	10	10
11	03-02-01	-8	-6	-5	-3	-2	-2	0	1	1	2	2	1	-2	-4	-5	-4	-3	-2	-2	-2	-2	-2	-1	-2
12	04-02-01	-2	-2	-3	-1	1	3	3	2	2	3	3	3	5	6	6	7	5	2	-1	1	3	5	7	7
13	18-02-01	-6	-5	-4	-4	-7	-6	-6	-6	-6	-4	-2	-3	-2	0	1	0	-1	2	5	7	7	5	2	1
14	25-02-01	1	2	2	2	5	6	9	11	10	7	6	7	5	4	4	4	6	7	6	6	8	9	8	6
15	15-03-01	-6	-6	-5	-4	-5	-5	-3	-5	-7	-10	-8	-7	-6	-7	-7	-6	-3	-2	0	2	2	-1	-1	0
16	16-03-01	3	4	3	3	4	4	3	3	3	3	3	5	8	7	2	0	0	1	2	5	3	2	2	5
17	30-04-01	-7	-8	-8	-6	-7	-8	-3	-1	0	1	-2	-2	2	2	0	-1	0	2	4	9	9	6	4	4
18	01-05-01	0	-3	-3	-5	0	2	6	8	6	2	3	3	4	4	4	4	4	5	6	6	4	5	4	4
19	05-05-01	9	6	4	4	5	5	6	6	7	8	7	8	7	7	6	7	4	2	1	4	6	5	3	6
20	30-05-01	-8	-10	-10	-9	-9	-7	-5	-2	0	0	-1	-2	-1	4	3	1	1	2	2	2	1	-1	-2	-2
21	31-05-01	0	3	4	5	4	2	3	4	4	6	6	6	2	-1	-1	0	6	8	10	16	18	20	17	16
22	23-06-01	-2	-2	-4	-5	-5	-6	-7	-5	-4	-3	-2	-1	0	-1	2	3	2	4	8	11	12	12	13	10
23	28-03-01	0	3	5	6	7	4	2	3	6	5	4	3	3	6	7	7	9	11	10	9	9	10	11	13
24	21-07-01	-5	-2	2	3	8	7	7	4	3	6	7	7	7	5	5	5	7	9	12	14	16	14	8	5
25	16-08-01	-1	-2	-3	-5	-5	-2	0	3	2	0	-2	-4	-4	-2	-1	-1	0	-2	-1	0	-1	1	4	5
26	24-08-01	-5	-2	0	1	2	3	1	-1	-2	-2	2	4	3	3	-1	-2	-2	-1	0	0	0	2	2	3
27	10-09-01	4	4	2	8	9	10	9	6	5	4	2	3	4	5	7	10	11	8	8	7	4	2	1	2
28	20-09-01	2	3	2	0	0	2	2	1	-2	-1	-2	2	5	5	8	5	4	4	6	6	9	14	10	10
29	18-10-01	-1	-1	0	1	3	4	5	6	7	6	7	7	7	6	8	10	13	7	-1	2	2	1	1	1
30	13-11-01	-2	1	-1	-2	-5	-3	-2	-2	2	2	1	0	2	5	7	4	3	2	4	-1	-8	-9	-3	0
31	14-11-01	2	2	2	3	6	7	7	9	7	6	5	6	6	7	9	9	11	11	9	8	7	7	9	10
32	29-11-01	-1	0	-4	-4	-4	-3	-4	-4	-2	1	1	2	0	1	3	1	0	1	3	1	1	0	-3	-3
33	30-11-01	-3	-5	-7	-3	0	2	2	4	4	3	2	2	5	8	8	7	7	7	10	14	15	15	12	14
34	09-12-01	-2	0	1	0	1	6	7	7	6	5	3	0	2	6	10	10	9	10	11	7	5	8	4	5
35	10-12-01	6	4	3	0	1	4	5	8	8	10	10	14	11	6	2	5	8	7	7	7	8	6	4	5

Table 3.3: D_{st} index for days used in modelling

The gap between April and November 2000 is solely due to non availability of data from Oersted.

In Table 3.3 it can be seen that for some dates, especially during the late hours, the D_{st} exceeded the limit of $\pm 10nT$. The data during these times was therefore removed. The suitability of the above dates was also confirmed also from the indices AE, AU, AO and AL provided by the Kyoto World Data Center for Geomagnetism. These indices for 2000 and 2001 are provisional and they are released for every minute. Due to the large number of data points for each day, these indices are not given here. They are available from the Kyoto World Data Center. The confirmation of low polar magnetic activity comes from the low K_p values, as it describes the overall magnetic disturbance.

Measurements from these dates that satisfied the criteria of quiet activity were then divided into night and day measurements. The nightside measurements were collected from all dates into one pool of data from which the subsets for each segments were acquired. Finally after the subsets were formed the models were developed and evaluated using the same data pool.

In order to confirm the validity of the models, a second set of quiet days was used. The same division of data was performed and the models were evaluated for the corresponding locations. The difference between models and real measurements provided the validation of the error figures of the models.

The dates included in the validation set are shown in Tables 3.4 and 3.5 with the corresponding K_p and D_{st} indices.

Date	1	2	3	4	5	6	7	8	Average
00-03-26	0+	0	1-	1-	1-	2-	1+	1+	7-
00-03-28	2-	2-	1+	1+	1-	1-	0+	0	8-
00-12-31	1+	0	0+	1	1-	0	0	0+	4-
01-01-01	0	0+	1	1	0+	0+	1-	1-	4+
01-02-03	0+	0	0+	0+	1-	0+	0	0	2
01-03-15	0	0+	1	0+	1-	0+	0+	1-	4-
01-05-31	0+	0+	0	0+	1	1-	1-	1-	4
01-06-28	0	0+	0+	0+	0+	0+	0+	1-	3-
01-07-15	1-	1-	2	1+	3-	4-	4-	2+	17
01-08-15	2-	2-	1+	1-	1	1	2	2-	11
01-09-16	2+	1+	1-	1	2	3-	3-	2+	15
01-10-16	3	2	2	2	-2	2-	2-	1+	15+
01-11-15	0	0	0+	1	1+	4-	4+	2-	12+
01-12-08	3+	1+	2-	2-	2	1	1-	1-	12+

Table 3.4: K_p index for days used for validation

Date Yr-Mn-Da	1	2	3	4	5	6	7	8	9	10	11	12	13	14	15	16	17	18	19	20	21	22	23	24
00-03-26	-1	-2	-3	-3	-3	-2	-1	2	2	0	-1	-3	-2	-1	0	3	0	0	2	-1	-1	-1	-2	-5
00-03-28	0	-2	1	6	9	5	2	1	2	2	0	-2	-2	-1	-1	-1	-2	2	2	2	2	2	1	-2
00-12-31	-2	-1	1	1	1	3	5	7	7	7	3	0	-2	-4	-2	2	2	4	6	7	6	8	9	8
01-01-01	2	4	5	7	7	6	6	8	6	2	3	7	10	15	15	15	13	9	10	8	7	9	11	8
01-02-03	-8	-6	-5	-3	-2	-2	0	1	1	2	2	1	-2	-4	-5	-4	-3	-2	-2	-2	-2	-2	-1	-2
01-03-15	-6	-6	-5	-4	-5	-5	-3	-5	-7	-10	-8	-7	-6	-7	-7	-6	-3	-2	0	2	2	-1	-1	0
01-05-31	0	3	4	5	4	2	3	4	4	6	6	6	2	-1	-1	0	6	8	10	16	18	20	17	16
01-06-28	0	3	5	6	7	4	2	3	6	5	4	3	3	6	7	7	9	11	10	9	9	10	11	13
01-07-15	-3	-4	-2	0	0	3	6	6	3	5	7	5	6	7	7	0	-15	-23	-21	-18	-21	-20	-16	-9
01-08-15	-9	-10	-11	-11	-13	-14	-16	-12	-9	-9	-9	-9	-9	-9	-7	-6	-7	-7	-5	-4	-6	-6	-4	-2
01-09-16	-7	-4	-6	-10	-9	-9	-9	-8	-6	-7	-6	-6	-7	-11	-10	-11	-13	-10	-13	-13	-9	-5	-3	-3
01-10-16	-1	1	5	-4	-5	-8	-13	-11	-13	-11	-16	-18	-15	-13	-12	-5	0	-1	-7	-7	-7	-9	-14	-17
01-11-15	11	11	13	15	15	12	10	10	11	11	12	16	13	15	16	29	32	12	5	-10	-10	-8	-11	-6
01-12-08	-9	-12	-8	-6	-2	1	6	5	0	0	-1	-2	-3	-4	-7	-8	-2	2	2	5	6	4	2	1

Table 3.5: D_{st} index for days used in modelling

After the validation of the models in the nightside, they were also tested in the dayside for both days used in the modelling and in the validation separately. This was done in order to avoid biasing from the data used for the derivation of the models. The expected error to be encountered was from the quiet ionospheric currents in the dayside, present mainly in low and middle latitudes. The main target of this test is the evaluation of the deterioration of the models' performance by the presence of this disturbance field.

3.2.2 Model Fitting Algorithm

The algorithm employed to fit for fitting the spherical harmonics coefficients to the pool of data is the same as the one used for the Olsen2000 model, developed by Olsen [1]. From (2.80), the algorithm of iteratively reweighted least squares algorithm (IRLS) is as follows:

$$a_{i+1} = a_i + \Delta a_i = (D_i^T C_i^{-1} D_i)^{-1} (D_i^T C_i E_i) \tag{3.10}$$

The covariance matrix C here is evaluated as:

$$C^{-1} = S^T W_i S^T \tag{3.11}$$

where S is a diagonal matrix constructed from the standard deviation for the geomagnetic field measurements. As the modelling is performed using only vector data, there will be a different standard deviation for each of the three vector components B_r, B_θ and B_ϕ, denoted here by σ_r, σ_θ and σ_ϕ respectively. Thus if there are n triplets of measurements which are sorted in the factor matrix D sequentially, i.e first the factors for all measured B_r's, then the ones for B_θ's and then the ones for B_ϕ's, S will have the form:

$$S = \begin{bmatrix} \frac{1}{\sigma_r} & 0 & 0 & 0 & 0 & 0 & 0 & 0 & \cdots \\ \cdots & \cdots & \cdots & \cdots & \cdots & \cdots & \cdots & \cdots & \cdots \\ \cdots & 0 & \frac{1}{\sigma_r} & 0 & 0 & 0 & 0 & 0 & \cdots \\ \cdots & 0 & 0 & \frac{1}{\sigma_\theta} & 0 & 0 & 0 & 0 & \cdots \\ \cdots & \cdots & \cdots & \cdots & \cdots & \cdots & \cdots & \cdots & \cdots \\ \cdots & 0 & 0 & 0 & 0 & \frac{1}{\sigma_\theta} & 0 & 0 & \cdots \\ \cdots & 0 & 0 & 0 & 0 & 0 & \frac{1}{\sigma_\phi} & 0 & \cdots \\ \cdots & \cdots & \cdots & \cdots & \cdots & \cdots & \cdots & \cdots & \cdots \\ \cdots & 0 & 0 & 0 & 0 & 0 & 0 & 0 & \frac{1}{\sigma_\phi} \end{bmatrix} \tag{3.12}$$

The weighting matrix W is a diagonal matrix containing the Huber weight for each measurement. The Huber weight is defined as [1]:

$$w_{k,i} = max\left(\frac{c}{\epsilon_{k,i}}, 1\right) \tag{3.13}$$

where $c = 1.5$ is a constant and $\epsilon_{k,i} = \frac{(d_{obs,k} - d^{(i)}_{mod,k})}{\sigma_k}$ is the normalized residual of the k^{th} data point in the i^{th} iteration. During the i^{th} iteration, σ_k will be the same for all data points referring to a vector component. Consequently for all factors derived from the B_r equation σ_k it will be the same. The same holds for all the data points referring to B_θ and all the data points referring to B_ϕ. This of course is not translated in that the weights will be identical, as the numerator of ϵ refers to the deviation of each data point from the model. Thus the weighting matrix for the i^{th} iteration will be:

$$W_i = \begin{bmatrix} w_{1,i} & 0 & 0 & 0 & 0 & 0 & 0 & 0 & \cdots \\ \cdots & \cdots & \cdots & \cdots & \cdots & \cdots & \cdots & \cdots & \cdots \\ \cdots & 0 & w_{n,i} & 0 & 0 & 0 & 0 & 0 & \cdots \\ \cdots & 0 & 0 & w_{n+1,i} & 0 & 0 & 0 & 0 & \cdots \\ \cdots & \cdots & \cdots & \cdots & \cdots & \cdots & \cdots & \cdots & \cdots \\ \cdots & 0 & 0 & 0 & 0 & w_{2n,i} & 0 & 0 & \cdots \\ \cdots & 0 & 0 & 0 & 0 & 0 & w_{2n+1,i} & 0 & \cdots \\ \cdots & \cdots & \cdots & \cdots & \cdots & \cdots & \cdots & \cdots & \cdots \\ \cdots & 0 & 0 & 0 & 0 & 0 & 0 & 0 & w_{3n,i} \end{bmatrix} \tag{3.14}$$

3.3 Modelling the effect of the ring current

3.3.1 Dynamic Character of the Geomagnetic Field Model

The latest quantitative modelling efforts for the geomagnetic field have adopted the same philosophy of separating the sources, in that these fall in two categories, static and dynamic. In the static category are the internal and the external fields as they have spatial but no temporal variance. In the dynamic category are the secular variation of the internal field, the ionospheric dynamo and the field caused by the magnetospheric ring current. The first two sources have a fixed period and their values depend on periodic variables such as the time of the year or the time of the day. However, the last source, the field from the ring current, cannot be predicted in any periodic basis. The technique for incorporating its effect is the

fitting of the coefficients of a harmonic function in data from days of difference disturbance levels, measured by the index D_{st} and the inclusion of this index in the model during the modelling process. This adds a dynamic character to the geomagnetic field model. However the provisional D_{st} index is not available instantly but only after of the elapse of some time. The fastest available estimate of the D_{st} index is published hourly by the World Centre for Geomagnetism in Kyoto, with a delay of one hour. Consequently this index cannot be used in real time applications.

To overcome this problem, a real-time dynamic index of geomagnetic activity must be used which will be available instantly to the satellite. The derivation of such an index on the ground from data available from observatories is completely impractical due to the unavailability of instant information and the fact that even if this was available, the uploading of the index to a satellite in a polar orbit in reasonable time for meaningful use, would be impossible. Consequently the only idea that could be used for the derivation of such a dynamic index is the use of onboard measurements. Before proceeding to develop this, it is useful to examine how the D_{st} index is evaluated.

The hourly D_{st} index is obtained from magnetometer stations near the equator but not so close that the E-region equatorial electrojet dominates the magnetic perturbations seen on the ground. At such latitudes the H (northward) component of the magnetic perturbation is dominated by the intensity of the magnetospheric ring current. The D_{st} index is a direct measure of the hourly average of this perturbation.

Large negative perturbations are indicative of an increase in the intensity of the ring current and typically appear on time scales of about an hour. The decrease in intensity may take much longer, on the order of several hours. Equatorial D_{st} indices are derived from low-latitude (but not equatorial) observatory records. After removal of secular variations from station records, the H-values are translated to equatorial values, averaged and then harmonically analyzed to give the first harmonic which is D_{st}. These indices measure the globally symmetrical contribution of the ring-current as it produces the large main-phase depression associated with major magnetic storms. Because D_{st} is derived from stations not actually near the equator, the problem of large variations due to the equatorial electrojet is avoided.

From the description of the method for deriving the D_{st} index it is straightforward to see that if onboard measurements are to be used directly in the calculation of an index, they should be acquired from the vicinity of the equator but not very close to the equatorial

plane. However the problem that then arises is that if the satellite attitude is not known, then the transformation of the measured deviation to the equatorial plane cannot be executed. Consequently we decided that the measurements for the index would be acquired from a narrow zone over the magnetic equator. As there is no information about the direction of the geomagnetic field vector due to lack of attitude knowledge, the most useful information that can be used for the derivation of an index is the deviation of the magnitude of the geomagnetic field vector. In the dayside an additional error will be introduced proportional to the magnitude of the disturbance from these ionosperic currents. In order to rule out single erroneous measurements, the methodology should involve the evaluation of the mean of deviations taken from a narrow area.

The average value of the deviation is then used as the new index. If we assume a mean LEO period of 90 minutes, then there will be two passes over the equator in this time. The purpose is to be able to derive a dipole model, similar to the one dependent on the D_{st} index, but using the new index instead. Every time a satellite will be over the equator, it will acquire the required number of measurements from the required locations and, based on them, the onboard model will predict what values of disturbance should be expected to be encountered in the time remaining until the next equatorial pass. This methodology gives a resolution of roughly 45min for a polar orbit with the above period. This resolution is adequate in terms of the timescale of changes of the ring current intensity for most of the cases. The only situation which may not be covered with this time resolution is the initial phase of a storm, which can last less than 40 minutes and during which there is a sudden decrease in the horizontal component.

This would cause high inaccuracy in the model until the next passage over the equator and the new derivation of the magnetic index. Keeping in mind that storms occur in average once per month and this situation could take place only during the initial phase, it is a tolerable time portion of non validity of the model.

Each measurement of the geomagnetic field over the narrow equatorial region is subtracted from the expected one from the geomagnetic field model. Note here that no information is required about the direction of the vector as only the magnitude is required. Another important fact is that the model used for the derivation of the residuals does not include the dipole part incorporating the new magnetic index in order to avoid biasing.

In order to test the above methodology, data for specific days with known D_{st} index values was used. The methodology to derive such an index is simple as the only analytical

tool required is the averaging of residuals.

Now consider a zone of latitude range L_{min} to L_{max} within which the satellite derives measurements for computation of the onboard magnetic activity index. For each measurement the expected magnitude $|B|$ is calculated from the onboard model and then the error between them is used as the magnetic activity index.

The use of a single measurement for the derivation of the index is not a feasible strategy as the model is contaminated by random noise which follows a Huber distribution. In order to eliminate the effect of that noise, it is straightforward to use a large number of measurements and derive the magnetic index from the mean error of them. By this method the mean of the inherent model error should approach zero.

Since the magnetic index is using the Mean Equatorial Magnitude Error it is named $MEME$. In mathematical terms it is given by:

$$MEME = \frac{1}{N_{L_{max}}} \sum_{n=N_{L_{min}}}^{N_{L_{max}}} (|B_{meas}(n)| - |B_{model}(n)|) \tag{3.15}$$

Here, variable n is the number of samples where $n_{min} = N_{L_{min}} = 0$ and $n_{max} = N_{L_{max}}$. This of course can also be expressed such that $n_{max} = N_{L_{min}}$ and $n_{min} = N_{L_{max}} = 0$. This notation is useful especially for polar orbits since during the passage of the satellite over the equator the latitude either increases or decreases monotonically.

One area of debate is the range of latitude L_{min} to L_{max}. In order to filter to the maximum possible the effect of the currents at higher latitudes, it was decided to make it as narrow as possible around the equator. Namely the range of colatitudes within which measurements for the $MEME$ index are derived is 85^o to 95^o around the equator.

Another area of debate is the sampling rate in this interval. In order to take advantage of the data available for Oersted, it was decided to use the same data pool with the corresponding sampling times as Oersted. This would provide a realistic environment for the evaluation of the new magnetic index methodology. For each measurement, the corresponding model value is calculated and subtracted from the measurement in order to be used in the evaluation of $MEME$. Thus it is necessary to ensure a adequate time interval between measurements so that the model calculation can be performed. This requirement is supplemented by the need for low computational labor due to limited power resources on board a small satellite. Thus it was arbitrarily decided to set the sampling time within the zone of colatitudes 85^o to 95^o at 10 sec. This interval is more than adequate for computation and ensures low computational labor. The magnitude error for each measurement is evaluated in

this time interval before the next sample is taken. After the last measurement is processed, the $MEME$ index is evaluated. This methodology has the advantage that the index will be almost instantly available after the last measurement. In comparison, it would not be immediately available if the measurements were batch processed after they were all collected.

Another important fact has to mentioned here. As the magnetometers consume little power and the computational expense for saving a measurement is low, a higher number of measurements can be acquired within the zone of 85^o to 95^o colatitude. The measurements used for the derivation of $MEME$ would still be separated by an interval of 10 sec. After $MEME$ is evaluated the rest of the measurements located within the same zone and which have not been used for the derivation of the magnetic index can then be used for the purpose of attitude determination. Most attitude determination techniques based on magnetometer measurements use time series of measurements rather than single data points. This is done in order to eliminate random noise and also to provide robustness against single erroneous measurements.

Using measurements from the same colatitude range as those used for the derivation of $MEME$ offers a significant advantage in terms of accuracy. In particular, as they refer to the same time interval for which the external disturbance is evaluated, the effect of elapsed time between index derivation and measurement is minimal.

As already noted before, the model used for the derivation of $MEME$ does not include the part dependent on it in order to avoid biases from previous evaluated indices.

The representation of the effect of the ring current by a model dependent on the $MEME$ possesses advantages and drawbacks which can foreseen before the derivation of the model.

The disadvantages can be summarized as follows:

1. The derivation of $MEME$ does not produce an index which as robust as D_{st} due to the fact that the measurements are spread in space and time. Additionally the error of the main model itself is introduced in the magnitude error.

2. The model must be used in both the day side and the night side. This means that a $MEME$ value evaluated in the dayside will be used in the nightside and vice versa. It is already expected to encounter higher errors in the dayside due to the higher conductivity of the ionosphere. Additionally it has been debated by various researchers that the ring current is asymmetric depending on location relevant to the sun. Thus it is expected that an oscillating $MEME$ will result as the satellite alternates between night and day sides.

3. The $MEME$ index is expected to be less consistent for quiet days. This is due to the fact that the rms error of the main model is expected to be within the range of $\pm 10nT$, similar to the refined Olsen2000. Thus such a $MEME$ value is very likely to be erroneous when the external disturbance is at this level.

Given these disadvantages the following conclusions were drawn prior to the modelling effort.

1. The temporal and spatial spread of measurements can be considered minimal for the dipole colatitude range of 85^o to 95^o. The main field for this area is least effected by polar ionospheric currents and the main field model is expected to achieve its highest accuracy at this area. In dayside, it is contaminated by the equatorial electrojet which is expected to create an additional deviation. However the level of the equatorial electrojet at the latitude of Oersted orbits is only of the order of -10nT. This value could be important for very quiet days but for higher ring current levels, its effect will be negligible. For very quiet days the $MEME$ index is expected to perform inconsistently due to the main field model error. Hence it was decided to employ the same dipole equatorial region in all cases.

2. The error in the dayside is expected to be different due to the asymmetry of the ring current and due to dayside ionospheric currents. Thus $MEME$ estimates are expected to oscillate between different states in subsequent equatorial passes. This means that the model will be derived for the same latitudes and longitudes with different values for $MEME$ depending on whether the measurement was taken in the day or nightside. This will create an ambiguity during the modelling process as the same external disturbance levels will be represented by different levels of $MEME$ depending on which side of the earth it was evaluated. This emphasizes the need to treat dayside and nightside separately. By developing a different model for each of them, it is expected that a more robust representation of the ring current field will result. In addition to the dependence of the $MEME$ on the side on which it is evaluated, its effectiveness is also dependant on which side it is used. There are four possible cases.

a. $MEME$ evaluated in nightside and used in dayside.

b. $MEME$ evaluated in nightside and used in nightside.

c. $MEME$ evaluated in dayside and used in dayside.

d. $MEME$ evaluated in dayside and used in nightside.

In cases b and c, $MEME$ is expected to provide a consistent representation of the ring current disturbance as it is derived and used on the same side.

In the other two cases, due to the change of sides between MEME measurement and the use of the model, different conditions are expected. This diversity of probable $MEME$ values depending on the side it is derived and used suggests that we should derive a different model for each case.

3. In the section describing the modelling of the main field it was seen that the effect of the ring current during quiet days was engulfed within the model of the internal and ambient external fields. Thus for quiet days the use of $MEME$ is not expected to lead to a significant improvement. This means that the accuracy of the model is expected to remain at the same level with or without the use of $MEME$. It is also probable that the use of $MEME$ during quiet days might introduce some additional error. Thus an erroneous ring current field would be added, while the real ring current field is already represented by the main model. This does not create a significant error since for quiet days the main field provides an accurate representation. $MEME$ is intended to be used in occasions that the ring current disturbance exceeds $-20nT$. Figure 3.3 shows the histogram of D_{st} hourly values for year 2000 as provided by the Kyoto World Center for Geomagnetism.

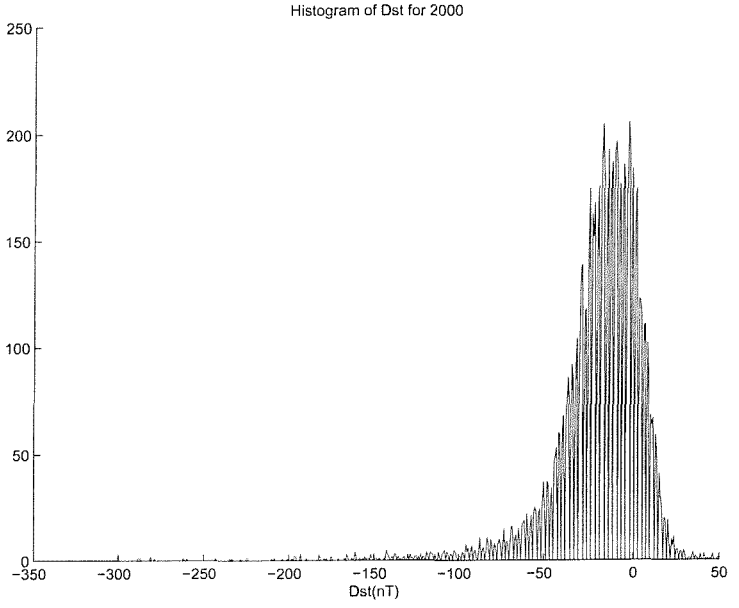

Figure 3.3: Histogram of D_{st} index for year 2000

The main envelope of D_{st} is located between $-60nT$ and $25nT$. This is the level of disturbance encountered in the near earth space for most of the time. The main lobe of the distribution is centered around $-10nT$ which signifies the quiet days. An on board model without a part describing the ring current field would experience an error of similar statistical figures. The role of $MEME$ is to eliminate the rms value of this error to levels similar to the ones for quiet days. If this is achieved for the ranges between moderately and highly disturbed days then this model can be confidently used for accurate attitude determination. It is the absence of such a dynamic part from on board geomagnetic field models that has prohibited their use as an accurate attitude determination reference vector.

3.3.2 Methodology and Data selection

3.3.2.1 Effect of Ring Current

The structure of the MEME dependent model is the same as the D_{st} dependent part of the Olsen2000 model [1]. It is dependent on the geographic coordinates in order to model the different effect of this external field on different areas of the geomagnetic field. The scalar potential function is described by:

$$V_{dist} = aMEME \cdot [(\frac{r}{a}) + Q_1(\frac{a}{r})^2] \times [\tilde{q}_1^0 P_1^0(\cos\theta) + (\tilde{q}_1^1 \cos\phi + \tilde{s}_1^1 \sin\phi) P_1^1(\cos\theta)] \quad (3.16)$$

For modelling of the ring current field days of all different levels of magnetic activity,measured by D_{st} index were used. They are listed in Table 3.7 with corresponding D_{st} values.

The mean equatorial magnitude error index (MEME) was first evaluated for this set of days and one of the main initial tasks was the evaluation of its performance as an index compared to the D_{st}. In order to achieve this, a large set of MEME equatorial measurements was separated into 10 categories spanning from positive to high negative values. For the same measurement the corresponding D_{st} values were collected, as published by the Kyoto World Data Center for Geomagnetism. The data sets were further quantified according to the side that the measurements of MEME was taken (night or day). The mean of each subgroup was evaluated together with the corresponding mean of the D_{st} values.

Days 1 to 19 represent disturbed days with most D_{st} values lower than $-20nT$ .They are used so that the model will adapt to high levels of ring current field. Days 20 to 37 are days of low activity with values higher than $-50nT$.

In earlier modelling efforts, the model describing the ring current effect was developed separately for distinct levels of magnetic activity, as measured by the D_{st} index. The physical

A(Quite)	B(Moderate)
$MEME > -20nT$	$-60nT < MEME < -20nT$

C(High)	D(Very High)
$-100nT < MEME < -60nT$	$MEME < -100nT$

Table 3.6: Categories of Ring Current Disturbance Levels

meaning of this is that the dipole formed by the ring current changes morphology according to the level of ring current. Stronger ring current is caused by intensified solar wind which suppresses the magnetosphere boundary and supplies the current system with more ionized particles and hence create a change in the shape of the dipole. Following the same philosophy we have divided the ring current activity, as measured by $MEME$ index, into four categories, which are shown in Table [?]. For each category a different model is developed. Following also the previously stated division according to which side $MEME$ is evaluated and which side is used, 16 different models are evaluated. After the models were developed, their accuracy was evaluated for the same days.

Another set of days with similar distribution of ring current activity was selected in order to validate the performance of the models for days not included in the modelling. These dates were selected from year 2002 so that they are located outside the time interval within which all modelling data is located. They are shown in Table 3.8 with the corresponding hourly D_{st} index values.

Date Yr-Mn-Da	1	2	3	4	5	6	7	8	9	10	11	12	13	14	15	16	17	18	19	20	21	22	23	24
00-02-11	-14	-9	-10	5	-1	-9	-3	-1	-4	-10	-18	-24	-25	-16	-15	-17	-20	-25	-24	-16	-17	-27	-36	-35
00-02-12	-24	-38	-42	-60	-47	-24	-30	-33	-29	-67	-98	-133	-108	-91	-105	-96	-103	-110	-109	-102	-95	-89	-84	-77
00-02-13	-61	-46	-55	-55	-55	-53	-54	-54	-57	-55	-55	-55	-57	-57	-58	-50	-41	-35	-32	-37	-41	-35	-31	-29
01-03-19	-8	-11	-12	-12	-12	-14	-19	-20	-16	-12	-15	0	-4	-28	-30	-19	-29	-59	-68	-81	-88	-105	-94	-84
01-03-20	-84	-73	-73	-78	-87	-106	-111	-130	-139	-137	-141	-152	-163	-165	-148	-160	-156	-142	-134	-136	-127	-119	-111	-100
01-03-21	-84	-77	-74	-74	-77	-79	-83	-81	-76	-70	-67	-65	-67	-66	-63	-61	-58	-53	-52	-52	-51	-52	-54	-51
01-03-22	-45	-42	-40	-38	-37	-35	-34	-29	-30	-23	-21	-17	-13	-3	5	-12	-24	-33	-36	-38	-36	-42	-45	-43
01-09-25	-21	-19	-18	-21	-21	-22	-23	-21	-20	-16	-13	-12	-14	-15	-13	-13	-12	-13	-11	-13	16	15	-14	-55
01-09-26	-75	-101	-91	-91	-82	-78	-89	-92	-83	-87	-85	-77	-75	-78	-76	-70	-65	-58	-52	-50	-47	-43	-40	-36
01-09-27	-34	-32	-33	-41	-44	-42	-38	-34	-33	-34	-37	-38	-35	-38	-38	-43	-45	-49	-46	-45	-48	-44	-39	-39
01-09-28	-40	-40	-38	-37	-36	-39	-42	-42	-33	-32	-34	-32	-29	-32	-35	-35	-31	-28	-27	-28	-28	-25	-27	-26
01-10-21	-35	-32	-31	-30	-29	-24	-22	-22	-24	-26	-24	-25	-24	-22	-22	-22	-9	-21	-88	-111	-163	-166	-158	-160
01-10-22	-161	-166	-163	-154	-158	-154	-150	-149	-136	-124	-136	-143	-145	-149	-136	-156	-145	-157	-137	-155	-155	-152	-149	-144
01-10-23	-155	-126	-114	-120	-116	-118	-120	-112	-109	-101	-96	-93	-96	-90	-83	-79	-78	-73	-68	-68	-68	-66	-65	-64
01-10-24	-63	-58	-52	-51	-49	-50	-50	-50	-52	-50	-49	-48	-47	-44	-42	-42	-42	-40	-37	-37	-35	-33	-35	-32
01-11-05	-13	-12	-9	0	3	5	7	10	21	15	16	25	24	30	37	25	20	22	34	13	-25	-37	-38	-41
01-11-06	-62	-54	-119	-267	-273	-277	-275	-254	-251	-233	-215	-198	-185	-166	-194	-210	-202	-178	-162	-137	-148	-159	-152	-155
01-11-07	-150	-138	-134	-130	-120	-106	-103	-102	-96	-92	-93	-95	-91	-82	-80	-82	-77	-72	-68	-67	-62	-60	-60	-59
01-11-08	-57	-58	-57	-51	-52	-53	-51	-51	-49	-42	-41	-39	-37	-34	-32	-31	-31	-30	-28	-28	-27	-30	-32	-31
00-01-09	-7	-9	-10	-11	-8	-6	-4	-3	-5	-7	-8	-7	-7	-9	-7	-8	-5	-3	-1	2	3	4	4	3
00-01-21	-3	-1	1	-1	-4	-5	-6	-4	-1	0	1	4	4	4	5	5	5	5	5	2	0	3	4	2
00-03-27	-3	-4	-2	-2	-3	-2	-2	-1	0	0	-1	-2	-2	-1	0	2	1	2	5	9	12	14	9	6
00-03-28	0	-2	1	6	9	5	2	1	2	2	0	-2	-2	-1	-1	-1	-2	2	2	2	2	2	1	-2
00-04-14	-6	-9	-9	-8	-6	-6	-8	-8	-4	-2	-3	-3	-3	-3	-1	-4	-4	-1	2	2	10	9	8	6
00-07-17	-2	-4	-6	-7	-3	1	2	2	3	1	-1	2	0	2	3	1	1	0	-1	-1	-3	-1	2	2
00-12-20	-8	-10	-7	-3	-1	-1	-1	-1	1	3	2	4	6	5	3	-2	-9	-12	-10	-9	-11	-11	-13	-9
00-12-31	-2	-1	1	1	1	3	5	7	7	7	3	0	-2	-4	-2	2	2	4	6	7	6	8	9	8
01-01-16	-2	-2	0	2	4	4	3	4	1	0	3	4	2	2	-1	-2	-4	-7	-9	-7	-5	-2	1	0
01-01-29	10	8	-11	-18	-12	-8	-20	-22	-19	-17	-16	-15	-12	-7	-5	-3	-5	-6	-6	-9	-9	-10	-12	-10
01-02-11	2	-4	-2	1	0	1	2	-5	-9	-8	-9	-11	-8	-6	-7	-5	-1	2	5	6	4	6	6	6
01-02-13	12	3	2	6	11	-8	-16	-9	-14	-22	-25	-17	-12	-11	-9	-12	-13	-11	-16	-19	-40	-50	-43	-45
01-03-15	-6	-6	-5	-4	-5	-5	-3	-5	-7	-10	-8	-7	-6	-7	-7	-6	-3	-2	0	2	2	-1	-1	0
01-05-15	-18	-17	-14	-12	-14	-19	-17	-15	-17	-18	-20	-18	-17	-16	-20	-20	-12	-14	-19	-18	-16	-9	-9	-9

Table 3.7: Days used for the Derivation of the MEME models and the values of the corresponding D_{st} index

Date Yr-Mn-Da	1	2	3	4	5	6	7	8	9	10	11	12	13	14	15	16	17	18	19	20	21	22	23	24
02-01-05	-3	-5	-5	-7	-6	-7	-6	-5	-3	-2	-3	-3	-6	-11	-9	-8	-7	-2	2	4	5	6	7	6
02-03-17	13	10	10	11	12	12	13	14	15	15	15	15	17	17	15	17	17	15	13	12	12	15	14	11
02-04-08	6	8	9	10	11	9	7	5	3	5	6	7	7	7	8	8	9	10	12	12	14	14	13	12
02-06-27	2	2	1	0	1	4	5	6	6	5	3	2	1	2	3	3	4	6	3	4	5	6	7	9
02-09-25	-21	-19	-18	-21	-21	-22	-23	-21	-20	-16	-13	-12	-14	-15	-13	-13	-12	-13	-11	-13	16	15	-14	-55
02-02-06	15	15	20	19	17	24	26	-4	-31	-27	-24	-18	-12	-12	-12	-8	-4	-9	-13	-10	-3	-4	-5	-9
02-03-25	-25	-26	-25	-25	-24	-20	-20	-24	-29	-29	-28	-25	-25	-24	-23	-20	-18	-15	-14	-15	-14	-14	-15	-16
02-04-21	-65	-57	-44	-50	-51	-50	-47	-43	-39	-41	-41	-40	-42	-45	-43	-41	-38	-33	-33	-32	-33	-34	-36	-38
02-05-24	-77	-72	-71	-71	-71	-68	-64	-59	-54	-53	-53	-55	-54	-51	-51	-50	-46	-44	-43	-44	-45	-45	-46	-45
02-08-02	-19	-43	-54	-60	-87	-96	-78	-60	-57	-49	-38	-32	-42	-50	-42	-38	-50	-43	-38	-40	-44	-49	-59	-47
02-03-24	-22	-37	-44	-51	-64	-78	-91	-87	-99	-101	-85	-80	-71	-80	-90	-95	-95	-87	-84	-87	-88	-85	-72	-66
02-04-19	-75	-64	-53	-41	-51	-57	-58	-57	-46	-40	-55	-49	-70	-96	-102	-90	-104	-120	-122	-110	-109	-117	-97	-85
02-04-18	-47	-60	-74	-86	-99	-113	-112	-126	-116	-114	-123	-123	-100	-105	-105	-101	-102	-102	-107	-105	-108	-102	-92	-80
02-04-20	-81	-88	-77	-89	-103	-145	-151	-148	-148	-140	-119	-107	-102	-99	-98	-94	-97	-91	-95	-66	-72	-80	-75	-70
02-05-11	-8	-6	-6	-6	-7	-7	-2	-2	-5	-2	10	-8	-19	-15	-30	-73	-84	-98	-100	-102	-96	-84	-78	-79
02-05-23	1	6	6	9	13	1	1	3	8	9	15	69	-22	-70	-55	-52	-73	-108	-103	-91	-90	-92	-88	-83

Table 3.8: Days used for the Derivation of the MEME models and the values of the corresponding D_{st} index

3.4 Error measure criteria

The criteria used for evaluation of the error are similar to those used for the Olsen2000 model. These are the mean error and the rms error. The mean shows how close the noise is to the assumption of Gaussian-like noise with zero mean.

These two error figures are useful for fitting accuracy evaluation of the model. As the model is to be used for attitude determination the effect of the model error on the attitude determination must be examined.

For this purpose a new measure of error has been introduced. Assuming that the measured vectors represent the real field, then angle of deviation between the modelled vector and the measured one, shows the error in orientation. This orientation error causes the error in the attitude determination as the orientation of the expected magnetic vector is in error compared to the real one.

The angle of deviation is measured directly on the plane defined by the modelled and the measured vectors and is always positive. Although this error does not translate algebraically to the attitude error, it shows in good physical sense in that the attitude error will be introduced due to the error in the model.

The algorithm for evaluation of the error angle is as follows:

1. Evaluate the projection of the model vector onto the direction of the real vector.
2. Evaluate the third side of the orthogonal triangle defined by the model vector and its projection.
3. Evaluate the angle between the model vector and its projection.

This angle is the same as the angle between the model vector and the real vector.

The projection of the model vector onto the direction of the real one is given by:

$$proj_{B_{obs}} B_{mod} = \left(\frac{B_{obs} \cdot B_{mod}}{B_{obs} \cdot B_{obs}} \right) B_{obs} \tag{3.17}$$

where the $\cdot$ operator denotes the dot product between vectors. The third side of the triangle defined by B_{mod} and $proj_{B_{obs}} B_{mod}$ is then evaluated by the theorem of *Pythagoras*. As it can be seen the angle found by this methodology is always positive. It gives the angle between the real and model vectors. There is no directional information about this angle, only its value. As it is always positive, its distribution is expected to be different from the distribution of the error for the geomagnetic field vector components and is not expected to follow a Gaussian-like distribution. Thus two new statistical measures were employed,

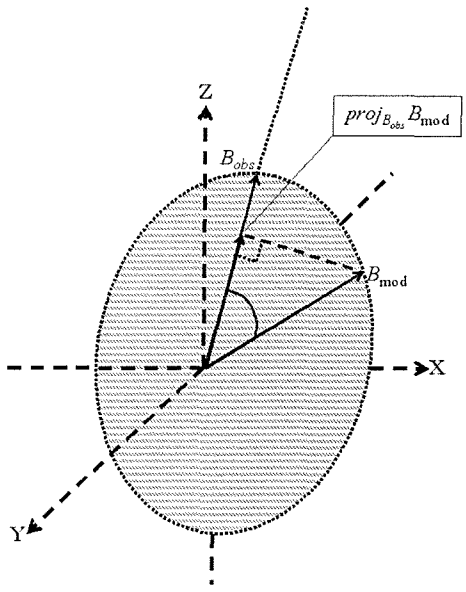

Figure 3.4: Error angle between the measued and observed magnetic field vector

instead of the rms error, in order to describe the distribution of the error. This is the angle threshold value below which lies 95% of the error. This measure is the most indicative of the high errors most likely to be encountered. The second statistical measure is the percentage of measurements with error below 0.1^o. This was decided on by the fact that one of the targets of this research is to bring the accuracy the resulting models as close as possible to this value, so that it can be used for applications with such accuracy requirements. Finally the third statistical measure is the mean orientation error.

Chapter 4

Results - Segmentation, MEME

In this chapter the results from the following experiments are given and analysed:

1. Derivation of models for the 7 different segments for the main and ambient external field from nightside measurements.
2. Evaluation of the models with measurements from the nightside of quiet days not included in the modelling.
3. Evaluation of the models for the dayside of the quiet days used in the modelling.
4. Evaluation of the models for quiet days not included in the modelling.
5. Evaluation of MEME consistency
6. Derivation of the MEME dependent Models
7. Evaluation of the MEME dependent models with measurements from days not included in the modelling.

After the discussion of the results is following the summary and conclusion.

In this section the Olsen2000 model will be referred to as IGRF due to the fact this notation has been used in all experiments and appears in all the graphs giving the results. This was due to the fact that Olsen2000 is a refined version of IGRF2000.

4.1 Modelling of the Main Field

After the modelling process, the mean and rms values of the error were calculated. Figures 4.1 to 4.10 show these descriptive statistics for each of the three vector components,

the magnitude and all the three vector components together. Figures 4.11 to 4.15 show the histograms of error distribution for the different models in each segment. These figures are given in Appendix B in greater detail and their inclusion in this section serves the purpose of illustrating the different morphology of error in different models. The actual values of the mean and rms errors are given in Table 4.1. This table has been included in order to give a more detailed description of the statistics observed on the graphs. Figures 4.16 to 4.18 show the orientation error statistics as described by the mean, the 95% percentile threshold and the percentage of samples for which the error is below 0.1^o. Figure 4.19 shows the histogram of the orientation error for each segment. The histograms in this figure are presented zoomed in the main lobe of the distribution in order to observe the differences between different models. The upper edges of the distributions observed in this figure are not the actual ones. The statistics of the orientation error for all models and for each segment are presented in Table 4.2. In this table are also presented the maximum orientation error values in order to show the upper edge of the error distribution.

4.1.1 Vector Components

Looking at Figures 4.1 to 4.6 and Figures 4.9, 4.10, the following common observations can be made. For segments 1 to 5, all the models except model 7 and IGRF have mean error within the region of $\pm 1nT$. In segment 6, the mean error values of the different models vary significantly. This behavior shows that segment 6 cannot provide consistent information about the model error during magnetically quiet days. This was expected as in the polar caps the ionospheric currents create large random disturbances which vary rapidly. In Segment 7 the models show a high mean error which is justified by the fact that this segment describes the entire latitude range including the polar caps. IGRF in segments 1 to 5 shows consistently a mean error greater than that of models 1, 2, 3, 4 and 5.

Similar behavior is observed in these segments for model 7 and this shows its low quality. The performance of models 1, 2, 3, 4 and 5 is satisfactory in terms of the mean error. The mean is a good indication of the level of randomness of the model error. For models 1 to 5 the mean is within $\pm 1nT$ and it is not practical to try and identify patterns of the mean error relative to each component or segment since all such values are close to zero. This is why the mean here is not indicative of the error that is more likely to be encountered. This is described by the rms value, which shows how far the most probable error is located from the mean value. The rms error in Figures 4.2, 4.4, 4.6 and 4.10 is more revealing about the

accuracy of the various models for different segments.

In all seven segments, the models developed from each segment, are performing significantly better than the IGRF model. Additionally an important pattern of the rms error is observed. In segment 1, close to the polar regions, the rms error has a high value. As we move to segment 2, closer to the equator, the rms error drops and the difference between the new models and IGRF also decreases. As we move closer to the equator the rms error in segment 3 and the difference between the new models and IGRF are further reduced. This shows the dependence of the error on latitude. The higher the latitude, the higher is the error. This fact is also observed in the segments which include all latitudes equatorward of their borders, namely 3, 4 and 5. Segment 4 includes latitudes equatorward of $\pm 60^o$.

As we move from this segment to segment 5, which is narrower, and then to segment 3, the narrowest, we observe that the rms error and the difference between the new models and IGRF are reducing. So we observe the same behaviour of the rms error as before. The rms error in segment 1 is higher than that of segment 4. This is due to the fact that segment 1 includes latitudes $60^o \rightarrow 30^o$ and $-60^o \rightarrow -30^o$ while segment 4 includes all the latitudes equatorward of ± 60. This indicates that the error is higher at higher latitudes and that when data from lower latitudes is included, the rms value drops as the error there is smaller. Segments 2 and 5 are including latitudes closer to the equator and for this reason the pattern of error is not as clear as in the previous case.

Models in segment 6 have a high rms error, something expected as the level of disturbance there is higher than in any other segment. In segment 7, models also have high rms error and this inaccuracy is due to the inclusion of polar data in the pool of measurements used for the model derivation.

The pattern of rms error observed in segments 1, 2, 3, 4 and 5 is the same for each of the vector components and for all the three components treated together. Table 4.1 also reveals some other interesting characteristics of the behavior of the rms error. In all segments the rms error for each of the components and all of them together is lower for the model developed from the corresponding segment. The only exception is B_r component in segment 1. There the rms error of model 1 is slightly higher than this of model 4. This is explained by the fact that the rms errors of models 1 and 4 are in all cases very close due to the similar latitude ranges. The same similarity is observed for models 2 and 5. In segment 3 all models perform worse than model 3. Finally the same behavior is observed in the least accurate segments 6 and 7. This pattern confirmed the prediction that treating the field in

segments would provide more accurate models than the case that a model for the entire field is developed.

As can be seen from the figures and the table presenting the rms error of the vector components, the IGRF performs significantly worse than the other models in all cases. This was theoretically expected as the IGRF was used without the part depending on D_{st}. Additionally, the division of latitudes was expected to result in a better fit of the higher spherical harmonics to regional anomalies. In order to investigate the reason behind the low performance of the IGRF model, the histograms of the error of different models for each segment were plotted. They are given in Figures 4.11 to 4.13 and in Figure 4.15. The same histograms are included in greater detail in appendix B. The purpose of including them here is to show a pattern of behavior of the IGRF error rather than examine the detail of them. The histogram of the IGRF error is plotted in magenta color in each segment. The rest of the colors correspond to the rest of the models. In segment 1 the IGRF error, apart from its main lobe, shows two additional symmetric smaller lobes. They are located around the value of 35nT in segment 1 which represents latitudes close to the polar caps where disturbances are higher.

As we move to segment 2, in lower latitudes the lobes move closer to the overall mean and their peak frequency diminishes. In segment 3 the lobes have disappeared and the IGRF error distribution is similar to the rest of the models with a higher spread away from the mean. Exactly the same behavior is observed as we move from segment 4 to segment 5 and then to segment 3 (from higher latitudes to lower latitudes again). The IGRF error in segment 6 shows the most prominent lobes fact that is justified by the high disturbances located in the polar areas. Finally in segment 7 the lobes of segment 6 have been smoothed out by the inclusion of more accurate data from lower latitudes. Exactly the same phenomenon is observed for each of the three components and all three components treated together.

This behavior of the IGRF error cannot be justified by the exclusion of the D_{st} dependent part from the model. First of all the low level of ring current field for the days used in this investigation would not lead to such a high deviation of the lobes for segments 1, 2, 4, 6 and 7. Secondly if the lobes were caused by this exclusion they would still persist in segment 3 and 5, closer to equatorial latitudes, where the effect of the ring current is observed more clearly. In segment 3, the IGRF error shows a more spread out distribution of the main lobe but no side lobes. This leads to the conclusion that the effect of the exclusion of the D_{st} dependent part is the widening of the main lobe. The lobes are created as we move into

higher latitudes and they have been clearly formed at latitudes of segment 2. They intensify and move further from the main lobe as we move closer to the poles. This indicates that the source of this error is located at the poles.

Since the only sources of disturbance there are ionospheric currents, only these can be the sources of this IGRF error lobes. Two questions which arise now are the following. Why do these lobes not appear during the modelling of the IGRF, as presented in Olsen 2002? And why do these lobes not appear in the error histograms for the other models? Both questions are answered by the examining the effect of data conditioning. During the process of derivation of the IGRF model, outliers were removed after each iteration in order to isolate the main internal and external fields. The outliers were defined as data points with deviations larger than 25 nT.

The resulting model's accuracy was obtained by comparing it to the measurements that remained in the last iteration after all the outliers had been removed. The resulting error (for the vector components not parallel to the magnetic field vector) showed a slightly increasing level of values for higher latitudes. Another important parameter was the value of K_p index. For the data used in the IGRF modelling process K_p was lower than 1+ while here the limit of K_p is set higher at 2. As K_p describes the overall magnetic activity including the ring current (which here is within the same limits as during the IGRF modelling process) and the polar ionospheric currents, this slightly increased value represents a more intense polar activity. However the value of 2 still represents a quiet day. Another reason for this deviation is that vector data had been used only for latitudes within $\pm 50^o$. For the remaining range of latitudes scalar data was used. Additionally scalar data was used for low latitudes for cases when attitude information (used in the transformation of measurements in another coordinate system) was not available. Polar scalar data represented 20% of the used data and non polar scalar data close to 25%. This high percentage of scalar data provided a good fit to the component parallel to the magnetic field vector even in higher latitudes (see Olsen [1]). However in the remaining two vector components the error levels increased with latitude. Here as the three components are treated is spherical coordinates the error in all of them appears to increase with latitude. Examining the error in the magnitude and the error in orientation reveals why the lobes have not been identified.

4.1.2 Magnitude

The mean and rms values of the magnitude error are given in Figures 4.7 and 4.8. All the new models apart from model 7 have a mean error very close to zero. Model 7 shows significant deviation is segments 3 and 6 while in all other segments it performs quite satisfactorily. Deviation in segment 6 is justified by the high disturbance present in polar latitudes. The deviation of mean in segment 3 can only be justified by the effect of the ring current in these low latitudes. IGRF performs significantly worse in all segments and the variation of its error with latitude shows the same pattern as in the case of the vector components. Looking at the rms error we see that there is an important difference compared to the rms error for the vector components. The rms error in segment 3 appears slightly higher than in segment 2. Also by looking at the error in segment 1 we see that as we move from segment 1 to segment 2 the rms error decreases but as we move in latitudes close to the equator in segment 3 the magnitude rms error increases. This same behavior arises in the component parallel to the magnetic field vector used during the modelling and evaluation of the IGRF (see Olsen [1]). This is occurring due to the effect of the quiet ring current which has not been adequately modelled in the external field part and adds a disturbance close to the equator. For segments 4 and 5, the rms error behaves in exactly the same way as in the case of the components and the highest values are observed in segments 6 and 7 again.

Considering the histograms of the magnitude error in Figure 4.14 it is clear that all the new models follow a Huber distribution. This, combined with the fact that the rms error is lower for segment 2 than segment 3, confirms the validity of the new models. Now, however, the IGRF model shows significant deviations. In segment 3 the main lobe of the IGRF error distribution is moved in the positive axis of error. As we move in middle latitudes an additional lobe is appearing at higher values in the error histogram of the IGRF. In high latitudes (segment 1) this lobe is dominant. In the segments engulfing the equator (4, 5, 3 and 7) the relative strength of the two sources of error can be seen. The lobe appearing in the histogram for segment 3 is the dominant one in the histogram of IGRF error in segment 4. The small lobe on the right of the main one, is the early version of the main lobe seen in the histogram of segment 1. The error lobe introduced in higher latitudes for the IGRF model is due to the presence of the quiet polar ionospheric currents.

From Table 4.1 it can be concluded that in each segment the model with the lowest rms value is the one developed from data within its boundaries. Again models 2 and 5 perform similarly in terms of the rms error and the same relation holds for segments 1 and 4.

The next stage of examination is that of the error in orientation between the model and observed vectors.

4.1.3 Orientation

Figure 4.19 shows the histograms generated for different models for each segment. As expected the distribution is not Huber, neither Gaussian or Laplacian as the error can take only positive values and there is no directional information about it. The shape of the distribution is the same for all models in all segments. These figures are zoomed in the main lobes of the histogram while the right tail is extending to higher values. The information about the maximum error for each model in each segment is given in Table 4.2 together with the three measures that have been employed for the characterization of the orientation error. These measures are the mean of the error angle, the threshold value below which lies the error for 95% of the time and finally the percentage of time for which the angle error is below 0.1^o.

These measures are shown in Figures 4.16 to 4.18 and are given in further detail in Table 4.2. All three measures show the same pattern of behavior with latitude. As we move from segment 1 to segment 2 the mean decreases. However as we move from segment 2 to segment 3 the mean increases. This fact shows that the error in orientation is higher in the equatorial latitudes than at the latitudes of segment 2. This can be explained by two facts. First at high latitudes the error for the polar regions creates a high orientation error. At the latitudes of segment 2 ($40^o \rightarrow 20^o$ and $-20^o \rightarrow -40^o$) the effect of the polar disturbance on the orientation of the vector becomes much lower as this segment is located away from the poles. Being also far from the equator where the ring current is located, it enjoys the highest possible level of immunity between these two disturbance sources.

In segment 3 although the effect of the polar disturbance is minimal, the effect of the ring current is maximum. This theory is further supported by the fact that the magnitude of the field vector is minimum at the equator so that even if the actual magnitude of disturbance is lower than in higher latitudes, its effect on the orientation is higher than it would be in higher latitudes.

By comparing the rms values for the three vector components in Table 4.1 we observe the following facts. In segment 1 the rms error of B_θ is significantly larger than that of the other two components for all models. As we move in segment 2 the rms error is significantly reduced and is at more similar levels for the three vector components. As we move closer to

the equator, there is a slight reduction of the rms error while the similarity is preserved for the three components. As there is only a slight reduction in rms error while the magnitude of the actual geomagnetic field vector has significantly decreased the resulting distortion of the vector orientation is expected to be higher, as observed. For the segments containing the equator(7, 4, 5, 3) this behavior is not observed. The mean angle error is monotonically reduced as we move from segment 4 to segment 5 and then to segment 3.

In order to investigate this phenomenon Figure 4.20 shows the error of model 5 in segment 5 and Figure 4.21 the error of model 5 in segments 2 and 3 versus colatitude. In Figure 4.20, the main body of the error forms a lobe around the 90 degrees colatitude while at the same time the error points falling outside the main envelope of error form a W shape with the two deep ends around colatitudes of 70^o and 110^o. These are the boundaries between segment 2 and segment 3. The error of segment 5 is shown in Figure 4.21, where we see that the main error body does not form the same lobe shape while simultaneously the W shape of higher errors has less deep ends around the boundaries between segments 3 and 5. The reason for this difference is mainly due to the fact that the data in segment 5 was also used for the derivation of model 5 and this has resulted in a smoothing of the W shape and a flattening of the lobe shape. The validity of model 5 is shown in segments 2 and 3 for which the data has not been used in its derivation. A more consistent verification is presented in the following section were the models are tested for days not included in the modelling process. The same phenomenon is observed for segments 4 and 1.

Figure 4.17 shows the threshold value below which the error lies for 95% of the time. Its behavior is the same as the mean. It can be seen that the for segments 2 and 3 the error remains well below 0.1^o while for segment 1 the threshold is close to this value. The values in segment 5 are around the same level but, due to the smoothing mentioned above, this value should be investigated (see the next section). The same holds for segment 4. Segments 6 and 7 show the highest error as expected.

Figure 4.18 shows the percentage of time for which the error lies below 0.1^o. The behavior again follows the same pattern. In segment 2 the models show the highest value. It important to note that in segments 1, 2, 3, 4 and 5 the error is lower than 0.1^o for more than 90% of the time. Especially in segments 1, 2, 3 and 5 the percentage exceeds 95%.

From Figures 4.16 to 4.18 and Table 4.2 it is observed than in terms of the three measures and in all segments, IGRF performs worse than the other models. Its accuracy is still comparable to the other models. This of course is due the low levels of disturbance for

the days in question. Additionally the relative variation of the rms error between the three different components in Table 4.1 as we move from segment to segment is identical to the variation for all the other models. Thus the error in orientation for IGRF is not significantly lower than for the other models. In Figure 4.19 can be seen that the IGRF error has a very similar distribution to the other models. The main observed difference is that the main lobe of the IGRF error distribution is spread more to the right and has a lower peak.

Here another observation must be made. In Table 4.2 can be seen that the maximum orientation error is higher for model 7 and the IGRF in segments 6 and 7. This is due to the high disturbance present in segment 6 (polar areas). We see that in this segment model 7 and IGRF have higher error than model 6 which was developed from this segment. This is due to the fact that model 6 has adapted to the high disturbance area better than model 7 which is developed from the entire range of latitudes. That is why model 7 experiences the same high error in segment 6 and segment 7. In all other segments the maximum error of model 7 is slightly higher than the maximum error of the other models. For the same reasons this high error also appears in the IGRF model.

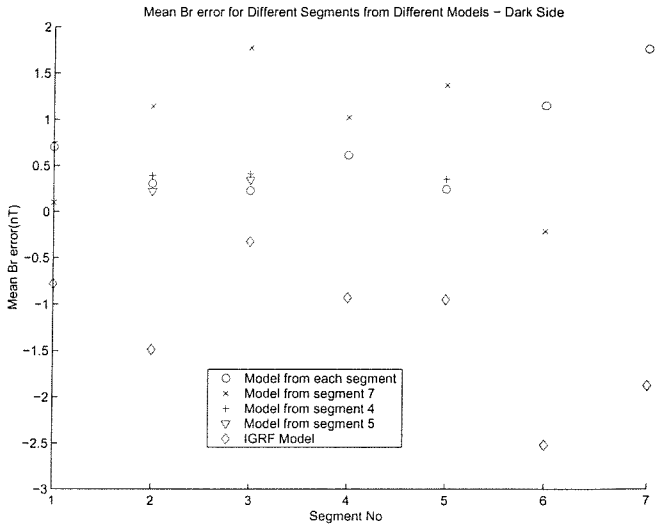

Figure 4.1: Mean B_r error for Different Segments from Different Models - Dark Side

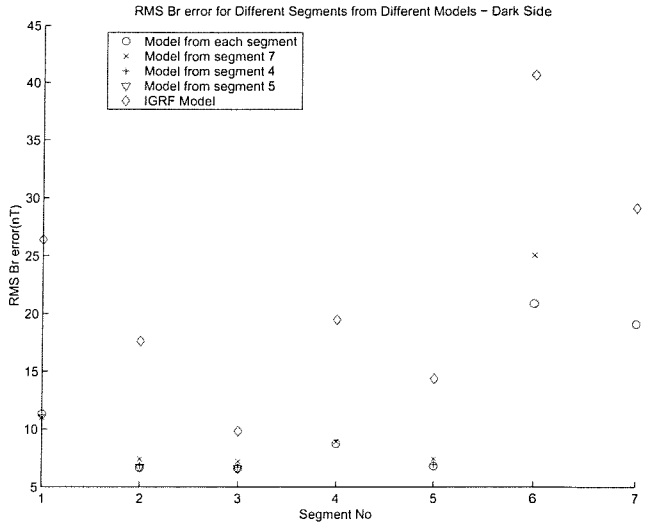

Figure 4.2: rms B_r error for Different Segments from Different Models - Dark Side

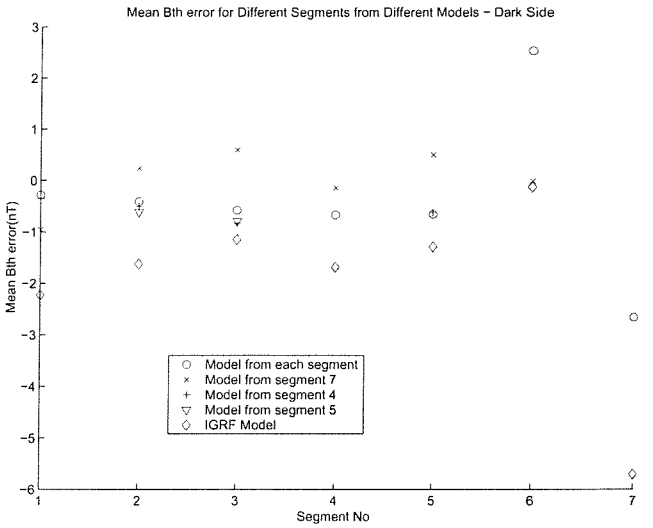

Figure 4.3: Mean B_θ error for Different Segments from Different Models - Dark Side

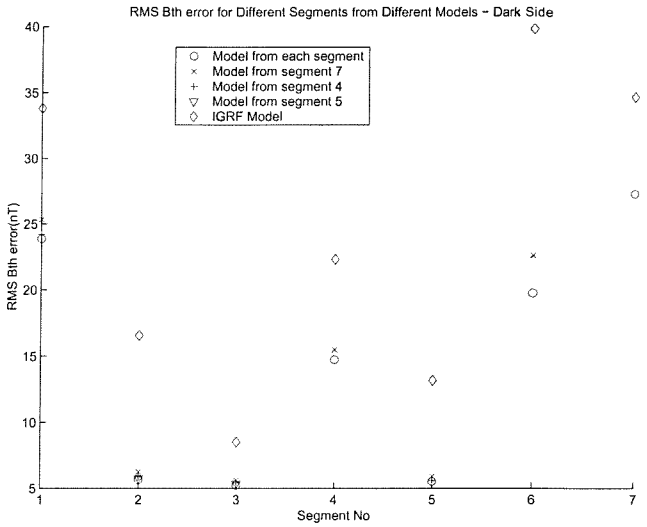

Figure 4.4: rms B_θ error for Different Segments from Different Models - Dark Side

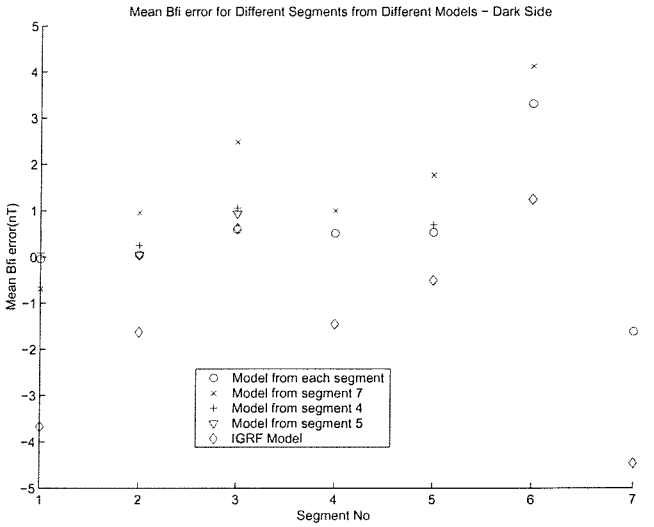

Figure 4.5: Mean B_ϕ error for Different Segments from Different Models - Dark Side

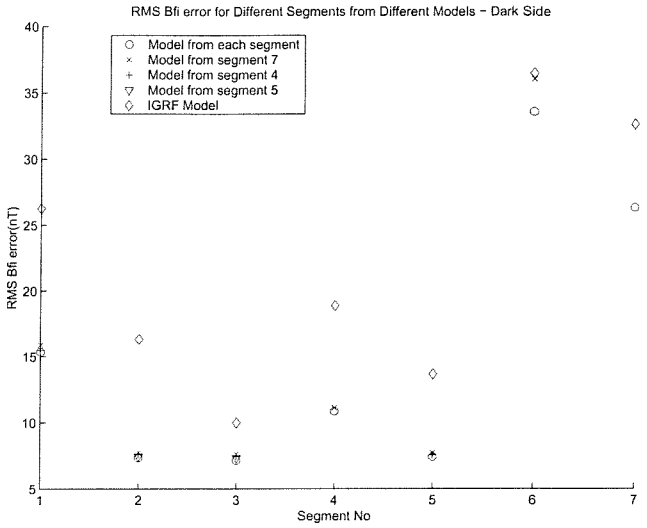

Figure 4.6: rms B_ϕ error for Different Segments from Different Models - Dark Side

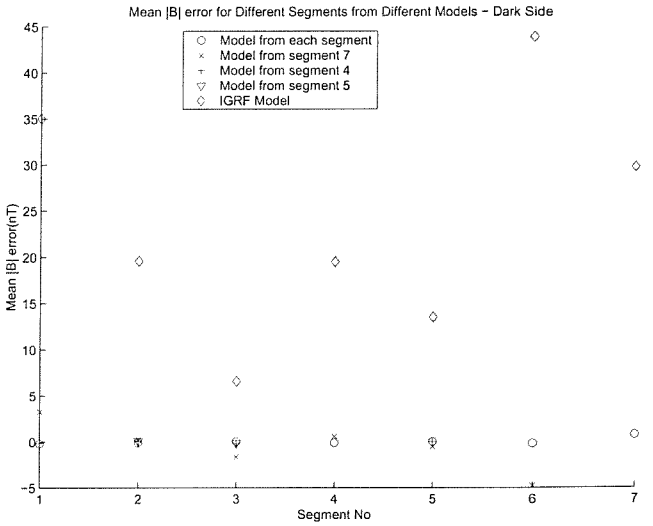

Figure 4.7: Mean $|B|$ error for Different Segments from Different Models - Dark Side

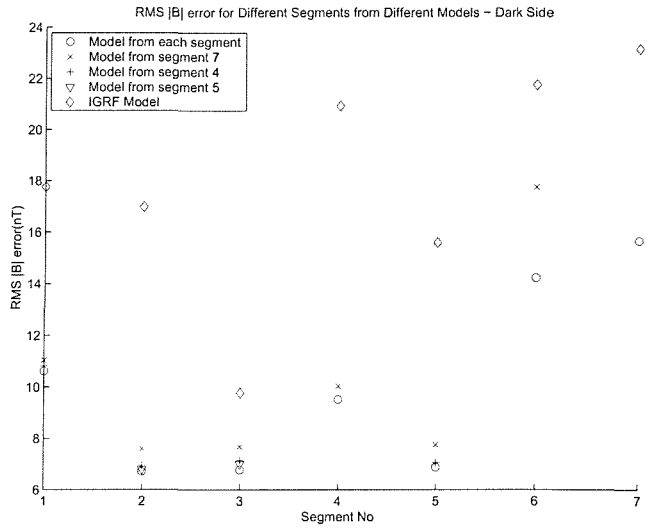

Figure 4.8: rms $|B|$ error for Different Segments from Different Models - Dark Side

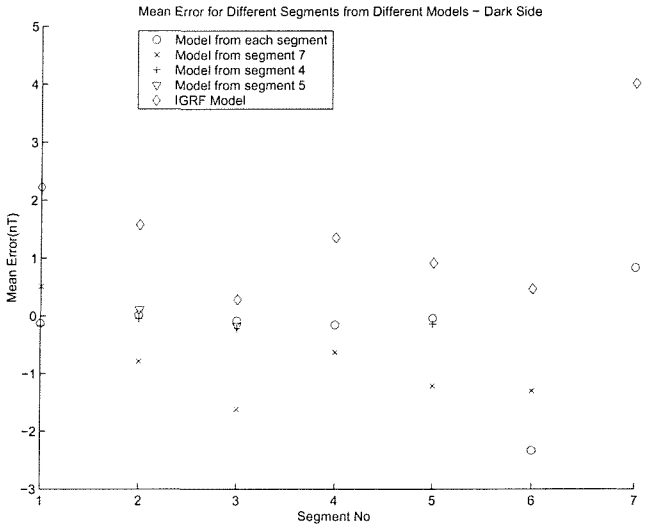

Figure 4.9: Mean error for Different Segments from Different Models - Dark Side

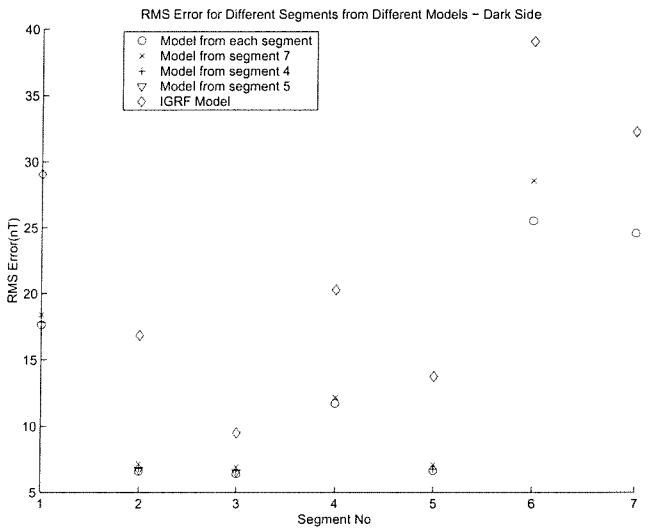

Figure 4.10: rms error for Different Segments from Different Models - Dark Side

Segment	Model	B_r Mean	B_θ Mean	B_ϕ Mean	|B| Mean	B_r&B_θ&B_ϕ Mean	B_r rms	B_θ rms	B_ϕ rms	|B| rms	B_r&B_θ&B_ϕ rms
1	1	0.702	-0.285	-0.038	-0.198	0.126	11.303	23.855	15.349	10.623	17.634
1	IRGF	-0.781	-2.225	-3.669	35.040	-2.225	26.392	33.808	26.252	17.758	29.056
1	7	0.100	-0.953	-0.688	3.283	-0.514	11.009	25.328	15.885	11.046	18.399
1	4	0.754	-0.351	0.092	-0.143	0.165	11.245	24.197	15.480	10.819	17.815
2	2	0.306	-0.414	0.049	-0.084	-0.019	6.670	5.643	7.340	6.707	6.595
2	IGRF	-1.489	-1.621	-1.625	19.590	-1.578	17.624	16.560	16.313	16.987	16.842
2	7	1.143	0.240	0.960	0.240	0.781	7.408	6.227	7.721	7.598	7.158
2	4	0.392	-0.507	0.254	0.095	0.046	6.869	5.863	7.584	6.949	6.820
2	5	0.225	-0.615	0.048	0.087	-0.114	6.725	5.762	7.467	6.794	6.697
3	3	0.230	-0.577	0.596	0.030	0.083	6.594	5.238	7.141	6.777	6.393
3	IGRF	-0.324	-1.148	0.620	6.581	-0.284	9.843	8.517	9.986	9.776	9.499
3	7	1.774	0.596	2.485	-1.626	1.618	7.218	5.608	7.623	7.683	6.915
3	4	0.408	-0.828	1.060	-0.205	0.214	6.712	5.404	7.456	7.143	6.625
3	5	0.346	-0.789	0.935	-0.135	0.164	6.633	5.352	7.331	7.003	6.530
4	4	0.616	-0.668	0.512	-0.112	0.153	8.752	14.723	10.854	9.519	11.722
4	IGRF	-0.930	-1.681	-1.451	19.499	-1.354	19.491	22.303	18.859	20.930	20.275
4	7	1.023	-0.144	1.002	0.590	0.627	8.940	15.481	11.118	10.034	12.167
5	5	0.244	-0.656	0.530	0.040	0.039	6.812	5.508	7.412	6.871	6.644
5	IGRF	-0.951	-1.289	-0.503	13.526	-0.914	14.374	13.157	13.661	15.594	13.743
5	7	1.373	0.500	1.765	-0.518	1.213	7.441	5.887	7.710	7.758	7.0787
5	4	0.354	-0.617	0.696	0.013	0.144	6.940	5.575	7.537	7.055	6.757
6	6	1.152	2.536	3.313	-0.174	2.334	20.872	19.744	33.574	14.232	25.526
6	IGRF	-2.519	-0.128	1.244	43.905	-0.468	40.674	39.851	36.468	21.756	39.068
6	7	-0.212	-0.014	4.129	-4.787	1.301	25.056	22.600	36.037	17.761	28.571
7	7	1.764	-2.657	-1.616	0.748	-0.836	19.121	27.330	26.364	15.678	24.618
7	IGRF	-1.876	-5.708	-4.465	29.763	-4.017	29.195	34.730	32.670	23.194	32.318

Table 4.1: Mean and rms error statistics for Different Segments and Different Models for Dark Side and days included in the modelling

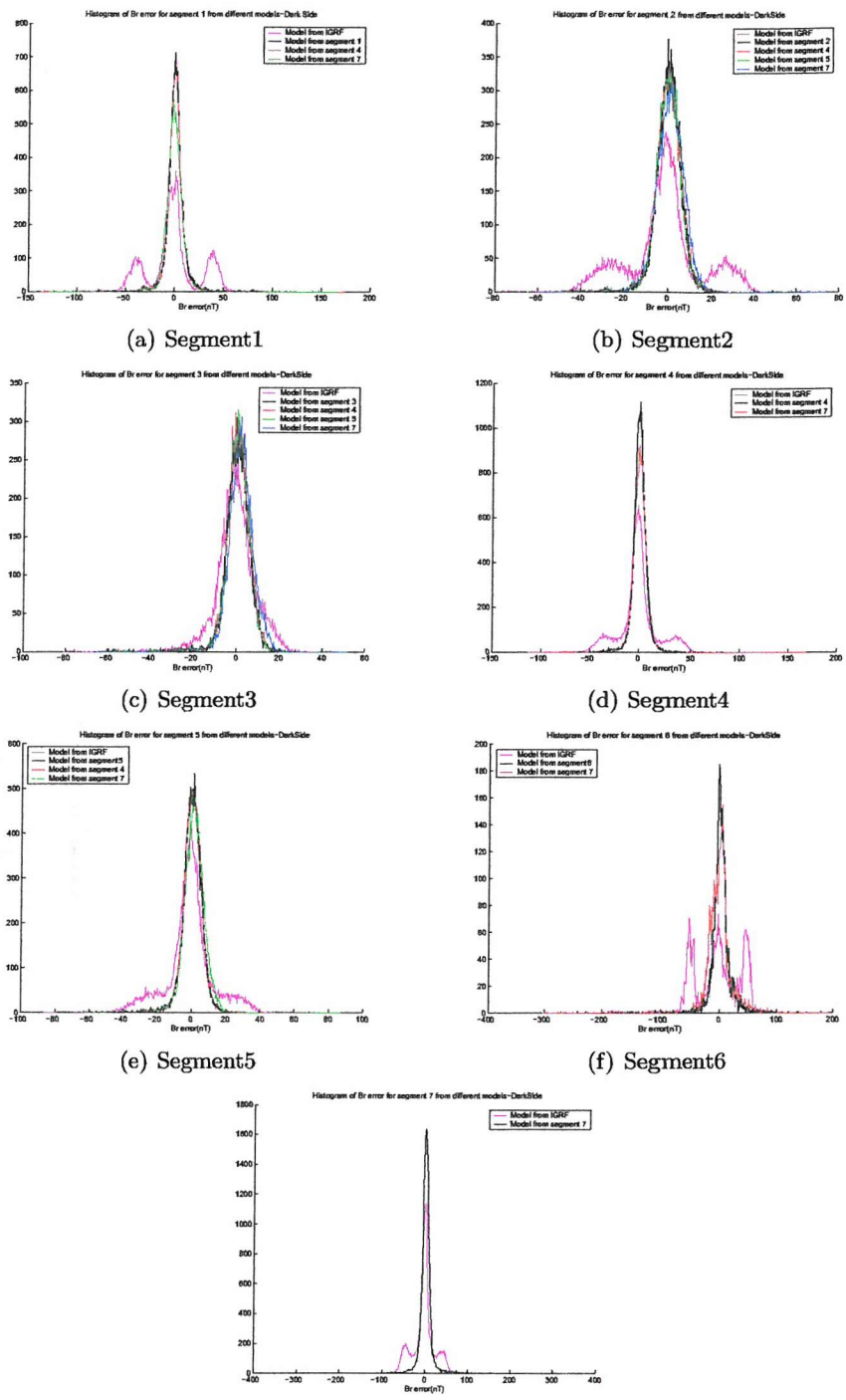

(a) Segment1

(b) Segment2

(c) Segment3

(d) Segment4

(e) Segment5

(f) Segment6

(g) Segment7

Figure 4.11: Histogram of B_r error for (a)segment 1 (b)segment 2 (c)segment 3 (c)segment 4 (d)segment 5 (e)segment 6 (f)segment 7 from different models-Dark Side

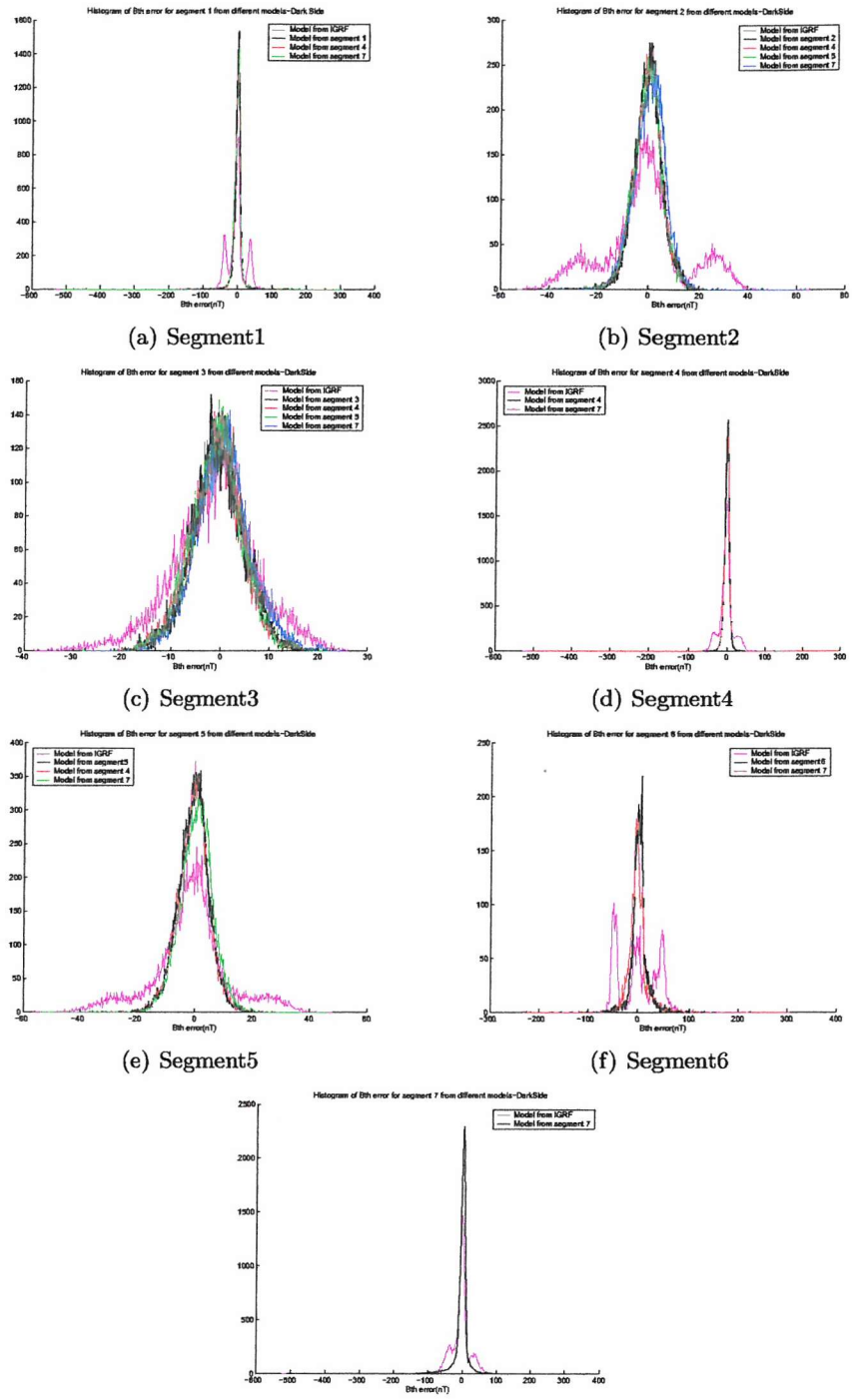

(a) Segment1 (b) Segment2

(c) Segment3 (d) Segment4

(e) Segment5 (f) Segment6

(g) Segment7

Figure 4.12: Histogram of B_ϕ error for (a)segment 1 (b)segment 2 (c)segment 3 (c)segment 4 (d)segment 5 (e)segment 6 (f)segment 7 from different models-Dark Side

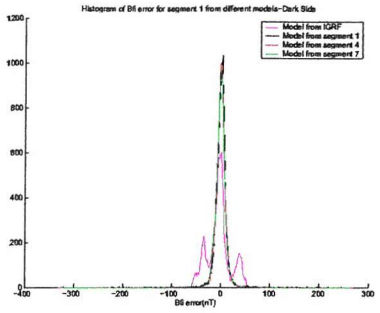

(a) Segment1

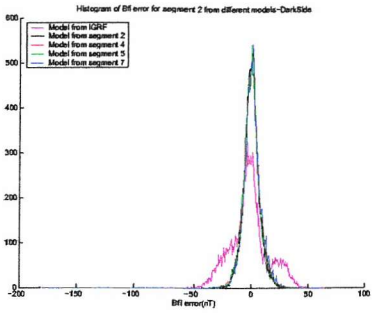

(b) Segment2

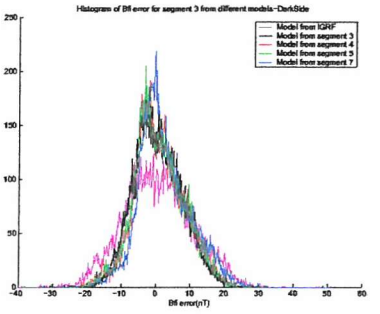

(c) Segment3

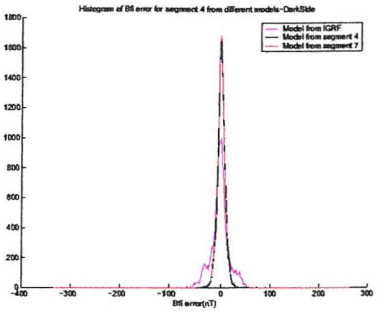

(d) Segment4

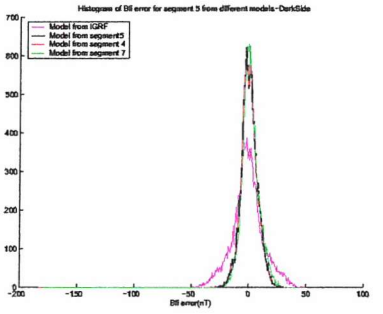

(e) Segment5

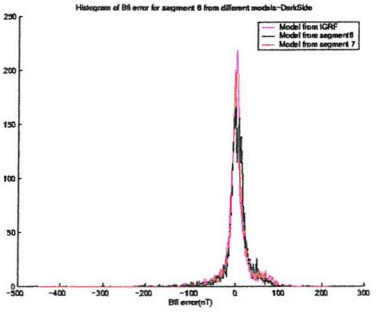

(f) Segment6

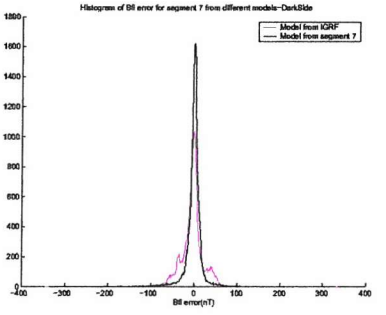

(g) Segment7

Figure 4.13: Histogram of B_θ error for (a)segment 1 (b)segment 2 (c)segment 3 (c)segment 4 (d)segment 5 (e)segment 6 (f)segment 7 from different models-Dark Side

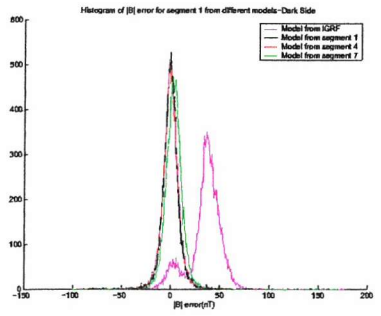

(a) Segment1

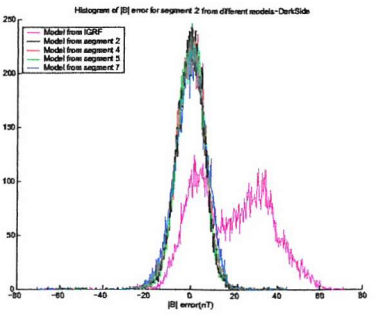

(b) Segment2

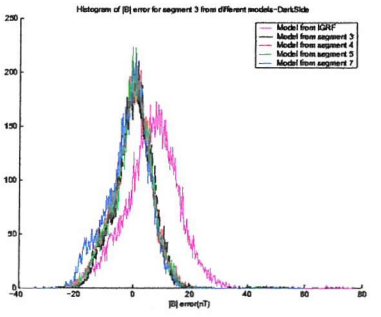

(c) Segment3

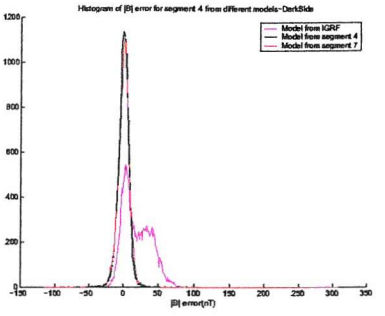

(d) Segment4

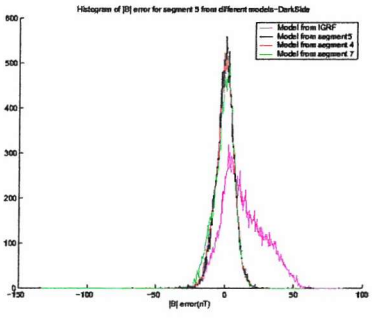

(e) Segment5

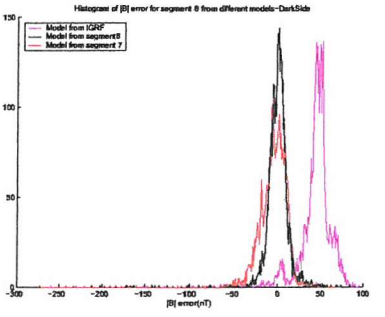

(f) Segment6

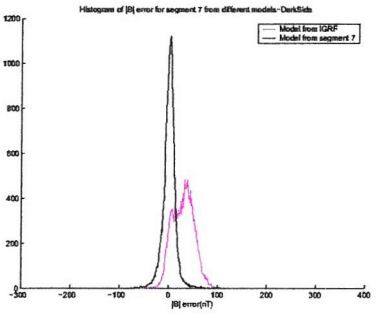

(g) Segment7

Figure 4.14: Histogram of $|B|$ error for (a)segment 1 (b)segment 2 (c)segment 3 (c)segment 4 (d)segment 5 (e)segment 6 (f)segment 7 from different models-Dark Side

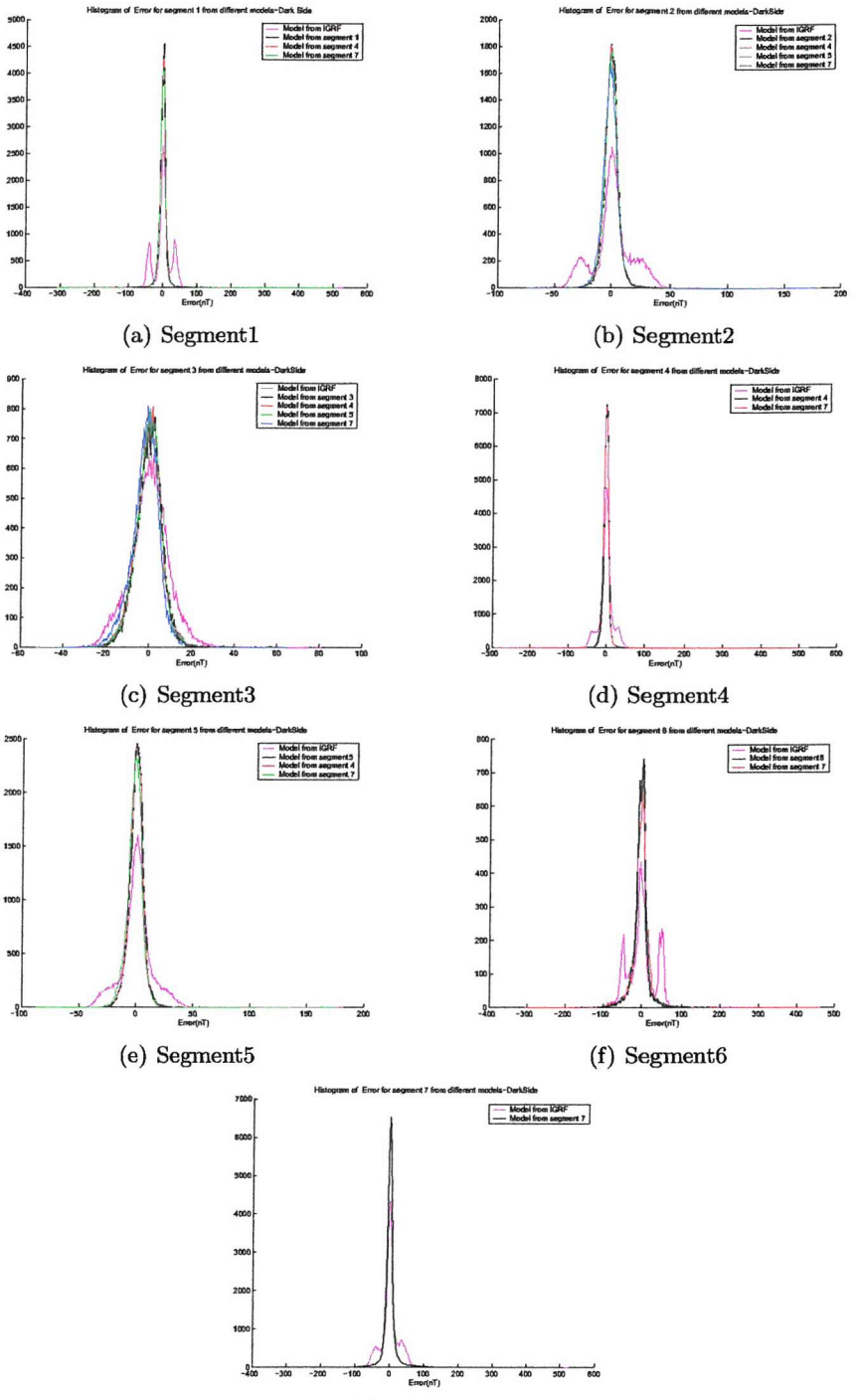

(a) Segment1 (b) Segment2

(c) Segment3 (d) Segment4

(e) Segment5 (f) Segment6

(g) Segment7

Figure 4.15: Histogram of Error for (a)segment 1 (b)segment 2 (c)segment 3 (c)segment 4 (d)segment 5 (e)segment 6 (f)segment 7 from different models-Dark Side

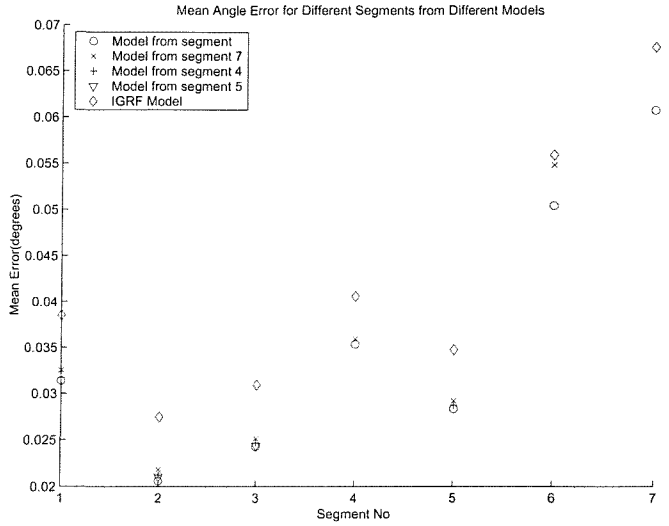

Figure 4.16: Mean Angle Error for Different Segments from Different Models-Dark Side

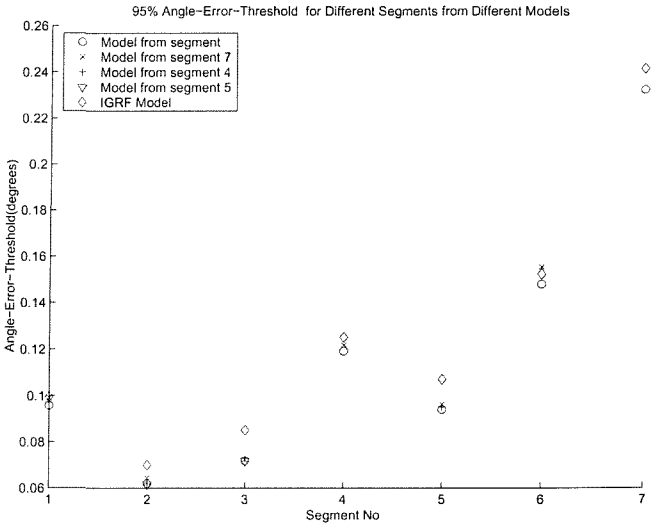

Figure 4.17: '95 % Angle-Error-Threshold for Different Segments from Different Models'

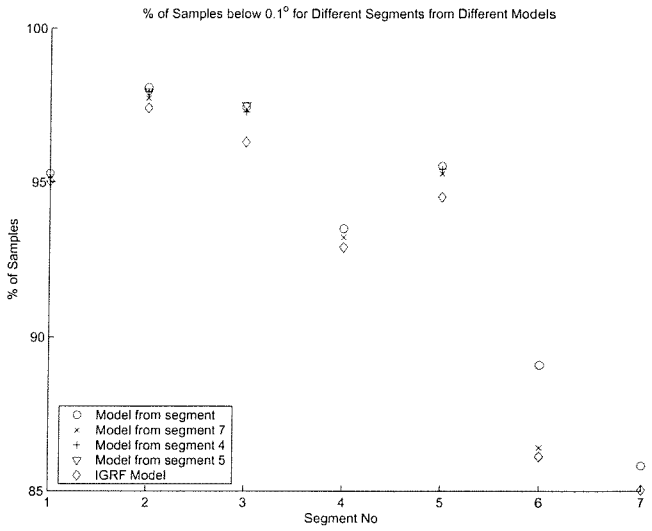

Figure 4.18: % of Samples below 0.1^o for Different Segments from Different Models

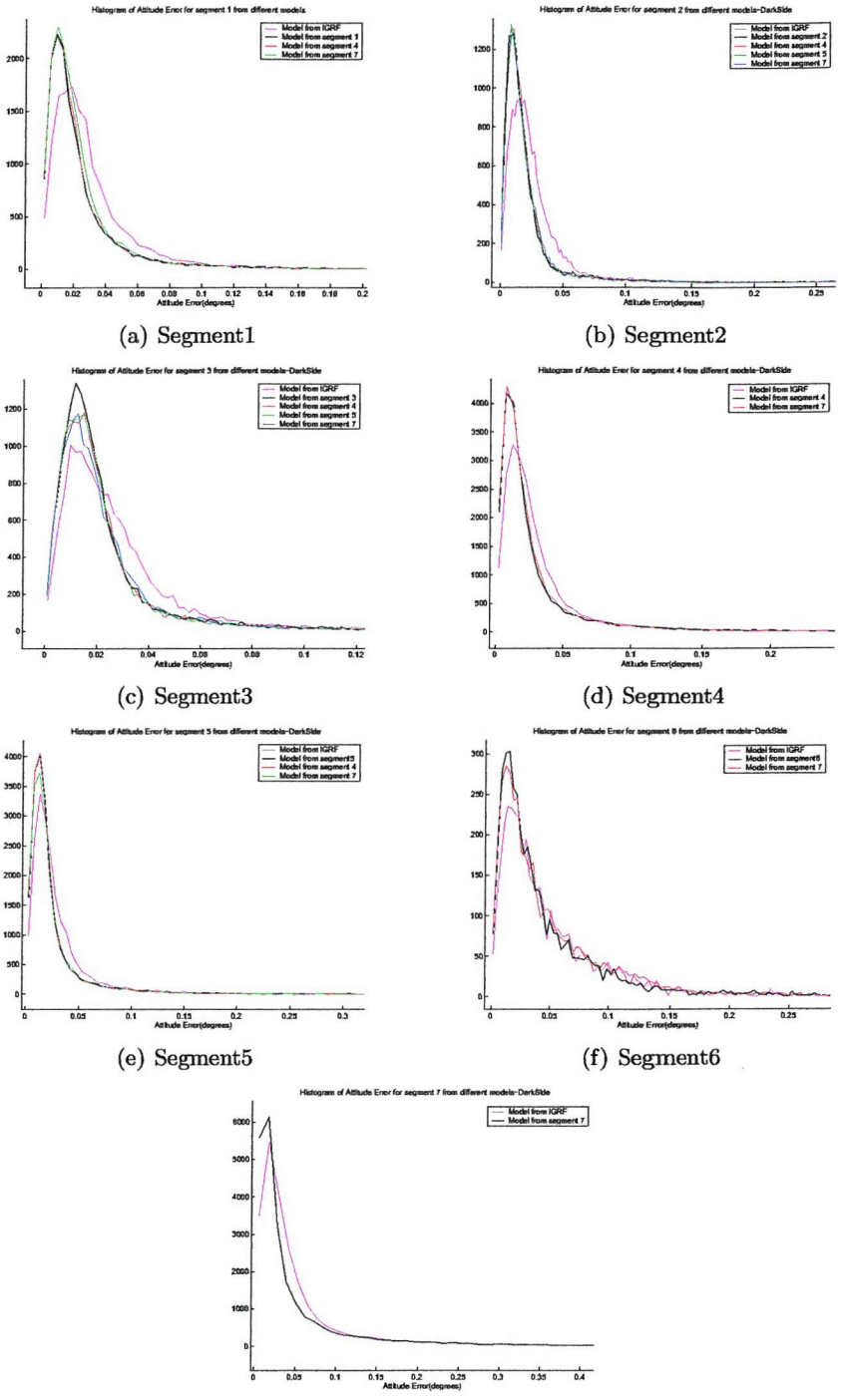

(a) Segment1

(b) Segment2

(c) Segment3

(d) Segment4

(e) Segment5

(f) Segment6

(g) Segment7

Figure 4.19: Histogram of Attitude error for (a)segment 1 (b)segment 2 (c)segment 3 (c)segment 4 (d)segment 5 (e)segment 6 (f)segment 7 from different models-Dark Side

Segment	Model	Mean(^{o})	95%Threshold(^{o})	% below 0.1^o	Maximum(^{o})
1	1	0.031	0.096	95.280	1.849
1	IGRF	0.039	0.100	95.030	2.095
1	7	0.033	0.099	95.090	2.021
1	4	0.032	0.097	95.230	1.899
2	2	0.021	0.062	98.080	0.021
2	IGRF	0.027	0.070	97.410	0.994
2	7	0.022	0.064	97.730	0.913
2	4	0.021	0.062	97.930	0.915
2	5	0.021	0.062	97.940	0.885
3	3	0.024	0.072	97.450	1.012
3	IGRF	0.031	0.085	96.300	1.050
3	7	0.025	0.072	97.370	0.971
3	4	0.025	0.073	97.280	0.982
3	5	0.024	0.072	97.500	0.981
4	4	0.028	0.082	96.500	1.883
4	IGRF	0.033	0.086	95.900	2.096
4	7	0.029	0.083	96.220	2.013
5	5	0.022	0.064	97.530	0.981
5	IGRF	0.029	0.078	96.520	1.010
5	7	0.024	0.066	97.480	0.968
5	4	0.024	0.065	97.420	0.979
6	6	0.050	0.148	89.100	2.608
6	IGRF	0.056	0.152	86.130	3.534
6	7	0.055	0.155	86.420	3.681
7	7	0.039	0.129	92.830	3.441
7	IGRF	0.045	0.134	92.040	3.502

Table 4.2: Mean,95%percentile and % below 0.1^o angle error statistics for Different Segments and Different Models for Dark Side and days included in the modelling

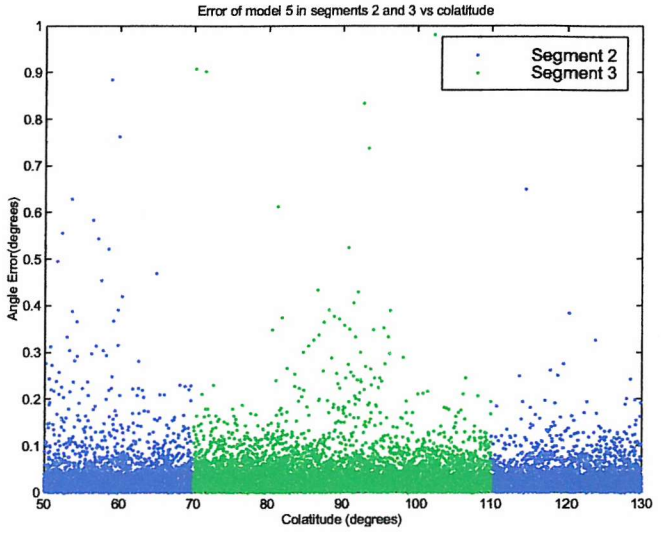

Figure 4.20: Error of model 5 in segments 2 and 3 vs Colatitude

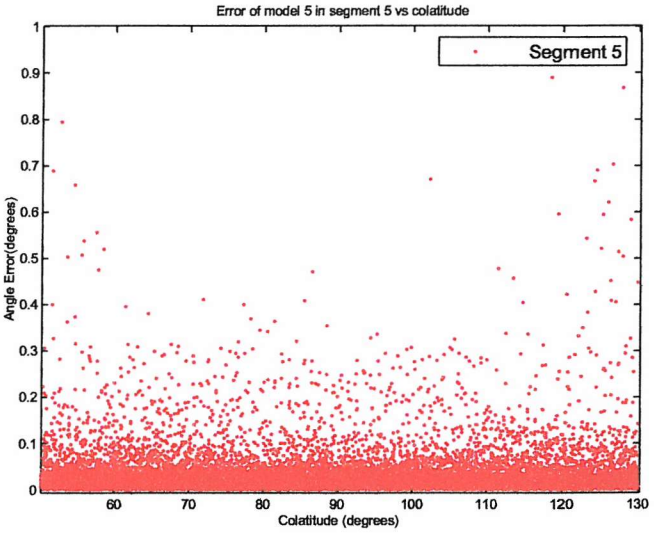

Figure 4.21: Error of model 5 in segment 5 vs Colatitude

4.2 Validation of the Models in the Nightside for quiet days not included in the modelling

This test was the most important for the validation of the models in the nightside. The data used is collected from quiet days, different to the ones used for the modelling. Depending of the availability of such days it was decided to try to keep them as far as possible from days included in the modelling process. The discussion of the results follows the same structure as the previous section. First commenting on the different vector components, then on the magnitude and then on the orientation. The figures and tables referred to in this section are presented in Appendix C.

4.2.1 Vector Components

Figures C.1 to C.6 and Figures C.9, C.10 show the mean and rms error for each of the three components and for all the three components together. These statistics are presented in detail in Table C.3.

The mean of each of the three components enables us to make the following observations. The mean of B_r has been slightly shifted downwards in the negative spectrum compared to the mean of B_r for the days used in the modelling. Models 1, 2, 3, 4 and 5 vary around the same mean value while IGRF lies in all cases higher than the other models and model 4 lower than the other segments. This is the same pattern of behavior as for the days used in the modelling but small positive DC components is present. The same deviation is observed for B_θ where the relationship between different models remains the same but the error is shifted slightly in the negative direction. For the B_ϕ component the same relationship holds but now the error has slightly moved in the positive direction. When all the components are treated together in Figures C.9 and C.10 the mean error behavior is the same as in the case of the days used in the modelling. In segments 1, 2, 3, 4 and 5 the mean error of all models, apart from IGRF and model 7, lies in the region $-1nT \rightarrow 1nT$. The mean error of IGRF is in all cases higher. The mean error of model 4 is higher than all of the other new models. Again in segments 6 and 7 the highest mean errors are observed. As the mean indicates the level of randomness of the error, it can be said that the model has a similar mean accuracy as at its derivation, when this mean error is evaluated for all three components together. Keeping in mind that the models were developed with measurements from all three vector components, the treatment of the model mean error as a whole is more appropriate than its

treatment in vector components. The DC components present in the individual components are small and they give an indication of misfit of each individual component of the model to the real one during quiet days.

In order to investigate the error that is more likely to be experienced we examine the rms values in Figures C.9, C.2, C.4, C.6 and C.10. The behavior for B_θ, B_ϕ and all the three components together is exactly the same as for the days used in the modelling. As we move from segments in higher latitudes to segments in lower latitudes, the rms error decreases. The same behavior is observed for B_r component with the difference that the rms error in segment 3 is identical to the rms error in segment 2. This most probably happens due to low values of the B_r component at these latitudes and also due to the low disturbance experienced along this vector direction. The B_r rms error values for these two segments are so close that any distinction between them is inconsistent.

This is also reflected by the similar levels of error in segment 5 which engulfs the latitudes of segment 2 and segment 3. For the other two components the error decreases as we move from higher to lower latitudes, although the value differences are small for segments 2, 3 and 5. Segments 6 and 7 experience the highest rms errors as in the days used in the modelling.

By examining the Tables 4.1 and C.1, we can compare the rms error values for all the three components treated together, for the days used in the modelling and the days not used in the modelling. Based on these, we come to the following conclusions. The rms error of all models in segments 2, 3, 4 and 5 is very similar for days included in the modelling and those not included. The difference is smaller than $1nT$. The biggest differences are experienced in segments 1, 6 and 7 and they reach a maximum value of $3.6nT$(IGRF) in segment 6. This is as expected since these three models are more contaminated by errors in higher latitudes.

This similarity of rms values for days included and not included in the modelling verifies the validity of the models, especially for segments 1, 2, 3, 4 and 5 which represent middle and low latitudes, away from the polar regions.

An important observation for these segments arises from looking at the relative values of rms error for each of the three components. For days included in modelling as it can be seen in Table 4.1, that in segments 2 and 3 all the models, apart from IGRF, exhibit the following pattern:

$$rms(B_\phi) > rms(B_r) > rms(B_\theta) \tag{4.1}$$

and for days not included in the modelling :

$$rms(B_\phi) > rms(B_\theta) > rms(B_r) \tag{4.2}$$

Additionally we see that for all models in these two segments the rms error of B_r drops in the case of the days not included in the modelling. The rms error of B_θ and B_ϕ increases for the same case. This pattern is also observed in segment 5 which engulfs both segments.

Following these observations and noting the above inequalities we conclude that for middle to low latitudes, where the effect of the polar disturbance is minimum, the error in B_θ increases for the days not included in the modelling. For these days, inequality 4.1 shows that the error of B_θ is the lowest at middle to low latitudes. This is mainly due to the fact that the ring current effect has been absorbed by the main model. As the effect of the ring current is mainly on the horizontal plane, it affects more the B_θ component. In the case of days not used in the modelling the effect of the ring current is similar but not exactly the same. This adds an extra error to the models, especially for the segments closer to the equator. This additional error is translated into an increase of the rms error of B_θ and B_ϕ for days not included in the modelling process. It is also important to note the fact that the rms value of B_r drops for these days. This means that during the derivation of the model there was a smoothing error which provided a better fit for B_θ which was contaminated by the ring current, and a worse fit for B_r which is less contaminated. B_ϕ is affected in a similar way to B_θ as close to the equator it is located around the horizontal plane.

The histograms for the three components are given in appendix A. Their behavior is similar as for the days used in the modelling. The phenomenon of the two additional lobes for the IGRF error appears with the same dependence on latitude. The location of the lobes for the IGRF model in segment 1 is very similar to the one for days included in the modelling. This confirms the fact that the new models, which show a Huber error distribution, are adopted to a magnetically quiet day, which also includes the effect of the quiet polar disturbance.

4.2.2 Magnitude

The mean and rms error of the magnitude are shown in Figures C.7 and C.8. In all segments apart from 6 the mean magnitude error for all models, apart from the IGRF, is very close to zero and this fact shows the good quality of the models. The mean error of the IGRF is high and varies with latitude, in a similar manner to the days included in the modelling. Segment 6 shows the highest deviation, a fact explained by the high disturbance in the polar areas.

By examining at Tables 4.3 and C.3, the level of the mean error can be compared for

the days included and not included in the modelling. For all segments apart from segment 6, models 1, 2, 3, 4 and 5 produce mean errors close to zero and well below 1nT (in absolute value). These shows that the magnitude error of these models created during quiet days has a random variation around 0. Model 6 in segment 6 has a mean magnitude error close to zero as well. Model 7 shows higher residuals in all segments. The IGRF model shows the highest deviations. In all segments the value of the mean magnitude error of the IGRF is very similar for days included and days not included in the modelling. This confirms that the days used for the verification of the models are of similar activity to those used for the modelling.

Considering the rms value of the magnitude error, we arrive at the following conclusions. Firstly, the variation of the rms error with latitude, as we move from segment 1 to segment 2 and to segment 3, or from segment 4 to segment 5 and to segment 3 is exactly the same as for the days included in the modelling. The fact that in segment 3 the rms magnitude error is higher than the one on segment 2 is confirmed. This is again due to the influence of the ring current and the equatorial electrojet. Again segments 6 and 7 show the highest deviations. By examining Tables 4.1 and C.1,we see that the rms values are very similar for days included and not included in the modelling. This confirms further the validity of the models. In various segments some models show a slight increase in rms while in other cases some show a slight decrease. Excluding the IGRF model and model 6 these differences never exceed the value of $1nT$. It is important to note that the rms error of the IGRF in all segments apart from 6 is slightly lower when compared to the corresponding IGRF error values for the days included in the modelling. The histograms (appendix B) of the various models for the magnitude error are identical for all segments to the ones for days not included in the modelling.

Having examined the magnitude error, it now remains to investigate the error in orientation.

4.2.3 Orientation

The error in orientation is examined again with the three measures mentioned in the previous sections. They are shown in Figures C.11 to C.11 and the actual values are given in Table C.4.

Examining Figure C.11 and comparing it with Figure 4.16 the following facts are observed. As we move from segment 1 to segment 2 the mean angle error drops and as we move to segment 3 it increases again. The reasons are the same as in the case of the days

included in the modelling. In Figure 4.16 (for days used in modelling process), this behavior is not observed if we move from segment 4 to segment 5 and then to segment 3. The reason for this unusual fact was suspected to be the smoothing experienced as segments 4 and 5 include all the latitudes equatorward of their borders. It was suggested that in order to confirm this assumption the models should be tested for days not included in the modelling. So here, by examining Figure C.11, we see that this unusual behaviour is not further observed. The mean angle error of segment 5 is lower than the one for segment 3 and the mean error for segment 4 is lower than the one for segment 1. This is expected as the error in model 5 should be at a level between those of segment 2 and segment 3. Similarly, the mean error in segment 4 should be at a level between those for 1, 2 and 3. In terms of the actual values, by examining Tables 4.2 and C.2 a very interesting fact arises. In segments 2, 3, 4 and 5, all models except IGRF show a lower mean angle error for the days not included in the modelling than those included. In segments 1 and 6 the mean error increases. These two segments are most effected by the polar current systems and that is why such an increase was expected. This increase results in an increase of the mean angle error in segment 7 as well since it includes the entire range of latitudes. The fact that in segments 2, 3, 4, 5 the mean angle error is reduced (slightly) is further evidence of the validity of the models. Here it must be noted that, since the angle error is always positive, the mean value is not indicative of the randomness of the error but of the location of the main lobe of the error distribution. In all segments IGRF has the highest mean angle error.

In Figure C.12 we see the threshold value below which the error for 95% of time lies. In segments 2, 3, 4 and 5 the threshold value is well below 0.1^o with the lowest value in segment 2. In segment 1 it exceeds 0.1^o while in segments 6 and 7 it reaches the highest values, over 0.3^o. Similarly to the mean angle error, the threshold value in segment 5 is lower than the one of segment 3, as expected, and not higher as observed for the days used in the modelling. The same happens for segments 1 and 4. By examining Tables 4.2 and C.2 we see that the threshold values drop in segments 2, 3, 4, 5 significantly for the days not included in the modelling. In segment 6 which includes polar latitudes, the threshold increases, a fact which reflects the low consistency of models in these segment. Segment 1 includes latitudes adjacent to segment 6 and thus we see that there is an increase there as well, of smaller level.

The improvement in the threshold value confirms that the use of a large number of quiet days in the modelling process resulted in a very high accuracy but in overvalued statistical measures, such as mean and rms, that describe this accuracy. From the testing is seen that

the accuracy of the model is higher than expected.

Using the same tables we can compare the values of the percentage of error below 0.1^o for different segments and models. The behavior is similar to that of the mean angle error and the threshold value. In segments 2, 3, 4, 5 the percentage increases for days not included in the modelling. For segments 1, 6 and 7 the percentage falls.

Keeping in mind that there is no interdependence between the mean , the threshold value and the percentage value, this pattern of behavior shows that the models are more accurate for low latitudes than for higher ones. The accuracy of the models is very high and this confirms that they are satisfactory for representation of the quiet geomagnetic field.

The histograms of the angle error are given in Appendix B and they are very similar to the ones for the days included in the modelling.

The next phase of validation of the model is the examination of its performance in the day side. This examination is performed in two steps. First for the days used in the modelling and then for the days not included.

4.3 Validation of the models in the Day side for days included in the modelling

All the new models and the IGRF were tested for day side measurements. The measurements were collected from the same days which were used for modelling. The examination of results is performed in the order of vector components, the magnitude, and finally the orientation.

4.3.1 Components

The mean and rms error values of each component and all the components together for all models and segments are shown in Figures 4.22 to 4.27 and Figures 4.30 and 4.31. In terms of the mean error a negative dc shift is observed for B_r, a positive shift for B_θ, and a negative shift for B_ϕ. When the three components are treated as a whole, it is observed that there is a spread of the mean values for different models around zero. The mean error for models 1, 2, 3, 4, 5 is confined within the region of $\pm 1nT$ for all segments apart from segments 6 and 7. Model 7 and IGRF show the greatest deviations in all segments. The fact that the mean error for model 1, 2, 3, 4 and 5 remains at very low levels, when all three components are treated together, shows that the model can be assumed to have a random noise.

Examining the rms error in Figures 4.23, 4.25, 4.27 and 4.31, we see a major difference

for all components, compared to their characteristics in the nightside. Here for all models, apart from IGRF, the rms error drops as we go from segment 1 to segment 2, similar to what happened in the nightside. However, when we move to segment 3 the rms error increases. This is observed for each of the three components and for the case when they are treated together. Two more important observations can be made. Firstly, the rms error in segment 5 is lower than in segment 3. As segment 5 is the combination of segments 2 and 3 this is expected. But this time the segment with the highest error is segment 3 and not segment 2 as in the nightside case. Another important fact is also that the rms error values for segments 2, 3, and 4 are in close proximity.

The IGRF model still has the highest rms error in all segments. In Table 4.3 the actual rms values are given. Comparing them with those in Table 4.1 for the nightside of the same days we make the following observations. Firstly, if we ignore segment 6 then the highest increase occurs in segments 3. A significant increase also occurs in segments 2 and 5. Segment 1 experiences the smallest increase. This sequence shows that in equatorial latitudes there is a source of error. That is because, as we go to higher latitudes, the effect of this disturbance is small. This is well explained by the presence of the equatorial electrojet. In particular, since located over segment 3, it creates the highest disturbance there. As we move away from equator its effect is decreasing and that is why we see hardly any effect in segment 1 compared to the nightside.

IGRF has experienced a slight increase and it basically has a performance similar to the one in the nightside. In segment 3 the rms of all other models has increased to a level comparable to that of the IGRF, although they still remain lower. In all the other segments the difference is more distinct. The lowest rms error is in segment 2. The rest of the segments (4 and 7) are an averaged version of segments 1, 2, 3 and 6. Figures 4.32, 4.33, 4.34 and 4.36 show the histograms of B_r, B_θ,B_ϕ and of all the three components together respectively.

The lobes observed in the IGRF error distribution in the nightside are still observed, most clearly for segment 1 which experiences the lowest contamination from the equatorial electrojet. In the rest of the segments the error introduced appears to follow the same distribution as for the error in the nightside and the lobes for all models are widened. The same also happens for the IGRF model. As the central main lobe expands, it absorbs the side lobes in higher latitudes, present in the case of the nightside. This can be seen for each component and for all the components together. Especially for segment 3 the performance of IGRF is very close to the performance of all other models. This is due to the increase of

the error in the other models and not the increase in accuracy of the IGRF. Although the distribution of the new introduced error appears to be similar to the one of the nightside models (except IGRF), its main effect can be more clearly seen by examining the magnitude.

4.3.2 Magnitude

Figures 4.28 and 4.29 show the mean and rms error of the magnitude respectively. As seen, the mean error is shifted in all segments for all models. Models 1, 2, 3, 4, 5 and 6 show a negative mean error around the value of -5nT. Model 7 in most segments is close to this value, except in segment 6. IGRF model shows large mean error values and their distribution in segments is similar to the one for the nightside. A more careful examination shows that IGRF has been shifted by the same amount. This can be clearly seen by comparing the values in Table 4.3 with the nightside values in Table 4.1. All models experience the same positive shift and hence it was concluded that this error must be caused by the dayside solar quiet field usually denoted in literature by S_q. This system of currents is located in the dayside ionosphere and on the earth's surface it reinforces the main internal field. However in Oersted's orbit (higher than the ionosphere) this system of currents causes exactly opposite effect, as the field created by each current element is opposite to that on earth's surface. The level of disturbance varies with altitude.

Sabaka et al. [52] used MAGSAT data to observe the effect of these currents. The magnitude of the disturbance for MAGSAT orbit, which is similar to that for Oersted, reached values of up to -20nT, a fact that shows that it can be the reason for this dc shift as well. Another noticed fact in the work of Sabaka et al. [52] was that although polewards of $\pm 45^o$ latitude on earth the effect is reversed, in the orbit of MAGSAT the dominant disturbance in all the three vector components was negative. This behavior was reversed at around 80^o and -80^0 latitude, where the positive error became the dominant one. However, in Oersted data there is only a very small number of measurements poleward of these latitudes. The dominant negative error in all the latitudes creates this negative dc component.

The confirmation of the fact that this negative dc error is not due to the model comes from the comparison with the IGRF performance. In the terms of the mean magnitude error, in all segments, the IGRF experiences the same negative shift as the other models and additionally the values for the individual vector components are exactly the same. This means that the error is not due to the inaccuracy of the derived new models, since if it

were this behavior would be observed only in them and not in IGRF. The exact ionospheric conditions that create the residuals cannot be identified by the mean and rms values of the individual components as the pool of data includes a large number of days from different seasons and different ionospheric conditions. What is more important is that the overall performance is consistent with the effects of these phenomena.

Although the performance of all the new models is similar to the performance of the IGRF in terms of the mean magnitude error, the situation is different for the rms magnitude error. The IGRF magnitude rms error is very similar to the one for the nightside. For all the new models though, the rms magnitude error has increased to levels similar to the IGRF rms error values. Starting from the poles, we see that the rms magnitude error for model 6 and 7 has increased significantly. The rms error of IGRF has increased by a lesser amount. The resulting values for the three models are identical. In segment 1 we see that the increase in the IGRF is significant, while the increase in the other models is smaller. In segment 2, closer to the equator, models 2, 7, 4 and 5 have identical increase, up to a similar rms error. IGRF still has a higher rms error but it experiences no additional increase compared to the nightside. Exactly same behavior occurs in segment 3, around the equator.

This characteristic shows that the variance of the error around the mean has increased. In segment 3 all the models, including IGRF, have very similar rms values, which shows that this noise is uncorrelated to the higher error of the IGRF observed in the nightside. If the source of error was the same then in this segment IGRF should have a higher rms value. As we move up to segment 2 we see that IGRF has a higher rms than the other models but it has not changed compared to the nightside. This means that although the variance of the new dayside error is higher, it is still smaller than the IGRF error in the same segment in the nightside. As we move in segment 1 we see that the rms error of the IGRF is significantly increased. The same happens for all other models, but IGRF has a much higher rms error increase. At the same time the rms error of the other models is only slightly higher than in segments 3 and 2. This shows that the error of the IGRF now becomes correlated with the error of the nightside as it increases significantly. Finally in segment 6 we see that the increase is much higher for models 6 and 7 than for the IGRF and they all attain a similar level. The above discussion is confirmed if the magnitude error histograms for the night and daysides are compared in Figures 4.14 and 4.35.

Examining the histogram of IGRF error in these two figures gives a good insight of the error sources. In segment 1 for the nightside, the IGRF error shows a main lobe on the

positive axis while a much smaller lobe is located around zero. As we move in segment 2 the main lobe decreases while the secondary lobe strengthens. In segment 3, on the equator, the small lobe has become the main one and the large lobe of segment 1 has diminished. As its effect still exists the histogram is shifted towards the positive axis. In the dayside, in segment 1, the two lobes are comparable. In segment 2 they have already merged to one lobe and in segment 3 they have become identical so that the rms error decreases.

As already noted in the analysis of the nightside results, the lobe located closer to zero is connected to phenomena closer to equatorial latitudes, as it strengthens there. The lobe on the positive axis is connected to phenomena in the polar areas as there this lobe is strongest. As we see, the two lobes merge in higher latitudes than in the nightside. This means that the disturbance caused in the equatorial latitudes is stronger than in the dayside. This is well explained by the presence of the solar quiet ionospheric currents in the dayside. Apart from the mean magnitude deviation they cause, they also cause variations which are translated into additional rms error.

This new rms error is random around the mean magnitude error in segment 3 and this is why it is the same for all models in these segments. As we move in segment 2 the rms error for models 2, 7, 4 and 5 remains the same, while the IGRF rms error increases due to the introduction of the error from the polar sources. This error is present only in IGRF for this segment, due to the misfit to quiet polar activity. As we further move to segment 1, the rms error in IGRF has increased significantly while the other models show a slight decrease. Finally in segment 6, IGRF increases slightly while the other models increase significantly to the same. This behavior shows that all the new models are better fitted to the quiet polar activity, compared to the IGRF, as they have a much lower rms in segments 1 and 2. At the same time, the error in segment 1 is irrespective of model misfit, as it is for all models and IGRF. This shows that when the model is used during very quiet days in the dayside, it is expected that the rms will increase and that the mean magnitude to have a negative value for orbits higher than the ionosphere.

4.3.3 Orientation

Figure 4.37 shows the mean angle error for dayside.

For segment 1, 2 and 3 the pattern is similar to that in the nightside. As we go from segment 1 to 2 and then to 3, the mean angle error drops and increases again. The main difference here is that the mean angle error in segment 3 is higher than the angle error in

segment 1. This is due to the increase in the rms error of all models in segment 3. The same rms is experienced in segment 2 and a higher rms in segment 1. The magnitude of the geomagnetic field vector is lowest in segment 3 and increases with latitude. This means that in segment 3 the given rms error creates higher deviations in the orientation of the geomagnetic field vector. In segment 2 the effect of the rms error is smaller due to the fact that it is lowest as in segment 3 and the geomagnetic field vector magnitude is higher, so that any model is more immune to these variations. In segment 1 the rms increases significantly and this causes higher orientation errors. As the models in segments 4 and 5 are smoothed versions of those in segments 1, 2 and 3, their mean angle error is lower than that in segment 3.

Examining the threshold value below which the error lies for 95% of the time, we see that the behavior for segments 1, 2 and 3 is the same as for the nightside. Segment 2 has again the lowest value. However the threshold value is higher in segment 1 than in segment 3. This means that although in segment 3 models have a higher mean angle error, most of the errors are close to this mean value. In segment 3 the mean angle error is lower but the errors located at the tail of the distribution are higher. Due to the effect of smoothing the threshold value for models 4 and 5 is close to the value for segment 3 and lower than this of segment 1.

Examining the percentage of error below 0.1^o in Figure 4.39, we see some very interesting facts. In segment 2, the models have the highest value. Segment 1 has a lower value and segment 3 an even lower one. This means that in segment 2 a higher percentage of error is concentrated below 0.1^o, than in segment 1. In segment 3 an even lower percentage is concentrated below this value. Segments 4 and 5 are again smoothed versions of segments 1, 2 and 3. Fusing the information from all the three statistical measures of the orientation error, we make the following conclusions.

- In segment 1 the high geomagnetic field vector makes the models immune to the high rms error. The error is concentrated below 0.1^o but simultaneously we get higher values in the tails of the distribution due to the higher values of disturbance that take place in this segment.

- In segment 2 the rms error is smaller than in segment 1, while the geomagnetic field vector magnitude is still high, providing higher immunity to orientation error. As we move further away from the poles, the values of high errors drop as well and this is why we have a lower threshold value. Finally, a very high percentage of the error is

concentrated below 0.1^o.

- In segment 3 the rms error is identical to that in segment 2 but the geomagnetic field vector magnitude is smaller. This creates higher orientation error which is translated into a higher mean and a lower percentage of error concentrated below 0.1^o compared to segments 1 and 2 . As it is located in equatorial latitudes, however, the high error values are not as high as for segment 1 and this is why the threshold value is lower than segment 1.

These conclusions are also seen in the histograms of Figure 4.40. They are zoomed in the main lobes and the extent of the tail to the right cannot be seen. The maximum error is in Table 4.4. In segment 1 we see a more spread out distribution than segment 1 and segment 2 progressively. Also from the maximum error values in the table we see that the maximum error is in segment 1, then segment 3 and finally segment 2 as expected.

As already noted the performance of models in segments 4 and 5 are the smoothed version of segments 1, 2 and 3. In segment 6 the worst statistics are observed, compared to segments 1, 2, 3, 4 and 5. This is, of course, due to the highest values of disturbance there.

Finally, we see that in terms of maximum orientation error, the worst performance arises in segment 6 and 7 by model 7 and IGRF. The same is also true in the nightside due to the high error in segment 6 (polar areas). Model 6 is adopted to the character of quiet polar activity, unlike model 7, which is modelled from data spanning the entire range of latitude. Consequently it is logical that segment 7 will experience a high maximum error in the polar areas. For the same reason, IGRF has a similar maximum error.

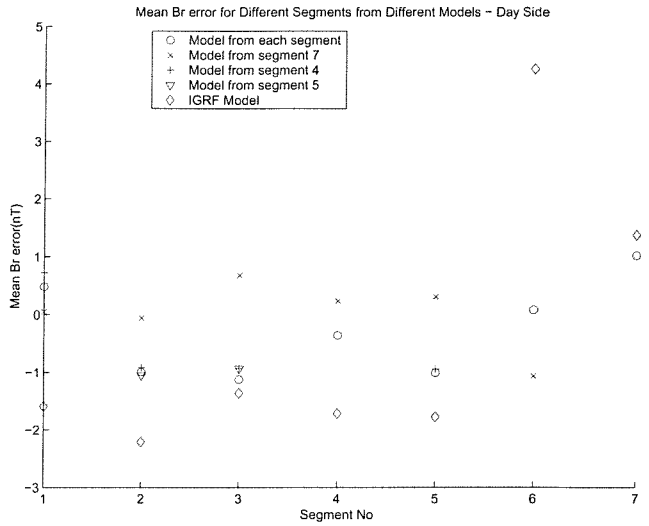

Figure 4.22: Mean B_r error for Different Segments from Different Models - Day Side

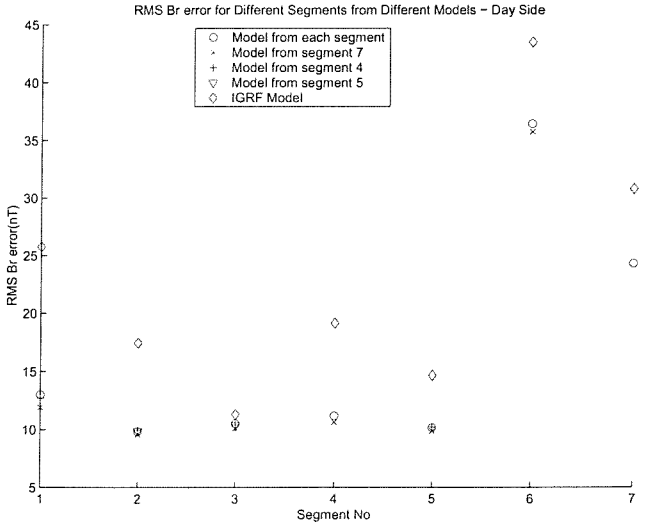

Figure 4.23: rms B_r error for Different Segments from Different Models - Day Side

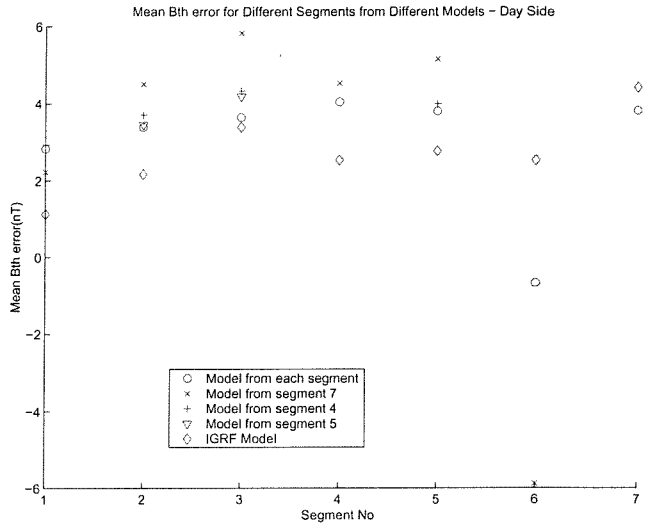

Figure 4.24: Mean B_θ error for Different Segments from Different Models - Day Side

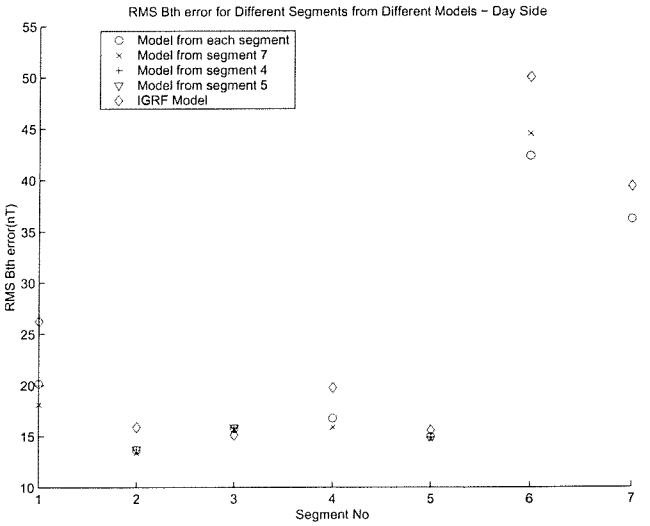

Figure 4.25: rms B_θ error for Different Segments from Different Models - Day Side

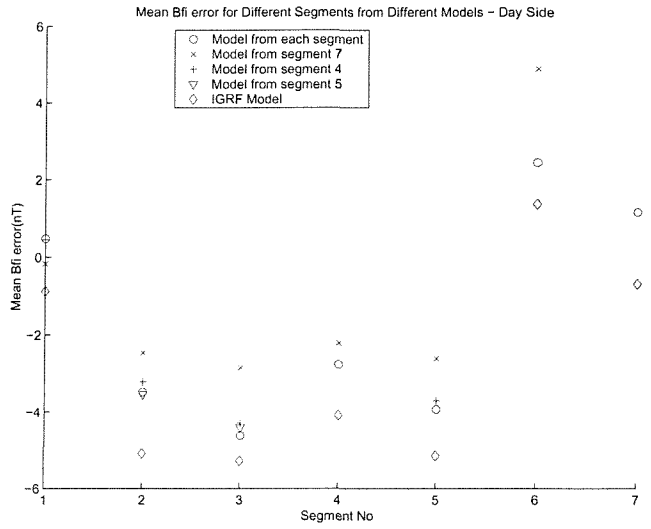

Figure 4.26: Mean B_ϕ error for Different Segments from Different Models - Day Side

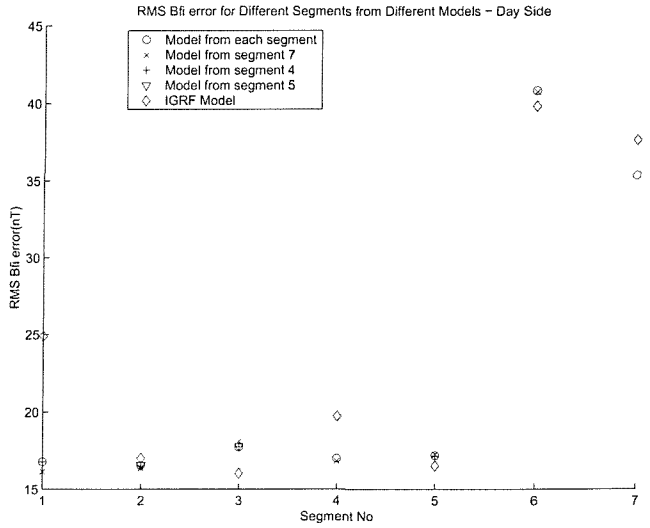

Figure 4.27: rms B_ϕ error for Different Segments from Different Models - Day Side

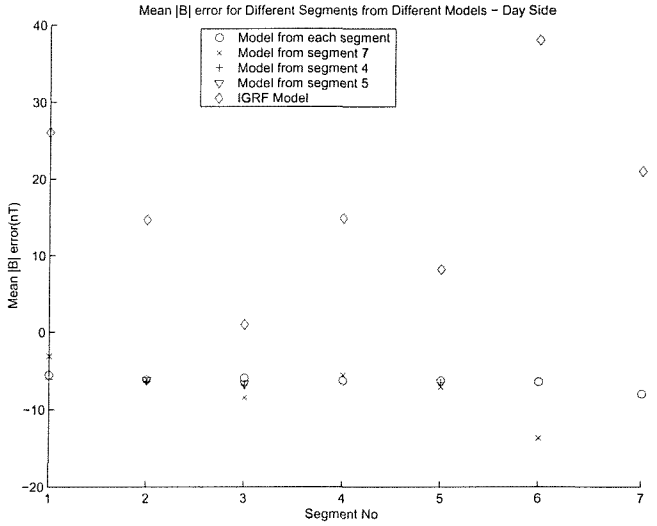

Figure 4.28: Mean $|B|$ error for Different Segments from Different Models - Day Side

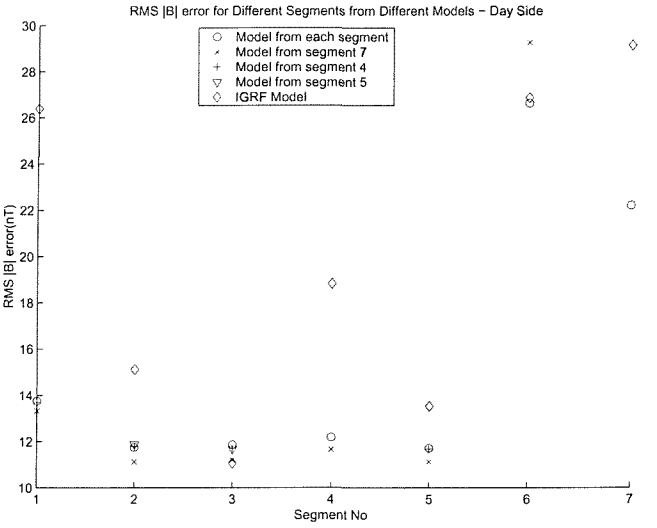

Figure 4.29: rms $|B|$ error for Different Segments from Different Models - Day Side

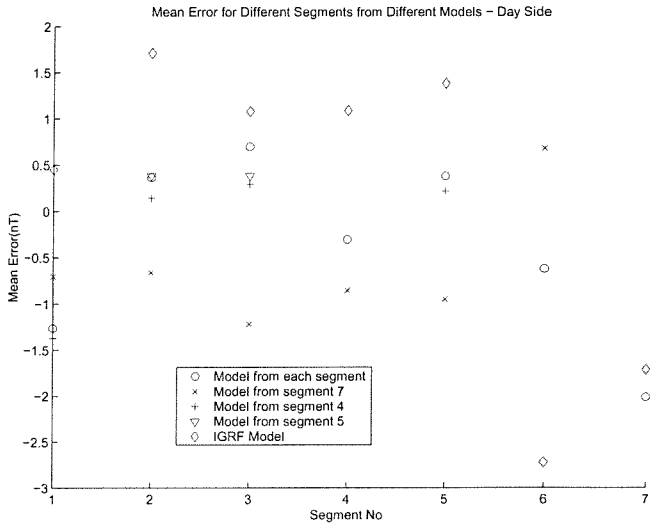

Figure 4.30: Mean error for Different Segments from Different Models - Day Side

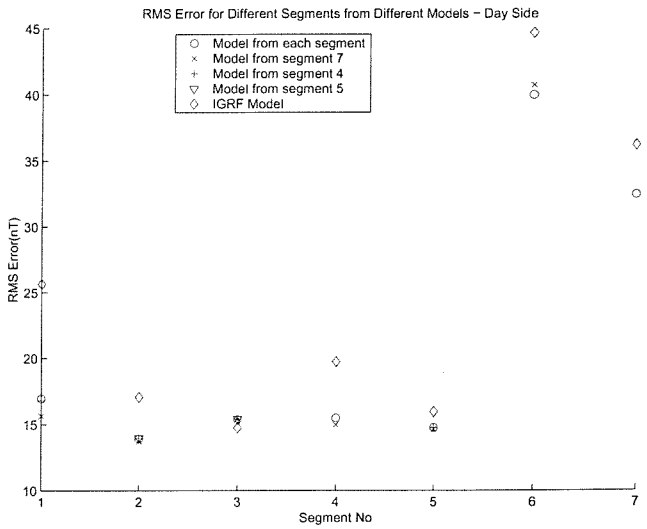

Figure 4.31: rms error for Different Segments from Different Models - Day Side

Segment	Model	B_r Mean	B_θ Mean	B_ϕ Mean	|B| Mean	B_r&B_θ&B_ϕ Mean	B_r rms	B_θ rms	B_ϕ rms	|B| rms	B_r&B_θ&B_ϕ rms
1	1	0.482	2.829	0.477	-5.528	1.263	13.006	20.153	16.785	13.744	16.938
1	IGRF	-1.589	1.122	-0.882	26.058	-0.450	25.766	26.233	24.891	26.377	25.661
1	7	0.053	2.222	-0.168	-3.093	0.702	11.922	18.094	16.141	13.317	15.637
1	4	0.728	2.933	0.451	-6.059	1.371	12.713	20.003	16.763	13.676	16.797
2	2	-0.993	3.385	-3.481	-6.125	-0.363	9.830	13.641	16.550	11.753	13.914
2	IGRF	-2.209	2.161	-5.082	14.679	-1.710	17.448	15.880	17.018	15.121	17.057
2	7	-0.058	4.507	-2.461	-6.097	0.663	9.586	13.359	16.364	11.134	13.701
2	4	-0.921	3.706	-3.215	-6.432	-0.143	9.955	13.664	16.515	11.784	13.945
2	5	-1.054	3.450	-3.541	-6.177	-0.382	9.877	13.740	16.569	11.885	13.976
3	3	-1.124	3.645	-4.616	-5.907	-0.699	10.513	15.751	17.733	11.861	15.356
3	IGRF	-1.360	3.393	-5.276	1.004	-1.081	11.319	15.135	16.035	11.061	14.742
3	7	0.680	5.829	-2.852	-8.434	1.219	10.101	15.683	18.111	11.199	15.428
3	4	-0.928	4.334	-4.283	-6.839	-0.292	10.425	15.849	17.746	11.716	15.411
3	5	-0.936	4.190	-4.401	-6.649	-0.382	10.387	15.865	17.778	11.679	15.416
4	4	-0.360	4.043	-2.767	-6.277	0.305	11.186	16.751	17.002	12.185	15.477
4	IGRF	-1.714	2.531	-4.084	14.872	-1.089	19.150	19.751	19.727	18.821	19.735
4	7	0.239	4.530	-2.204	-5.568	0.855	10.641	15.896	16.837	11.664	14.973
5	5	-1.010	3.804	-3.931	-6.249	-0.379	10.151	14.939	17.190	11.713	14.745
5	IGRF	-1.777	2.768	-5.142	8.189	-1.384	14.659	15.579	16.518	13.532	15.936
5	7	0.306	5.154	-2.607	-7.051	0.951	9.877	14.692	17.256	11.127	14.627
5	4	-0.944	4.001	-3.706	-6.471	-0.217	10.207	14.901	17.148	11.671	14.728
6	6	0.084	-0.671	2.455	-6.404	0.622	36.432	42.366	40.836	26.624	39.976
6	IGRF	4.264	2.524	1.378	38.040	2.722	43.501	50.037	39.843	26.861	44.671
6	7	-1.065	-5.880	4.903	-13.673	-0.681	35.745	44.518	40.752	29.267	40.734
7	7	1.023	3.832	1.173	-7.950	2.009	24.302	36.209	35.370	22.201	32.443
7	IGRF	1.377	4.437	-0.683	21.082	1.711	30.799	39.405	37.662	29.141	36.208

Table 4.3: Mean and rms error statistics for Different Segments and Different Models for Day Side and days included in the modelling

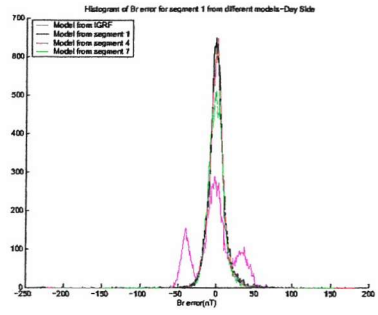

(a) Segment1

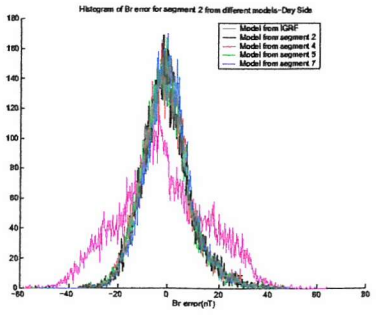

(b) Segment2

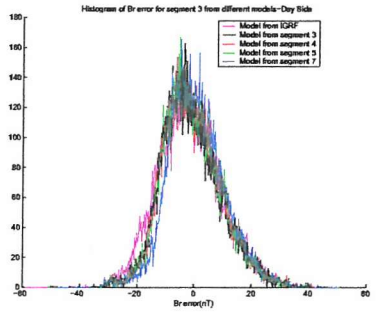

(c) Segment3

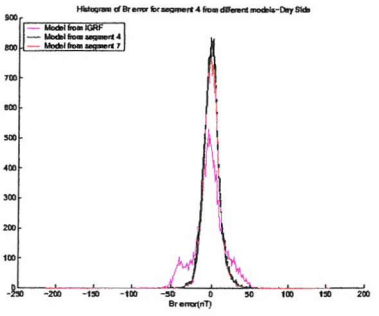

(d) Segment4

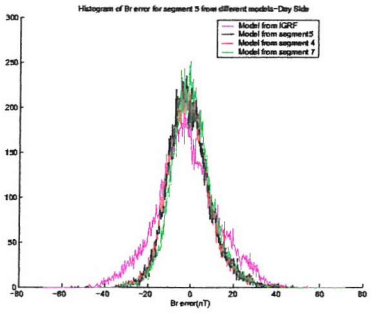

(e) Segment5

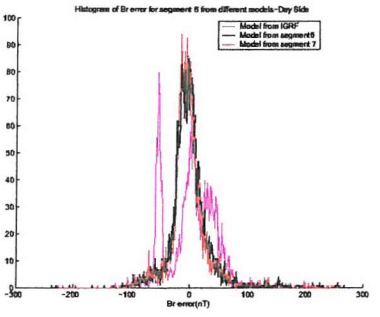

(f) Segment6

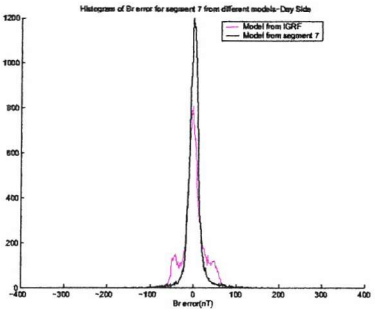

(g) Segment7

Figure 4.32: Histogram of B_r error for (a)segment 1 (b)segment 2 (c)segment 3 (c)segment 4 (d)segment 5 (e)segment 6 (f)segment 7 from different models-Day Side

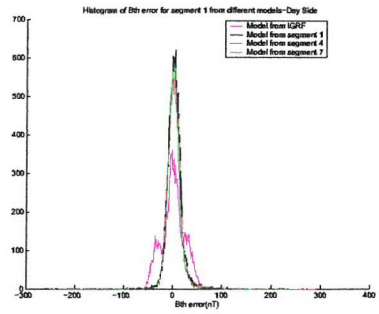

(a) Segment1

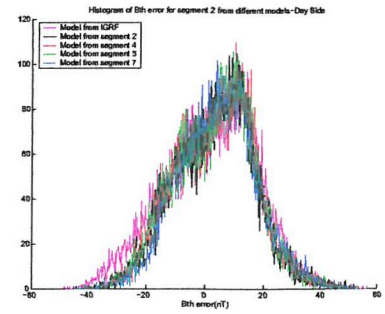

(b) Segment2

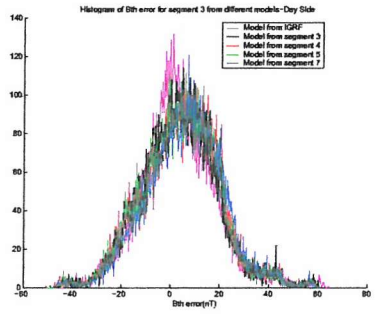

(c) Segment3

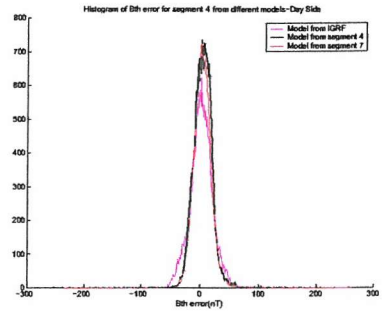

(d) Segment4

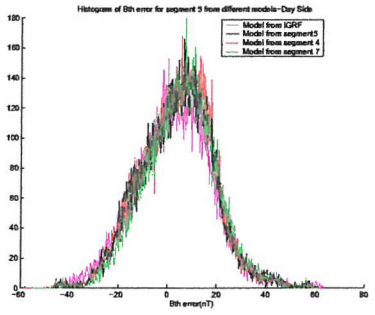

(e) Segment5

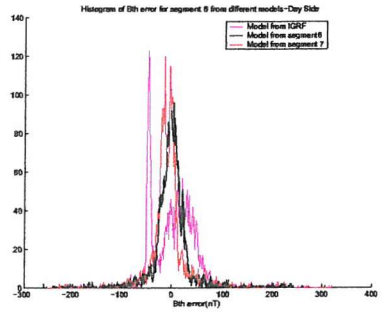

(f) Segment6

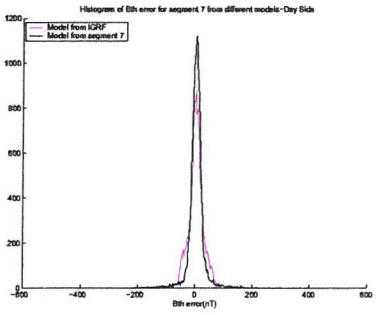

(g) Segment7

Figure 4.33: Histogram of B_ϕ error for (a)segment 1 (b)segment 2 (c)segment 3 (c)segment 4 (d)segment 5 (e)segment 6 (f)segment 7 from different models-Day Side

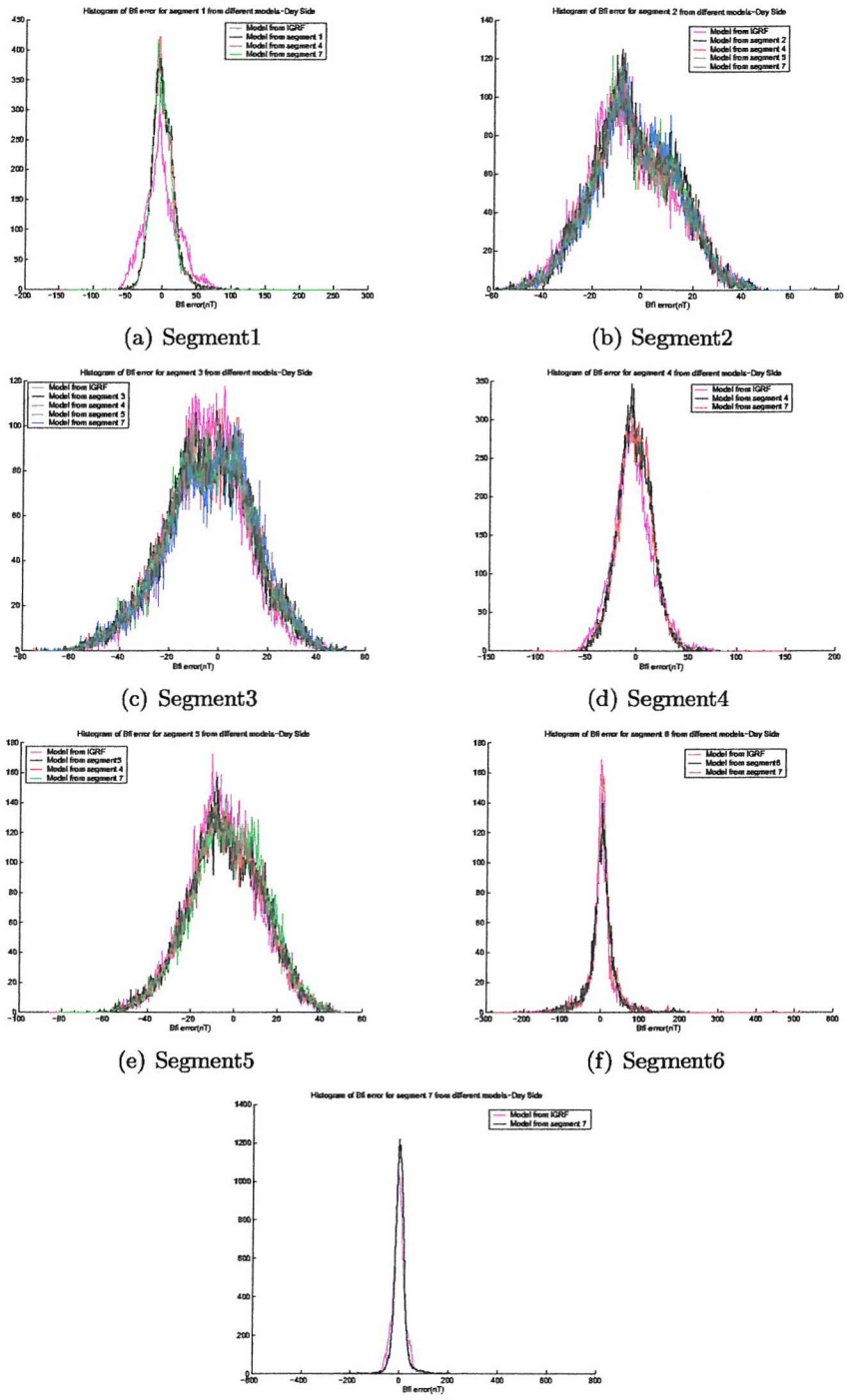

(a) Segment1

(b) Segment2

(c) Segment3

(d) Segment4

(e) Segment5

(f) Segment6

(g) Segment7

Figure 4.34: Histogram of B_θ error for (a)segment 1 (b)segment 2 (c)segment 3 (c)segment 4 (d)segment 5 (e)segment 6 (f)segment 7 from different models-Day Side

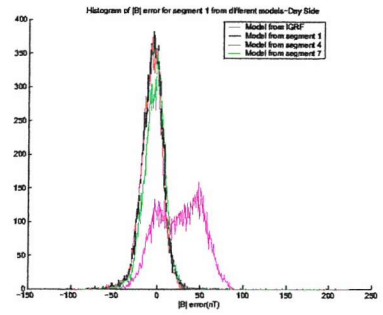

(a) Segment1

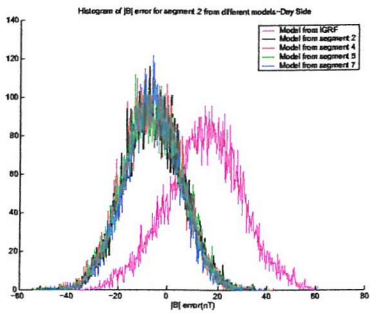

(b) Segment2

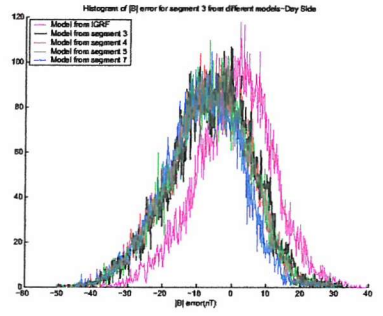

(c) Segment3

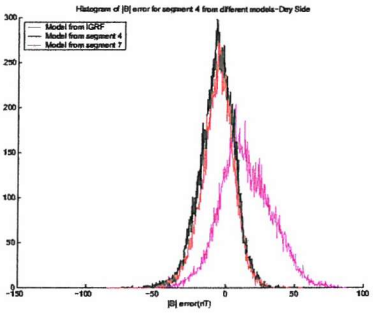

(d) Segment4

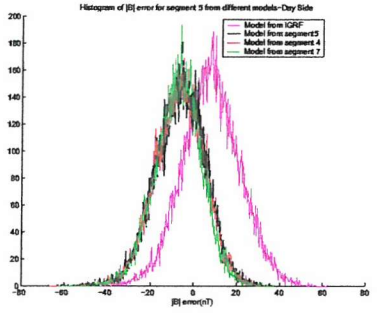

(e) Segment5

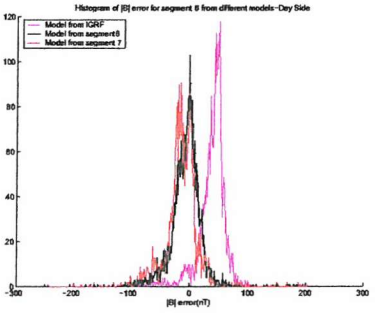

(f) Segment6

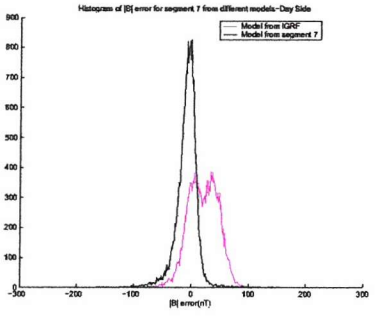

(g) Segment7

Figure 4.35: Histogram of $|B|$ error for (a)segment 1 (b)segment 2 (c)segment 3 (c)segment 4 (d)segment 5 (e)segment 6 (f)segment 7 from different models-Day Side

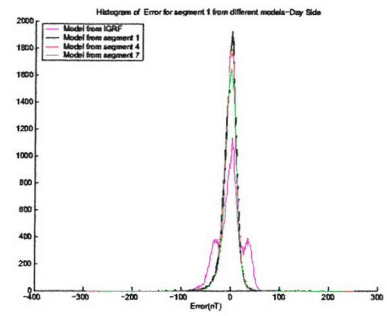

(a) Segment1

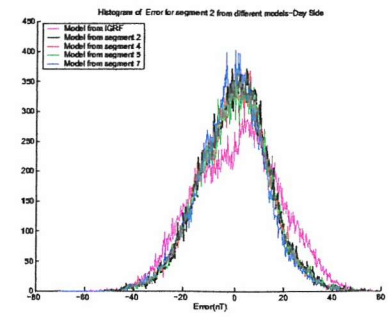

(b) Segment2

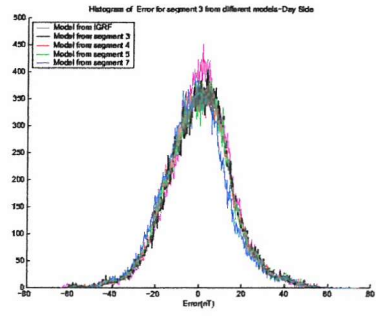

(c) Segment3

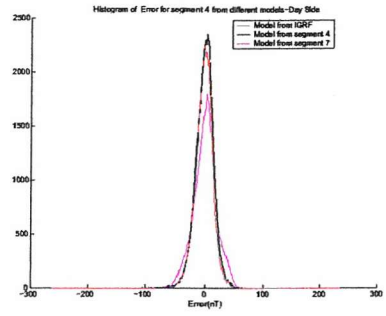

(d) Segment4

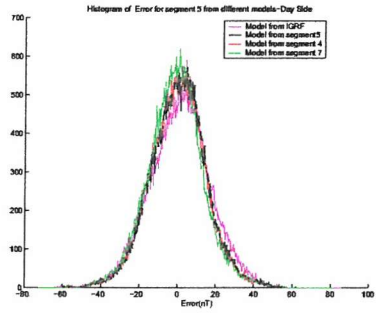

(e) Segment5

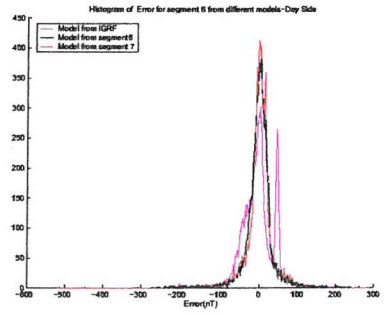

(f) Segment6

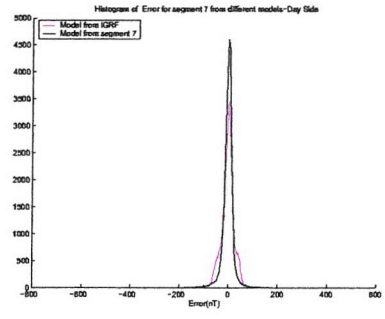

(g) Segment7

Figure 4.36: Histogram of Error for (a)segment 1 (b)segment 2 (c)segment 3 (c)segment 4 (d)segment 5 (e)segment 6 (f)segment 7 from different models-Day Side

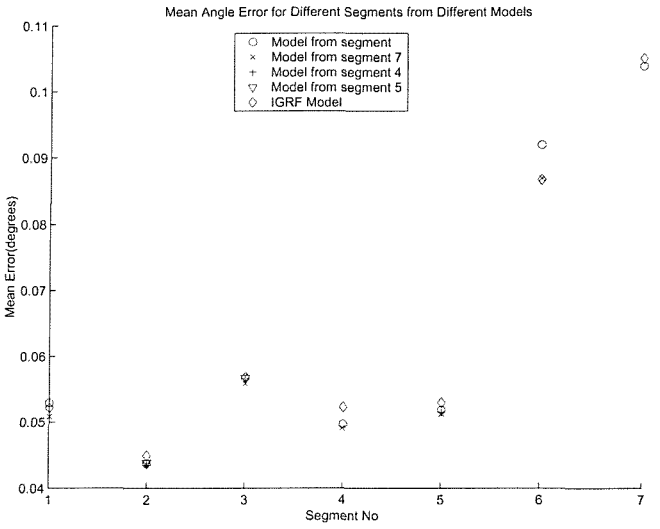

Figure 4.37: Mean Angle Error for Different Segments from Different Models-Day Side

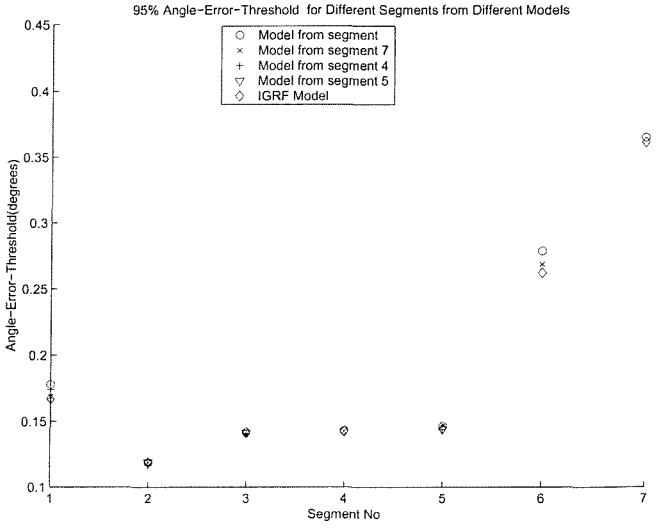

Figure 4.38: '95 % Angle-Error-Threshold for Different Segments from Different Models'

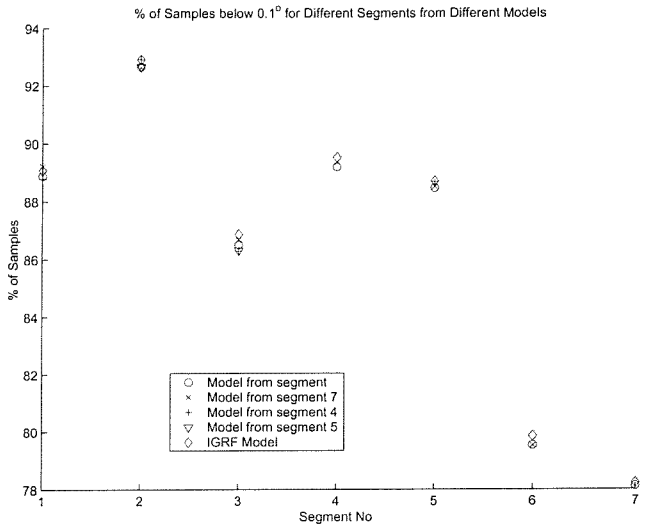

Figure 4.39: % of Samples below 0.1^o for Different Segments from Different Models

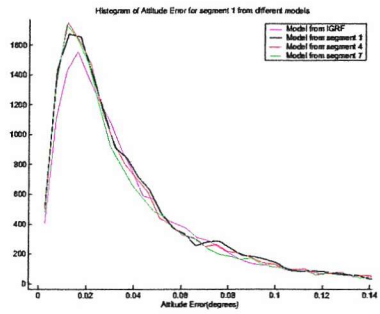

(a) Segment1

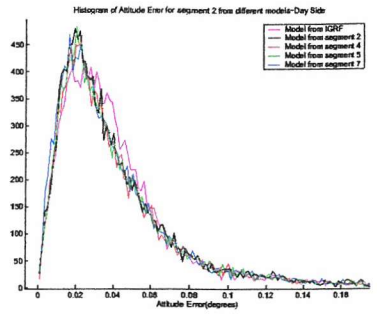

(b) Segment2

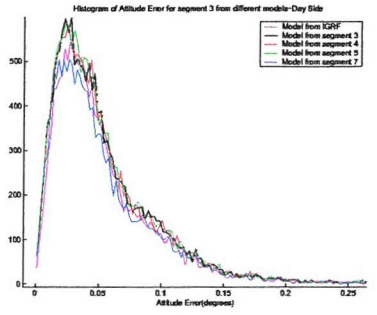

(c) Segment3

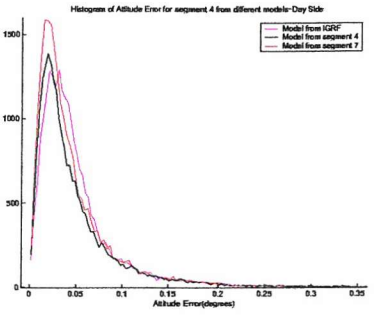

(d) Segment4

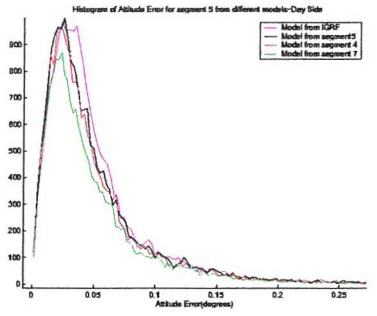

(e) Segment5

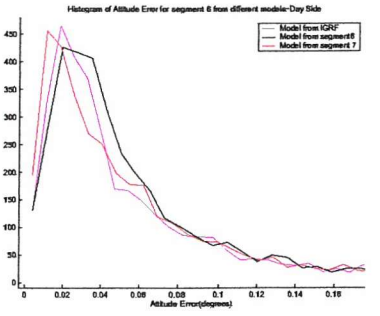

(f) Segment6

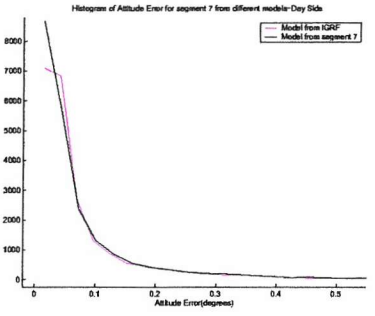

(g) Segment7

Figure 4.40: Histogram of Attitude error for (a)segment 1 (b)segment 2 (c)segment 3 (c)segment 4 (d)segment 5 (e)segment 6 (f)segment 7 from different models-Day Side

Segment	Model	Mean(^{o})	95%Threshold(^{o})	% below 0.1^o	Maximum(^{o})
1	1	0.053	0.178	88.880	2.455
1	IGRF	0.052	0.167	89.070	2.296
1	7	0.051	0.169	89.220	2.305
1	4	0.052	0.174	88.780	2.422
2	2	0.044	0.119	92.650	0.044
2	IGRF	0.045	0.119	92.910	0.713
2	7	0.044	0.120	92.630	0.709
2	4	0.043	0.117	92.910	0.681
2	5	0.044	0.119	92.650	0.686
3	3	0.057	0.142	86.500	1.190
3	IGRF	0.057	0.141	86.860	1.075
3	7	0.056	0.140	86.670	1.046
3	4	0.057	0.141	86.280	1.183
3	5	0.057	0.141	86.300	1.211
4	4	0.050	0.143	89.180	1.471
4	IGRF	0.052	0.142	89.510	1.623
4	7	0.049	0.143	89.350	1.707
5	5	0.052	0.147	88.450	1.326
5	IGRF	0.053	0.144	88.680	1.406
5	7	0.051	0.147	88.500	1.114
5	4	0.051	0.144	88.660	1.271
6	6	0.092	0.279	79.530	3.873
6	IGRF	0.087	0.262	79.850	3.574
6	7	0.087	0.269	79.520	3.661
7	7	0.104	0.365	78.110	14.496
7	IGRF	0.105	0.362	78.220	14.057

Table 4.4: Mean,95%percentile and % below 0.1^o angle error statistics for Different Segments and Different Models for Day Side and days included in the modelling

4.4 Validation of the models in the Day side for days not included in the modelling

This test was performed in order to confirm the performance of the models in the dayside, for days not included in their derivation. The examination of results will be carried out in comparison to the dayside performance for days used in the modelling. The figures and tables referred to in this section are presented in Appendix C.

4.4.1 Components

The mean and rms error values for each of the vector components are given in Figures C.14 to C.19. In terms of the mean error we see that there is a difference for each of the three components, compared to the days used for the modelling.

The mean error of B_r has increased in segments 2 and 3, now in the positive axis. In segment 1 the mean is very similar to the one for the days used in the modelling. The same is true for models in segment 6. The behavior of models 4, 5 and 7 is a smoothed version of the behavior of models in segments 1,2,3 and 6.

The mean error of B_θ in segments 2 and 3 has moved to the negative axis. The mean of the models in segment 1 is very close to the value for the days used in the modelling. The same is true for segment 6.

The mean error of B_ϕ in segments 1, 2, 3 has been shifted, while in segment 6 it remains very close to the value in the case of days used in the modelling. This shift is higher for segments 2 and 3 and smaller for segment 1.

Now examining the mean of the three vector components together in Figure C.22, in the same way they were used for the derivation of the model, we see that there is a very slight decrease in all segments of magnitude approximately $0.5nT$. The variation of mean error, as we move to different segments, is identical to the one for days used in the modelling. Finally for segments 2, 3 and consequently 4 and 5, all models apart from model 7 and IGRF have a mean error within the $-1nT$ to $1nT$ region.

The mean error for each individual component has therefore been altered compared to the days used for the modelling. This reflects the fact that the conditions are different for this set of days. This can be justified by different ionospheric conditions due to the use of a diverse set of days. What is more important for the model evaluation is that the mean error remains within the boundaries of $-1nT$ to $1nT$ and its variation, as we move to different

segments, is identical to that in the case of days used in the modelling process.

The fact that each component shows a different behavior and the overall performance is similar means that the field has been changed around a mean condition and although the morphology of the error is different, its effect creates approximately the same mean error.

Examining the rms errors we see that there is only a very slight increase for B_r and B_ϕ in segments 2 and 3. More importantly the rms errors of B_θ and B_ϕ in segment 1 have been decreased . This is an indication of lower polar activity during these days compared to the days used for the modelling.

The rms error of all the three components, treated together, is shown in Figure C.23. In segments 2 and 3, it is identical to the rms error for the days used for modelling. In segment 1 there is a small decrease in the rms value which confirms the fact that we have an overall lower polar activity. For the most of the models the rms error is identical to the one for the days used in the modelling. Also the pattern of rms error, as we move from segment to segment, stays the same.

This first examination shows that the model performed identically when compared to the days used in the modelling. In terms of mathematical accuracy, the most appropriate measure for the evaluation of the model is the error of the three components treated together, in the same way as they were used in the modelling. In terms of this criterion the model performs identically to the data set used for its derivation. This confirms that the model itself is accurate.

The examination of the individual components reveals that the conditions have changed for these days. For example in segment 1 the mean error values are the same, while in segment 2 and 3 they have changed. This shows that closer to the poles the conditions are similar, but closer to the equator they have changed.

4.4.2 Magnitude

Examination of the magnitude, in Figures C.20 to C.21, confirms the effect of the dayside on the model. The mean magnitude error in all segments and for all models (apart from IGRF) is shifted onto the negative axis in the same way it was shifted in the dayside for the days used in the modelling. The main difference is that the amplitude of the negative shift is slightly higher, a fact that reflects different ionospheric conditions.

The rms magnitude error values are identical to the ones for days used in the modelling, for all segments and models. Hence the negative shift in magnitude is confirmed for use of

the model in the quiet dayside.

4.4.3 Orientation

The three statistical measures for examination of the orientation error are given in Figures C.24 to C.26. Here the mean angle error is increased for segments 2 to 5 with the highest increase observed in segment 2. Conversely the mean angle error in segment 1 has decreased. Still in segment 3 we see higher mean angle error than in segments 2 and 3. This confirms the sensitivity of the equatorial model to disturbances. The decrease in the mean error in segment 1 suggests that the model is very close to the real situation observed in this segment. Conversely in segment 2 and 3 we see that the behavior of the field not as well approximated by the models.

Examining the threshold value under which 95% of the error lies, we see again that in segment 1 it has decreased, while in segments 2 and 3 it has increased. It is still a bit higher than in segment 2 but is lower than in segment 3. The behavior of models in segments 4 and 5 is a smoothed version of those in segments 1, 2 and 3.

Now examining the percentage of error below 0.1^o we see that the pattern is very similar to the days used for the modelling. The main difference is that in segment 1 the percentage has significantly increased. In segment 3 we also see a small increase, while in segment 2 it has slightly decreased. The pattern of behavior is the same, but the differences in segment 1 illustrate how important are the effects of the dayside ionospheric currents on the orientation accuracy even in quiet days.

The most important confirmation from this test was that for quiet conditions in segments 2 and 1 a very high percentage of the error remains below 0.1^o and hence the probability of error higher than this value is small. In segment 3 the percentage is still high but lower than in these two segments. Finally in segment 6 the percentage is lower although it remains higher than 70%.

4.5 Examination of MEME consistency

A large number of data for days was collected from the years, 2000, 2001 and 2002, in order to evaluate the performance of MEME, to derive a model proportional to it and test it for days not included in the modelling.

The first quantity which was evaluated was the degree of agreement between the values of MEME and the values of D_{st} for the same time intervals. In order to perform this evaluation,

the algorithm for the evaluation of MEME was run for each of the days selected, and the two indices were plotted. This gave an initial indication of the level of agreement.

Figures 4.41 and 4.42 show examples of MEME performance against the D_{st}, as published by the Kyoto World Data Center for Geomagnetism, for days during which a magnetic storm took place. Figure 4.43 shows the MEME performance against D_{st} for magnetically quiet days.

As can be seen, in all cases the MEME follows the shape the D_{st} index. The most obvious characteristic of MEME is that it oscillates. The frequency of the oscillation is the time interval between day and night passes over the equator. In order to illustrate this we have plotted in Figures 4.41 to 4.43 an indicator of the location of measurement (day or night). The upper step of the indicator, plotted with the dotted black line, denotes the fact that MEME was measured over the equator in the dayside, while the lower step denotes the fact that the measurement was taken in the nightside.

In all three figures, MEME has a negative maximum for nightside locations compared to the preceding or following dayside measurements. This happens for both the storm and quiet days. Also the peak to peak level of oscillation is increasing as the average disturbance increases. Another important feature is that while in some cases MEME oscillates around the D_{st} value,in other cases it is offset for both the nightside and the dayside measurements.

The reason for the oscillation between nightside and dayside is well explained by the theory of asymmetry of the ring current. At the beginning of the 20^{th} century Chapman [53] observed an azimuthal asymmetry in the low latitude H-component of the geomagnetic field. He mistakenly attributed its sources to ionospheric currents. Kirkpatrick [54] suggested that this asymmetry is caused by an asymmetric equatorial ring current. Later in 1964 Akasofu et al. [55] supported this suggestion. Ijima et al. [10], by using satellite data to map the inner magnetosphere, confined the asymmetry of the ring current, with the peak in the nightside. Other researchers (i.e. Luiet al. [11]) later confirmed experimentally this observation. More recently De Michelis et al. [12] used satellite data to derive a map of the average ring current and they found a strong asymmetric ring current having its peak close to midnight. The same observation was made in the same year by Nakabe et al. [13] while investigating the current structure in the inner magnetosphere. The most recent examination of this asymmetry was carried out by Jorgensen et al. in 1999 [56] who used measurements from the CRES satellite.

This satellite provided a very suitable opportunity for examination of the ring current as its orbit was elliptic with a low inclination giving high coverage of equatorial plane in

various altitudes. In their work they showed that the ring current is indeed asymmetric and they derived a linear expression for the derivation of the peak longitude dependent on the D_{st} index. They found that the peak is located in the nightside between midnight and dusk moving closer to the midnight for higher values of D_{st}. The asymmetry was found to vary between 0.175 and 0.4 for D_{st} values between 0 and -130 while it significantly increased to 0.7 for D_{st} values between -130 and -140. The authors suggested that for very low values of D_{st} the results are inconsistent.

Based on these observations of Jorgensen et al. [56] we decided to investigate the level of asymmetry between nightside and dayside MEME measurements.

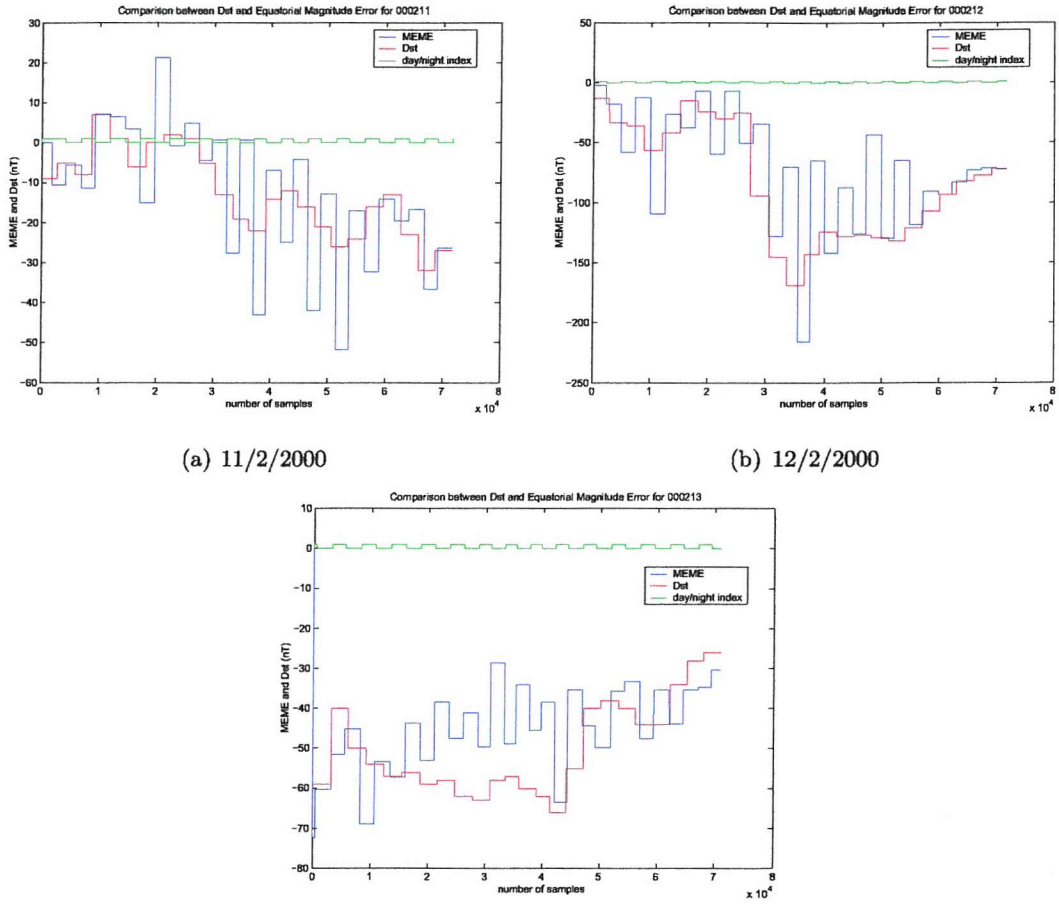

(a) 11/2/2000

(b) 12/2/2000

(c) 13/2/2000

Figure 4.41: $MEME$ vs D_{st} for a magnetic storm -(a) 11/2/2000 (b) 12/2/2000 (c) 13/2/2000

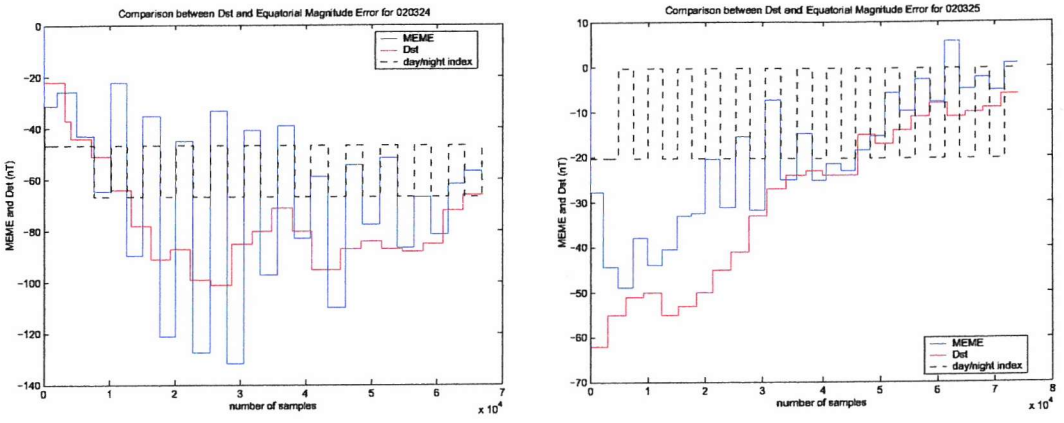

(a) 24/3/2002 (b) 25/3/2002

Figure 4.42: $MEME$ vs D_{st} for a magnetic storm February 2000-(a) 24/3/2000 (b) 25/3/2000

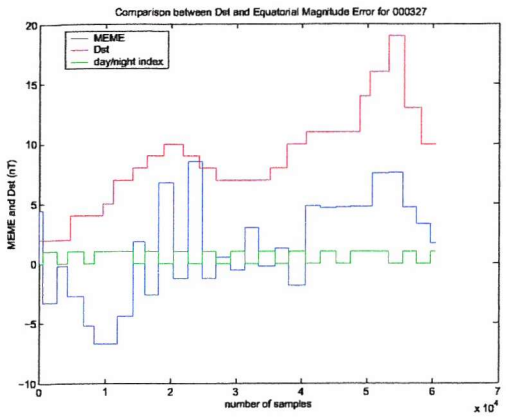

(a) 27/3/2000

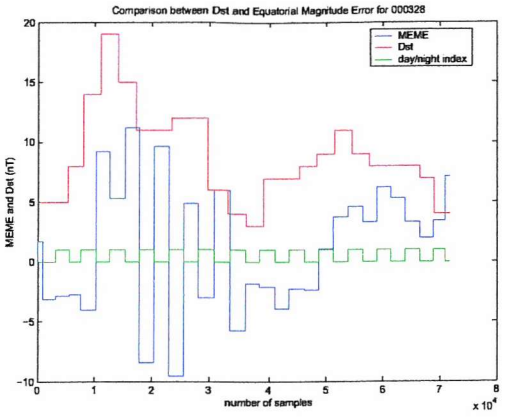

(b) 28/3/2000

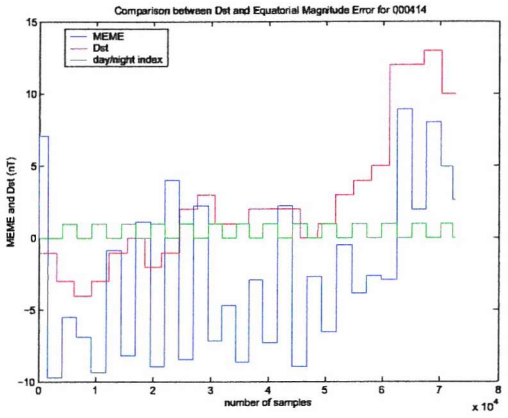

(c) 14/4/2000

Figure 4.43: $MEME$ vs D_{st} for 3 magnetically quiet days- (a) 27/3/2000 (b) 28/3/2000 (c) 14/4/2000

4.5.1 Asymmetry of the Ring Current Observed by MEME

The data from all available days was conditioned as follows:

The first MEME measurement was collected from every equatorial pass together with the corresponding D_{st} index. This data was divided into day and nightside measurements according to the MLT of Oersted satellite at the time of each measurement. Figures 4.44 and 4.45 show the MEME values for day and night side respectively. The corresponding D_{st} values are also plotted for comparison. As can be seen in both cases MEME follows the course of D_{st} index. A closer look reveals that the dayside MEME measurements are in average higher (less negative) than D_{st} while in the nightside the MEME measurements are in average lower (more negative) than D_{st}. In order to show this phenomenon in a clearer way each of the two sets of data (night and day sides) was further divided into 10 groups each corresponding to a different value of D_{st}. The groups with the corresponding D_{st} values and the number of measurements used for each group are shown in Table 4.5. The

Group	D_{st} Level(nT)	No.of Day Measurements	No.of Night Measurements
1	$D_{st} > 0$	98	98
2	$0 > D_{st} > -20$	132	132
3	$-40 > D_{st} > -20$	68	64
4	$-60 > D_{st} > -40$	47	44
5	$-80 > D_{st} > -60$	29	31
6	$-100 > D_{st} > -80$	27	25
7	$-120 > D_{st} > -100$	11	8
8	$-140 > D_{st} > -120$	12	10
9	$-160 > D_{st} > -140$	13	16
10	$-180 > D_{st} > -160$	5	4

Table 4.5: Groups of different D_{st} values with the corresponding number of equatorial passes giving measurements in each group - For day and night sides

MEME values were averaged for each group as were the D_{st} values corresponding to each measurement. The mean value of each group for day and night side was plotted on the same graph together with the corresponding mean D_{st} values. This graph is shown in Figure 4.46. Clearly the nightside average MEME is stronger for all levels of D_{st}. The dayside averaged MEME is weaker for all levels of D_{st}. The averaged D_{st} is located in between day and night

side MEME values for all groups. The difference between the different side MEME values also increases with the level of D_{st} which illustrates the activity of the ring current. This figure verifies the existence of asymmetry of the ring current, and establishes the validity of MEME index as a consistent measure of the ring current activity. In order to be able to compare our results with the observations of Jorgensen et al. [56] the level of asymmetry was evaluated as:

$$Asym = \frac{MEME_{night} - MEME_{day}}{MEME_{night} + MEME_{day}} \tag{4.3}$$

This is a similar formula to that used by Jorgensen [56] with the main difference being that Jorgensen et al. used current values instead of magnetic field values. As $MEME_{night}$ is in all cases lower (more negative) than $MEME_{day}$ the numerator difference will be negative. In all the examined groups $MEME_{night}$ was found to be negative. Hence in all cases the asymmetry is a positive number. The only case when this formula was not applied was in the case of group 1, representing positive D_{st}. There the value of average $MEME_{day}$ was found to be positive namely $5.7nT$, while $MEME_{night}$ was still negative namely $-3.1nT$. These values cause a negative asymmetry index. Noting that this level of disturbance, measured by MEME, is not consistent as is within the boundaries of the model error, we decided to discard this group from the evaluation of asymmetry. For the rest of the groups the asymmetry was plotted versus the mean D_{st} for each group. See Figure 4.47.

To discuss these results, first note that for group 2 ($0nT > D_{st} > -20nT$) the asymmetry appears high around 58% while Jorgensen et al. [56] observed a lower asymmetry of 37%. This difference is possibly due to the model error which is comparable with the field created by the ring current for this case. As we move to group 3 ($-20nT > D_{st} > -40nT$) the asymmetry falls to 22% and remains around this value up to group 7 ($-100nT > D_{st} > -120nT$). After this point the asymmetry increases up to the value 36% for group 10. Jorgensen et al. [56] found that up to group 2 values the asymmetry was about 30%. Then from group 3 to group 7 values the asymmetry dropped to roughly 20%. For group 8 it jumped up to 30% and there was a further increase for group 9 values up to 37%. Finally for group 10 the asymmetry was significantly increased to 80%.

We see that in the case of MEME measurements the asymmetry is following a similar course to that found by Jorgensen et al. [56]. The main differences are that the group 2 value is very high, but this was expected due to the error introduced by the model. From group 2 to group 8 the behavior is the same. It is notable that Jorgensen et al. [56] observed a sharp increase only for group 7 values which is also observed in our results. Finally the

value for group 9 is about 5% lower and for group 10 is significantly lower(37%) compared to that found by Jorgensen(71%).

This latter difference is probably due to the lack of adequate information for modelling such high disturbance intervals. This is due to the fact that Oersted satellite was in a polar orbit giving 2 passes over equatorial latitudes for each orbit. Noting that these values last for only the initial phases of a storm, it is normal that only a small number of measurements could be collected. This pool of data cannot adequately represent the asymmetry as the values do not correspond to the point of maximum deviation between peak and off-peak currents. Apart from this difference, the values of group 3 to group 9 are very consistent. This is an indication that MEME identifies this asymmetry, something that cannot be done by the D_{st} index. Consequently MEME can be consistently used in a model, in a way similar to the D_{st} dependent model developed by Olsen [1] in the context of the latest version of IGRF2000.

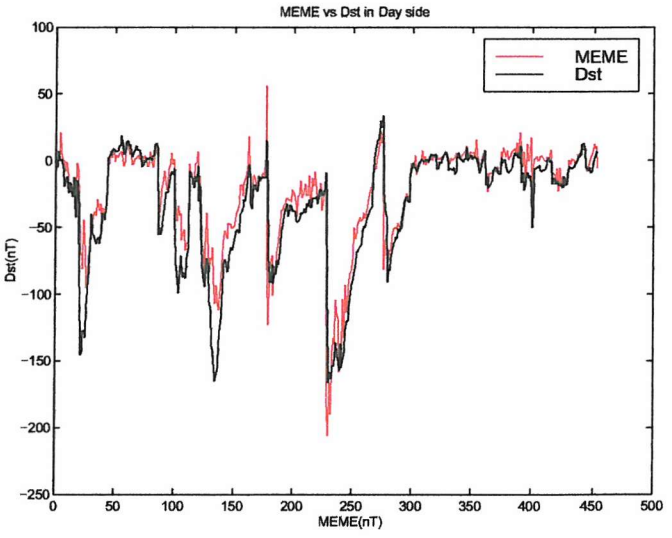

Figure 4.44: MEME vs Dst for dayside

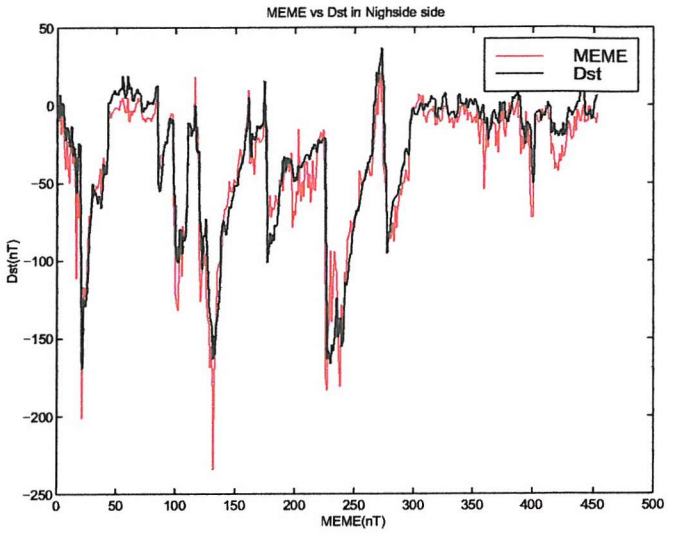

Figure 4.45: MEME vs Dst for nightside

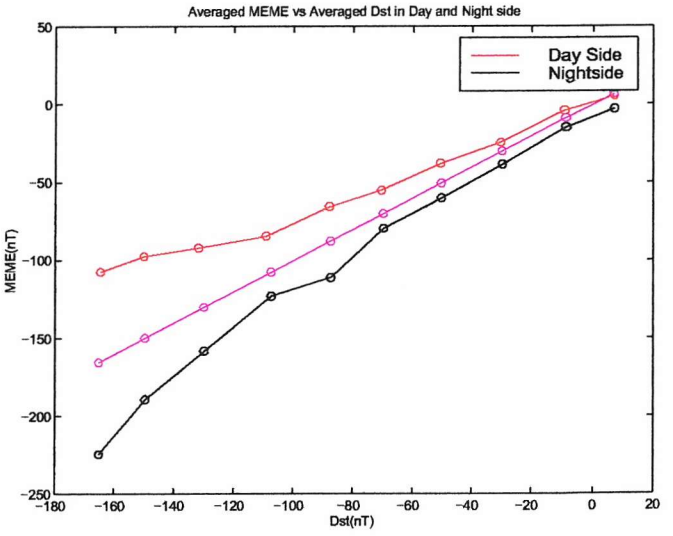

Figure 4.46: Averaged MEME vs Averaged Dst for day- and nightside

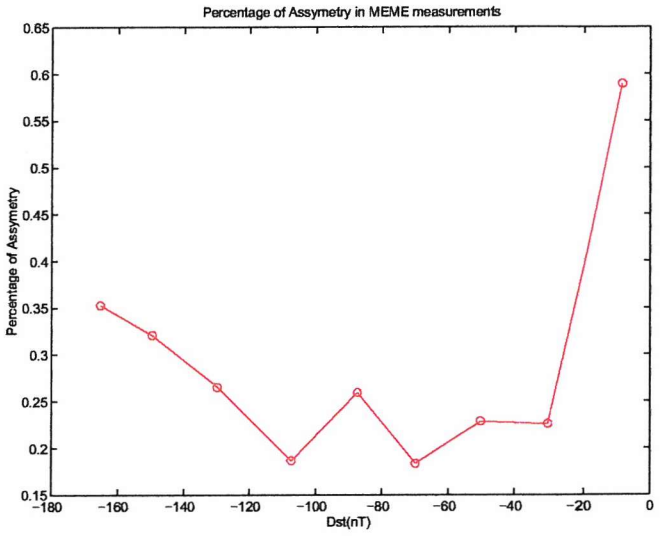

Figure 4.47: Percentage of asymmetry between night- and dayside MEME measurements

4.6 Derivation of the MEME dependent Models

The asymmetry of the ring current suggested that a single model dependent on MEME would not describe the effect of the ring current adequately. When MEME is measured in the nightside and used in the dayside it is expected to create high errors due to the asymmetry. The same is expected for the opposite case when MEME is derived in dayside and used in the nightside. Additionally as the ring current activity increases, the night and dayside error increases with a different rate and this is revealed by the variation of the asymmetry. Thus even a single model would not be adequate to represent the ring current effect in the day and nightside only.

This last fact led to the decision to develop a different model for each case. Additionally in order to provide a better fit for specific ranges of ring current activity, each case (Night-Night, Day-Day, Night-Day, Day-Night) was subdivided into 4 Categories A, B, C and D according to the level of measured MEME. This division was detailed earlier in Chapter 3. For each case and each category a different model was developed. The resulting models were then subtracted from the measurements in order to identify their error. This investigation was performed for each of the 7 segments of the division of the main field.

In each of segments 1, 2, 3 and 6, the model that was used for the main field was the one developed only from measurements confined within this segment. The resulting pool of residuals was then divided in the 16 subgroups according to case and category. From each of these, a different model emerged. In the model error evaluation phase, except from segments 1, 2, 3 and 6 where the error statistics were evaluated directly from the MEME dependent models and the residuals used for modelling, the error for segments 4, 5 and 7 was also evaluated. This was done by using models 4, 5 and 7 for the main field and adding the MEME dependent part according to the corresponding subgroup case. Finally the error statistics were developed for each subgroup and each segment for the case when the MEME dependent part is not used. This is the error that would be encountered if models 1, 2, 3, 4, 5, 6 and 7 were used on board a satellite without any correction for the activity of the ring current.

The following error statistics were evaluated:

- The mean and rms error for each of the vector components.
- The mean and rms error for the magnitude of the field vector.
- The orientation error statistics as computed in the modelling of the main field.

In this section we give the figures and tables of the magnitude and orientation error statistics as they are more important for evaluation of the performance of different models.

For brevity, each graph corresponds to a case (Night-Night, Night-Day, Day-Day, Day-Night) and the corresponding statistics are presented for all segments and for all categories of MEME level. Additionally on the same graph are shown the same statistics for the case when a model was used without the MEME dependent part in order to get an indication of the gained improvement. Figures 4.48 to 4.51 show the mean magnitude error. Figures 4.52 to 4.55 show the rms magnitude error. Figures 4.56 to 4.59 show the mean angle error and Figures 4.60 to 4.63 show the threshold value below which lies 95% of the error values. Figures 4.64 to 4.67 show the percentage of error which lie below 0.1^o. The same statistics are given in detail in Tables 4.6 to 4.10.

4.6.1 Mean Magnitude Error

4.6.1.1 Night - Night

Figure 4.48

Without MEME model in use, the error is higher for categories A, B, C and D progressively. The error is smaller in segment 1 were the effect of the ring current is lower than in segments 2 and 3. The error is highest for segment 3 as it is the narrowest segment around the equator. After the use of MEME we see a very significant improvement especially for categories B, C and D. Segment 6 has a positive error and this shows that this segment is least effected by the ring current and the error is dominated by polar currents. The error reduction in this segment is smaller. Segment 4 and 5 are smoothed versions of segments 1, 2 and 3. Segment 7 is contaminated by segment 6 and performance is worse than in segments 1, 2, 3 and 5.

4.6.1.2 Night - Day

Figure 4.49

The error increases again with category, when the MEME dependent model is not used. This is true for segments 2, 3 and 5. Segment 1 is less effected. For category D in segment 1 the mean error has a positive value, as in segment 6. This shows that polar phenomena during such high magnetic activity are intensified and contaminate lower latitudes. After the use of MEME the improvement gained is high in segments 2, 3, 4 and 5 for categories A, B and C. Segment 6 again shows a positive error due to polar currents. As the activity of

the currents depends on the magnetospheric activity some reduction is achieved by the use of the MEME dependent model.

4.6.1.3 Day - Day

Figure 4.50

When MEME dependent model is not used, the error is higher for categories A, B, C and D progressively. This is true again for segments 2, 3, 4 and 5. Segment 1 is least effected by the ring current effect. Segment 6 again shows different behavior to the other segments due to the effect of the polar currents. After the use of the MEME dependent model there is a high reduction of the error in segments 2, 3, 4 and 5, especially for categories B, C and D. The different character of disturbance in segment 6 can be seen by the fact that when MEME is used in segment 6 it creates additional error.

4.6.1.4 Day - Night

Figure 4.51

Without the MEME model, the error is again increases progressively for categories A, B, C and D in segments 2, 3, 4 and 5. Segment 1 is still least effected by the ring current. This segment preserved its diverse character due to polar activity. After the use of the MEME model, we see again a high reduction of mean magnitude error for segments 1, 2, 3 and 4.

4.6.2 rms Magnitude Error

4.6.2.1 Night-Night

Figure 4.52

When the MEME model is not used the rms magnitude error is lower in segments 2 and 3 than in segment 1 only for category C. For category D it is higher in segments 2 and 3 while for B and D they are similar. Segment 6 has the highest value due to the polar currents. After the use of the MEME model the rms error in segments 2 and 3 is dramatically reduced while the reduction in segment 1 is smaller. This is more obvious for categories B,C and D due to the fact the error due to the ring current is removed by the use of the new model. The remaining high error in segment 1 especially for categories C and D, is due to the high polar magnetic activity. In segments 4 and 5 the performance is smoothed, between that in segments 1, 2 and 3.

4.6.2.2 Night - Day

Figure 4.53

When the MEME model is not used the rms error is lower in segments 2 and 3 than in segment 1, however it is at a similar level. The rms error also increases progressively for categories A, B, C and for all segments. Segment 6 again shows the most diverse behavior. After the use of the MEME model, the magnitude rms error reduces significantly in segments 2 and 3 while there is a much smaller decrease in segment 1. The rms error in segments 2 and 3 is then significantly smaller than in segment 1. The performance in segments 4 and 5 is again a smoothed version of that in segments 1, 2 and 3.

4.6.2.3 Day-Day

Figure 4.54

When MEME models are not used, the rms error increases progressively for categories A, B, C and D. The rms error in segment 3 is higher than in segments 2 and 1. After the use of MEME models, the rms error is reduced significantly for categories B, C and D in segments 2 and 3. In segment 1, the reduction is significant, especially for categories C and D. This is probably due to the fact that the polar currents have the least effect in this case. The resulting rms error in segment 1 is much higher than that in segments 2 and 3. Consequently the rms error in segment 4 is significantly higher than that in segment 5.

4.6.2.4 Day - Night

Figure 4.55

Without the use of the MEME model, the error is progressively higher for categories A, B, C and D. In this case segment 1 has a higher rms error compared to segments 2 and 3. After the use of the MEME model, the reduction is similar in segments 1, 2 and 3. This reduction is high especially for categories B, C and D. The resulting rms error is much lower in segments 2 and 3 than in segment 1 for categories B and D as it was before the use of MEME. For categories C and A the rms error in segment 1 is smaller than in segments 2 and 3 as it was before the use of MEME. This phenomenon arises due to the fact that in the data used the effect of the ring current in the latitudes of segment 1 was dominant over the effect of the polar currents.

4.6.3 Mean Orientation Error

4.6.3.1 Night-Night

Figure 4.56

When no MEME model is used, the mean angle error increases progressively for categories A, B, C and D. The mean error is higher for segment 1 than for segments 2 and 3. For this reason, the error in segment 4 is higher than the error in segment 5. In segment 6, the error is maximum. For this reason, in segment 4 the error is higher than in segments 1, 2, 3, 4 and 5. After the use of the MEME model, there is a significant error reduction in segments 2 and 3 for categories C and D. The reduction is much smaller in segment 1. Segments 2 and 3 then have the lowest mean angle error.

4.6.3.2 Night - Day

Figure 4.57

Without the use of the MEME model, the error progressively increases for categories A, B, C and D. In segment 1 again the mean angle error is higher than in segments 2 and 3. Again segment 6 shows the highest residual. After the use of the MEME model, a significant error reduction occurs in segments 2 and 3. In segment 1 the reduction is again much smaller. Segments 2 and 3 have the smallest mean angle error in all categories.

4.6.3.3 Day-Day

Figure 4.58

The error, without the use of the MEME model, in segments 1, 2, 3, 4 and 5 progressively increases for categories A, B, C and D. In segment 6 the error is smaller for category D than for category C. This ambiguity is a result of the irregular disturbance during high magnetic activity in this segment. After the use of the MEME model, the error reduction is high for segments 2 and 3 while there is a significant reduction also in segment 1. For categories B, C and D the resulting mean angle error is smaller in segments 2 and 3 than in segment 1. For category A the resulting error is smaller in segment 1 than in segment 3 and the lowest error occurs in segment 2.

4.6.3.4 Day - Night

Figure 4.59

With no MEME model involved, the mean angle error increases progressively for categories A,B and C. However for category D the mean angle error in segment 2 is lower then the error in the same segment for category C. In all other segments it increases. The reason for this phenomenon can be explained if we look at the mean error of the vector components for this particular case in segment 2. The most dominant error, when no MEME is used, is in the B_θ component and this is expected due to the nature of the disturbance from the ring current. In segment 2, the mean error of B_θ is higher for category C than for category D while B_r and B_ϕ are lower. This means that the disturbance is more diverted from the horizontal plane and the orientation of the disturbance vector is closer to the orientation of the quiet field vector in segment 2. That is why the mean angle error there is lower than in segments 1 and 3. After the use of the MEME model a significant error reduction is achieved in segments 1, 2 and 3. The resulting error in segment 2 for category D remains lower than this for category C, a fact that reinforces the belief that this situation is caused by the ring current and no other phenomenon. For category D and B segment 2 has the smallest error. For category C, the smallest error is observed in segment 3 and for category A, the quietest conditions, the error is identical for segments 1 and 2.

4.6.4 95% Threshold Error

4.6.4.1 Night-Night

Figure 4.60

When no MEME model is used, the threshold value increases progressively for categories A, B, C and D. Highest error threshold is observed in segment 6 where polar activity has increased according to magnetic activity. The error threshold is lower in segments 2 and 3 than is segment 1. After the use of MEME, there is a significant reduction for segments 2 and 3 while in segment 1 hardly any reduction is observed for categories C and D. For categories A and B the reduction is very small. No reduction is observed in segment 6. After the reduction, segments 2 and 3 have the lowest error threshold for categories C and D.

4.6.4.2 Night - Day

Figure 4.61

Without the MEME model, the error increases progressively for categories A, B, C and D. The lowest error is observed in segments 2 and 3. After the use of MEME the reduction is significant for categories C and D in segments 2 and 3. In segment 1 there is no reduction

and instead a small increase of the error threshold. This shows that the high errors in this segment are not caused by the ring current but by the dominant polar disturbance. This also affects the error threshold in segment 4 where a slight increase is observed. The resulting error threshold is again lower in segments 2 and 3.

4.6.4.3 Day-Day

Figure 4.62

In the case when no MEME model is used, the error threshold progressively increases for categories A, B, C and D. The only exception is in segment 6 where the error is higher for category C than category D. This is due to the high polar disturbance in this segment which makes it the most inconsistent for use by any model. After the use of MEME the reduction is significant for categories C and D and segments 1, 2 and 3. The resulting error is lower in segments 2 and 3 for categories C and D while for categories A and B the error threshold is lower in segment 2 and very similar in segments 1 and 3.

4.6.4.4 Day - Night

Figure 4.63

When no MEME model is used, the error threshold increases progressively for categories A, B, C and D. The only exception is for segment 2 where the error for category C is higher than for category D. This is exactly the same phenomenon observed for these cases in the mean angle error. It is caused by the fact that the disturbance vector is closer to the orientation of the quiet field vector in segment 2 when the category C measurements were taken than when the measurements in category D were taken. The observation of this phenomenon here is confirmation of our suggestion about its cause. After the use of MEME, there is a significant reduction of the error threshold for categories B, C and D in segments 1, 2 and 3, but still no improvement is segment 6. The resulting lowest error threshold is in segments 2 and 3 for categories B,C and D and in segments 1 and 2 for category A.

4.6.5 Percentage of Orientation Error below 0.1^o

4.6.5.1 Night-Night

Figure 4.64

Without the use of MEME, the percentage of error below 0.1^o decreases for categories A, B, C and D. The only diverse behavior is observed in segment 2 where the percentage for

category B is higher than that for category A. This also causes the percentage in segment 5 to follow the same behavior. Using Table D.4, we see that for this case the threshold value is lower for category B than A in segment 2 while for all other segments this relationship is reversed. This shows that the error caused by the disturbance in this category is closer to the mean angle error than in category A. This is explained if during the time that the measurements in category C where taken, the disturbance in segment 2 remained consistently around a certain level that created less than 0.1^o deviation for most of the time. For other categories A, B and C the disturbance in segment 2 varies more creating a higher percentage of error to exceed 0.1^o. After the use of MEME, there is a significant increase of the percentage especially for categories B, C and D. The resulting percentage is higher in segments 2 and 3 for categories C and D. For categories A and B the highest percentage is in segment 2 and it is similar in segments 1 and 3. The increase is smaller in segment 1 and for segment 6 no significant increase is observed.

4.6.5.2 Night - Day

Figure 4.65

When MEME models are not used the percentage decreases progressively for categories A, B, C and D. The percentage is higher for segments 2 and 3 than segment 1. After the use of MEME, there is a significant increase in segments 2 and 3 for categories B, C and D. In segment 1 the increase is much smaller. For categories B, C and D the highest percentage is in segment 3 while for category A it is in segment 2.

4.6.5.3 Day-Day

Figure 4.66

Again when no MEME models are used, the percentage decreases progressively for categories A, B, C and D. After the use of MEME the increase is high for segments 1, 2 and 3. Segment 6 experiences little improvement from the use of the MEME models. The resulting percentage is higher in segment 3 for categories C and D. For categories A and B the percentage is higher in segment 2.

4.6.5.4 Day - Night

Figure 4.67

Without the use of MEME models, the percentage progressively decreases for categories

A, B, C and D. After the use of MEME, the increase is higher in segments 2 and 3. In segment 1 it is smaller. The resulting percentage is higher in segment 3 for categories C and D. For categories A and B the percentage is higher in segment 2.

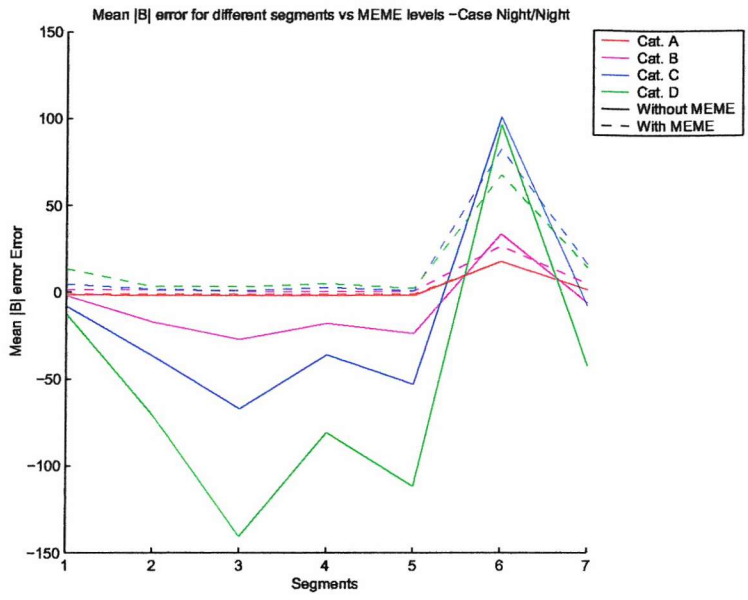

Figure 4.48: Mean $|B|$ error for Different Segments and Categories - NN

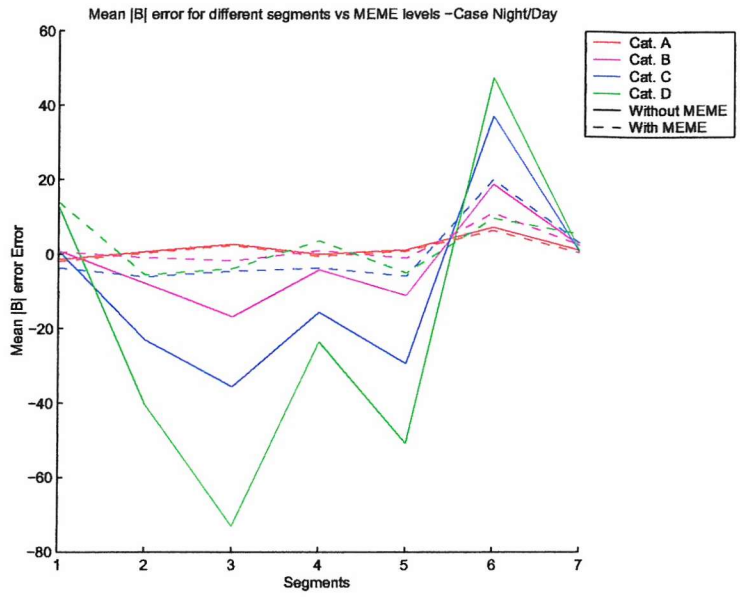

Figure 4.49: Mean $|B|$ error for Different Segments and Categories - ND

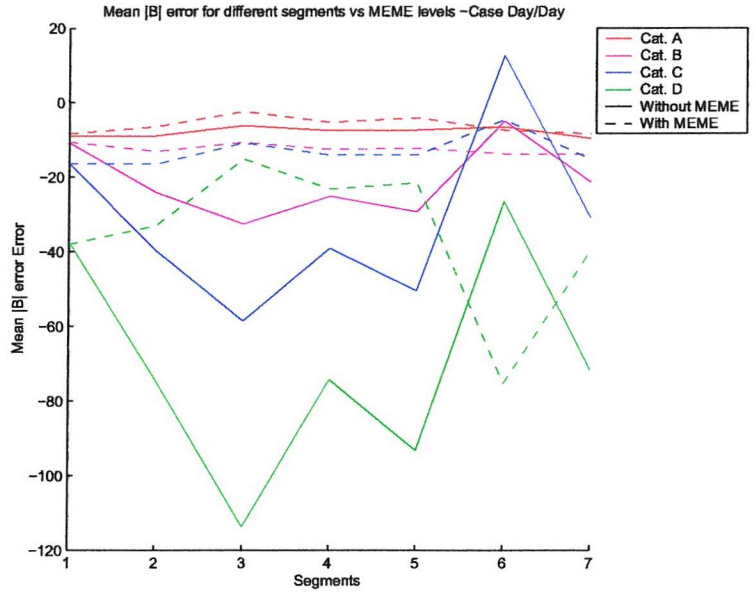

Figure 4.50: Mean $|B|$ error for Different Segments and Categories - DD

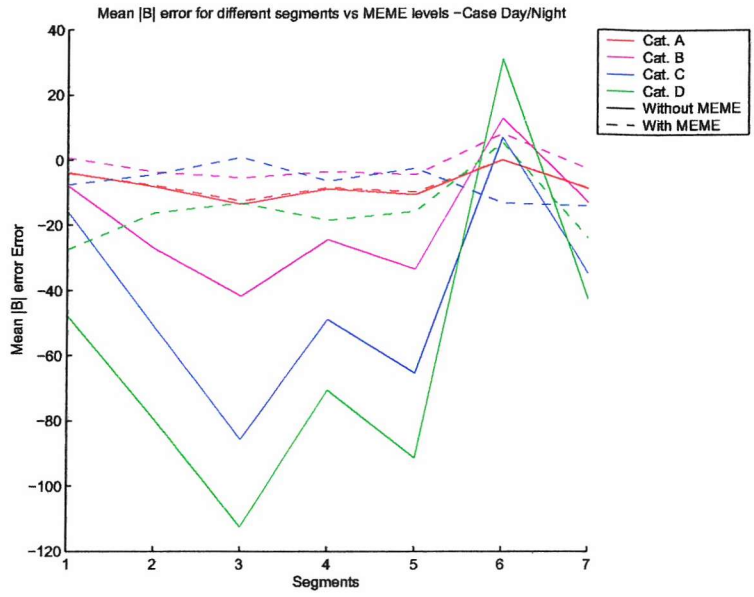

Figure 4.51: Mean $|B|$ error for Different Segments and Categories - DN

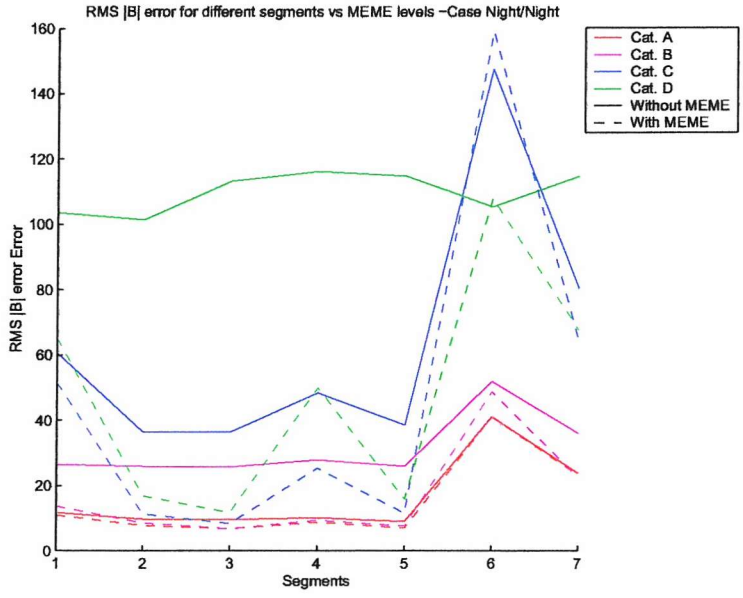

Figure 4.52: rms $|B|$ error for Different Segments and Categories - NN

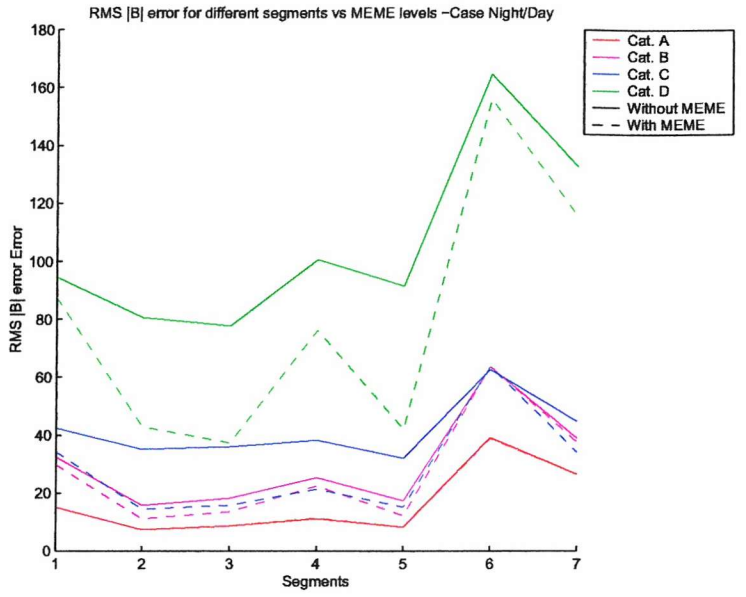

Figure 4.53: rms $|B|$ error for Different Segments and Categories - ND

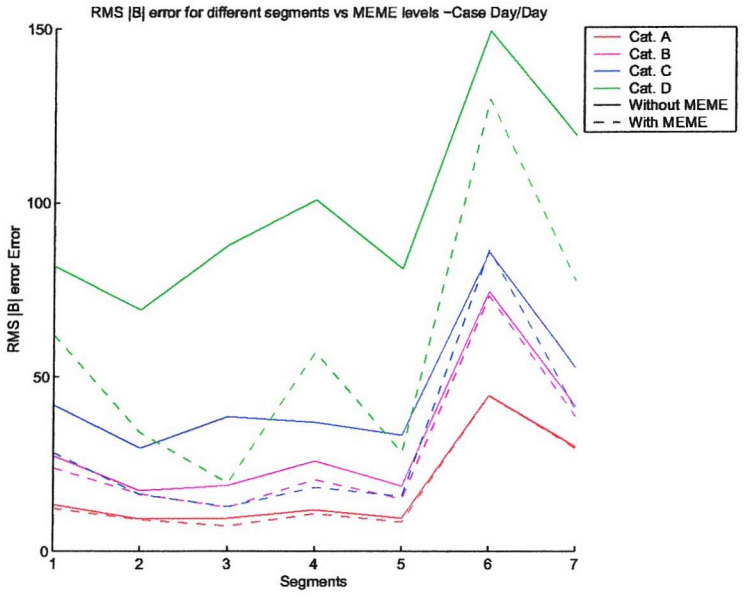

Figure 4.54: rms $|B|$ error for Different Segments and Categories - DD

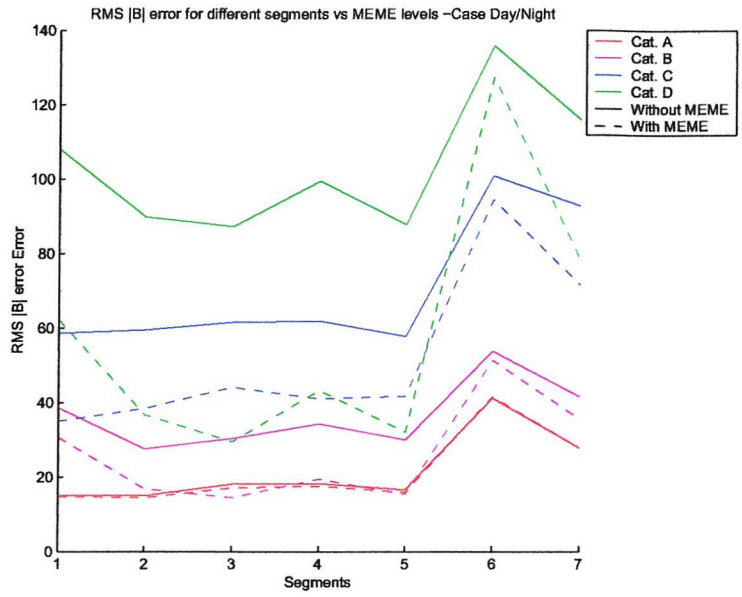

Figure 4.55: rms $|B|$ error for Different Segments and Categories - DN

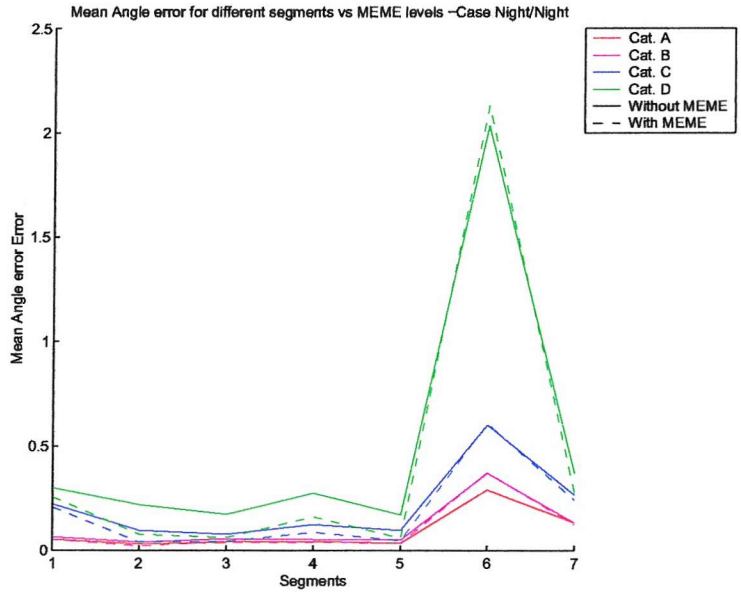

Figure 4.56: Mean Angle Error for Different Segments and Categories - NN

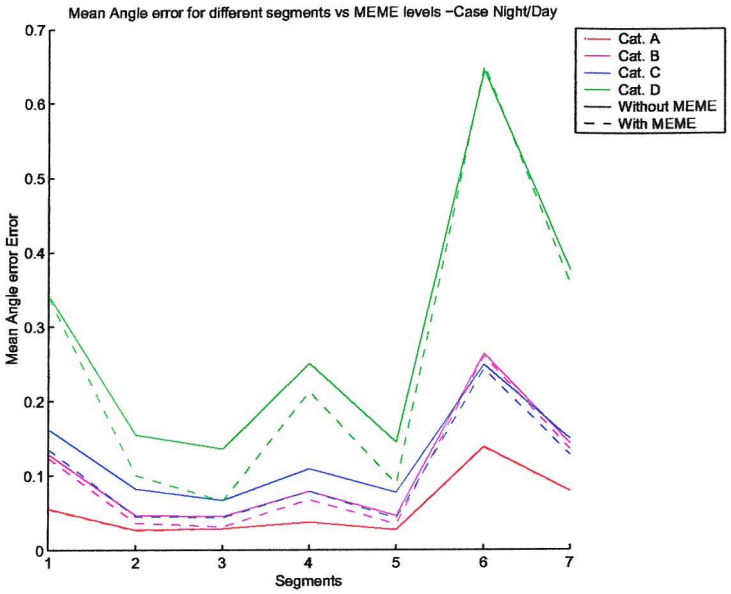

Figure 4.57: Mean Angle Error for Different Segments and Categories - ND

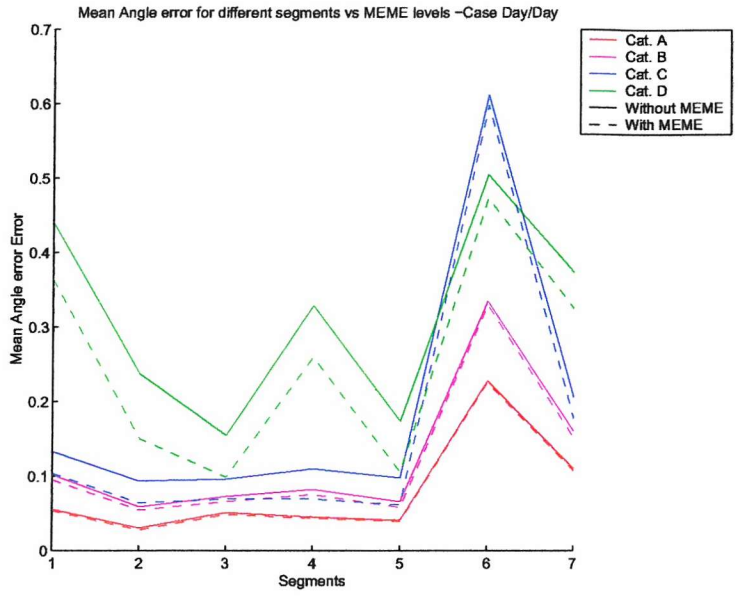

Figure 4.58: Mean Angle Error for Different Segments and Categories - DD

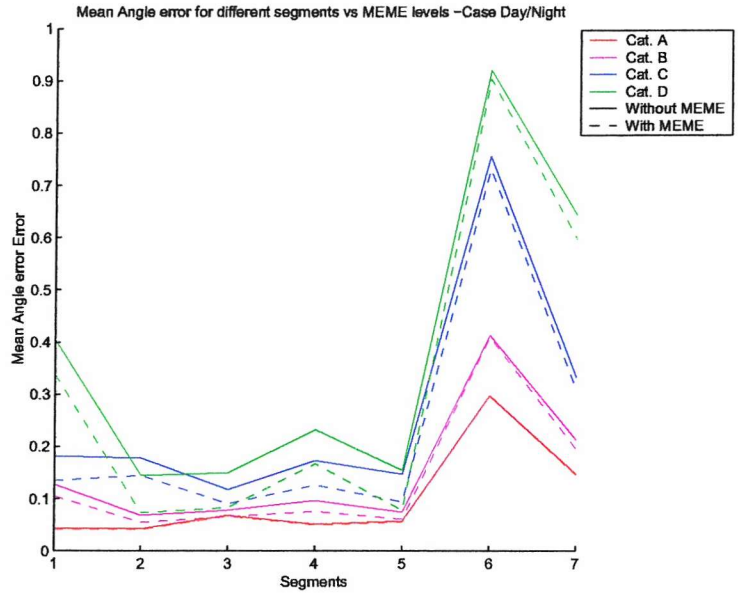

Figure 4.59: Mean Angle Error for Different Segments and Categories - DN

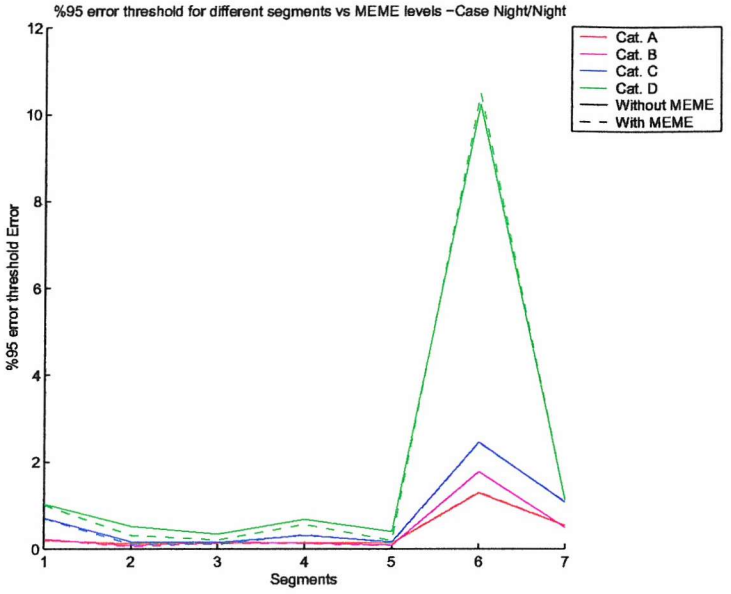

Figure 4.60: 95 % Angle-Error-Threshold for Different Segments and Categories - NN

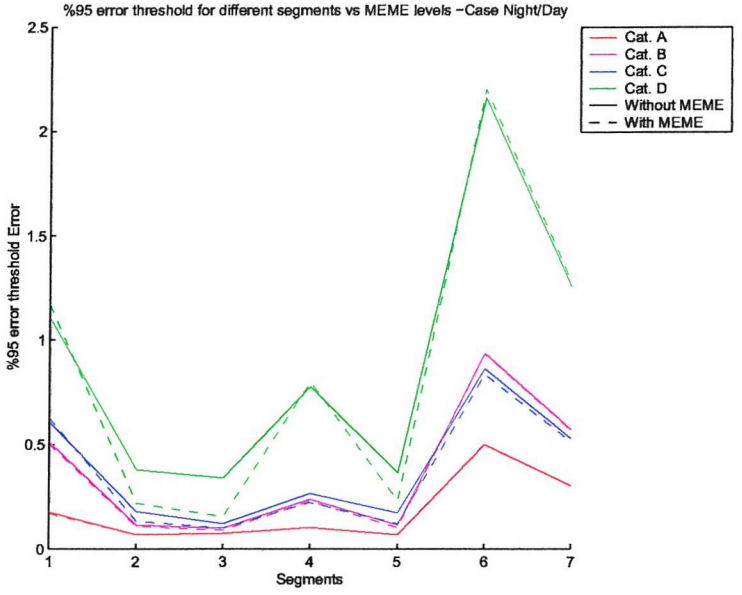

Figure 4.61: 95 % Angle-Error-Threshold for Different Segments and Categories - ND

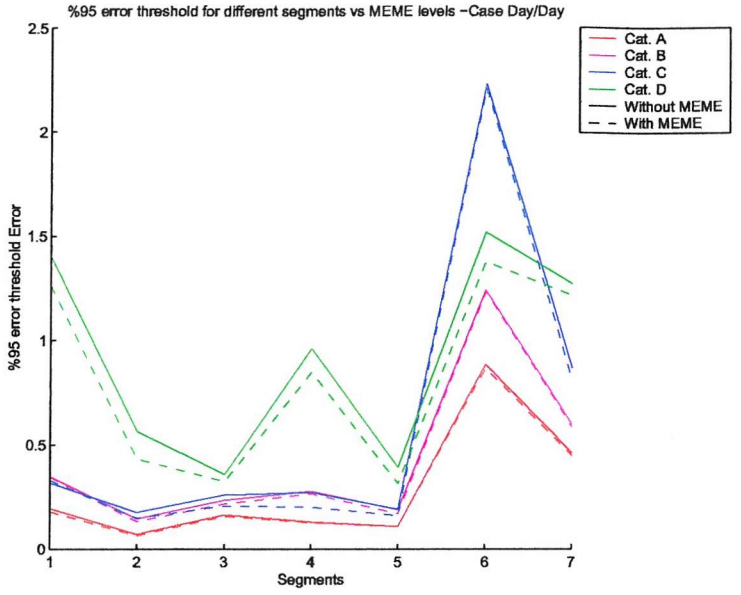

Figure 4.62: 95 % Angle-Error-Threshold for Different Segments and Categories - DD

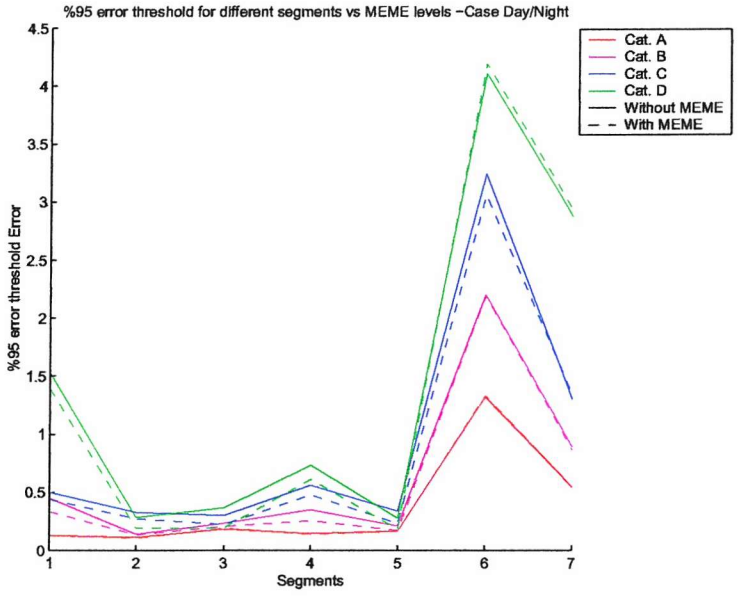

Figure 4.63: 95 % Angle-Error-Threshold for Different Segments and Categories - DN

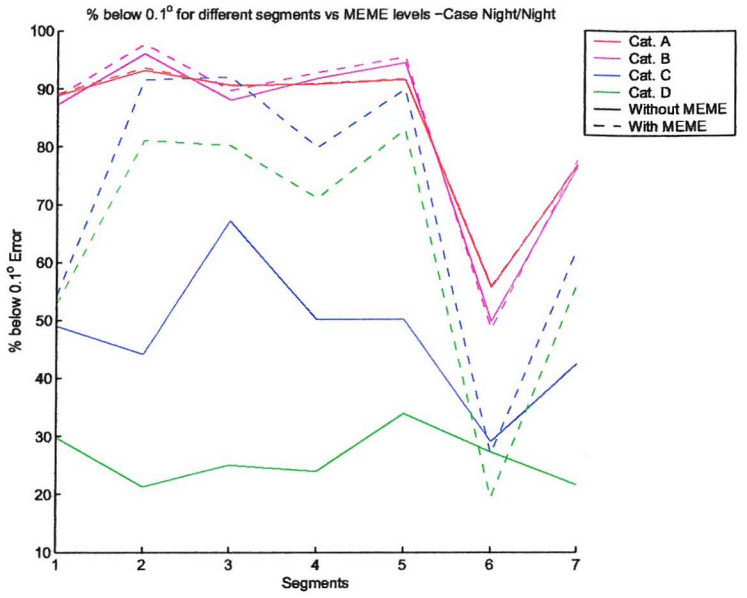

Figure 4.64: % of Samples below 0.1^o for Different Segments and Categories - NN

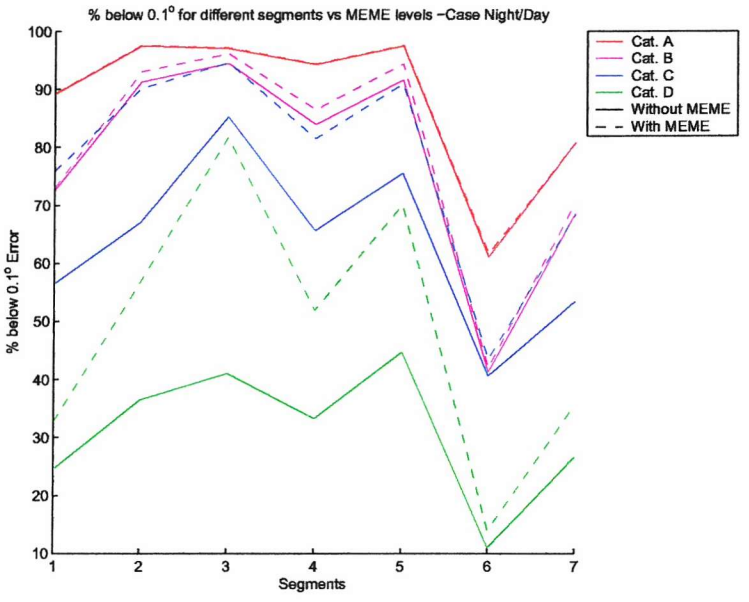

Figure 4.65: % of Samples below 0.1^o for Different Segments and Categories - ND

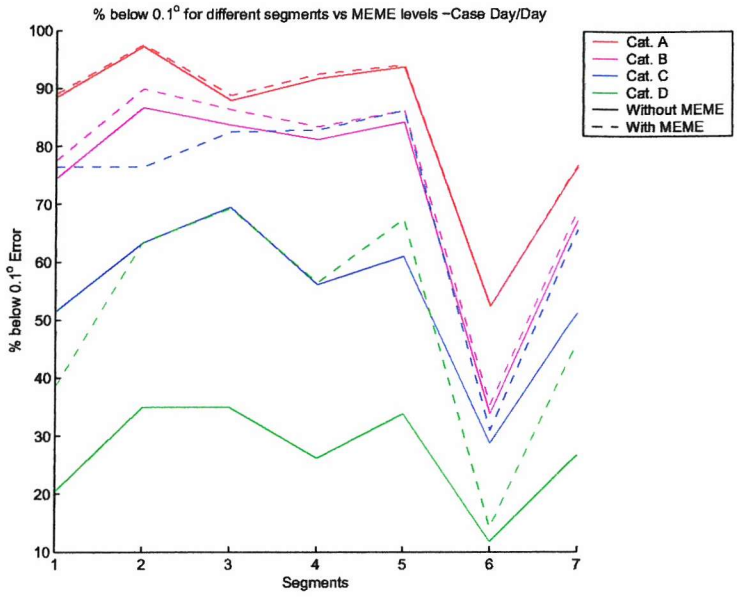

Figure 4.66: % of Samples below 0.1^o for Different Segments and Categories - DD

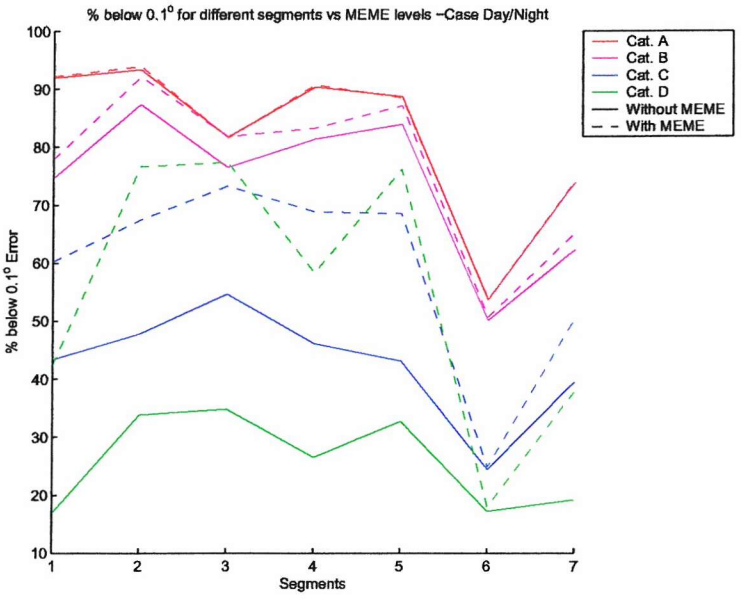

Figure 4.67: % of Samples below 0.1^o for Different Segments and Categories - DN

Case	Category	meme s1	meme s2	meme s3	meme s4	meme s5	meme s6	meme s7	- s1	- s2	- s3	- s4	- s5	- s6	s7
NN	A	-1.099	-1.976	-1.033	-1.132	-1.141	10.537	0.615	-1.536	-1.112	1.703	-0.100	0.628	8.149	0.334
NN	B	-6.918	-7.995	-2.249	-7.906	-5.730	45.336	8.392	-6.588	-20.714	-32.521	-21.753	-28.157	60.129	6.371
NN	C	-12.105	-10.795	-1.113	-10.901	-7.179	-56.222	-7.619	-5.467	-33.820	-54.664	-35.337	-45.629	85.344	4.232
NN	D	-5.836	-16.351	2.703	-10.632	-8.561	-9.096	-16.822	-3.940	-59.097	-89.708	-50.244	-73.987	30.374	-19.758
ND	A	-3.404	0.891	-0.956	-0.971	-0.644	3.274	-1.760	-3.257	0.977	-0.456	-0.763	-0.350	3.272	-1.579
ND	B	-6.005	-10.232	-12.129	-9.732	-11.941	6.709	-4.574	-8.567	-21.234	-28.467	-19.982	-25.492	11.274	-11.076
ND	C	-11.907	-7.511	-1.888	-8.249	-4.578	8.333	-1.190	-24.325	-34.253	-44.191	-33.910	-38.920	18.183	-16.021
ND	D	-25.942	2.457	22.512	2.271	12.278	-1.215	-2.928	-31.677	-40.414	-51.063	-39.415	-45.837	16.423	-33.233
DD	A	-3.795	1.575	-1.007	0.573	0.051	-3.198	-1.937	3.161	2.704	1.989	1.843	2.071	-5.764	-2.321
DD	B	-1.781	-0.740	-7.559	-2.437	-4.490	-9.558	-7.493	1.228	-13.557	-34.632	-15.406	-24.531	-1.322	-11.694
DD	C	-1.630	0.369	-7.615	-1.661	-3.010	-18.215	-15.634	-1.119	-25.211	-58.841	-24.876	-42.794	4.763	-22.062
DD	D	-3.349	3.839	-4.074	1.328	0.164	-64.802	-31.205	-8.790	-45.576	-100.798	-48.033	-75.071	-28.581	-44.768
DN	A	-0.118	-3.410	-7.998	-3.974	-6.284	5.314	-2.463	-1.095	-2.332	-3.403	-2.689	-3.531	3.396	-2.034
DN	B	-9.215	-9.239	-7.507	-5.980	-8.176	20.533	-0.069	-10.651	-22.789	-34.102	-18.866	-26.764	34.168	-9.423
DN	C	-0.197	-5.860	-6.324	-6.352	-6.008	15.882	1.395	-2.274	-35.850	-72.066	-33.809	-51.968	35.210	-6.679
DN	D	14.811	-4.966	-3.989	2.862	-3.679	37.815	16.651	-21.361	-29.628	-66.976	-17.545	-45.424	64.790	5.543

Table 4.6: Mean Magnitude Error(in nanoTesla) Comparison in Different Segments for Different Cases(NN/ND/DD/DN) and different Categories(A/B/C/D)

		meme	meme	meme	meme	meme	meme	meme	-	-	-	-	-	-	
Case	Category	s1	s2	s3	s4	s5	s6	s7	s1	s2	s3	s4	s5	s6	s7
NN	A	16.768	11.490	10.477	11.441	10.461	43.727	26.589	16.675	11.221	13.036	12.377	11.731	43.485	26.861
NN	B	55.077	13.511	11.698	40.494	14.258	131.800	77.225	56.912	20.247	20.213	44.621	21.856	130.101	79.910
NN	C	48.017	18.441	14.132	34.212	16.227	143.654	72.489	53.802	37.296	42.404	47.470	40.145	139.169	79.321
NN	D	79.190	10.783	6.180	42.906	11.726	79.307	58.934	78.121	28.508	17.579	62.670	28.413	101.600	80.642
ND	A	16.879	18.291	19.032	17.095	18.766	41.806	21.231	16.431	17.789	18.637	16.690	18.450	41.484	20.897
ND	B	17.985	12.933	13.935	15.658	13.639	87.509	39.960	23.950	19.909	22.840	24.196	21.531	91.056	45.861
ND	C	26.558	16.329	17.400	20.500	21.628	124.103	53.802	40.816	32.494	32.310	34.467	35.992	133.080	66.836
ND	D	46.808	28.493	34.950	43.629	34.409	109.712	65.046	66.621	33.545	36.859	45.314	34.900	136.142	74.130
DD	A	15.640	16.899	21.186	16.526	17.957	53.260	29.746	16.353	15.594	17.644	15.170	16.240	53.877	29.614
DD	B	16.389	8.934	8.150	13.359	9.404	80.608	33.895	23.965	22.776	23.887	26.148	23.860	82.475	39.615
DD	C	30.962	9.857	8.333	25.502	9.991	88.847	62.046	49.121	45.239	45.965	52.793	45.426	82.971	68.791
DD	D	52.096	17.328	10.010	41.253	15.727	113.737	81.640	81.497	66.032	64.060	76.141	62.533	118.992	95.644
DN	A	29.399	17.671	27.168	23.081	22.788	35.884	29.425	29.359	18.643	25.749	24.072	22.983	35.300	29.465
DN	B	35.510	24.234	21.994	41.379	24.029	85.890	54.944	53.319	40.719	35.860	54.149	38.955	78.278	65.513
DN	C	76.129	28.407	25.776	59.096	27.126	98.378	65.183	74.151	63.790	56.497	83.852	61.327	87.997	71.519
DN	D	67.458	10.119	12.927	43.121	15.034	62.989	54.577	56.897	34.921	28.898	50.021	34.410	67.656	54.955

Table 4.7: Magnitude rms Error(in nanoTesla) Comparison in Different Segments for Different Cases(NN/ND/DD/DN) and different Categories(A/B/C/D)

		meme	meme	meme	meme	meme	meme	meme	-	-	-	-	-	-	
Case	Category	s1	s2	s3	s4	s5	s6	s7	s1	s2	s3	s4	s5	s6	s7
NN	A	0.048	0.037	0.064	0.043	0.056	0.164	0.085	0.049	0.041	0.068	0.047	0.060	0.165	0.087
NN	B	0.215	0.058	0.077	0.122	0.068	0.357	0.236	0.223	0.069	0.084	0.132	0.078	0.360	0.244
NN	C	0.195	0.060	0.074	0.119	0.072	0.526	0.250	0.217	0.099	0.105	0.155	0.110	0.536	0.275
NN	D	0.279	0.106	0.080	0.145	0.091	0.304	0.219	0.362	0.145	0.090	0.198	0.127	0.328	0.263
ND	A	0.065	0.045	0.070	0.055	0.060	0.330	0.119	0.062	0.044	0.068	0.052	0.057	0.329	0.117
ND	B	0.058	0.051	0.066	0.070	0.057	0.900	0.293	0.067	0.063	0.070	0.079	0.065	0.904	0.303
ND	C	0.119	0.062	0.080	0.097	0.064	1.635	0.620	0.123	0.072	0.094	0.107	0.075	1.660	0.642
ND	D	0.262	0.081	0.075	0.145	0.076	1.003	0.317	0.253	0.091	0.091	0.150	0.089	1.039	0.336
DD	A	0.051	0.048	0.047	0.050	0.045	0.490	0.215	0.050	0.046	0.045	0.049	0.044	0.488	0.214
DD	B	0.081	0.032	0.039	0.064	0.037	1.016	0.225	0.090	0.050	0.047	0.077	0.051	1.016	0.235
DD	C	0.149	0.041	0.051	0.092	0.045	0.849	0.360	0.166	0.080	0.080	0.120	0.082	0.858	0.379
DD	D	0.217	0.052	0.069	0.137	0.062	1.086	0.549	0.266	0.119	0.096	0.198	0.127	1.099	0.580
DN	A	0.091	0.041	0.039	0.059	0.040	0.134	0.077	0.091	0.042	0.043	0.059	0.041	0.133	0.077
DN	B	0.153	0.064	0.051	0.113	0.058	0.327	0.180	0.161	0.079	0.062	0.122	0.073	0.324	0.184
DN	C	0.246	0.084	0.064	0.157	0.074	0.355	0.203	0.297	0.145	0.116	0.208	0.133	0.350	0.241
DN	D	0.323	0.099	0.068	0.185	0.084	0.233	0.211	0.343	0.186	0.108	0.238	0.161	0.192	0.253

Table 4.8: Mean Angle Error (in ^{o}) Comparison in Different Segments for Different Cases(NN/ND/DD/DN) and different Categories(A/B/C/D)

		meme	meme	meme	meme	meme	meme	meme	-	-	-	-	-	-	
Case	Category	s1	s2	s3	s4	s5	s6	s7	s1	s2	s3	s4	s5	s6	s7
NN	A	0.128	0.098	0.205	0.122	0.154	0.569	0.322	0.129	0.099	0.202	0.124	0.151	0.564	0.320
NN	B	0.911	0.176	0.304	0.509	0.225	1.353	0.933	0.906	0.170	0.312	0.518	0.219	1.371	0.939
NN	C	0.712	0.153	0.261	0.384	0.230	1.900	0.962	0.750	0.170	0.266	0.416	0.248	1.956	0.969
NN	D	1.162	0.276	0.106	0.457	0.175	1.114	1.075	1.236	0.218	0.175	0.526	0.180	1.224	1.108
ND	A	0.216	0.085	0.211	0.205	0.226	1.754	0.494	0.197	0.083	0.214	0.190	0.214	1.732	0.488
ND	B	0.196	0.108	0.215	0.189	0.183	4.710	0.951	0.208	0.119	0.215	0.195	0.180	4.686	0.993
ND	C	0.366	0.151	0.231	0.414	0.165	6.414	2.918	0.383	0.141	0.228	0.414	0.186	6.542	2.969
ND	D	0.969	0.182	0.234	0.456	0.175	4.047	1.432	0.956	0.194	0.243	0.441	0.183	4.297	1.474
DD	A	0.180	0.217	0.167	0.188	0.183	2.214	0.843	0.171	0.211	0.150	0.167	0.174	2.206	0.832
DD	B	0.313	0.084	0.084	0.201	0.096	4.957	0.935	0.312	0.101	0.102	0.197	0.111	4.911	0.939
DD	C	0.583	0.109	0.151	0.380	0.135	3.853	1.468	0.565	0.158	0.179	0.378	0.171	3.908	1.512
DD	D	0.745	0.116	0.180	0.488	0.167	5.273	2.507	0.774	0.231	0.228	0.569	0.251	5.273	2.544
DN	A	0.380	0.159	0.138	0.202	0.141	0.578	0.272	0.393	0.145	0.170	0.218	0.146	0.581	0.290
DN	B	0.478	0.136	0.104	0.333	0.136	0.969	0.692	0.479	0.164	0.142	0.358	0.174	0.962	0.681
DN	C	0.901	0.214	0.193	0.621	0.192	0.963	0.717	0.963	0.288	0.228	0.656	0.276	0.952	0.719
DN	D	1.256	0.313	0.166	0.796	0.246	0.548	0.850	1.295	0.336	0.197	0.842	0.261	0.516	0.806

Table 4.9: %95 Angle Error Threshold (in ^{o}) Comparison in Different Segments for Different Cases(NN/ND/DD/DN) and different Categories(A/B/C/D)

		meme	meme	meme	meme	meme	meme	meme	-	-	-	-	-	-	
Case	Category	s1	s2	s3	s4	s5	s6	s7	s1	s2	s3	s4	s5	s6	s7
NN	A	92.870	95.170	83.330	92.570	90.160	59.320	80.680	92.490	95.120	83.590	92.430	90.800	59.310	80.410
NN	B	56.490	85.430	79.920	72.990	80.540	33.010	57.510	51.740	81.530	78.100	70.250	78.720	32.100	56.200
NN	C	51.270	80.060	78.310	70.520	80.570	20.840	45.430	39.280	52.390	62.460	46.590	51.510	19.610	28.570
NN	D	55.170	57.370	88.380	65.190	58.620	18.530	50.080	3.360	7.690	65.450	12.200	23.480	11.090	17.120
ND	A	87.570	96.120	80.800	89.580	86.480	60.540	78.300	88.060	96.520	81.730	89.780	87.320	60.920	78.550
ND	B	87.890	94.720	82.120	86.930	87.900	32.780	68.730	83.250	93.310	80.750	86.010	87.350	32.450	66.100
ND	C	72.240	87.770	72.480	78.080	81.600	26.080	53.280	71.240	84.780	65.840	75.510	80.580	24.680	47.740
ND	D	36.850	69.610	82.230	61.190	73.440	16.000	51.470	40.290	61.340	68.070	58.520	65.900	14.170	43.150
DD	A	91.190	88.960	87.260	89.480	87.650	48.910	72.250	91.140	88.170	89.600	89.740	89.180	48.770	72.470
DD	A	79.660	97.310	96.360	89.070	95.660	37.170	63.640	79.200	94.940	94.610	85.610	91.900	36.820	60.150
DD	C	61.360	93.800	88.110	78.390	90.210	17.240	46.760	51.060	63.920	70.040	57.790	66.500	18.550	37.970
DD	D	55.160	88.840	85.100	75.270	86.050	11.090	36.740	28.920	43.590	63.730	40.070	44.710	10.400	21.330
DN	A	81.800	90.700	91.940	87.360	90.780	67.330	82.980	81.810	88.910	91.330	87.290	89.400	67.950	82.500
DN	B	54.190	82.290	94.350	68.990	86.030	28.130	56.070	46.980	69.420	81.480	63.740	71.410	29.930	53.730
DN	C	46.710	68.620	87.010	62.820	76.590	27.440	46.320	26.170	33.750	43.740	32.930	39.380	30.960	27.510
DN	D	38.830	59.750	88.110	56.090	76.950	13.690	51.030	19.000	0.000	43.440	14.110	10.810	30.830	12.310

Table 4.10: Percentage of Angle Error below 0.1^o Comparison in Different Segments for Different Cases(NN/ND/DD/DN) and different Categories(A/B/C/D)

4.7 Evaluation of the MEME dependent models with measurements from days not included in the modelling

The figures and tables referred to in this section are presented in Appendix D.

4.7.1 Mean Magnitude Error

4.7.1.1 Night-Night

: Figure D.1

When MEME is not used, the error is progressively increasing for categories A, B, C and D in segment 2 to 5. Segment 6 again shows a positive magnitude error, a fact that confirms the existence of high polar disturbance. After the use of MEME, the reduction of the mean magnitude error is high in segments 2 and 3. There is no significant error error reduction in segment 1 as already the error there has not been influenced by the presence of the ring current effect. The lowest error for categories B, C and D is in segment 3. For category A the lowest error is in segment 2.

4.7.1.2 Night - Day

: Figure D.2

Without the use of MEME, the error is progressively increasing for categories A, B, C and D in segments 1 to 5. After the use of MEME, there is a significant error reduction in segments 1, 2 and 3. However we see that for category D in segment 3 the resulting error is high and in the positive axis. The only reason for this is that the indication by MEME of a high activity is not consistent and the real one corresponded to a lower MEME value. For the same category D in segment 1 there is little reduction while for segment 2 the reduction is high. From all the previous experiments we have observed that the resulting error for category D is lower is segment 3 than in segment 2. This means that the model for this case and category gives a higher gain for latitudes in segment 3 than in segment 2. This has happened here with the error of segment 2 reaching the value 0, lower than for the other categories in the same segment, something that has been observed before. It is obvious that the disturbance level is overestimated by MEME and thus the resulting model gives higher than appropriate values. This higher reduction in segment 3 results in positive magnitude error while in segment 2 the higher model value actually brings the error exactly to zero. In categories B and C the highest reduction is for segments 2 and 3.

4.7.1.3 Day-Day

: Figure D.3

When the MEME models are not used, the error increases progressively for categories A, B, C and D in segments 1 to 5. After the use of MEME, there is a high error reduction in segments 2 and 3. The resulting error is lowest in segment 3 for category A and in segment 2 for categories B, C and D.

4.7.1.4 Day - Night

: Figure D.4

The error, without the use of MEME, is increasing progressively for categories A, B and C. For category D the error is lower than category C. This ambiguity has two possible causes. One is the overestimation of disturbance by the MEME index such that these measurements belong to category D while they are lower than this category. The second reason is that the high MEME values were taken at the peak of a storm disturbance which lasts for a very small period of time and decays fast to lower values. This means that the interval between the equatorial pass in the dayside and the entrance to segments 1 in the nightside is enough for the disturbance to decay. This is also justified by the small number of available measurements for such a high disturbance for the days used in the verification phase. Only three passes were identified with such high disturbances while from the table listing the days we would expect a higher number. During these passes MEME identified category C disturbance but in reality it was axially much smaller. This shows that the MEME in these cases was much higher than expected. This can also happen for single cases even if the disturbance is lower. It is possibly caused by intensified ionospheric phenomena with much sorter periods and narrower effect. Even under this ambiguity, we see that after the use of MEME the reduction for all categories in segments 2 and 3 is very high.

4.7.2 rms Magnitude Error

4.7.2.1 Night-Night

Figure D.5

When the MEME models are not used the rms error increases progressively in segments 2 and 3 for categories A,B and C. For category D the error is higher than for category C in segment 1 and lower in segments 2 and 3. The fact that it is higher is segment 1 is justified by the high polar activity. In segments 2 and 3 we see that the real rms error is smaller than

that in the D category. This shows a smaller variability of error around the mean in these segments. After the MEME is used there is a significant reduction of error in segments 2 and 3 for all categories. In segments 1 there is not a significant reduction. For all categories the resulting lowest error is in segment 3.

4.7.2.2 Night - Day

Figure D.6

Without the MEME dependent models, the rms error increases progressively for segments 1, 2 and 3. After the use of MEME the error is significantly reduced especially for categories B and C. For category D the improvement is smaller and this is justified by the fact that the model produced higher than appropriate values, as we saw in the discussion of the mean magnitude error for this case. Segment 2 has the lowest resulting rms error for all categories.

4.7.2.3 Day-Day

Figure D.7

The error, when the MEME model is not used, is increasing progressively for categories A, B, C and D in segments 1 to 5. After the use of the MEME model, there is a high error reduction in segments B, C and D in segments 1. A smaller reduction is observed in segment 1. The resulting error is lower in segment 2 for category A and in segment 3 for categories B,C and D.

4.7.2.4 Day - Night

Figure D.8

Without the use of MEME, the rms error progressively increases for categories A, B and C. For category D the rms error in segments 2 and 3 is smaller than that for categories B and C. This ambiguity is connected directly to the phenomenon observed for the same case in the examination of the mean magnitude error. The real disturbance is lower than expected for category D measurements and its variability is smaller as confirmed here. This effect is due to the ambiguity created by MEME for category D. After the use of MEME models the reduction is high for all categories in segments 2 and 3. Segment 1 shows reduction in some cases and not in others for categories B, C and D. For category A there is no reduction. The resulting error is smaller in segment 2 for category A, in segment 3 for categories B and C and in segment 2 for category D.

4.7.3 Mean Orientation Error

4.7.3.1 Night-Night

Figure D.9

When MEME is not used the mean error progressively increases for categories A, B and C in segments 2 and 3. The only exception is in segment 3 for which the mean angle error for category D is smaller than for category C. This means that in this case the orientation of the disturbance is closer to the orientation of the quiet vector than for category D. After the use of the MEME model there is a significant error reduction in segments 2 and 3 and a lower reduction in segment 1. The resulting error is smaller in segment 2 for categories A, B and C and in segment 3 for category D.

4.7.3.2 Night - Day

Figure D.10

Without MEME models, the error is increasing progressively for categories A, B and C and D. The only exception is in segment 3 where for category D the mean angle is smaller than for category C. There is no ambiguity for this segment in terms of the mean magnitude error and this means that this phenomenon is due to the closer resemblance of the disturbance vector to the quiet geomagnetic field vector for category D (compared to category C). After the use of MEME there is a significant reduction in segments 2 and 3 for categories B, C and D. In segment 1 no reduction is observed. The resulting error is lower in segment 2 for categories A, B and C. For category D the lowest error is observed in segment 3.

4.7.3.3 Day-Day

Figure D.11

If MEME is not used, the error progressively increases for categories A, B, C and D. After the use of MEME the error reduction is high in segments 2 and 3 and lower in segment 1. The resulting error is lowest in segment 3 for category A and in segment 2 for categories B, C and D.

4.7.3.4 Day - Night

Figure D.12

When MEME is not used the error increases progressively in segments 1 to 5 for categories A, B, C and D. The only exception is in segment 3 for category D, where the mean

angle error is smaller than for category C. In this case we encounter the mean magnitude error ambiguity. The effect on the mean angle error for category D is probably caused by the smaller magnitude with smaller effect on the orientation or from the fact that the duisturbance vector is more similar in orientation to the quiet field vector, compared to category C. After the use of MEME there is a significant error reduction for categories B, C and D in segments 2 and 3. In segment 1 the reduction is much smaller. The resulting error is minimum for all categories in segment 3.

4.7.4 95% Threshold Error

4.7.4.1 Night-Night

Figure D.13

Without the use of MEME, the threshold value follows a irregular pattern. The only consistent information is that the threshold for category A is smaller than for the other categories in all segments. This irregular behavior is due to the fact that the high errors at the tail of the error distribution increase with magnetic activity and these errors are of comparable frequency and magnitude. The 95% error threshold tends to show at what value the high errors, which account for the 5% of the distribution, start . However this threshold is usually quite high and higher than the errors created by the ring current. The errors above this threshold tend to increase with higher magnetic activity but nothing ensures that they do not occur at lower levels of magnetic activity. This is also confirmed by the fact that after the use of MEME models there is only a significant reduction in segments 2 and 3 for category D, the highest level of disturbance. For the rest of the cases no real reduction is observed.

4.7.4.2 Night - Day

Figure D.14

When MEME is not used, the error threshold is increased progressively for categories A, B, C and D in segments 2 and 3 but this increase is negligible. After the use of MEME no reduction is observed.

4.7.4.3 Day-Day

Figure D.15

Without MEME the thresholds increase progressively for categories B, C and D in segments 2 and 3. For category A the threshold is higher than categories B and C and lower than category D. Again we see an irregular behavior. After the use of MEME some reduction is observed in segments 2 and 3 for categories C and D. This means that the error above this value was due to the ring current before the application of the MEME model. After its application, this error was removed and the threshold dropped. For categories B the reduction is small and there is no reduction for category A.

4.7.4.4 Day - Night

Figure D.16

When MEME models are not used, the error in segments 2 and 3 exhibits an irregular pattern for different categories. After the MEME models are used, there is some important reduction in segments 2 and 3 for categories B, C and D. For category A no reduction was achieved.

4.7.5 Percentage of Error below 0.1^o

4.7.5.1 Night-Night

Figure D.17

Without the use of MEME models, the percentage progressively decreased for categories A, B, C and D. The only exception was in segment 3 for category D for which the percentage is higher than for category C. This shows that in this case a higher percentage of the error is lower than 0.1^o than for category D. This can only be explained by the fact that the disturbance vector is for most of the time closer to the quiet field vector than for category C. After the use of MEME models, there is a significant percentage increase in segments 2 and 3 for categories B, C and D. An important increase is also observed in segment 1. The resulting percentage is higher in segment 2 for categories A and B and in segment 3 for categories C and D.

4.7.5.2 Night - Day

Figure D.18

If MEME models are not used, the percentage of error below 0.1^o decreases progressively for categories A, B, C and D. The only exception is again for category D in segment 3. For this category the percentage is higher than for category C. The reason is assumed to be

the same as above. After the use of the MEME models, significant increase is observed in segments 2 and 3 for categories B, C and D. The resulting percentage is higher in segment 2 for category A and in segment 3 for categories B,C and D.

4.7.5.3 Day-Day

Figure D.19

Without MEME models, the error percentage decreases progressively for categories B, C and D. For category A in segments 2 and 3 the percentage is lower than that for category B. This is probably explained by the fact that in category B the orientation of the disturbance vector was closer to the orientation of the quiet field vector than in category A. After the application of the MEME models there is a high percentage increase in segments 2 and 3 for categories B, C and D. The resulting percentage is higher in segment 2 for categories A and B and in segment 3 for categories C and D.

4.7.5.4 Day - Night

Figure D.20

When MEME is not used the percentage decreases for categories A, B, C and D in segments 1 to 5. After the application of the MEME models, there is a high percentage increase in segments 2 and 3 for categories B, C and D. The resulting percentage is higher in segment 2 for categories A and B and in segment 3 for categories C and D.

An overall summary of the results and the conclusions is given in Chapter 7, at the end of this thesis.

Chapter 5

The Model in an Attitude Determination System

The results from the previous chapter have shown that the new magnetic field model offers a high accuracy not only due to the segmentation procedure but mainly because of the inclusion of the dynamic part dependent on MEME, the new index derived by a satellite over the equatorial region.

The improved accuracy of the model offers the opportunity for an improved attitude accuracy. The improved accuracy from direct use of the model in conjunction with another sensor is a straight forward procedure, since then the accuracy is that of the model (dependent, of course, on how accurate the magnetometer itself actually is).

The idea for a system examination came from the design of a nanosatellite. The University of Southampton in cooperation with the University of Cranfield were assigned by the British Space Centre a project to design 2 nanosatellites in order to demonstrate formation flying. The small size and dimensions of the nanosatellites made it difficult to identify suitable sensors for the mission requirements. The operation of a ranging device was initially assigned a required accuracy of 0.125^o although the use of a wider beam could relax the specifications. In any case the required accuracy created the quest for suitable methodologies and sensors for this purpose. This also created an opportunity to test the effectiveness of the new geomagnetic field models for attitude determination.

Magnetometers were quickly identified as light weight and power efficient instruments. The accuracy they offer is limited due to the inaccuracy of the reference geomagnetic field model. This was an ideal opportunity to examine the feasibility of methodologies for attitude determination based on magnetometers measurements.

First a short introduction to attitude dynamics is presented, followed by a presentation of identified sensors suitable for a nanosatellite. This is followed by a review of the methodologies for attitude determination based on magnetometer measurements. Finally a system is chosen for testing of the MEME model for attitude determination

5.1 Theory

Attitude dynamics describe the orientation of a body in an orbit and can be explained using rotations. When examining attitude dynamics, it is important to describe the reference frames being used to give a basis for the rotations.

5.1.1 Reference Frames

Three main reference frames are used to describe the orientation, or attitude, of a spacecraft in orbit. These are the inertial, orbital, and body frames, as discussed in turn next.

5.1.1.1 Inertial Frame

An inertial frame is used for attitude applications. The X direction points from the focus of the orbit to the vernal equinox, γ, the Z direction is in the orbital angular velocity direction, and Y is perpendicular to X and Z. See Figure 5.1 reproduced from [57].

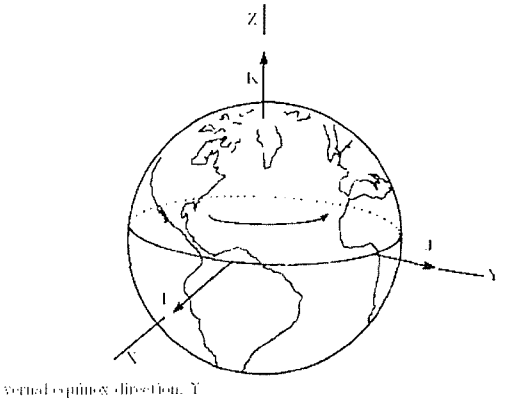

Figure 5.1: Inertial coordinate system

5.1.1.2 Orbital Frame

The orbital frame is located at the mass center of the spacecraft, and the motion of the frame depends on the orbit. This frame is non inertial because of orbital acceleration and the rotation of the frame. The $\hat{o}_3$ axis is in the direction from the spacecraft to the Earth, $\hat{o}_2$ is the direction opposite to the orbit normal, and $\hat{o}_1$ is perpendicular to $\hat{o}_2$ and $\hat{o}_3$. In circular orbits, $\hat{o}_1$ is the direction of the spacecraft velocity. The three directions $\hat{o}_1$, $\hat{o}_2$, and $\hat{o}_3$ are also known as the roll, pitch, and yaw axes, respectively. Figure 5.2 shows a comparison of the inertial and orbital frames in an equatorial orbit.

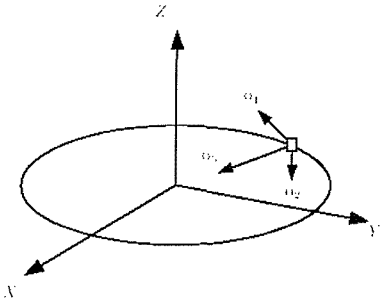

Figure 5.2: Orbital coordinate system

5.1.1.3 Body Frame

Like the orbital frame, the body frame has its origin at the spacecrafts center of mass. This frame is fixed in the body, and therefore is non-inertial. The relative orientation between the orbital and body frames is the basis of attitude dynamics and control.

5.1.1.4 Principal Axis

Principal axes are a specific body-fixed reference frame. This axis system has its origin at the mass center, and is oriented such that the moment of inertia matrix is diagonal and known as the principal moments of inertia.

5.1.2 Euler axis and Quaternions

Attitude is defined as the required transformation such that the body axis of the spacecraft will coincide with the reference coordinate system. The most common representation of such a transformation is the transformation matrix A which for transformation in the 3-dimensional Euclidian space is defined as:

$$A = \begin{bmatrix} u_1 & u_2 & u_3 \\ v_1 & v_2 & v_3 \\ w_1 & w_2 & w_3 \end{bmatrix} \tag{5.1}$$

where each element is the cosine of the angle between a body unit vector and a reference axis. The elements of the attitude matrix are not independent. There are two forms of dependency.

$$u_1^2 + u_2^2 + u_3^2 = 1 \quad \text{Unit Vector} \tag{5.2}$$

$$u_1 v_1 + u_2 v_2 + u_3 v_3 = 0 \quad \text{Orthogonality} \tag{5.3}$$

These two properties of the elements of the attitude matrix can be summarized as the following matrix identity:

$$A \cdot A^T = \mathbf{1} \tag{5.4}$$

Also $detA = \hat{u} \cdot (\hat{v} \times \hat{w})$. As $\hat{u}, \hat{v}, \hat{w}$ form a right-handed triad we have that $detA = 1$. Thus A is a proper real orthogonal matrix and matrix A maps vectors from the reference frame to the body frame.

Since the inverse of an orthogonal matrix is its transpose, A^T maps vectors from the body frame to the reference frame. A proper real orthogonal 3×3 matrix has at least one eigenvector $\hat{e}$ with eigenvalue unity for which:

$$A \cdot \hat{e} = \hat{e} \tag{5.5}$$

The vector $\hat{e}$ represents the axis described by *Euler*'s theorem:
" *The most general displacement of a rigid body with one point fixed is a rotation about some axis.*"

The vector $\hat{e}$ has the same components along the body axes and the along the reference axes so that $\hat{e}$ is a vector along the axis of rotation. In general, the axis of rotation does not coincide with any of the axis of the reference or body coordinate system. In terms of the unit vector along the direction of $\hat{e}$ and the angle of rotation Φ around this axis, the most general attitude matrix is of the form:

$$A = \begin{bmatrix} \cos\Phi + e_1^2(1-\cos\Phi) & e_1e_2(1-\cos\Phi) + e_3\sin\Phi & e_1e_3(1-\cos\Phi) - e_2\sin\Phi \\ e_1e_2(1-\cos\Phi) - e_3\sin\Phi & \cos\Phi + e_2^2(1-\cos\Phi) & e_2e_3(1-\cos\Phi) + e_1\sin\Phi \\ e_1e_3(1-\cos\Phi) + e_2\sin\Phi & e_2e_3(1-\cos\Phi) - e_1\sin\Phi & \cos\Phi + e_3^2(1-\cos\Phi) \end{bmatrix} \Leftrightarrow$$

$$A = \cos\Phi\mathbf{1} + (1-\cos\Phi)\hat{e}\hat{e}^T - \sin\Phi E \tag{5.6}$$

where:

$\hat{e}\hat{e}^T$ is the outer product and E is the skew-symmetric matrix :

$$E = \begin{bmatrix} 0 & -e_3 & e_2 \\ e_3 & 0 & -e_1 \\ -e_2 & e_1 & 0 \end{bmatrix} \tag{5.7}$$

The rotation angle Φ can be expressed in terms of the direction cosine matrix elements by:

$$\cos\Phi = \frac{1}{2}[tr(A) - 1] \tag{5.8}$$

The most popular parameterization of the direction cosine matrix A in satellite work is the *Euler symmetric parameters.* They are based on the representation and algebra of quaternions, developed by Hamilton in the first half of the 19^{th} century. The Euler symmetric parameters are four terms denoted by q_1, q_2, q_3, q_4 and defined as:

$$q_1 \equiv e_1 \sin\frac{\Phi}{2} \tag{5.9}$$

$$q_2 \equiv e_2 \sin\frac{\Phi}{2} \tag{5.10}$$

$$q_3 \equiv e_3 \sin\frac{\Phi}{2} \tag{5.11}$$

$$q_4 \equiv \cos\frac{\Phi}{2} \tag{5.12}$$

The four terms of the quaternion are not independent but they satisfy:

$$q_1^2 + q_2^2 + q_3^2 + q_4^2 = 1 \tag{5.13}$$

While q_1,q_2 and q_3 represent the three vector components, q_4 is a scalar quantity. Thus the quaternion is usually represented in terms of a vector and a scalar as:

$$\boldsymbol{q} \equiv \begin{bmatrix} q_1 \\ q_2 \\ q_3 \\ q_4 \end{bmatrix} \equiv \begin{bmatrix} \mathbf{q} \\ q_4 \end{bmatrix} \tag{5.14}$$

While the initial idea behind quaternions was the comprehensive description of a quantity in space and time [58], (vector representing space and scalar representing time), the use of a quaternion in the formulation of the Euler symmetric parameters has no such physical interpretation. The advantage of using a quaternion is obvious when the attitude direction matrix is expressed in terms of the quaternion components:

$$A(\boldsymbol{q}) = \begin{bmatrix} q_1^2 - q_2^2 - q_3^2 + q_4^2 & 2(q_1q_2 + q_3q_4) & 2(q_1q_3 - q_2q_4) \\ 2(q_1q_2 - q_3q_4) & -q_1^2 + q_2^2 - q_3^2 + q_4^2 & 2(q_2q_3 + q_1q_4) \\ 2(q_1q_3 + q_2q_4) & 2(q_2q_3 - q_1q_4) & -q_1^2 - q_2^2 + q_3^2 + q_4^2 \end{bmatrix} \tag{5.15}$$

$$= (q_4^2 - \mathbf{q}^2)\mathbf{1} + 2\mathbf{q}\mathbf{q}^T - 2q_4Q \tag{5.16}$$

where Q is the skew symmetric matrix

$$Q = \begin{bmatrix} 0 & -q_3 & q_2 \\ q_3 & 0 & -q_1 \\ -q_2 & q_1 & 0 \end{bmatrix} \tag{5.17}$$

Euler symmetric parameters provide a very convenient parameterization of the attitude. They are more compact than the direction cosine matrix because only four, rather than 9, parameters are needed. The calculation of the direction matrix from the quaternion components is a efficient procedure too, because there are no trigonometric functions, which require time consuming computer operations, involved in the calculations. However the most important advantage of the Euler symmetric parameters is the simple means of combing the terms for two individual rotations in order to derive the terms for the product of the two rotations. If the direction cosine matrices for the first and second rotations are denoted by $A(\boldsymbol{q}')$ and $A(\boldsymbol{q})$ respectively and $A(\boldsymbol{q}'')$ is the direction cosine matrix for the combined rotations then:

$$A(\boldsymbol{q}'') = A(\boldsymbol{q}') \cdot A(\boldsymbol{q}) \tag{5.18}$$

$$\boldsymbol{q}'' = \begin{bmatrix} q_4' & q_3' & -q_2' & q_1' \\ -q_3' & q_4' & q_1' & q_2' \\ q_2' & -q_1' & q_4' & q_3' \\ -q_1' & -q_2' & -q_3' & q_4' \end{bmatrix} \boldsymbol{q} \tag{5.19}$$

5.1.3 Euler's Equation - Attitude Dynamics

Euler's equations for the attitude rate vector's dynamics for satellite are:

$$I_m\dot{\omega} + \omega \times (I_m\omega) = \mathbf{w}_n + \mathbf{g} \tag{5.20}$$

where

I_m : Satellite Mass Moment of Inertia

ω : rotational velocity of satellite in body coordinate system

$\mathbf{g}$: Control torque

$\mathbf{w}_n$: Disturbance torque

The variable $\mathbf{g}$ represents the control torque applied by the on board actuators. If it assumed that no control torques are applied then the only torque present is $\mathbf{w}_n$, which represents the external disturbances. There are always external disturbances that apply forces of low magnitude, such as the solar radiation pressure, gravity gradient and atmospheric drag for LEOs.

When the applied torques are assumed zero then we have the torque free motion equation which is:

$$\begin{aligned} I_m\dot{\omega} + \omega \times (I_m\omega) = 0 \Leftrightarrow \\ I_m\dot{\omega} = -\omega \times (I_m\omega) \Leftrightarrow \\ \dot{\omega} = -I_m^{-1}\omega \times (I_m\omega) \end{aligned}$$

The above dynamic equations of motion were solved by Jabobi in 1849 and the solutions involve the Jacobi elliptic function [59], [60]. The solution is discomposed into the angular velocity components of the three principal axes of the body coordinate system. The solutions are as follows:

$$\omega_1 = \omega_{1m}cn(\Phi|m) \tag{5.21}$$

$$\omega_2 = -\omega_{2m}sn(\Phi|m) \tag{5.22}$$

$$\omega_3 = \omega_{3m}dn(\Phi|m) \tag{5.23}$$

where cn,sn,dn are the Jacobi elliptic functions. The argument Φ and parameter m are defined as :

$$\Phi = \omega_p(t - t_1) \tag{5.24}$$

$$m = \frac{(I_1 - I_2)(L^2 - 2I_3E_k)}{(I_3 - I_2)(L^2 - 2I_1E_k)} \tag{5.25}$$

The variables ω_{1m},ω_{2m} and ω_{3m} are the maximum values of the angular velocity components and they are defined as:

$$\omega_{1m} = \frac{L^2 - 2I_3E_k}{I_1(I_1 - I_3)} \tag{5.26}$$

$$\omega_{2m} = \frac{L^2 - 2I_3E_k}{I_2(I_2 - I_3)} \tag{5.27}$$

$$\omega_{3m} = \frac{L^2 - 2I_1E_k}{I_3(I_3 - I_1)} \tag{5.28}$$

$$\tag{5.29}$$

The variable ω_p is the body nutation rate and is defined as:

$$\omega_p = \pm\left[\frac{(I_3 - I_2)(L^2 - 2I_1E_k)}{I_1I_2I_3}\right]^{\frac{1}{2}} \tag{5.30}$$

$$\tag{5.31}$$

In the last equation the upper sign applies for $I_1 > I_2 > I_3$ and the lower for $I_1 > I_2 > I_3$. The indexing of the moments of inertia of the principal axes with 1, 2, 3 is in accordance with the following convention [25].

Assuming that no two moments of inertia are equal, the intermediate moment of inertia is labelled I_2 and the corresponding angular rate ω_2. L is the amplitude of the angular momentum defined as:

$$\mathbf{L} = \mathbf{I}\omega \tag{5.32}$$

and E_k is the angular kinetic energy of the satellite defined as:

$$E_k = \omega^{\mathbf{T}}\mathbf{I}\omega \tag{5.33}$$

If $L^2 < 2I_2E_k$ the moments of inertia are labelled such that $I3 < I2 < I1$. If $L^2 > 2I_2E_k$ the moments of inertia are labelled such that $I1 < I2 < I3$. If $L^2 = 2I_2E_k$ either labelling can be used. With this convention L^2 always lies between $2I_2E_k$ and $2I_3E_k$. An additional convention concerns the ω_3 component. The elliptic function dn is always positive and consequently the sense of this principal axis must be such that the angular rate will be positive. After the evaluation of the rotational velocity this axis can, of course, be rotated so that ω_3 appears negative.

The values of the parameter m are always between 0 and 1. The equations for the angular rate components have as time reference the time t_1 at which $\omega_1 = \omega_{1m}$. This is the maximum value for the axis indexed as 1. If another time reference other than t_1 needs to be used and t_1 is known in this reference frame, then from the addition laws of elliptic functions the following formulas can be used to derive the angular components:

$$\omega_1 = \frac{\omega_{01}cn(\omega_p t) + (v\omega_{02}\omega_{03}/\omega_{3m})sn(\omega_p t)dn(\omega_p t)}{1 - (\mu\omega_{02}/\omega_{3m})^2 sn^2(\omega_p t)} \tag{5.34}$$

$$\omega_1 = \frac{\omega_{02}cn(\omega_p t)dn(\omega_p t) - (\omega_{03}\omega_{01}/v\omega_{3m})sn(\omega_p t)}{1 - (\mu\omega_{02}/\omega_{3m})^2 sn^2(\omega_p t)} \tag{5.35}$$

$$\omega_1 = \frac{\omega_{03}dn(\omega_p t) + \mu^2(\omega_{01}\omega_{02}/v\omega_{3m})sn(\omega_p t)cn(\omega_p t)}{1 - (\mu\omega_{02}/\omega_{3m})^2 sn^2(\omega_p t)} \tag{5.36}$$

where:

$$\mu = \left[\frac{I_2(I_2 - I_1)}{I_3(I_3 - I_1)}\right]^{\frac{1}{2}} \tag{5.37}$$

$$v = \left[\frac{I_2(I_2 - I_3)}{I_1(I_1 - I_3)}\right]^{\frac{1}{2}} \tag{5.38}$$

and

$$\omega_{01} = \omega_{1m}cn(\omega_p t_1) \tag{5.39}$$

$$\omega_{02} = -\omega_{2m}sn(\omega_p t_1) \tag{5.40}$$

$$\omega_{03} = \omega_{3m}dn(\omega_p t_1) \tag{5.41}$$

and

$$\omega_{3m} = (\omega_{03}^2 + \mu^2\omega_{02}^2)^{\frac{1}{2}} \tag{5.42}$$

$$\tag{5.43}$$

In the above equations, the dependence of the Jacobi elliptic function on the parameter m has been omitted for notational convenience.

The above equations can be used to propagate the rotational velocity of a spacecraft if the moments of inertia,the angular momentum, the angular kinetic energy and the time t_1 are known.

5.1.4 Attitude Kinematics

The determination of angular velocity or attitude from magnetometer measurements involves the representation of the geomagnetic field vector in two reference systems. The inertial coordinate system, which serves as a reference and which is also the coordinate system for the geomagnetic field model that was developed in Chapter 3, and the spacecraft or body coordinate system in which all the original measurements are acquired. Here we represent them as (r_x, r_y, r_z) and (s_x, s_y, s_z) respectively. In order to present a physical representation of the operation of rate estimation we consider two time instances, namely t and $t + \Delta t$ where Δt is the time interval between the two instances. If at time t the attitude of the spacecraft is known relative to the inertial coordinate system, then it is represented by the quaternion $\boldsymbol{q}$. Now let the attitude of the spacecraft at time $t + \Delta t$ relative to that at time t be represented by the quaternion $\boldsymbol{q}'$. Finally let $\boldsymbol{q}''$ be the attitude of the spacecraft at time $t + \Delta t$ relative to the reference coordinate system. The derivation of $\boldsymbol{q}''$ naturally follows from a first transformation from the reference coordinate system to position $\boldsymbol{q}$ and a subsequent transformation to position $\boldsymbol{q}'$. This is expressed through the multiplication of the two quaternions and the result is $\boldsymbol{q}''$, the attitude at time $t+\Delta t$, relative to the reference coordinate system:

$$\boldsymbol{q}'' = \boldsymbol{q}\boldsymbol{q}' = (q_4 + iq_1 + jq_2 + kq_3)(q_4' + iq_1' + jq_2' + kq_3') \tag{5.44}$$

Using the properties of quaternion calculus the above equation becomes:

$$\begin{aligned} \boldsymbol{q}'' = \boldsymbol{q}\boldsymbol{q}' = \quad & (-q_1q_1' - q_2q_2' - q_3q_3' + q_4q_4') \\ + \quad & i(q_1q_4' + q_2q_3' - q_3q_2' + q_4q_1') \\ + \quad & j(-q_1q_3' + q_2q_4' + q_3q_1' + q_4q_2') \\ + \quad & k(q_1q_2' - q_2q_1' + q_3q_4' + q_4q_3') \end{aligned}$$

The above equation can be compactly represented by the following matrix equation:

$$\boldsymbol{q}'' = \begin{bmatrix} q_4' & q_3' & -q_2' & q_1' \\ -q_3' & q_4' & q_1' & q_2' \\ q_2' & -q_1' & q_4' & q_3' \\ -q_1' & -q_2' & -q_3' & q_4' \end{bmatrix} \boldsymbol{q} \tag{5.45}$$

If the analytical expressions for q_i' are used and $\boldsymbol{q}$ and $\boldsymbol{q}''$ are replaced by $\boldsymbol{q}(t)$ and $\boldsymbol{q}(t+\Delta t)$ respectively the above matrix equation takes the form:

$$\boldsymbol{q}(t+\Delta t) = \left\{ \cos\frac{\Delta\phi}{2}\mathbf{1} + \sin\frac{\Delta\phi}{2} \begin{bmatrix} 0 & e_{s_z} & -e_{s_y} & e_{s_x} \\ -e_{s_z} & 0 & e_{s_x} & e_{s_y} \\ e_{s_y} & -e_{s_x} & 0 & e_{s_z} \\ -e_{s_x} & -e_{s_y} & -e_{s_z} & 0 \end{bmatrix} \right\} \boldsymbol{q}(t) \tag{5.46}$$

As $\Delta t \to 0$, the above equation becomes a differential equation. The assumption that Δt becomes very small immediately implies that the rotational velocity ω can be considered as constant for this small interval. If ω is assumed constant then the rotation angle $\Delta\phi$ around the Euler axis e_s can be approximated by the linear equation:

$$\Delta\phi = \omega \cdot \Delta t \tag{5.47}$$

and (5.46) can be rewritten as:

$$\boldsymbol{q}(t+\Delta t) = \left\{ \cos\frac{\omega\Delta t}{2}\mathbf{1} + \sin\frac{\omega\Delta t}{2} \begin{bmatrix} 0 & e_{s_z} & -e_{s_y} & e_{s_x} \\ -e_{s_z} & 0 & e_{s_x} & e_{s_y} \\ e_{s_y} & -e_{s_x} & 0 & e_{s_z} \\ -e_{s_x} & -e_{s_y} & -e_{s_z} & 0 \end{bmatrix} \right\} \boldsymbol{q}(t) \tag{5.48}$$

Note that ω in the last equation is a scalar since it is the magnitude of the instantaneous rotational velocity around e_s.

Another implication of allowing δt to become infinitely small is that $\Delta\phi$ also tends to zero and thus the following angle approximations can be made:

$$\begin{aligned} \cos\frac{\Delta\phi}{2} = \cos\frac{\omega\Delta t}{2} &\approx 1 \\ \sin\frac{\Delta\phi}{2} = \sin\frac{\omega\Delta t}{2} &\approx \frac{\omega\Delta t}{2} \end{aligned}$$

Using these approximations, (5.48) becomes:

$$\boldsymbol{q}(t+\Delta t)=\left\{\mathbf{1}+\frac{\omega\Delta t}{2}\begin{bmatrix}0 & e_{s_z} & -e_{s_y} & e_{s_x}\\ -e_{s_z} & 0 & e_{s_x} & e_{s_y}\\ e_{s_y} & -e_{s_x} & 0 & e_{s_z}\\ -e_{s_x} & -e_{s_y} & -e_{s_z} & 0\end{bmatrix}\right\}\boldsymbol{q}(t) \tag{5.49}$$

If now ω is inserted into the skew symmetric matrix containing the vector components of the Euler axis e_s and $\omega \cdot e_{s_x} = \omega_{s_x}$,$\omega \cdot e_{s_y} = \omega_{s_y}$,$\omega \cdot e_{s_z} = \omega_{s_z}$ is used then (5.49) becomes:

$$\boldsymbol{q}(t+\Delta t)=\left\{\mathbf{1}+\frac{\Delta t}{2}\begin{bmatrix}0 & \omega_{s_z} & -\omega_{s_y} & \omega_{s_x}\\ -\omega_{s_z} & 0 & \omega_{s_x} & \omega_{s_y}\\ \omega_{s_y} & -\omega_{s_x} & 0 & \omega_{s_z}\\ -\omega_{s_x} & -\omega_{s_y} & -\omega_{s_z} & 0\end{bmatrix}\right\}\boldsymbol{q}(t) \tag{5.50}$$

and denoting the new skew symmetric matrix by Ω we have:

$$\boldsymbol{q}(t+\Delta t)=\left\{\mathbf{1}+\frac{\Delta t}{2}\Omega\right\}\boldsymbol{q}(t) \tag{5.51}$$

This is an ordinary differential equation which has an exponential solution. In order to see this more clearly, write:

$$\begin{aligned}
&\boldsymbol{q}(t+\Delta t)=\left\{\mathbf{1}+\frac{\Delta t}{2}\Omega\right\}\boldsymbol{q}(t) \Leftrightarrow\\
&\boldsymbol{q}(t+\Delta t)-\boldsymbol{q}(t)=\frac{1}{2}\Delta t\Omega\boldsymbol{q}(t) \Leftrightarrow\\
&\frac{\boldsymbol{q}(t+\Delta t)-\boldsymbol{q}(t)}{\Delta t}=\frac{1}{2}\Omega\boldsymbol{q}(t) \Leftrightarrow\\
&\dot{\boldsymbol{q}}=\frac{1}{2}\Omega\boldsymbol{q}
\end{aligned} \tag{5.52}$$

If Ω and the Euler axis e are assumed constant then this is an ordinary differential question and has the following analytical solution:

$$\boldsymbol{q}(t)=\exp\left\{\frac{1}{2}\Omega t\right\}\boldsymbol{q}(0) \tag{5.53}$$

In order to use this exact solution, an analytical representation of Ω must be available. This analytical representation may be the information from an estimator which fuses information from the attitude control system in order to predict the angular velocity and angular acceleration based on the applied torques. When no control torques are applied, angular acceleration can be caused from either the cross coupling between the

If the Euler axis e is assumed constant while Ω is varying in time then the solution of (5.52) is derived by using the integral of Ω instead of itself:

$$\boldsymbol{q}(t) = \exp\left\{\frac{1}{2}\int_0^t \Omega(t')dt'\right\}\boldsymbol{q}(0) \tag{5.54}$$

5.1.5 Wahba's problem

Comparing the attitude representation summarized earlier in this chapter, it is recognized that the most efficient of them is the method of quaternions. In 1965 Wahba [61] introduced the problem of attitude determination and, more specifically, the problem of minimizing the squares of residuals in vector observations.

5.1.5.1 Problem formulation

The quaternion represents the rotation that will make one vector coincide with each other. This can also be treated as the error between the real and the desired position of a vector. Following the classical treatment of error in squared form rather than the famous Wahba problem enables us to formulate the problem as:

Minimize $f(\mathbf{q})$ subject to $\mathbf{q} = (\mathbf{q_1}, \mathbf{q_2}, \mathbf{q_3}, \mathbf{q_4})^{\mathbf{T}}$ and $\mathbf{q^T q} = \mathbf{1}$. The quaternion function is then defined as:

$$f(\mathbf{q}) = -\mathbf{q^T K q} \tag{5.55}$$

where K is a 4×4 matrix defined as follows:

$$K = \begin{bmatrix} S - \sigma I & Z \\ Z^T & \sigma \end{bmatrix} \tag{5.56}$$

$$\sigma = trB = \sum_{i=1}^{n} = a_i w_i^T v_i \tag{5.57}$$

$$S = B + B^T = \sum_{i=1}^{n} a_i(w_i v_i + v_i w_i^T) \tag{5.58}$$

$$Z = [B - B^T] = \sum_{i=1}^{n} a_i w_i \times v_i \tag{5.59}$$

in (5.57) tr denotes the trace of a square matrix, and in (5.59) the notation [] denotes a conversion from a skew matrix to a corresponding three dimensional vector.

The quaternion is used as a four-dimensional vector but with a constraint of unit length. This means that the locus of the attitude quaternion is the surface of the unit sphere S^3 as a smooth manifold in the Eucledian space R^4.

5.1.6 Problem Solution

5.1.6.1 The q method

To maximize the gain function [25], we take the derivative with respect to $\mathbf{q}$, but since the quaternion elements are not independent, the constraint must also be satisfied. Adding the constraint to the gain function with a Lagrange multiplier yields a new gain function, $f_\lambda(\mathbf{q}) = \mathbf{q_T K q} - \lambda \mathbf{q^T q}$. Differentiating this gain function shows that $f_\lambda(\mathbf{q})$ has a stationary value when $K\mathbf{q} = \lambda\mathbf{q}$. This equation is easily recognized as an eigenvalue problem. The optimal attitude is thus an eigenvector of the K matrix. However, there are four eigenvalues and they each have different eigenvectors.

To see which eigenvalue corresponds to the optimal eigenvector (quaternion) which maximizes the gain function, recall that $f(\mathbf{q}) = \mathbf{q}^T K\mathbf{q} = \mathbf{q}^T\lambda\mathbf{q} = \lambda\mathbf{q}^T\mathbf{q} = \lambda$. The largest eigenvalue of K maximizes the gain function and the eigenvector corresponding to this largest eigenvalue is the least-squares optimal estimate of the attitude. There are many methods for directly calculating the eigenvalues and eigenvectors of a matrix, or approximating them. The q-method involves solving the eigenvalue/vector problem directly but QUEST, see the next section, approximates the largest eigenvalue and solves for the corresponding eigenvector.

5.1.6.2 QUEST

The q-method provides an optimal least-squares estimate of the attitude, given vector measurements in the body frame and information on those same vectors in some reference (often inertial) frame. The key to the method is to solve for the eigenvalues and eigenvectors of the K matrix. While the eigenproblem may be solved easily using, for example, Matlab, the solution is numerically intensive. On-board computing requirements are a concern for satellite designers, so a more efficient way of solving the eigenproblem is needed. The QUEST algorithm, similar in structure, to other algorithms such as FOAM [62], provides a *"cheaper"* way to estimate the solution to the eigenproblem [63]. Representing the Wahba problem of minimization of the residuals between vector observations in terms of the vectors and the corresponding transformation matrix, gives the form of loss function described next.

In vector form and not in quaternion form, the least-squares optimal attitude minimizes the loss function

$$J = \frac{1}{2}\sum_{k=1}^{N} w_k |v_k - Au_k|^2 \tag{5.60}$$

where u and v are the two unit vectors and A is the transformation matrix. Another way to express the loss function is

$$J = \sum_{k=1}^{N} w_k (1 - v_k^T A u_k) \tag{5.61}$$

and maximize the gain function

$$f = \sum w_k v_k^T A u_k \tag{5.62}$$

$$f = \lambda_{opt} \tag{5.63}$$

Rearranging these two expressions provides a useful result

$$\lambda_{opt} = \sum w_k - J \tag{5.64}$$

$$\tag{5.65}$$

For the optimal eigenvalue, the loss function should be *"small"*. Thus a good approximation for the optimal eigenvalue is

$$\lambda_{opt} \approx \sum w_k \tag{5.66}$$

For many applications this approximation may be accurate enough. Reference [63] includes a Newton-Raphson method which uses the approximate eigenvalue as an initial guess.

Once the optimal eigenvalue has been estimated, the corresponding eigenvector must be estimated. The eigenvector is the quaternion which corresponds to the optimal attitude estimate. One way here is to convert the quaternion in the eigenproblem to Rodriguez parameters, defined as:

$$p = \frac{q}{q_4} = a\tan\frac{\Phi}{2} \tag{5.67}$$

The eigenproblem can then be rearranged as

$$p = [(\lambda_{opt} + \sigma)\mathbf{1} - \mathbf{S}]^{-1}\mathbf{Z} \tag{5.68}$$

Taking the inverse of this expression is also a computationally intensive operation. Again, Matlab does it effortlessly, but solving for the inverse is not necessary. An efficient approach is to use Gaussian elimination, or other linear system methods, to solve the equation:

$$[(\lambda_{opt} + \sigma)\mathbf{1} - \mathbf{S}]\mathbf{p} = \mathbf{Z} \tag{5.69}$$

Once the Rodriguez parameters are found, the quaternion is calculated using:

$$\mathbf{q} = \frac{1}{\sqrt{1 + \mathbf{p}^T\mathbf{p}}} \begin{bmatrix} \mathbf{p} \\ 1 \end{bmatrix} \tag{5.70}$$

5.2 The space environment

5.2.1 Sources of disturbance to spacecraft dynamics

Assessment of expected disturbance torques is an essential part of rigorous spacecraft attitude determination design. The relevant ones here are as follows:

- Gravity Gradient: Tidal Force due to $1/r^2$ gravitational field variation for long, extended bodies (e.g.magnetometer booms)
- Aerodynamic Drag: Weathervane Effect due to an offset between the CM and the drag center of Pressure (CP). Only a factor in LEO.
- Magnetic Torques: Induced by residual magnetic moment. Model the spacecraft as a magnetic dipole. Only within magnetosphere.
- Solar Radiation: Torques induced by CM and solar CP offset. These can be compensated for by differential reflectivity or reaction wheels.
- Mass Expulsion: Torques induced by leaks or jettisoned objects

5.2.2 Environmental Disturbance Torques

Figure 5.3 shows a graph of the most dominant disturbance torques for a spacecraft.(Reproduced from [64]).

5.2.2.1 Gravity Gradient Torque

The variation of the gravity force on an asymmetric body travelling in orbit causes a torque emanating from the inverse square gravitational force. This disturbance can be explicitly

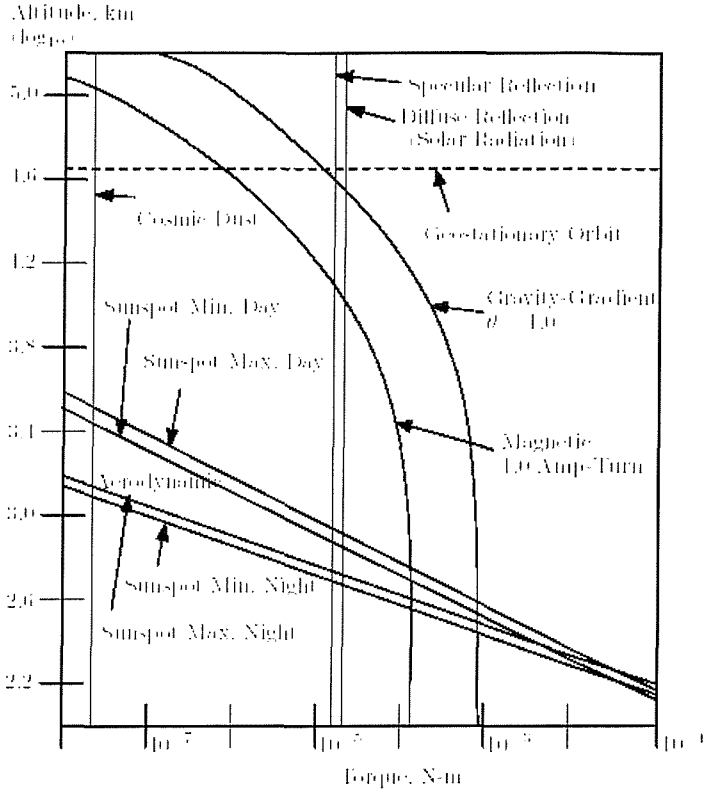

Figure 5.3: Environmental disturbance torques

modelled as:

$$\mathbf{N}_{gg}(t) = \frac{3\mu}{r^3(t)}(\mathbf{n}_b(t) \times \mathbf{In}_b(t)) \tag{5.71}$$

where μ is the Earth Gravitational constant,r is the geocentric distance,$\mathbf{n}_b$ is the unit direction vector in the body coordinates from the center of the mass to the center of the Earth and $\mathbf{I}$ is the inertia matrix of the spacecraft.

5.2.2.2 Aerodynamic drag

The aerodynamic torque is caused by the collision of atmospheric particles with the satellite in the direction of the orbital velocity. The effect of the force that is applied on the satellite is described by

$$d\mathbf{f}_{aero} = -\frac{1}{2}C_D\rho u^2(\hat{\mathbf{n}}\hat{\mathbf{v}_b}) \tag{5.72}$$

where ρ is the atmospheric density at the given altitude, C_D is the drag coefficient, (typically set as 2 when not known [25]) and dA is a surface element,$\hat{\mathbf{n}}$ is the normal vector outward of

the surface element,$\hat{\mathbf{v}}_b$ is the unit vector in the direction of the orbital velocity in the body coordinate system.

By approximating the structure of the satellite by a number of plane surfaces A_i, the aerodynamic torque is calculated as the integral of all the individual torques applied on each surface element. This simplifying approximation leads to the formula. Hence

$$\mathbf{n}_{aero} = \sum_{i=1}^{k} \mathbf{r}_i \times \mathbf{F}_i \tag{5.73}$$

where $\mathbf{r}_i$ is the CM(center of mass) to CAP(Center of Pressure) of the i^{th} element. Consequently

$$\mathbf{n}_{aero} = -\frac{1}{2} C_D \rho u^2 \sum_{i=1}^{k} A_i(\hat{\mathbf{n}}_i \mathbf{r}_i) \times \mathbf{r}_i \tag{5.74}$$

where A_i are the surface elements and $\mathbf{r}_i$ is the CM (center of mass) to CAP (Center of Pressure) of the i^{th} element.

5.3 Attitude Determination Sensors

5.3.1 Sun Sensors

Sun sensors are used in the first instance to acquire spacecraft attitude from unknown orientation, since the Sun is normally the brightest object in the sky and therefore unambiguous. The sun subtends an angle of about 32 arc minutes at the Earth. Sun sensors may be used to provide coarse attitude information, but are able to provide attitude sensing to 1 arc minute accuracy, with suitable sensor design.

5.3.1.1 Sun Presence Sensors

These devices merely sense whether the Sun is in a particular region of the sky, for example to actuate shutters on more sensitive instruments, or as the first stage in an attitude acquisition sequence. Typically the output of such a sensor is a step function with the 1 state indicating Sun presence, and the 0 state, Sun absence. A variety of devices are used with optical arrangements designed to give an appropriately narrow field of view. The simplest of these is a pair of apertures separated by a few centimeters, and sharing the same optical axis.

5.3.1.2 Analogue Sun Sensors

A simple sun sensor may be constructed by exploiting the angular dependence of output current of a silicon photocell with Sun angle, which depends upon the cosine of the Sun angle. Sensors may be arranged in pairs to resolve directional ambiguities, and the field of view may be varied by appropriate design. The resolution depends upon the sensing element and electronic design. These designs have intermediate resolution of $1 - 5^o$. An aperture is often used to limit the field of view, which as a result is often conical.

5.3.1.3 Digital Sun Sensors

Most digital sun sensors consist of two parts, a command section, which is functionally similar to a slit based Sun presence sensor, and a measurement section. Typically a sun sensor will have a field of view (FOV) in the region of 60^o, and so the sensors are often used in pairs to obtain 180^o coverage. Two sensors may be mounted at right angles in order to sense elevation and azimuthal direction to the Sun. Full 3D coverage of the sky can be obtained by use of multiple sensors with overlapping fields of view.

5.3.2 Earth horizon sensors

There are a variety of devices which can be used for Earth/planet sensing, and the designs arise from spacecraft configuration (e.g. spinning or non-spinning), mission goals, pointing accuracy requirements, cost, mass etc.. The main technologies and principles are outlined below, but the list is not exhaustive.

5.3.2.1 Body Mounted Horizon Sensor (BMS)

For spinning spacecraft, the simplest Earth sensor is the Body Mounted Horizon Sensor (BMS) operating in the visible part of the spectrum, which consists of a lens and aperture which define a narrow field of view, and a photo sensor. Improved, but more complex body-mounted sensors operating in the infrared region may also be used. The optical axis of the sensor is usually mounted at an angle to the spin axis of the spacecraft, and as the spacecraft spins, a conical scan is executed. Since the sensor is fixed to the body of the spacecraft, target acquisition may be a problem under certain circumstances.

5.3.2.2 Panoramic and scanning attitude sensors (PAS)

A PAS is a versatile device that can use the scanning provided by a spinning spacecraft, or can use an internal scanning system. It has an effective mounting angle that is commandable. These devices usually have an integral Sun presence sensor. A rotating turret telescope is used to provide the scanning when the spacecraft is not spinning. The turret provides the variable mounting angle for a spinning spacecraft.

5.3.3 Magnetometers

Magnetometers have several advantages over optical attitude sensors, and are widely used. They can in principle sense both magnitude and direction of the Earth's magnetic field, and as such are vector sensors. They are lightweight, reliable, and have low power consumption. They operate over a wide temperature range and have no moving parts. However, due to the inaccuracy of the geomagnetic field model predictions of field direction and magnitude at the position of the spacecraft, are subject to substantial error. Also the Earth's field strength diminishes as $1/r^2$, and hence magnetometers are not normally used at altitudes above 2000km.

5.3.3.1 Quantum magnetometer

This uses Zeeman splitting or nuclear magnetic resonance. The device is complex and heavy, and so is normally used only for research purposes.

5.3.3.2 Induction magnetometer

Uses Faraday's law of magnetic induction.

5.3.3.3 Fluxgate magnetometer

This is a more sophisticated induction device and is commonly used. It exploits magnetic saturation and hysteresis in a ferromagnetic material. It is the most widely used type of magnetometers for attitude determination.

5.3.4 Star Sensors

Star sensors give down to 1 arc-second accuracy, at the expense of size, weight, power and cost. There is also a need to identify the stars in the field of view. The field of view is typically narrow and less than 10^o. Scanning or gimbal systems are used to acquire other stars. These

sensors usually consist of some sort of telescopic optical system, with an appropriate detector and electronics. It may have a sun shade and field of view limiters in order to eliminate stray light, and it may be equipped with a shutter which may be used to protect the star tracker when bright objects such as the Sun and Earth are in the field of view. The systems usually detect position and magnitude of a star. Star trackers may be scanning devices, using spacecraft rotation to effect the scan, gimbaled devices which execute scans mechanically, or extend the field of view of a scanning tracker, or fixed head devices which have electronic scanning over a small field of view. The scanning devices which exploit spacecraft rotation have no moving parts. A telescopic optical system focuses the star image onto the focal plane. A slit or slits is often placed at the focal plane, to define the instantaneous field of view of the sensor.

5.3.5 Inertial sensors - gyroscopes

It is possible to use inertial space to sense attitude changes, by the use of gyroscopes. It is possible to generate torques for attitude control by the use of control moment gyros. For attitude determination, two basic types of gyro are used, Rate Gyro(RG) and the Rate-Integrating Gyro (RIG).All mechanical gyro systems share a common construction geometry The spinning rotor fixes the angular momentum vector in magnitude, with direction along the rotor spin axis. In the absence of applied torques, this vector maintains its inertial orientation. The gyro is mounted in a gimbal. If the spacecraft changes attitude about the gyro's input axis, the gyro begins to precess about the gimbal output axis.

5.3.5.1 Rate Gyro Rate Gyros (RGs)

These measure spacecraft angular rates directly. They may be used in a feedback system for controlling spin rate or for attitude stabilization. The angular rates can be integrated by computer to give an estimate of attitude displacement with respect to some reference. The output of an RG is obtained by measuring the rotation of the gimbal about the output axis. The movement of the gimbal is restrained by a spring, with relatively light viscous damping to prevent oscillation. We will show that in the steady state. the angular displacement of the output axis is directly proportional to the angular rate of the input axis.

5.3.5.2 Rate Integrating Gyro

A Rate Integrating Gyro (RIG) measures an angular displacement directly. It may be used to provide an incremental displacement measurement, or a total displacement measurement from some inertial reference. RIGs are more accurate in general than RGs, but are also more expensive. Drift rates of better than 0.01 degree per hour are attainable in the best systems.

5.3.6 Laser gyro

The laser gyro is a device with no moving parts. The time taken for light to travel the length of fibre in a fibre-optic coil will change if the coil is rotated about its axis. The difference in time is a measure of the angular rate. Although the optical fibre component is attractively robust, the laser itself is a single-point failure item. Stabilities of down to 0.1 degree per hour are achievable.

5.3.6.1 Silicon Gyroscopes

These represent the state of the art technology in gyroscopes. Their operation is based on the Coriolis force. Coriolis acceleration is induced on a proof mass that vibrates along a direction orthogonal to the axis about which the input rotation is applied. By sensing the secondary vibration, the rate can be detected. Resolution, drift and zero rate output are the factors that determine the performance of a gyroscope.

5.4 Identification of suitable components for the nanosatellite

A nanosatellite has a weight lower than 10 kilograms and accordingly small dimensions. Correspondingly, the available power from solar cells is also limited. This means that heavy sensors such as star cameras are not considered for such a small mass and power budget. The following components were identified as the more suitable components for a nanosatellite to date.

5.4.1 Horizon sensors

Horizon sensors are infrared devices that detect the contrast between the cold of deep space and the heat of the Earths atmosphere (about 40 km above the surface in the sensed band). Horizon sensors can provide pitch and roll attitude knowledge for Earth-pointing spacecraft, with an accuracy of 0.1 to 0.25. For the highest accuracy in low Earth orbit (LEO), it is

necessary to correct the data for the Earth oblateness and seasonal changes in the apparent horizon [65].

The most effective of the existing devices in this class is the EDO Barnes Model 13-500 wide-angle miniature solid-state horizon sensor. These sensors have been space-proven on six missions to date. The sensors have fields of view sufficient to allow pointing at off-nadir angles of up to 11^o, but peak performance is limited to angles less than 9^o. Each sensor has a mass of $0.113kg$ and is roughly cylindrical with a diameter of about $4.1cm$ and a height of about 5.6 cm [66].

5.4.2 Magnetometers

Magnetometers are simple, lightweight sensors that measure both the direction and magnitude of the Earths magnetic field. They are reliable but require complex software for interpretation and provide relatively coarse attitude determination as compared to horizon, sun, and star sensors. GPS position measurements are used with a computer model of the Earths magnetic field to approximate the field direction at the spacecrafts current position. The measured and calculated fields are compared, establishing two-axis spacecraft attitude. Over the course of an orbit, the Earths magnetic field direction usually changes rapidly enough with respect to the spacecraft to make computation of the fields time derivative possible. These field variations are large enough to enable determination of all three Euler angles using only a three axis magnetometer [67]. The Earths magnetic field also varies with time and cannot be calculated precisely, so a magnetometer is often used with another sensor such as a sun, horizon or star sensor or a gyroscope in order to improve the accuracy. The Applied Physics Systems Model 533 miniature three-axis fluxgate magnetometer can provide direction accuracy to better than 0.1^o in a laboratory environment. This model is well suited for use in the nanosatellite because of its extremely low $18g$ mass and its small size [68]. The Model 533 was flown aboard Stanford Universitys Opal satellite in late 1999. The Model 533 can tolerate a local magnetic field strength of up to one Gauss before significant errors appear in its measurements, and damage will occur when a two-Gauss source is placed within six inches of the powered-on sensor.

The most accurate magnetometer in the range considered for a nanosatellite is the Billingsley TFM100S Magnetometer. The magnetometer has an error of $\pm 60nT$ for a full scale of $600mG$. The magnetometer was used onboard the SNAP mission of the Surrey Space Center [69], [70].

The accuracy of these miniature magnetometers is moderate and limits the capabilities of accurate attitude determination. Apart from the inaccuracy of the hardware itself, the error of the reference geomagnetic field model further increases the overall error. It is important to note that the magnetometer used in Oersted, very precise ($\pm 0.5^o$), has a mass of 3 kilograms and a power requirement of 3.5 Watts [3]. These characteristics are prohibitive for a nanosatellite. However 2 years ago NASA, JPL and Polatonic started a project to design a miniature laser-pumped self-calibrating vector magnetometer for space applications. The magnetometer has low mass and its operation is based on extracting magnetic field information from a He^4 cell [71]. The design was targeted for use in very small satellites. The tested prototype demonstrated an accuracy of 1nT in 100000nT [71]. Although not commercially available, this miniature magnetometer is definitely the state of the art in miniature magnetometers and it is most definite that it will form the favorite solution for nanosatellites.

5.4.3 Micromechanical gyroscope

Micromachined solid-state gyroscopes use vibrating mechanical elements to sense rotation. They have no rotating parts that require bearings, so they can be easily miniaturized. All vibration gyroscopes are based on the transfer of energy between two vibration modes of a mechanical structure, caused by Coriolis acceleration [72]. The highest rotation sensitivity is obtained when the drive and sense modes have the same resonant frequency. Resolution, drift rate, zero-rate output, and scale factor are the most important factors that determine the performance of a gyroscope. When a gyroscope is inertially static, the output signal is a random function that is the sum of white noise and a cyclic noise function of the mechanical resonant frequencies. Based on resolution, drift rate, and zero-rate output, the Systron Donner QRS-11 micromachined angular rate sensor is the most accurate. This gyroscope has a resolution of $0.004^o/s$ and a short-term bias stability (100 s at constant temperature) of $0.004^o/s$. The gyroscope has a mass of $60g$ [73].

Although the performance of the above gyroscope is impressive, NASA has signed a contract with Boeing for the developement of an even more impressive module. A silicon gyroscope named "mesogyro" which has already been tested as a prototype in mid 2002 and is due to have its first real demostration in mid 2004. The measured accuracy in the prototype evaluation phase was $0.1^o/3000sec$ or $0.0000333^o/sec$ [74]. This, of course, is the short term stability and in this work we do not assume the resolution is as low. As there is no more technical information about the gyro we assume that, with such a low error, the

output resolution and stability will result in a single point error of $0.001^o/sec$.

5.4.4 Sensors for Orbital location

Knowledge of orbital location is crucial for accuracy of the geomagnetic field model. The most suitable and accurate GPS system that has been identified is the SSTL Mitel Chipset with accuracy of better than 15 meters [69]. It has been used in SNAP nanosatellite.

5.5 Choice of Attitude Determination Methodology and Hardware

The sensors considered up to this point have been identified as the current and near future state of the art components that can form the attitude determination suite of a nanosatellite. Because the horizon sensors require attitude information in order to operate and this would impose constraints, we have decided to consider a nanosatellite attitude determination system based only on a gyroscope as the rate information source and a magnetometer as the only attitude sensor. Having identified the above components we decided to examine four possible attitude determination systems in order to investigate their feasibility and accuracy for attitude measurement. These are all the possible combinations of the two gyros and the two magnetometers identified.

The feasibility of a system with only a magnetometer as a 3 axis attitude sensor has been demonstrated both in theory and in practise. In 1992 Natason [75] showed how attitude can be estimated by a deterministic algorithm only from magnetometer measurements. This work was developed for SAMPEX satellite, a small explorer spacecraft [76]. The deterministic algorithm assumed knowledge of the angular velocity and it was the theoretical proof of how the derivative of the geomagnetic field can be used in order to identify the attitude of a spacecraft.

Under the condition that the angular velocity is not known, the algorithm cannot be used. Other researchers have tackled this problem before and after Natason. Psiaki et al. [77], used a Kalman filter with no angular velocity knowledge in order to identify the attitude of a spacecraft from magnetometer measurements. The same methodology had also been investigated for general single vector observations by Lefferts et al. [78]. Following the results from this research more and more researchers became interested in the use of single magnetometer data. An overview of the methods is given in by Landiech [79]. The

methodology of using Kalman filters with single magnetometers after this work became a standard procedure for coarse attitude determination as a back up for big satellites or as the main system for small satellites that cannot afford to carry high accuracy sensors.

Other researchers concentrated their work on the development of Kalman filters only for determination of the angular velocity. An overview of the methods is given by Bar-Itzhack [2]. The most sophisticated of the methods use a Kalman filter with a priori attitude estimate in order to be able to converge [80], [81], [82]. Oshman et al. [83] developed a methodology based on a Kalman filter which makes no assumption about the initial attitude and assumes that the geomagnetic field vector remains fixed between measurements. Consequently there is no need for evaluation of the geomagnetic field model is required.

All this work was mainly performed at the theoretical level. However recently these methods have been used onboard satellites, thus demonstrating their suitability.

These methodologies were applied when Oersted was launched. Oersted [3] used a star camera as the primary attitude sensor in order to be able to derive accurate measurements of the geomagnetic field. Additionally Oersted was equipped with a highly accurate magnetometer which had less than $0.5nT$ noise. Although equipped with a star camera, Oersted used, during various phases of the mission, an extended Kalman filter in conjunction with the accurate magnetometer in order to estimate its attitude. This was the first demonstration of the methodology. Soon after the SNAP nanosatellite was launched. Its attitude determination was dependent only a single magnetometer and an extended Kalman filter.

SNAP was the first nanosatellite [69] that performed attitude determination using only a single magnetometer. The magnetometer was used in conjunction with an extended Kalman filter. It was also the first nanosatellite that demonstrated 3-axis attitude control. Given the basic theory and the success of the methods in Oersted and SNAP, the use of a single magnetometery in conjunction with Kalman filters became a very favorable option for nanosatellites. The ION F mission comprising of 3 nanosats [84], DAWGSTAR (University of Washington), HOKIESAT (Virginia Polytechnic Institute) and USUSAT (Utah State University) have all considered the use of such a system for attitude determination. Additionally they have considered the use of miniature gyroscopes, the input of the solar cells for sun detection and finally the use of 4 CMOS cameras as star sensors used for rate estimation as an alternative to gyros. The magnetometer approach has been considered the most secure option. The extended Kalman filter [85] is very similar to the one used for Oersted mission. The accuracy requirements set by the 3 teams was $\pm 3^o$.

From the above review it was concluded that although the approach of using a Kalman filter, combined with a magnetometer has proved to be a good solution for using a low cost system, the accuracy offered by all the above methods cannot satisfy high pointing requirements. For example although Oersted had a highly accurate magnetometer onboard the satellite, achieved accuracies through this method were 0.9^o, 1.2^o and 3.1^o for the roll, yaw and pitch angles [3]. The rest of the applications had even lower accuracies as the magnetometers used had higher errors. This made their use for evaluation of the improvement offered by MEME unsuitable.

The high errors experienced in the above cases are large enough not to allow identification of the improvement in attitude determination that can be offered with the new models derived from the segmentation of the field and the use of the MEME dependent dynamic part. From the identified sensors suitable for a nanosatellite, the horizon sensor was disregarded as it has a narrow field of view and this would constraint the attitude determination capability when the satellite is rotating. So the only sensors that can actually be used are magnetometers and gyroscopes. From the existing sensors that have been identified, two magnetometers and two gyroscopes have been chosen.

The Billingsley TFM100S Magnetometer and the Polycon He^4 Magnetometers are two examples of sensors that can be used onboard a nanosatellite. The former when used in SNAP had an inaccuracy of $\pm 60nT$. The latter has been through the prototype testing phase, demonstrating an accuracy of $\pm 1nT$ in a full range of $10^5 nT$.

The two gyroscopes identified as suitable for a nanosatellite were the Systron Donner QRS-11 and the BSS Mesogyro. The first has a drift of $0.004^o/s$ plus the same resolution. Thus the accuracy of the system was taken as $0.01^o/sec$ for consistency. The second has been shown in the prototyping phase to have a extremely small drift and very high resolution. Thus here it has been assumed that the short term error is $0.001^o/s$. Of course here we have ignored the fact that the drift is accumulating. Instead we assume that the gyro is switched on and provides an instant measurement of the angular velocity and then is switched off in order to avoid accumulation of the error in time. By this method the effect of changing temperature can also be avoided which can cause significant drift. The Systron Donner QRS-11 gyro has a switch on time of less than 1 second. Start up errors of the gyros have been completely ignored. This is the only assumption that has been made and that indeed is unrealistic. This was ignored in order to be able to test the feasibility of identifying the attitude under the assumption that the angular velocity is known at the levels of the above

System	Magnetometer	No	Gyroscopes	No
A	Accurate	1	Accurate Gyroscope	3
B	Moderate	1	Accurate Gyroscope	3
C	Accurate	1	Moderate Gyroscope	3
D	Moderate	1	Moderate Gyroscope	3

Table 5.1: Different attitude determination systems with corresponding type and number of sensors

sensors. Indeed the system is not realistic unless the start up noise is precisely known. This noise can be eliminated through accurate calibration and the application of filtering techniques, such as extended Kalman filters, and here the start up noise is assumed negligible.

This study can be extended to the case of a single magnetometer used for attitude determination when the angular velocity is known within the error boundaries specified for the angular rate sensors by any other type of sensor employed. The useful insight in this method is not only the level of accuracy that can be achieved but also what the error reduction due to the use of the MEME dependent dynamic part of the geomagnetic field model would be. Under these assumptions the investigation was carried through based on a simple algorithm which evaluates the attitude by comparing the derivative of the measured geomagnetic field vector with that of the reference model. The technique is similar to the one used by Natanson [75]. The choice of the two different magnetometers and the two different gyroscopes is to allow investigation of the accuracy of all the possible combinations of these two groups of sensors. Here a further explanatory comment is required. Each magnetometer provides 3-axis information. Each gyroscope provides 1 axis information. So each considered attitude determination system will consist of 1 magnetometer and 3 gyroscopes in order the required amount of information for the spacecraft dynamics and mechanics to be acquired. So the four attitude determination systems under examination are shown in table 5.1.

5.6 Single Frame Attitude Measurement

One magnetometer measurement provides attitude information for the spacecraft axis parallel to the magnetic field vector but no attitude information is provided around this axis. In this arrangement, no attitude information is provided about the position of the three spacecraft axes about the measured vector. This means that if the spacecraft is rotated about the

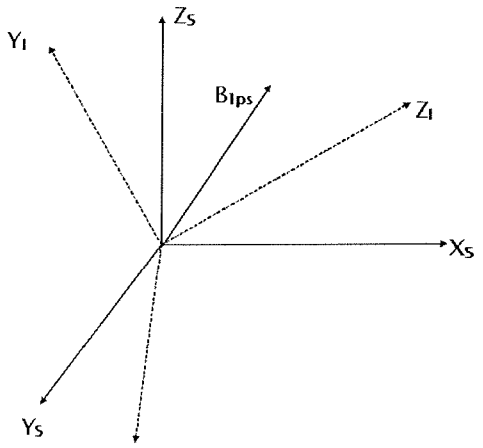

Figure 5.4: Magnetic field vector B, spacecraft coordinate system and inertial coordinate system at the time of measurement

field vector, the angles between it and the three axes will remain the same for any rotation.

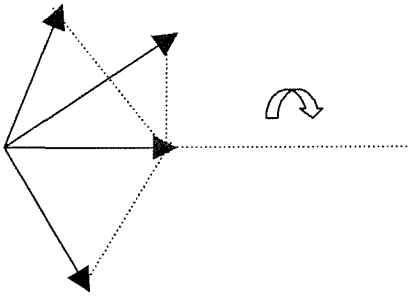

Figure 5.5: No information is provided around the vector of the model field

The transformation between the body and the reference frame is given by $AB_I = B_S S$. If we differentiate we get:

$$\frac{dB_S}{dt} = \frac{dA(t)}{dt} B_I(t) + A(t) \frac{dB_I(t)}{dt} \tag{5.75}$$

but

$$\frac{dA(t)}{dt} = -\omega(t) \times A(t) \tag{5.76}$$

and hence

$$\frac{dB_S}{dt} = -\omega(t) \times B_I + A(t) \frac{dB_I}{dt} \tag{5.77}$$

or

$$A(t) \frac{dB_I}{dt} = \frac{dB_S}{dt} + \omega(t) \times B_I \tag{5.78}$$

where ω is the angular velocity in the spacecraft coordinate frame. From (5.78), it can be seen that if the angular velocity ω is known, and the vectors $B, \dot{B}$ and $\dot{S}$ are known for a specific time point then the only unknown is the transformation matrix. Of course a solution cannot be evaluated as there are three equations with nine unknowns (A is a 3×3 matrix). However the solution can be found by one of the methods that solve the Wahba problem. These methods,i.e. the q method, use the two sets of vectors:

$$(B_I, B_S) \tag{5.79}$$

and

$$(\frac{dB_I}{dt}, \frac{dB_S}{dt} + \omega \times B_S) \tag{5.80}$$

At time t_1 a first measurement B_{S1} is taken by the spacecraft.Then at a later time a second measurement B_{S2} is taken. If the satellite has no angular velocity then the difference between the measured vectors in only due to the inertial rotation of the geomagnetic field in the time interval between the measurements. If the satellite has a rotational velocity then the difference vector includes this rotation. If the angular velocity is known then by integration of the Euler equation from time t_1 to time t_2 the initial measurement can be transformed. If we assume that the integration results in no error, then after the second measurement is taken, the difference vector is the real one. If we denote the transformed vector B_{1ps} (p stands for propagated) then at the time of the second measurement the configuration of the vectors is shown in Figure 5.6.

As seen, the spacecraft coordinate systems not aligned with the spacecraft coordinate system. Figure 5.7 shows the same situation as Figure 5.6 but from the perspective of the inertial coordinate system. Now if the vectors are represented on the same coordinate system, then we get what is presented in Figure 5.8. The transformation of the system of vectors from the spacecraft coordinate system to those of the inertial coordinate system is unique and provides the attitude of the spacecraft. In order to be able to solve the system both the derivative and at least one of the vectors is required. Then the vectors can be entered in any of the algorithms that solve the Wahba problem and obtain a solution. The fastest algorithms are FOAM, TRAD and QUEST [62] and [63]. We have chosen the q method presented earlier due to the simplicity in obtaining a solution for the eigeanvalue problem through MATLAB.

This method of attitude determination requires the following assumptions.

- The angular acceleration and velocity are known to very high accuracy.

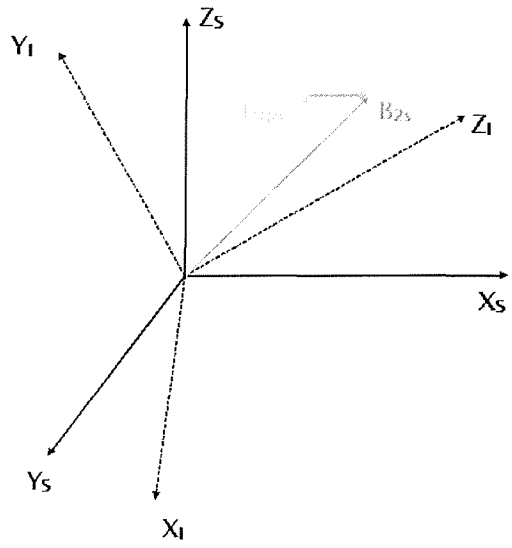

Figure 5.6: Time t_2 - Tranfsormed initial measurement and new measurement in spacecraft coordinates

- The difference vector of the field model is very accurate.

In fact, however, these assumptions are very unrealistic in the case when we are using magnetometer measurements. As a result, there is a very high chance that the following errors will occur.

- Even if the satellite has no rotational velocity and the attitude remains fixed between two measurements, the measured difference vector may be different from its expected value (computed from the model). This error is due to the inaccuracy of the model.
- When the first measurement is propagated through time between measurements using the opposite rotational velocity, an error in the velocity will cause an error in the co-ordinate position of the transformed vector.

The investigation of these errors is now examined in simulation by considering 2 magnetometers of different accuracy and two magnetometers of different accuracy. The fact that the derivatives of the geomagnetic field are used for the determination of attitude makes the system very sensitive to error. This is due to the fact that the geomagnetic field of the earth rotates inertially with a specific rate. This has a maximum value of roughly $0.12/sec$.

Figure 5.9 shows the derivatives of each of the field components and of the magnitude. The shape of the error is more obvious in Figure 5.10 (a) where it can be seen that the error

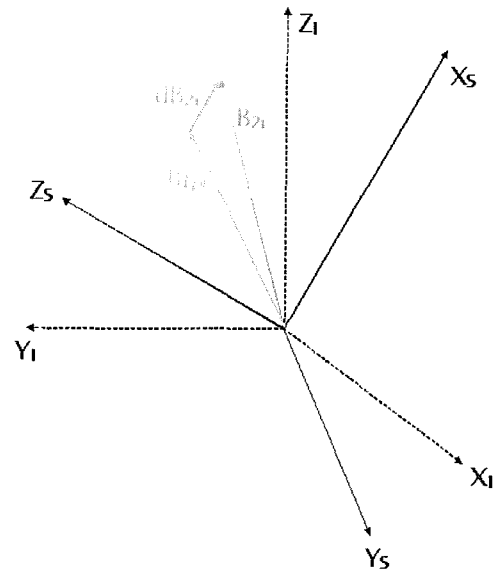

Figure 5.7: Time t_2 - Tranfsormed initial measurement and new measurement in inertial coordinates

is maximum close to the equator and is slightly higher than $0.2^o/sec$ if the method were used on the same orbit as Oersted. The error shows no strong dependency on longitude. Figure 5.11 shows a 3D view of the error dependency on longitude and latitude.

From Figure 5.11 we can draw the conclusion that for small angles the derivative of the field is small enough to be highly corrupted by noise. This sensitivity factor the will be investigated in the following chapter. The strategy for the testing this method of attitude determination is also given in the next chapter. In what follows next, a conceptual nanosatellite design is developed and the expected disturbances are evaluated.

5.7 Specification of an abstract nanosatellite structure

In order to be able to develop a basis for the investigation the following nanosatellite abstract design was constructed as a first approach.

The mass of the structure is 10 kilograms. The boom is included as a standard option for eliminating the magnetic interference of the spacecraft ambient dipole on the magnetometer. This is standard policy when magnetometers are included in a mission.

The boom considered here is the so called "Astrid-2" type of boom, used for the Astrid -2 mission, Lunarsat and SMART-1 missions [86]. A portion of two meters length of such a

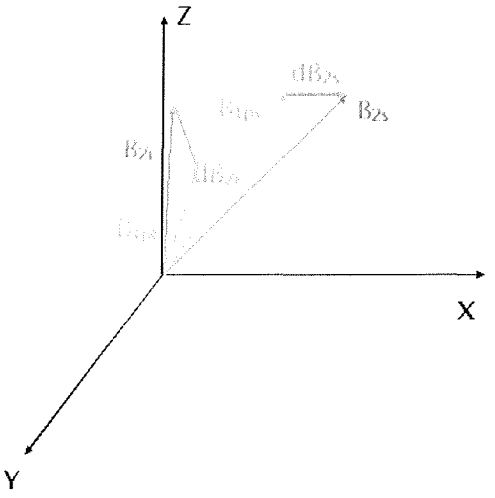

Figure 5.8: Time t_2 - Tranfsormed initial measurement and new measurement in inertial coordinates

boom weights less than 300 grams. On the outer tip of the boom is located the magnetometer. The axes of the boom are assumed parallel to spacecraft axes but not coinciding. The boom is displaced on the Z positive axis by half the height from the center of mass which coincides with the origin of the body coordinate system. The magnetometer is assumed to be a small cylinder of height $h = 6cm$, and radius $r = 3cm$ located on the outer tip of the boom. In all cases it has been assumed that the mass distribution is uniform.

The calculation of the moments of inertia is a simple process. The moment of inertia of the main body, the boom and the magnetometer were evaluated separately and by the parallel axis theorem [87] they were all added to give the final value. As expected, the moments of inertia of the X and Y axes were the same due to the symmetry of the cylindrical structure.

Two matrices of moments of inertia were calculated. One with the high precision magnetometer and the second with the low precision magnetometer. The calculated matrices were:

$$Ih = \left[\begin{pmatrix} 2.170415 & 0 & 0 \\ 0 & 2.170415 & 0 \\ 0 & 0 & 0.31265 \end{pmatrix} \right] \tag{5.81}$$

$$Il = \left[\begin{pmatrix} 1.202248925 & 0 & 0 \\ 0 & 1.20224892500000 & 0 \\ 0 & 0 & 0.31256765000000 \end{pmatrix}\right] \tag{5.82}$$

In reality, the moments of inertia of the X and Y axes will not be identical. in particular assuming identical moments of inertia also simplifies the behavior of the spacecraft. To avoid such a simplification the moments of inertia were scaled; the moment of inertia of the X axis of the main body was multiplied by 1.2 and the moment of inertia of the Y axis of the main body was multiplied by 0.8. The moments of inertia of the magnetometers and the boom were not altered. This was due to the fact that the boom has indeed a uniformly distributed mass and the magnetometer size is small relative to its distance from the center of mass of the main body.

The resulting moments of inertia were calculated as:

$$Ih = \left[\begin{pmatrix} 2.261665 & 0 & 0 \\ 0 & 2.079165 & 0 \\ 0 & 0 & 0.31265 \end{pmatrix}\right] \tag{5.83}$$

$$Il = \left[\begin{pmatrix} 1.293498925 & 0 & 0 \\ 0 & 1.110998925 & 0 \\ 0 & 0 & 0.31256765 \end{pmatrix}\right] \tag{5.84}$$

These two moments of inertia matrices were used as the basis for the following investigation of an attitude determination system. Based on them, and the dimensions of the spacecraft the disturbance torques were evaluated.

5.8 Sources of Disturbance and Sources of Error for AD Systems based on Magnetometers

Due to the importance of angular velocity accuracy in the determination of attitude, a good estimation of the expected disturbance torques should be obtained. In order to do so the theoretical disturbance models were evaluated for the mass and the size of the given design. The simulation of the orbit was performed through the use of the Oersted data files and the kinematic and dynamic equations of spacecraft motion. The Oersted data files provide, except for the magnetic field measurements, the corresponding spherical coordinates. The

spacecraft was simulated as if it had exactly the same orbit as Oersted. The reason for this is that the evaluation of the attitude determination will be performed through the measurements of Oersted and consequently it is good practice to consider exactly the same orbit.

5.8.1 Environmental Disturbance Torques

5.8.1.1 Atmospheric Disturbance Torque

The first parameter to be estimated is the aerodynamic drag. In order to do so, a simulation model was constructed for investigation. The satellite dynamics were simulated by the Euler equations with noise added. The satellite structure was divided into three parts; main body, boom and magnetometer. Due to the cylindrical shape of the satellite, the boom, and the assumed magnetometer, the side and top surfaces were treated differently. The side surface was divided into 6 parts in height and 10 parts in azimuth from the center of mass. This resulted in 60 tiles for the side surface of the main body. The top and bottom surfaces were divided into 3 radial sections and in 10 sections in azimuth. This gave 30 tiles for each of the top and the bottom surfaces.

The boom was divided into 10 parts in height and into 10 parts in azimuth, resulting in 100 tiles. The bottom and top surfaces, of course, were not included as they do not interact with the atmosphere. The magnetometer, treated as a cylinder itself, was divided into 10 parts in azimuth and 2 parts in height due to its low dimensions. For each tile, the distance vector from the center of mass was calculated and also the unit vector normal to the surface. All the vectors were stored as the columns of matrices and a corresponding matrix were stored all the area values for the tiles. The density of the atmosphere was evaluated from the geocentric distance according to the values given in Wertz [25]. The values were interpolated by a linear function in the logarithmic dimension for altitudes from 400 to 1000 kilometers.

The simulation was performed using data from Oersted. For each measurement in the data file the orbital velocity vector was calculated as the time derivative of the geocentric location vector of the satellite described by spherical coordinates. The values were stored in a corresponding matrix.

The simulation for identification of the aerodynamic drag was performed with zero angular velocity. The attitude of the satellite was set parallel to the inertial coordinate system. As the satellite progressed in orbit, the matrices of the unit vectors, the distance vectors from

the center of mass, and the unit vectors and the orbital velocity vectors were transformed by the opposite of the rotational velocity. In the case when the rotational velocity is zero the transformation did not result, of course, in any change. The philosophy of this transformation is that if the satellite attitude does not change then these vectors would be encountered in the given position. The difference in the observation is only due to the rotation of the satellite and is equal to the transformation with the opposite angular velocity. Figures 5.13 to 5.15 show the resulting disturbance torque, the resulting disturbance in angular velocity and the altitude of the satellite respectively.

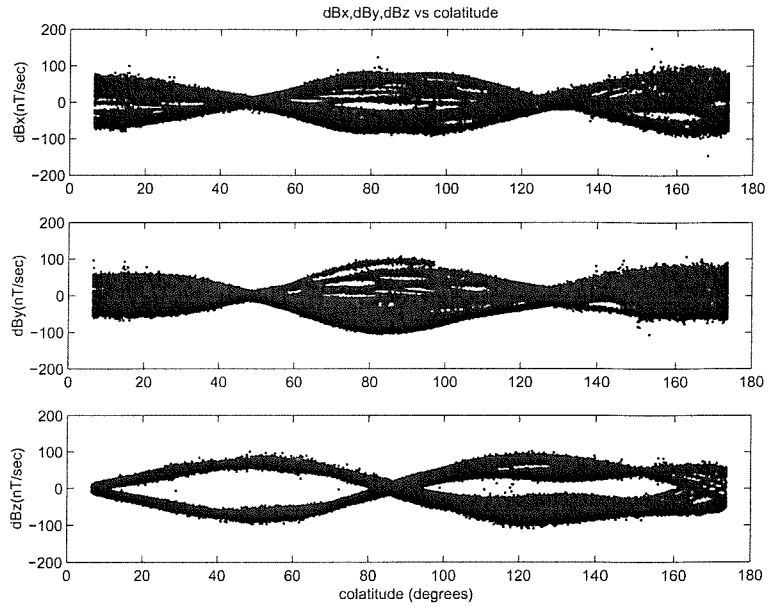

(a) Geomagnetic field vector components

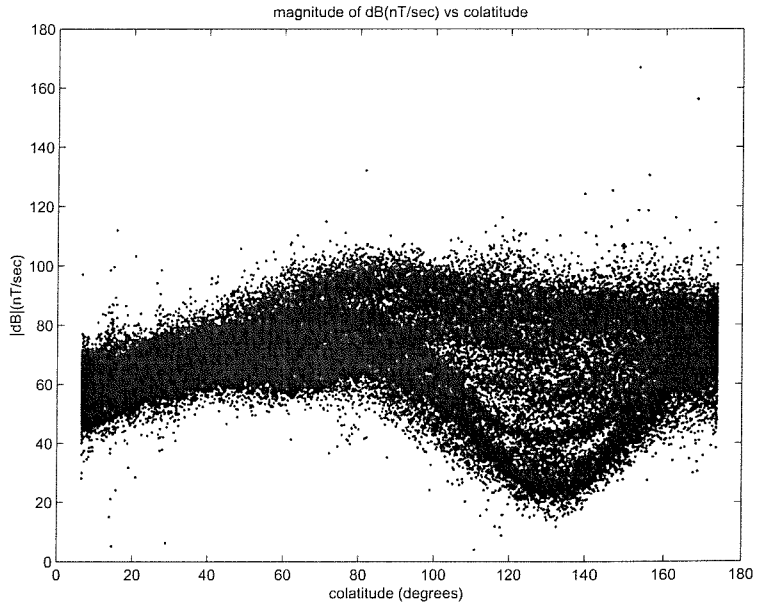

(b) Geomagnetic field vector magnitude

Figure 5.9: Derivative of geomagnetic field (a) Vector components (b) Vector magnitude vs colatitude

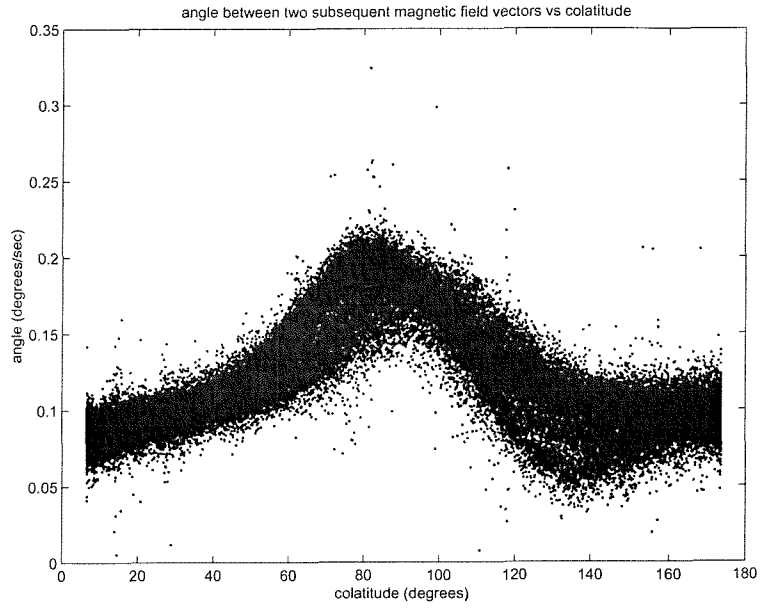

(a) Colatitude

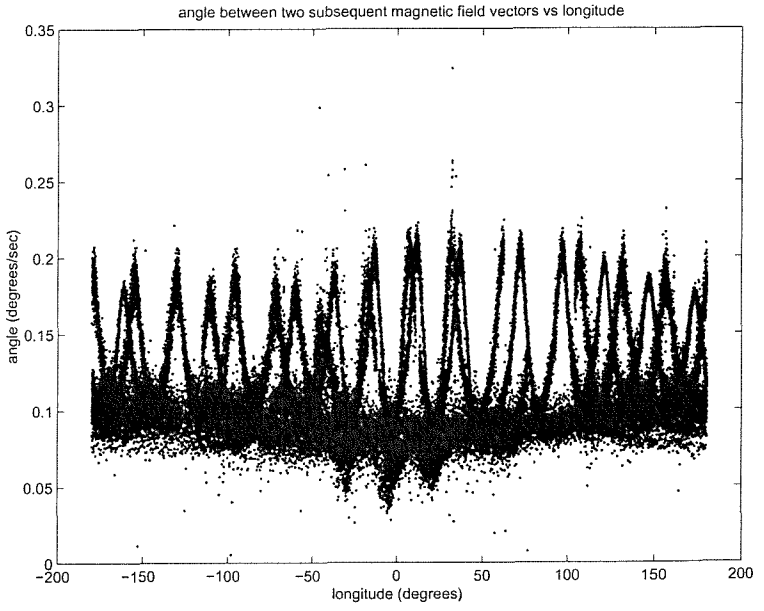

(b) Longitude

Figure 5.10: Angle between too subsequent measurements vs (a) Colatitude (b) Longitude

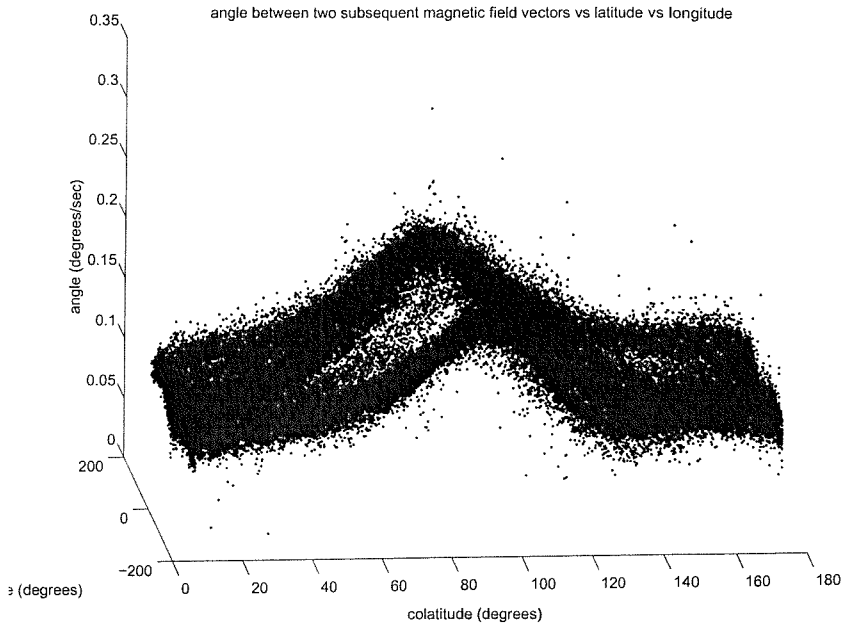

(a)

Figure 5.11: Angle between too subsequent measurements vs colatitude vs longitude

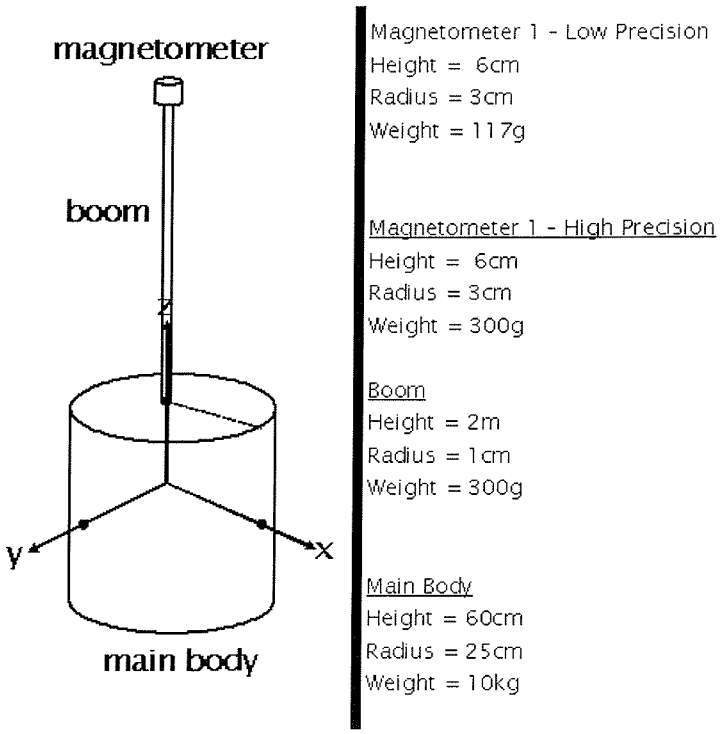

Figure 5.12: Nanosatellite coarse design

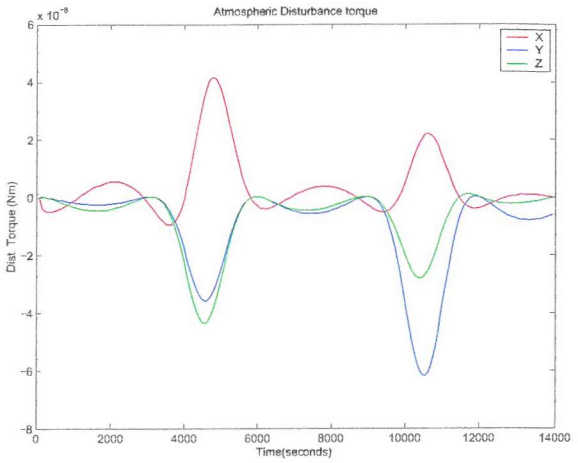

Figure 5.13: Aerodynamic disturbance dorque in spacecraft axes

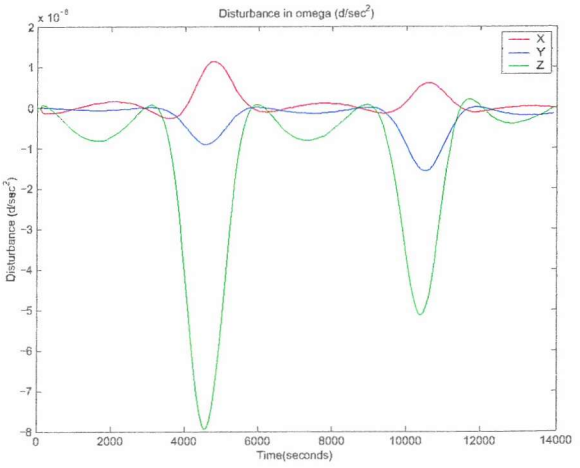

Figure 5.14: Angular velocity disturbance due to atmosperic disturbance torques in spacecraft axes

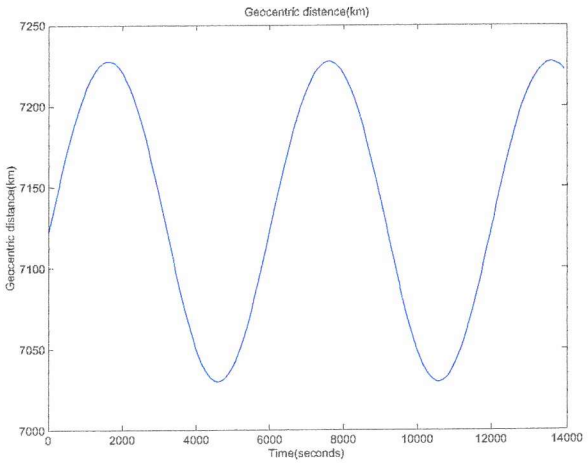

Figure 5.15: Altitude of satellite during evaluation of atmospheric disturbance

The order of magnitude of the disturbance is $10^{-9}Nm$. This was expected as in the simulation phase of Oersted the order of the aerodynamic drag was $10^{6} - 10^{-7}Nm$ [3]. According to Wertz [25] the drag is proportional to the difference between the moments of inertia of axis x and axis z. The difference in Oersted was roughly 200, while here it is roughly 2. This gives a factor of reduction 10^{-2} which shows up in the simulation. The periodicity of the drag is clear. Also the inequality in peak amplitude results from the difference in altitude and thus in the atmospheric density. The drag force is very small. Finally the overall error expected to be encountered is very small.

5.8.1.2 Gravity Gradient

The gravity gradient disturbance was also evaluated. The moment of inertia for the case of the heavier magnetometer was used as the resulting disturbance is expected to be higher. The unit vector from the center of mass to the center of the inertial coordinate system was evaluated for each orbital position. The angular velocity was set to 0 for all positions and the satellite was assumed to have attitude parallel with the inertial coordinate axes. Figure 5.16 shows the gravity gradient disturbance torque and Figure 5.17 the resulting disturbance in the angular velocity. The gravity gradient torque is greater than the aerodynamic disturbance torque. This is also due to inclusion of a boom in the structure. The level of disturbance on the angular velocity is of order $10^{-5}degrees/sec$. This can cause large deviations only in large time intervals and in order to keep the dynamics model simple, the gravity gradient was not included in the model of the spacecraft dynamics but was added as external noise.

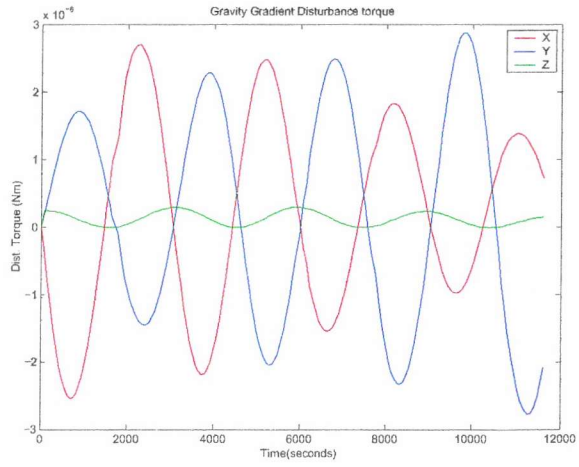

Figure 5.16: Gravity gradient disturbance torque in spacecraft axes

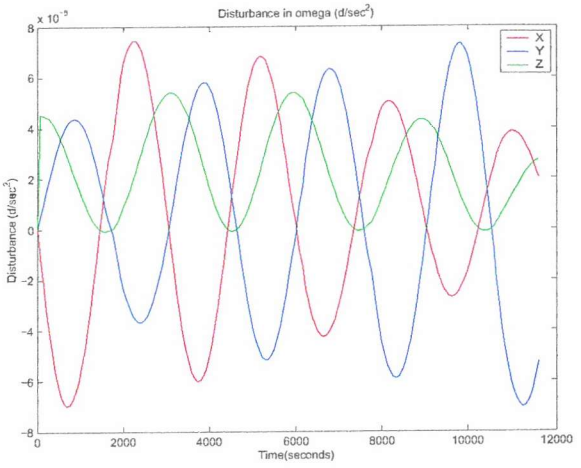

Figure 5.17: angular velocity disturbance due to gravity gradient torques in spacecraft axes

5.8.2 Magnetic Cleanliness

When a magnetometer is used onboard a satellite for accurate field measurements, it is very important to eliminate the interference from magnetic fields created within the electric circuits or the magnetic components in the spacecraft. It is thus important to design flight subsystems with low residual dipole magnetic fields to maintain the spacecrafts total static and dynamic magnetic fields within scientific requirements. Such a practice provides a magnetically clean spacecraft, which increases the quality and accuracy of magnetic field data gathered during the mission.

When the magnetometer is placed on a boom away from the spacecraft, the dipolar portion of a spacecrafts magnetic field at its magnetometer experiment sensor location dominates the nondipolar part. Each spacecraft subsystem is assigned a maximum allowable dipole magnetic field specification based on the magnetometer sensor sensitivity and the distance between the bulk of the subsystems and the sensor location. According to the NASA magnetic cleanliness certification program [88], a typical maximum dipolar field allocation is 10 nanoTeslas (gammas) at a distance of 1 meter from the geometric center of a spacecrafts subsystem, assuming the magnetometer sensor is mounted at the end of an 8-meter boom. To ensure that each subsystem meets its respective dipole field specification, several design practices are observed during the early stages of the subsystem design. These practices include the following:

5.8.2.1 Magnetic Shielding of Magnetic Components

A magnetic source can be enclosed in a high permeability material shield, which in effect confines the sources magnetic flux to within the walls of the shield enclosure. The shield should be completely enveloping, with the minimum number of holes and cutouts. The shield must be annealed after all machining and forming operations are completed. A general rule of thumb is to design the shield to operate within the linear range of the permeability curve.

5.8.2.2 Compensation of Magnetic Components

A magnetic component can be neutralized by placing on or near its surface an equal but opposite field vector using compensation magnets or current loops.

5.8.2.3 Redesign of Circuit Board Current Paths to Reduce Loop Area Coverage

Since a magnetic field B is proportional to loop area geometry A, the number of loop turns N, and the current flow I through a circuit, a reduction in A produces a reduction in the magnetic field B, whilst leaving I and N invariant.

$$B \propto NIA \tag{5.85}$$

5.8.2.4 Replacement of Ferromagnetic Parts with Nonmagnetic Parts

Another method for reducing magnetic fields is by simply replacing ferrous materials with nonmagnetic materials, preferably with relative permeability μ_r of approximately 1 so that the magnetic susceptibility χ_m is kept at approximately zero.

$$B = \mu H \tag{5.86}$$

where $\mu = \mu_0 \mu_r$, $\mu_r = 1 + cm$, and μ_0 is the permeability of a vacuum.

Based on the above techniques the desired magnetic cleanliness requirements can be achieved. A spacecrafts total allowable magnetic field at the magnetometer sensor location r is usually determined by the sensors sensitivity level or by an agreed upon science requirement. The total field can be approximated by a number of dipoles N, with N representing all of the spacecraft subsystems. To guarantee that the spacecrafts total magnetic field at r is within the desired allowable range, the individual moments due to N dipole sources must be kept to within predetermined dipole moment specifications. The magnitude of the spacecrafts dipole magnetic moment is approximated by the Pythagorean sum of these individual subsystem dipole moments, with the radial part tending to be greater than either of the transverse components for the dipole portion. The individual magnetic dipole field allocation, therefore, is determined from this model by the following equations:

$$[B^2_{R,dipole}]^{\frac{1}{2}} = \left[4 \sum_{j=1}^{N} \frac{M_j^2}{3r^6}\right]^{\frac{1}{2}} \tag{5.87}$$

$$\left[(B^2_{\Phi} + B^2_{\Theta})_{dipole}\right]^{\frac{1}{2}} = \left[2 \sum_{j=1}^{N} \frac{M_j^2}{3r^6}\right]^{\frac{1}{2}} \tag{5.88}$$

where B_R, B_Φ, and B_Θ are the field components of the spacecrafts magnetometer experiment sensor sensitivity or the scientific requirement levels at location r. Thus, M_j can be determined for each of the N spacecraft sources, assuming that M_j is the same for all j and the magnetic moments determining the far field are linear functions of the vectors M_j. Because the dipolar portion of the spacecraft magnetic field dominates the nondipolar part and the spacecraft is dominated by the few largest sources, the general field allocation, B_s, for a subsystem at a normalized distance of R meters is thus derived from M_j as follows:

$$B_s = \frac{2M_j}{R^3} \tag{5.89}$$

By ensuring that the dipole moment specifications of all spacecraft subsystems, as represented by the number N of dipolar sources, are within their respective allocated dipole moment specifications, the overall spacecraft magnetic field at the magnetometer sensor location can be kept to within its scientific requirement or below the magnetometers sensitivity level.

Using this methodology we adopt the typical requirement that the spacecraft ambient dipole should be $10nT$ at a distance of 1 meter from the geometric center of the spacecraft. We assume that the above techniques ensure that this requirement is fulfilled. If we approximate the spacecraft magnetic moment by a single dipole located at the geometric center then from the last equation we get that the ambient spacecraft dipole moment is:

$$M = 5nT/m^3 \tag{5.90}$$

Using this magnetic moment we see that if the magnetoometer was placed on the top facet of the satellite and not on a boom then the corresponding disturbance would be approximately 37 nT which a significant error. By placing the magnetometer 2 meters away from the geometric center the disturbance is $0.8219nT$. This value is below 1nT and is considered acceptable especially for the case of attitude determination. Instead of using the value of $0.8219nT$ in the rest of the work we use an ambient field disturbance of 1 nT.

5.8.3 Errors due to the use of the boom

The presence of the boom in the spacecraft design introduces additional sources of error for the attitude determination system. There are three main sources of error. The first one is the natural frequency of the boom, which can cause vibrations of the boom. The second is the uncertainty in the knowledge of the exact transformation matrix between the two ends of the boom. This means that the magnetometer coordinate system cannot be translated accurately

to the body coordinate system. The third is the variation of the structure characteristics based on the thermal properties of the materials used. For example when a satellite in its orbit passes from sunlight to eclipse, the drop in the temperature causes the material to stress and this changes the geometric properties of the structure. Each source of error is of a different nature but as far as attitude determination is concerned, their effect is observed as error in the moments of inertia for each axis. The boom considered here is 2 meters long which is a relatively small value (higher stiffness) and is constructed by carbon fiber composites which have a very high stiffness and very small elasticity. Details of the behavior of synthetic materials with temperature can be found in [89] and [90]. Here in order to incorporate the effect of the uncertainty in the moments of inertia due to these sources of error, we have chosen to introduce a 1% error in each element of the matrix of the moments of inertia by adding 1% of each current value for each element.

The effect in the error of the rotational velocity was evaluated for different angular velocities. The results are plotted in Figure 5.18 and confirm that such an error would

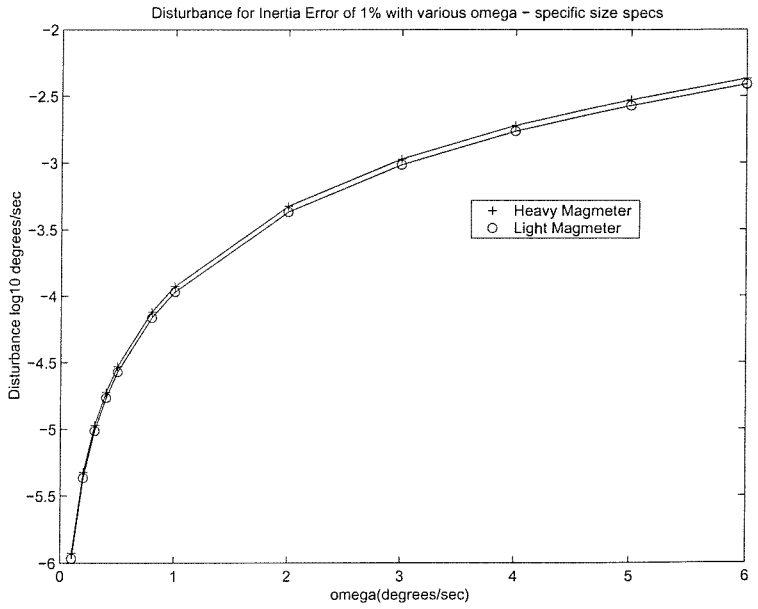

Figure 5.18: Inertia error disturbance with angular velocity for specific mass and dimensions

indeed result in a significant error above $1^o/sec$ when compared to the accuracy of the most accurate gyroscope considered. This showed that in the presence of uncertainty in the moment of inertia the error is indeed significant if large time intervals are used and if large angular rates are experienced. This indicates the range of correct operation for the system

if such an uncertainty exists.

Chapter 6

Testing and Results for Attitude Determination

6.1 Testing Strategy

Four different combinations of hardware were investigated in the first stage of testing. As seen in the previous chapter, two gyroscope and 2 magnetometers were selected with different accuracies. All the possible combinations of them formed the 4 different configurations.

All the 4 possible AD hardware configurations have been tested and errors for various sampling rates, various angular velocities, and in different segments investigated. This is performed first with Oersted data from data quiet days. Then the two subsystems with the accurate magnetometers are investigated for a set of magnetically disturbed days with and without the use of MEME.

Here we must note that the attitude has been identified through the q-method for simplicity and thus it is represented in quaternion form. In order to represent the attitude in a physically trackable way, another attitude error representation has been chosen. Although the most popular of such methods is representation by Euler angles, another non conventional measure has been chosen in order to give a better insight into the inaccuracy of the method.

The error in orientation has been characterized according to the direct angles between the inertial coordinate system axes and the corresponding axes of the spacecraft after the attitude has been measured, and a transformation by the corresponding matrix should ideally bring each spacecraft axis on the according inertial axis. The reason for the choice of such a measure is that it offers an indication of the cone of error for each axis and thus offers an

overall view of the uncertainty in the orientation of the satellite which is shown in Figure 6.1. Although such a measure cannot be used in satellite work, it is very useful in determining how accurately the attitude has been measured. The three error angles F_x, F_y, F_z characterize the cones within which the inertial axis are located. For accurate attitude determination the cones should have a small angle.

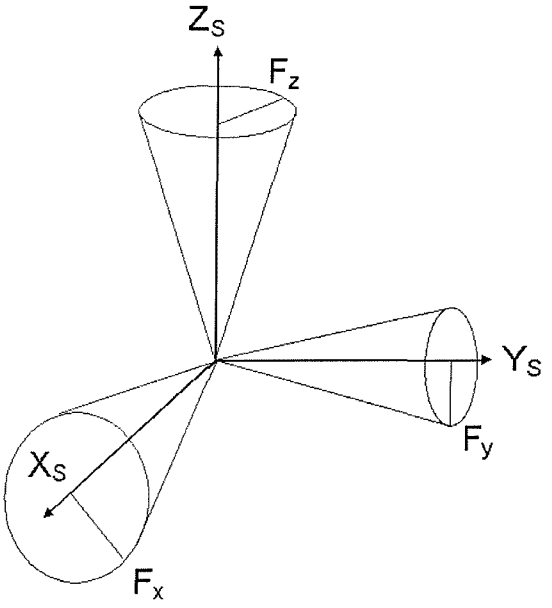

Figure 6.1: Attitude error representation by angles F_x,F_y,F_z

In this form of representation of the attitude error, it must be noted that the angles F_i are always positive and thus the error cannot be considered as having a Gaussian distribution. In a similar way to the results from the Geomagnetic field modelling, the mean error and the 95% percentile are used, which here characterizes the cone for each axis within which the corresponding inertial axis lies for 95% of the time.

The spacecraft dynamics and kinematics were simulated. At time zero, the angular velocities for the tests were entered into the Jacobi equation and the resulting actual angular velocities were computed at this point. Then they were propagated with the addition of the disturbance torques in time. The satellite at time zero was considered to be in parallel to the inertial frame and at each step its attitude was propagated with the angular velocities. The entire pool of data for the time span of the simulation was rotated at each instance with the opposite rotational velocities. This was done in order to transform the measurements to the body coordinate system at each point. The simulation was performed in Simulink.

At each time instance, the satellite was assumed to know its angular velocity with the hardware inaccuracy introduced. The measured magnetic field vector was then propagated through integration of the Euler equation to the next sampling instance were the attitude was evaluated. After the attitude was calculated the spacecraft coordinate system was transformed and the F_i angles were evaluated directly by the cosine rule. This created the pool of data. The environmental disturbance torques were calculated as described in the previous chapter and added at each step.

All the experiments were performed without any control torque in the dynamics equations. This was in order to simplify the testing methodology and concentrate only on attitude determination under natural rotations. In each experiment the initial input angular velocities in the Jacobi equations for the different axes are equal. This was in order to simulate the most complex of the situations. In what follows, if the rotational velocity is mentioned, this means that the same value was entered in Jacobi equation at the initial step of the simulation.

Having clarified these issues, we now describe the experiments and the results obtained.

6.2 Experiment 1. Attitude determination - Quiet Days - Accurate Magnetometer - Accurate gyro

This is the first experiment for validation of the single point attitude determination method. This test was performed for a magnetically quiet day. The data used for the verification was chosen for magnetically quiet days (not included in the derivation of the model) from the Oersted data files. This was to enable the performance to be investigated without the use of MEME. Later the performance is examined with the use of MEME and without it for a set of days of variable magnetic activity. Due to the high sensitivity of the algorithm in terms of the angular velocity knowledge as well as the accuracy of the magnetic field measurement, the test was performed for all different possible configurations of the attitude determination hardware. Here we present the case when the high accuracy gyro and the high accuracy magnetometer are used.

The attitude error is described by three angles F_x, F_y, F_z. These are the direct angles of deviation of the inertial frame from the body frame when the body coordinate system has been transformed with the evaluated quaternion to the ideally expected position, in parallel to the inertial coordinate system. This representation shows directly the deviation of the

axes of the spacecraft from the real attitude.

The first stage of the investigation was the evaluation of its performance for a fixed angular velocity and for different sampling rates. The high accuracy miniature gyro was used with an accuracy in the measurement of $0.001^o/sec$. This value could also represent rate information from any other source with this specific accuracy. Additionally the high accuracy magnetometer was used with an error of $1nT$ plus $1nT$ error from the spacecraft dipole. This configuration represents the best possible attitude determination components and this system is expected to offer the highest accuracy among all the other combinations of attitude determination components considered.

The satellite was simulated for the entire day using the Oersted data with an angular velocity of $0.5^o/sec$ in each axis. The gravity gradient and the atmospheric drag were calculated from the theoretical models and added as noise at each step of the simulation. The accuracy of the angular velocity knowledge is assumed to be $\pm 0.001^o/sec$ and is provided by the miniature gyro. Although this assumption is not realistic as the gyro will deviate for such a long time interval of operation, it was accepted in order to obtain an overall view of the single point measurement. In reality the gyro will drift and resetting will be required to regain this high accuracy.

Three main tests were performed. The first was the investigation of the mean and 95% percentile of the attitude error. The second was the evaluation of the error for different angular velocities for a fixed sampling rate. The third was the evaluation of the performance in each segment, as detailed in Chapter 2, for a fixed angular velocity and sampling frequency.

Figure 6.2 shows the effect of using different sampling rates, where for small sampling times, the attitude error is extremely high. This is to be expected, as the difference vector between subsequent measurements is of comparable size with the difference vectors due to the error in angular velocity measurement, the error due to the application of disturbance torques in between sampling instances, and, of course, due to the error of the geomagnetic field model. As the sampling time increases, the mean error decreases and at high sampling times it falls below 0.2^o, close to the region of $0.13^o/sec$. This is a very satisfactory mean error of attitude. In Figure 6.3 we see that the attitude 95% percentile follows exactly the same trend. It converges for higher sampling rates to value just above 0.2^o. This is also a satisfactory high error value. The error in most cases lies within these boundaries when the corresponding accuracy in magnetic and angular velocity measurements is achieved.

The next test was the evaluation of the error for different angular velocities with a fixed

rate of 15 samples, which has a low mean and percentile value and was small enough to have immunity against change in the angular velocity by disturbance torques.

The results are shown in Figures 6.4 and 6.5. The mean attitude error remains low in all cases. It increases for angular velocities higher than $1^o/sec$ but the maximum mean error is 0.4^o. This is a very satisfactory result and shows that the algorithm operates successfully in all ranges with the considered accurate hardware. The 95% percentile follows the same trend and up to velocities of $1^o/sec$ the boundary is identified as below 0.25^o. This value is very low. At higher angular velocities the error increases to 0.6^o maximum. The fact that higher angular velocities show higher error is due to the propagation of the magnetic field vector with the rotational velocity causing higher error due the error in the integration process. A step of 0.01 sec was used for the integration and no smaller step was considered since the computational requirements would increase dramatically. The results for velocities up to $1^o/sec$ create confidence about the suitability of the system for accurate attitude determination. Nominal satellite angular rates are below this value, especially when no control is applied. If a control system was applied and the rotational velocity was known to the accuracy provided by the gyro considered here, then attitude determination could take place with high accuracy for up to $1^o/sec$.

The third test was the examination of errors in different segments. The velocity was kept at $0.5^o/sec$ and the sampling rate at 15 sec. The errors were divided into categories according to the latitude of the measurement provided by the Oersted data files. The statistics for such measurements are shown in Figures 6.6 and 6.7. The mean error is smallest in segment 2. This is an interesting result as in Chapter 3, it was seen in the development and testing of the geomagnetic field model that the segment where the mean angle error of the model vector is smaller is number 3. This was confirmation that the dominant source of error for these highly accurate sensors and for velocities below $1^o/sec$ is the error of the geomagnetic field model. As the derivative of the geomagnetic field is used, it is normal that the mean error is located at a value around 0.1^o as the error increases through this process. Also additional error is due to the atmospheric drag and the gravity gradient disturbance on the spacecraft dynamics.

The 95% percentile shows the same behavior and the for segments 1, 2 and 3 remains low. Segment 6 shows the worst performance with a percentile value of 1.5^o.

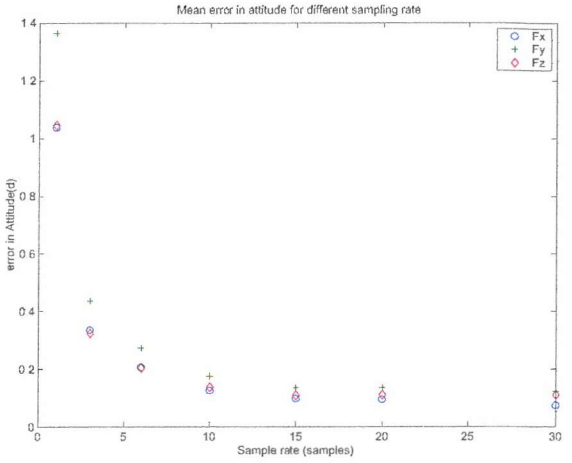

Figure 6.2: Mean attitude error vs sampling rate for $\omega = 0.5^o/sec$ with high accuracy magnetometer and high accuracy gyroscope

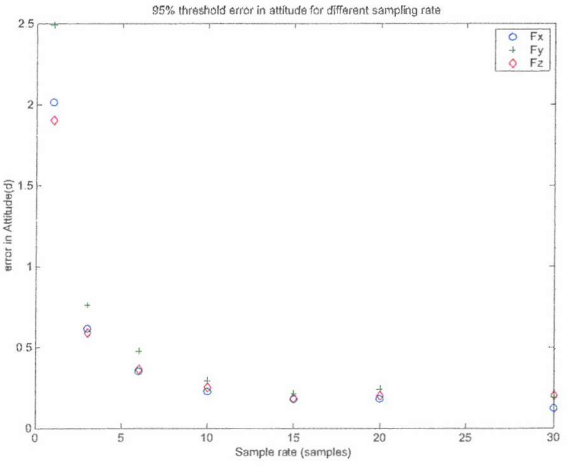

Figure 6.3: 95% Threshold attitude error vs sampling rate for $\omega = 0.5^o/sec$ with high accuracy magnetometer and high accuracy gyroscope

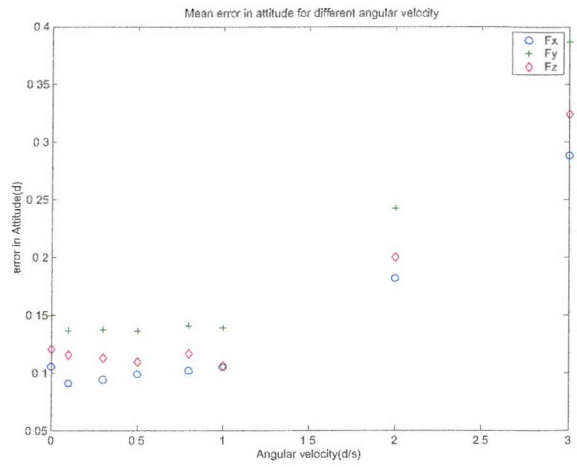

Figure 6.4: Mean attitude error vs Angular Velocity for sampling rate: 15 Oersted data samples (aprox. 16 seconds) with high accuracy magnetometer and high accuracy gyroscope

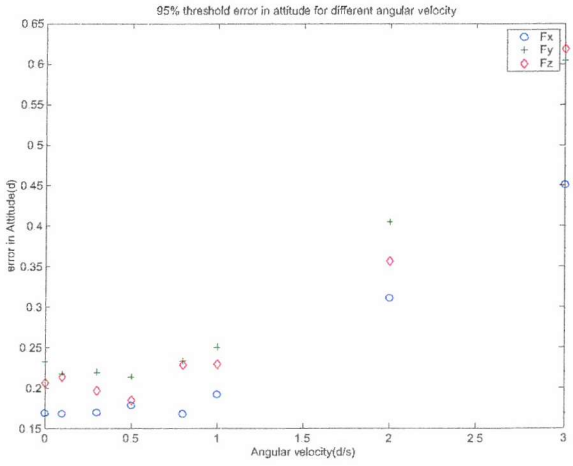

Figure 6.5: 95% Threshold attitude error vs angular velocity for sampling rate: 15 Oersted data samples (aprox. 16 seconds) with high accuracy magnetometer and high accuracy gyroscope

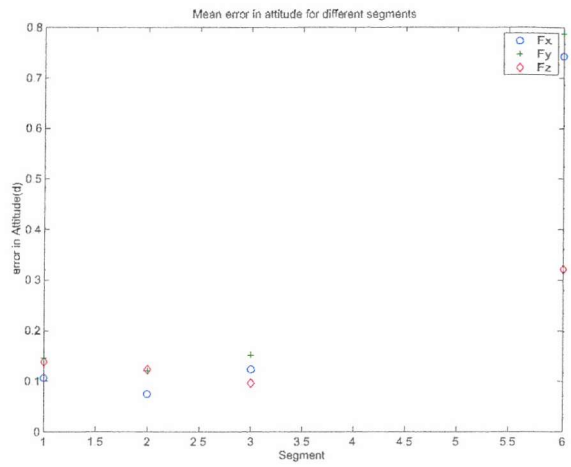

Figure 6.6: Mean attitude rrror for different segments for $\omega = 0.5^o/sec$ and sampling rate: 15 Oersted data samples (aprox. 16 seconds) with high accuracy magnetometer and high accuracy gyroscope

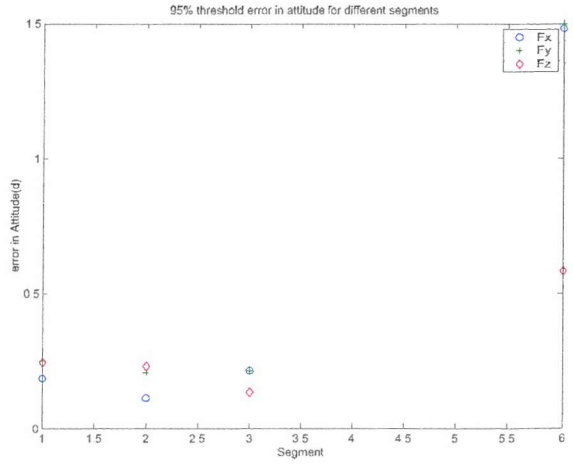

Figure 6.7: 95% Threshold attitude error for different segments for $\omega = 0.5^o/sec$ and sampling rate: 15 Oersted data samples (aprox. 16 seconds) with high accuracy magnetometer and high accuracy gyroscope

6.3 Experiment 2. Attitude determination - Quiet days - Accurate Magnetometer - Moderate Gyro.

Exactly the same methodology was followed as in the previous experiment with the difference that here the gyroscope used was the one with low accuracy. This was done in order to identify separately the effect of inaccurate angular velocity measurement.

Figure 6.8 shows the attitude error with sampling time. Here is seen that the behavior of the mean error has been altered. Indeed there is a high error for low sampling rate but for the rest of the values the error is very comparable. This is due to the fact that the error from the inaccuracy of the gyroscope has been introduced and consequently the errors for optimal sampling rates have also been raised. Another main difference here is that the attitude error appears much higher. The reason for this higher error is of course the error in the propagated angular velocity which is calculated in steps through numerical integration of the Euler equation. Hence if the initial conditions are in error then the values at each step and the final integrated value will be in error and this error will be summed at the end of the propagation procedure.

These values are also used to propagate the measured geomagnetic field vector, and thus the final transformed vector will also contain the error due to the inaccuracy in the angular velocity. The inaccuracy of the gyroscope here has been taken as $0.01^o/sec$ and the resulting mean error for sampling rates between 3 and higher are between 0.6^o to 1^o . This error is significant although the attitude is still consistent and in the neighborhood of the real one. Figure 6.9 shows the percentile of attitude error below 0.1^o. Its shape with sampling rate has been altered in a similar way to the mean, compared to the previous case with the accurate gyroscope. Again it is much higher in value for all cases and now the error for sampling rates higher than 3 are between 1^o and 2^o.

The next test was the evaluation for various angular velocities with a sampling rate of 15. Figure 6.10 shows that the error has increased for all angular rates and its mean value lies between 0.6^o and 1^o. Additionally the percentile value has been increased significantly - see Figure 6.11 - and is higher than 1^o in all cases.

The next test was the evaluation of the error in different components for a sampling rate of 15 and an angular velocity of $0.5^o/sec$. The results are shown in Figures 6.12 and 6.13. Both statistical measures have increased significantly. The man error for segments 1, 2 and 3 remains below 1^o and the percentile for the same segments remains below 2^o. Segment 6 against shows the highest deviation.

These results demonstrate that the low accuracy of the gyroscope cannot offer the capability of accurate attitude determination. However note that it can be used for coarse attitude estimation as the maximum is more likely to occur if the attitude error remains below 2^o. This can serve many mission objectives especially when no optical equipment is included. Also such a system could serve as a back up system in case the primary sensors fail.

As the effect of the gyroscope was to be investigated, the next 2 experiments examinine the effect of low accuracy magnetometer.

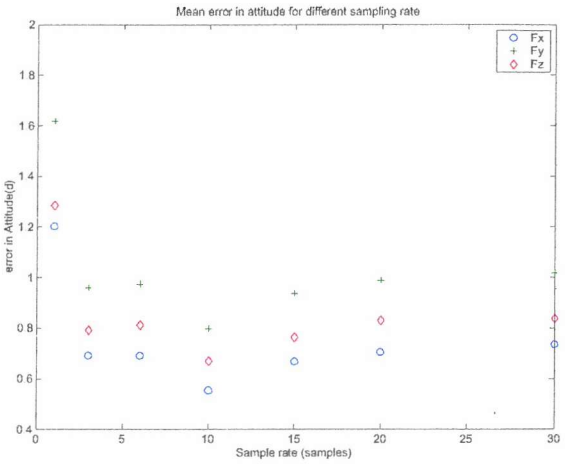

Figure 6.8: Mean attitude error vs sampling rate for $\omega = 0.5^o/sec$ with high accuracy magnetometer and low accuracy gyroscope

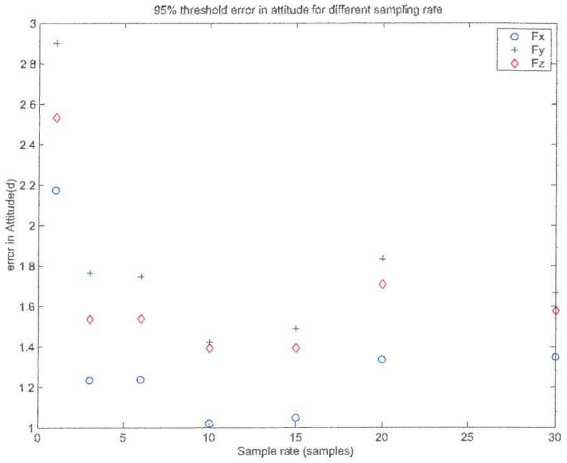

Figure 6.9: 95% Threshold attitude error vs sampling rate for $\omega = 0.5^o/sec$ with high accuracy magnetometer and low accuracy gyroscope

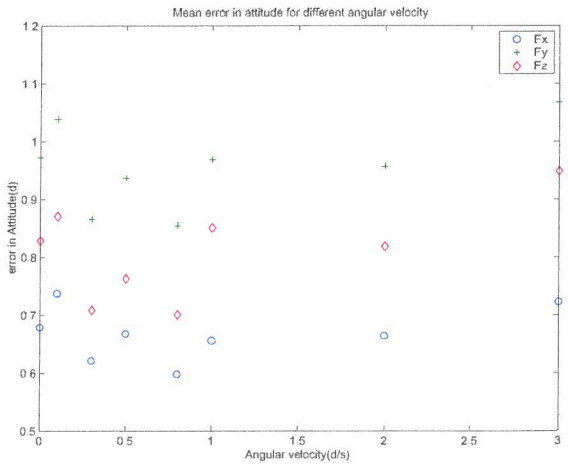

Figure 6.10: Mean attitude error vs angular velocity for sampling rate: 15 Oersted data samples (aprox. 16 seconds) with high accuracy magnetometer and low accuracy gyroscope

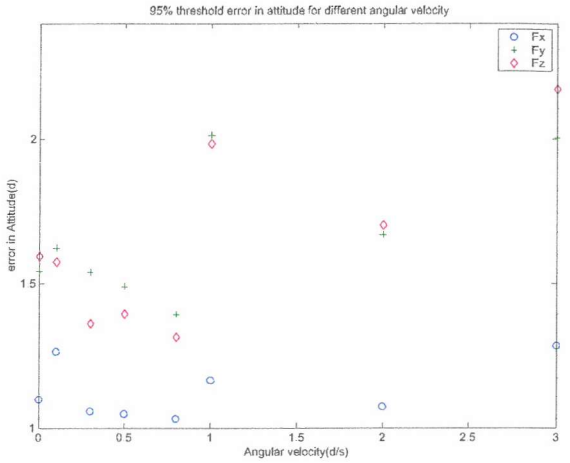

Figure 6.11: 95% Threshold attitude error vs angular velocity for sampling rate: 15 Oersted data samples (aprox. 16 seconds) with high accuracy magnetometer and low accuracy gyroscope

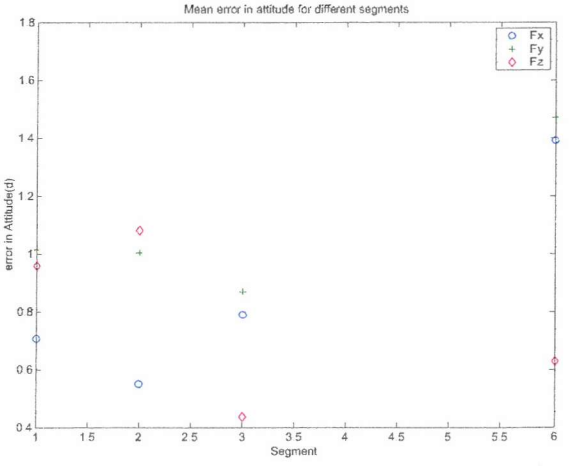

Figure 6.12: Mean attitude error for different segments for $\omega = 0.5^o/sec$ and sampling rate: 15 Oersted data samples (aprox. 16 seconds) with high accuracy magnetometer and low accuracy gyroscope

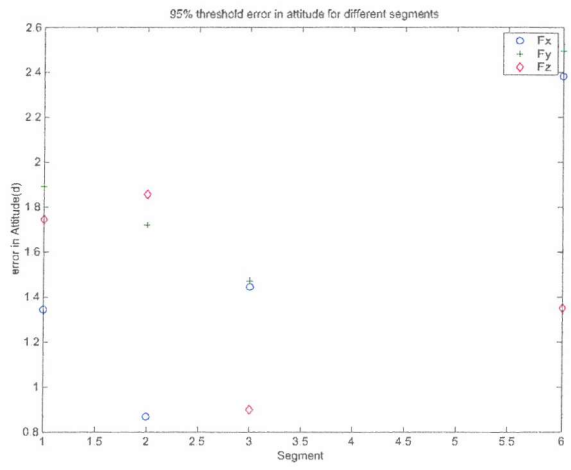

Figure 6.13: 95% Threshold attitude error for different segments for $\omega = 0.5^o/sec$ and sampling rate: 15 Oersted data samples (aprox. 16 seconds) with high accuracy magnetometer and low accuracy gyroscope

6.4 Experiment 3. Attitude determination - Quiet day - Moderate Magnetometer - Accurate Gyroscope.

Here we investigate the accuracy of the algorithm when the less accurate magnetometer with the most accurate gyroscope is used. The purpose of the experiment is to identify the effect of the measurement error in the single point attitude determination algorithm.

The first test was again the evaluation of the error for various sampling times. The statistics are shown in Figures 6.14 and 6.15. Here a very interesting feature is observed. In particular, the shape of variation of mean and the percentile are identical to those for the case when the accurate gyroscope and the accurate magnetometer were used but at a much higher scale. This occurs because the magnetometer error is more dominant than the error from the gyroscope.

The characteristic shape is mainly due to the inaccuracy of the measurement which could read as an error in the geomagnetic field model. The same was also true for experiment 5 with both the accurate magnetometer and gyro. As the main error results from the inaccuracy of the geomagnetic field model, the error is distributed equally between the three components and this results in a raised profile similar to the case when the highly accurate magnetometer was used. The percentile also follows the same pattern. The main difference is the high error encountered and the mean and the percentile have been increased significantly. The mean error for sampling rates higher than 10 show further convergence. To avoid a high sampling interval and preserve immunity to external torques, the sampling frequency for the next of the experiments was again chosen as 15.

The next test was the evaluation of the error for different rotational velocities. Figures 6.16 and 6.17 show the error statistics where the figures of interest have significantly increased and this shows more clearly the effect of an inaccurate magnetometer. The errors are higher than the previous experiment and this shows how significant is the effect of the inaccurate magnetometer. The errors are significant for all angular velocities with means are between 1.4^o and 2.2^o. The percentile reaches a maximum of 4^o.

The next test is the evaluation of the error for various segments for a fixed sample rate and velocity. The statistics are shown in Figures 6.18 and 6.19. The error appears high in all segments and the lowest values in overall are seen in segment 2.

The evaluation of this attitude determination configuration shows that the use of an inaccurate magnetometer creates a very significant error which was of course expected as the value of inaccuracy in the measurement is comparable to the difference vector of the

geomagnetic field.

The results showed that this system provides a quite low attitude accuracy. For the last test, for example, the accuracy is 3.4^o. This is a coarse attitude determination and this mode can be used for recovery or, for example, if the satellite must be rotated towards the sun for charging. For demanding tasks this accuracy is not satisfactory.

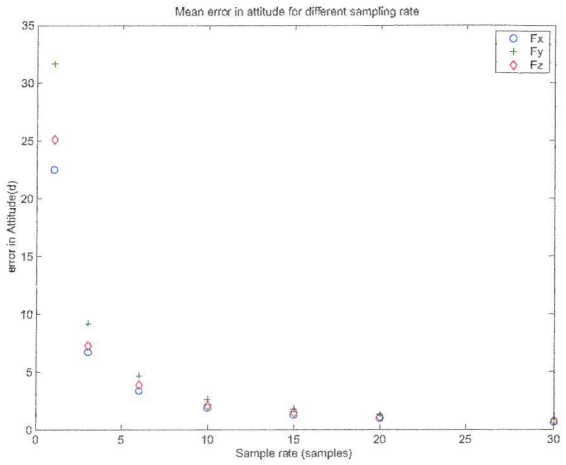

Figure 6.14: Mean attitude error vs sampling rate for $\omega = 0.5^o/sec$ with low accuracy magnetometer and high accuracy gyroscope

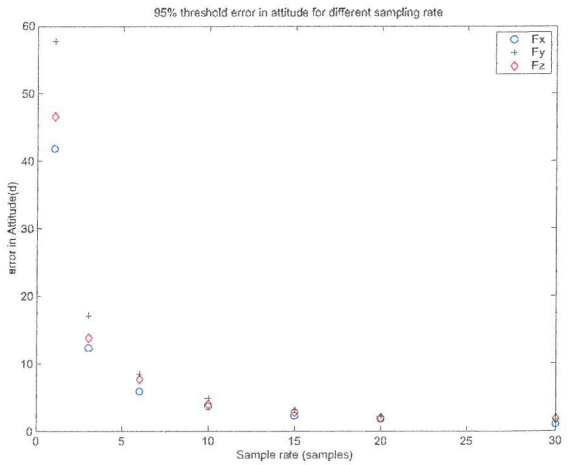

Figure 6.15: 95% Threshold attitude error vs sampling rate for $\omega = 0.5^o/sec$ with low accuracy magnetometer and high accuracy gyroscope

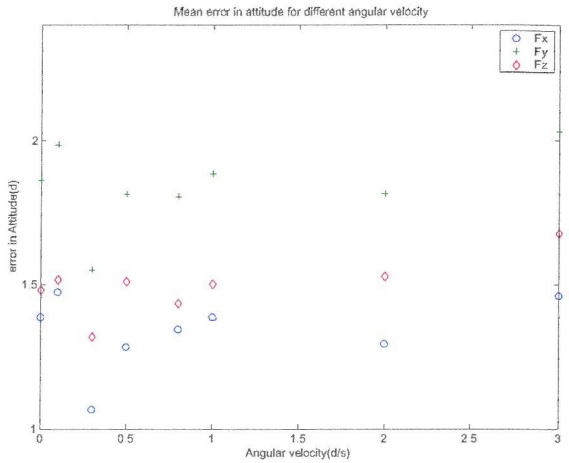

Figure 6.16: Mean attitude error vs angular velocity for sampling rate: 15 Oersted data samples (aprox. 16 seconds) with low accuracy magnetometer and high accuracy gyroscope

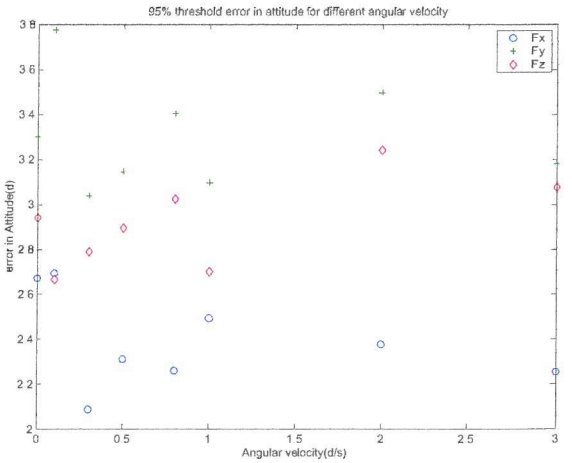

Figure 6.17: 95% Threshold attitude error vs angular velocity for sampling rate: 15 Oersted data samples (aprox. 16 seconds) with low accuracy magnetometer and high accuracy gyroscope

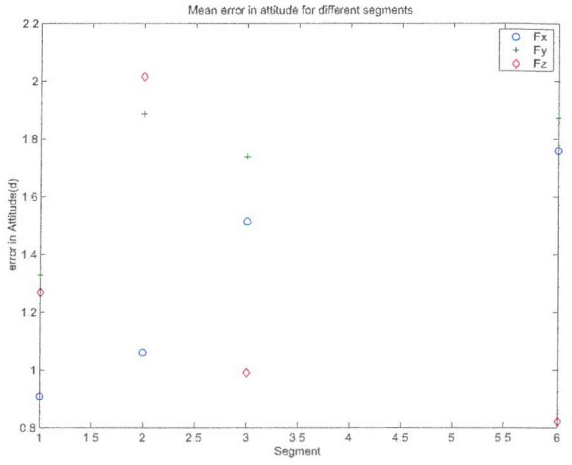

Figure 6.18: Mean attitude error for different segments for $\omega = 0.5^o/sec$ and sampling rate: 15 Oersted data samples (aprox. 16 seconds) with low accuracy magnetometer and high accuracy gyroscope

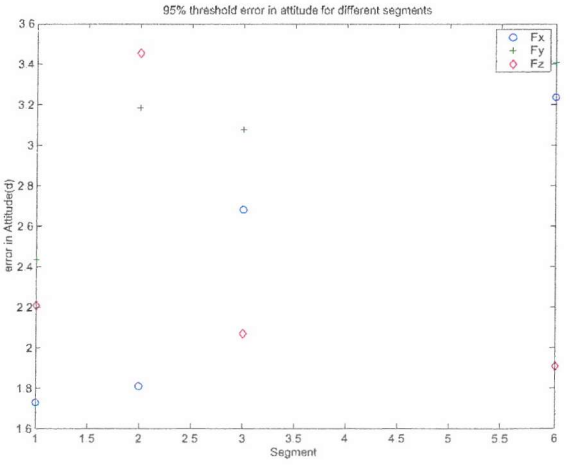

Figure 6.19: 95% Threshold attitude error for different segments for $\omega = 0.5^o/sec$ and sampling rate: 15 Oersted data samples (aprox. 16 seconds) with low accuracy magnetometer and high accuracy gyroscope

6.5 Experiment 4. - Attitude determination - Quiet day - Moderate magnetometer - Moderate Gyro.

The final experiment for the quiet day case is with a low accuracy magnetometer and a low accuracy gyroscope. This experiment reflects the accuracy that would be achieved with components that could be bought off-the self today. Many missions have used these sensors separately, but no mission has used them together.

From Figures 6.20 and 6.21 it is seen that the sampling has the same effect as in experiments 5 and 7. This was expected as the error due to the inaccuracy of the moderate magnetometer is higher than this due to the inaccuracy of the moderate gyroscope. The main observation here is that the error has even further been increased and also errors due to the gyro error and the magnetometer error have accumulated a much higher inaccuracy in the attitude.

The test for various angular velocities in Figures 6.22 and 6.23 shows that the error similar for all the values and is located between 1.2^o and 2.6^o in mean. The percentile values are between 2^o and 5^o.

The test for the different segments has also shown an increased error with segment 2 again having the smallest error. The statistics are shown in Figures 6.24 and 6.25 and it is seen that the errors are the highest observed compared to all the other configurations. Attitude determination with such a system and this algorithm for single point measurement of attitude would result in a likely maximum error of 4.5^o and mean error 2.6^o. This performance is the worst of all the possible configurations although it can still be used for coarse attitude determination.

Note again that the above tests were performed for a magnetically quiet day and these error figures do not reflect the error that could be encountered due to high magnetic activity. This is the purpose of the two final experiments.

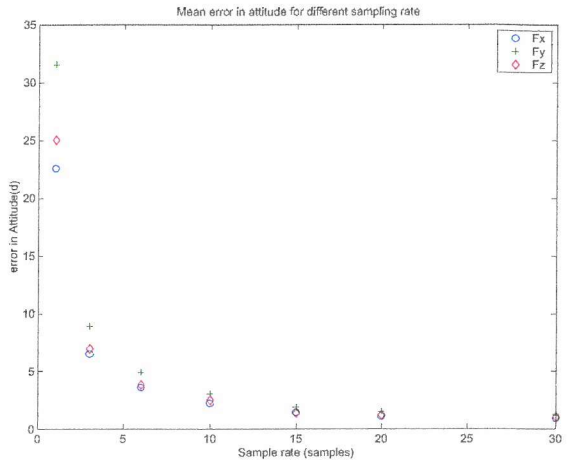

Figure 6.20: Mean attitude error vs sampling rate for $\omega = 0.5^o/sec$ with low accuracy magnetometer and low accuracy gyroscope

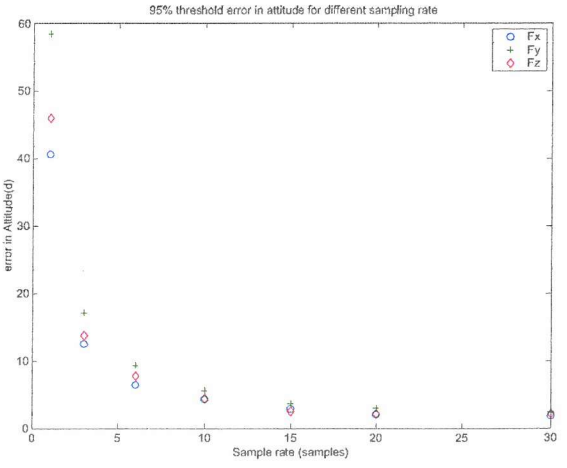

Figure 6.21: 95% Threshold attitude error vs sampling rate for $\omega = 0.5^o/sec$ with low accuracy magnetometer and low accuracy gyroscope

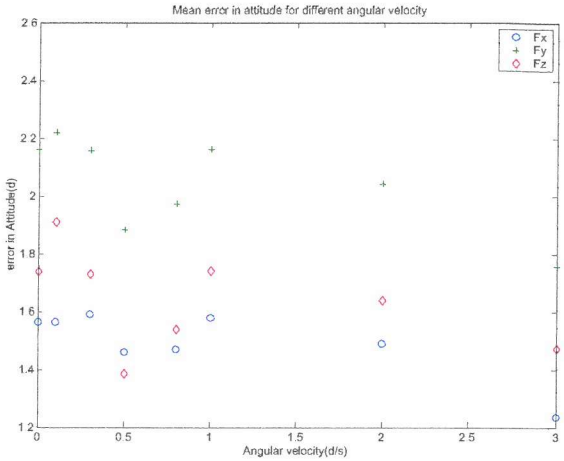

Figure 6.22: Mean attitude error vs angular velocity for sampling rate: 15 Oersted data samples (aprox. 16 seconds) with low accuracy magnetometer and low accuracy gyroscope

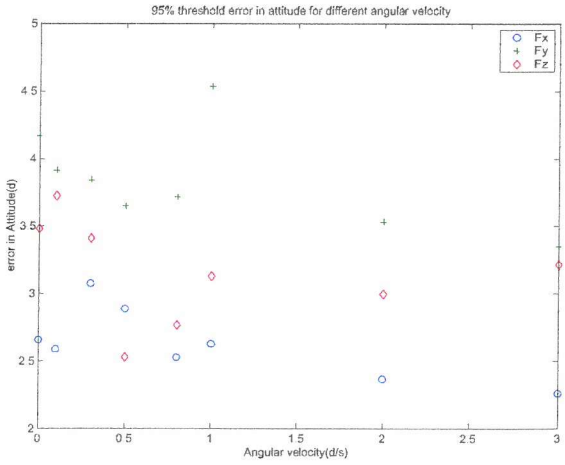

Figure 6.23: 95% Threshold attitude error vs angular velocity for sampling rate: 15 Oersted data samples (aprox. 16 seconds) with low accuracy magnetometer and low accuracy gyroscope

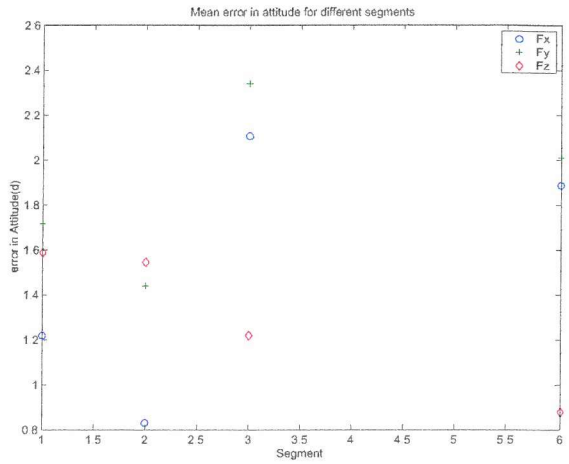

Figure 6.24: Mean attitude error for different segments for $\omega = 0.5^o/sec$ and sampling rate: 15 Oersted data samples (aprox. 16 seconds) with low accuracy magnetometer and low accuracy gyroscope

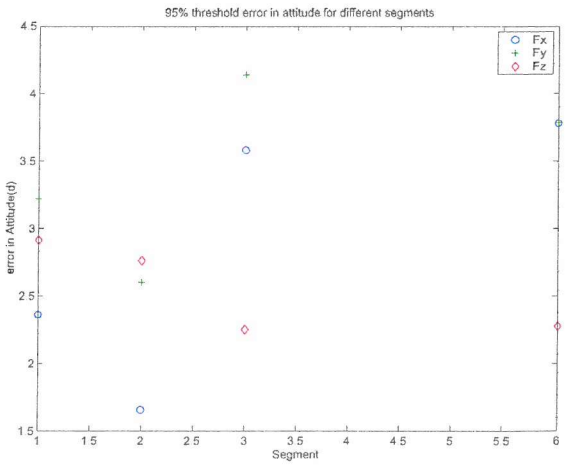

Figure 6.25: 95% Threshold attitude error for different segments for $\omega = 0.5^o/sec$ and sampling rate: 15 Oersted data samples (aprox. 16 seconds) with low accuracy magnetometer and low accuracy gyroscope

6.6 Experiment 5. Attitude determination under Magnetic Disturbance - Accurate Magnetometer - Accurate gyro

This experiment was performed in order to investigate the performance of the attitude determination algorithm during a set of days with different levels of magnetic disturbance. The days were selected from the pool of days used for the verification models in Chapter 3. The satellite dynamics were simulated with the data from the Oersted data files. A sampling rate and an angular velocity were chosen for the experiments. Sampling rate = 15 Oersted data samples and angular velocity = $0.5^o/sec$. The sampling rate was the most appropriate in terms of immunity to external disturbances and good accuracy. In this experiment the accurate magnetometer is used in order to reflect the performance of the most accurate configuration. These tests were performed using only the accurate magnetometer. The use of the magnetometer with moderate accuracy created, during the quiet day experiments, the highest errors. The two most accurate systems are the ones that use the magnetometer of high accuracy. Consequently the performance in a magnetically disturbed day will still be worse. Additionally the system is evaluated with and without the use of the MEME index in order to investigate the reduction of error it offers in a magnetically disturbed day.

The MEME index was evaluated by averaging the measurements over the narrow equatorial zone (Chapter 2) and assigning the measurements as the magnetic index for the next half orbit. In order to minimize the division of results, the MEME performance was evaluated for all cases of passage from night- or day- to night- or dayside. This gave a view of the overall MEME performance in combination with the single point magnetometer measurement. The results were evaluated in terms of the mean 95% percentile, as before, for all the three angles F_x, F_y, F_z. The results are given in Figures 6.26 to 6.31 and in detail in Table 6.7.

Figure 6.26 shows that the mean of the F_x error component is dramatically reduced by the use of MEME index in the dynamic model of the geomagnetic field. For category A, which corresponds to quiet magnetic activity of the ring current, the improvement is very small. However it is very important to note that an improvement has been observed in all cases. This is mainly due to the fact that more days with disturbance in the B, C and D levels were chosen in order to evaluate the performance of MEME. This resulted in a concentration of the A category measurements in the upper boundary rather than in the lower boundary and this resulted in an improvement by the use of MEME. However, the improvement is small. Most important is the improvement for categories B, C and D. Especially for category D it can be seen that, for example component F_x, in Figure 6.26 in segment 3 is reduced form

1.137^o error to 0.289^o. This reduction is significant and is observed in all components.

Components F_x and F_y are consistently showing the least error in segment 2. The error when the MEME index is not used is consistently increasing with category. This is mainly explained by the fact that the accurate gyro is used so no significant additional error is introduced. When the initial measurement is propagated to the time instance of the second measurement, the error due to inaccuracy of the angular velocity is small and the error is mainly due to the error in the orientation caused by the magnetic disturbance. From the large increase in the reduction of attitude error it is obvious that the use of MEME is beneficial not only because it reduced the error of the geomagnetic field model but also because it also described the orientation of the external dipole. As the geomagnetic field vector changes direction from the effect of this dipole, this error is increasing. The model that is proportional to MEME, represents a dipole and from the great reduction observed in the attitude error it is evident that this dipole approximates correctly the direction of the real one.

Table 6.1 shows the level of error reduction, especially for categories C and D. In segments 2 and 3 the mean error remains smaller than 0.2^o for categories A, B and C. For category D, the error for these segments has a maximum of 0.355^o. The percentiles which determine the 95% percent boundaries are the most important measure of the maximum likely error to be encountered and the maximum errors have also been drastically reduced. The highest errors after the use of MEME occur naturally in segment 6. From the rest of segments and for categories A, B, C the highest error is 0.333^o. For category D, the percentile value has a maximum of 0.684^o for segment 2 and 3 which are more likely to be used for the attitude determination as they are closer to the equatorial plane where the MEME index is derived.

It is important to note that the percentile for these two segments remains smaller than 0.263^o for all axes. Compared to the values that occur in the case when no MEME is used, these values are beneficially smaller. For category C, the accuracy is not as good, but the reduction is much higher and for category D the reduction is the largest. The order of reduction is roughly 1^o for segment 6 and this is an important improvement. In particular, it gives the confidence in the suitability of the MEME dependent model for attitude determination. The next stage of the examination was the performance of the system with the low accuracy gyro under the same conditions.

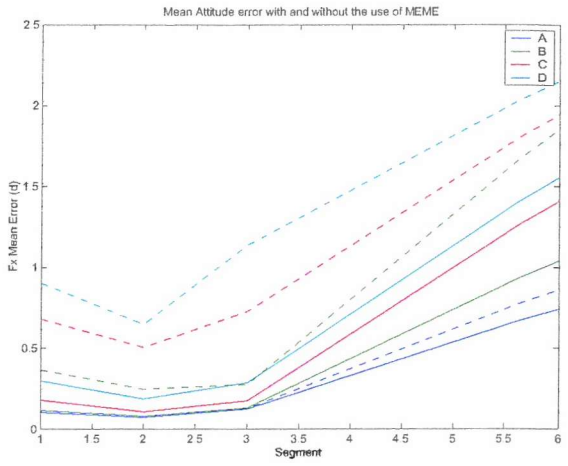

Figure 6.26: Mean attitude error F_x with and without (dotted lines) MEME for different categories and different segments with high accuracy gyroscope

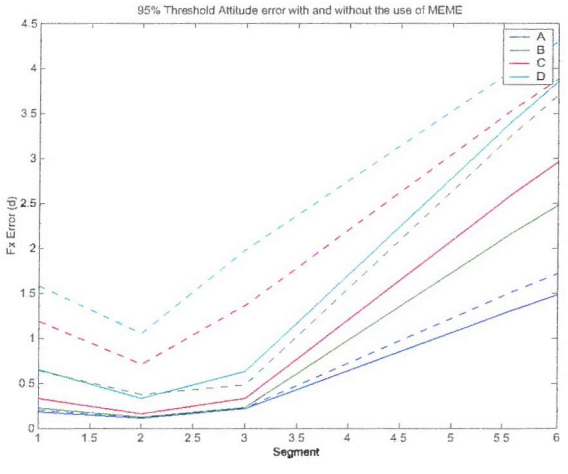

Figure 6.27: 95% Threshold attitude error F_x with and without (dotted lines) MEME for different categories and different segments with high accuracy gyroscope

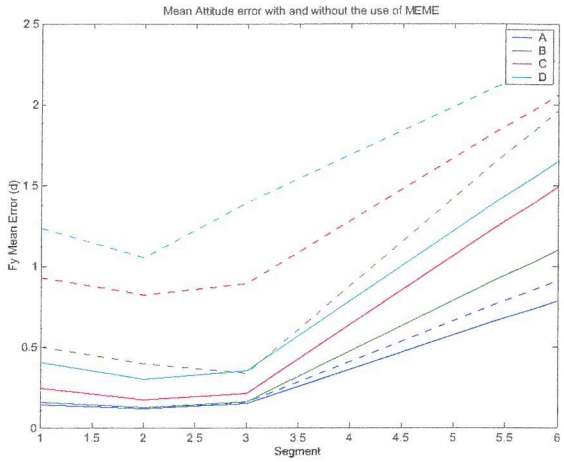

Figure 6.28: Mean attitude error F_y with and without (dotted lines) MEME for different categories and different segments with high accuracy gyroscope

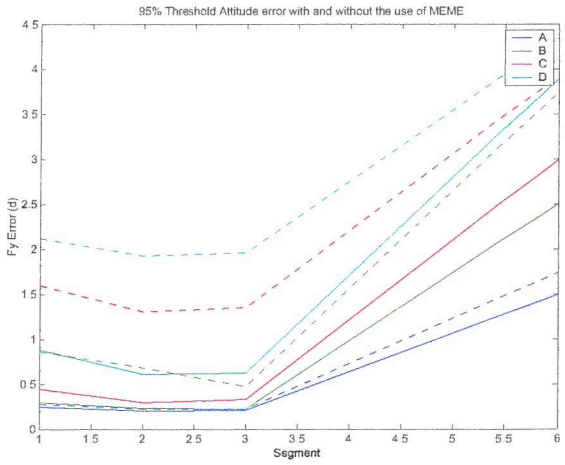

Figure 6.29: 95% Threshold attitude error F_y with and without (dotted lines) MEME for different categories and different segments with high accuracy gyroscope

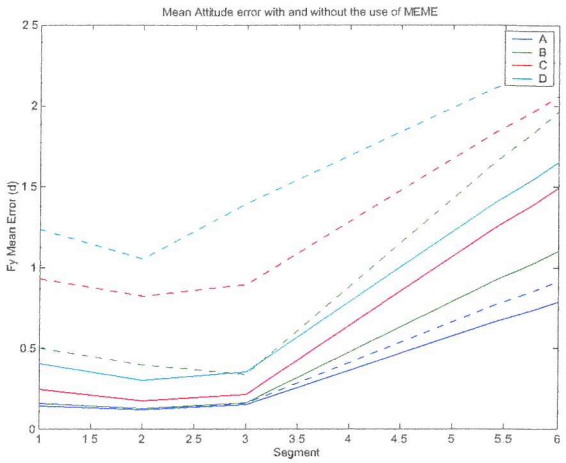

Figure 6.30: Mean attitude error F_z with and without (dotted lines) MEME for different categories and different segments with high accuracy gyroscope

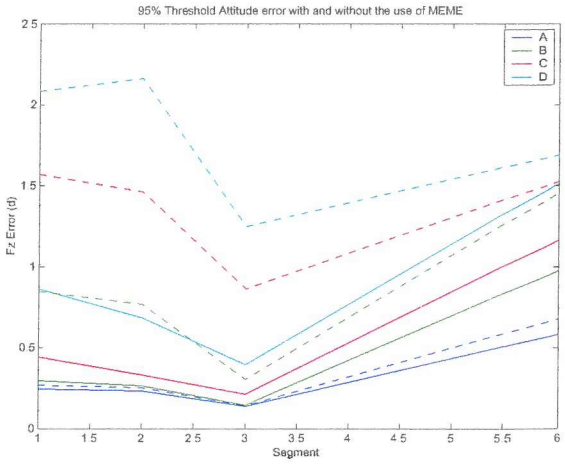

Figure 6.31: 95% Threshold attitude error F_z with and without (dotted lines) MEME for different categories and different segments with high accuracy gyroscope

		mean	mean	mean	mean	mean	mean	mean	mean	ptile	ptile	ptile	ptile	ptile	ptile	ptile	ptile
		meme	meme	meme	meme	no meme	no meme	no meme	no meme	meme	meme	meme	meme	no meme	no meme	no meme	no meme
seg		1.000	2.000	3.000	6.000	1.000	2.000	3.000	6.000	1.000	2.000	3.000	6.000	1.000	2.000	3.000	6.000
F_x	A	0.106	0.075	0.124	0.743	0.117	0.081	0.130	0.862	0.186	0.113	0.216	1.482	0.205	0.122	0.226	1.719
F_x	B	0.117	0.081	0.132	1.040	0.367	0.247	0.277	1.857	0.223	0.128	0.231	2.475	0.642	0.375	0.483	3.706
F_x	C	0.181	0.108	0.175	1.411	0.680	0.508	0.729	1.946	0.335	0.161	0.336	2.964	1.192	0.714	1.369	3.883
F_x	D	0.298	0.187	0.289	1.560	0.903	0.650	1.137	2.154	0.657	0.333	0.630	3.854	1.583	1.053	1.984	4.298
F_y	A	0.146	0.121	0.152	0.787	0.160	0.131	0.159	0.913	0.250	0.207	0.214	1.500	0.275	0.224	0.224	1.740
F_y	B	0.160	0.131	0.162	1.102	0.503	0.400	0.340	1.968	0.299	0.234	0.229	2.505	0.861	0.687	0.479	3.749
F_y	C	0.248	0.175	0.215	1.496	0.932	0.822	0.894	2.063	0.449	0.295	0.333	2.999	1.597	1.307	1.357	3.929
F_y	D	0.408	0.302	0.355	1.653	1.238	1.052	1.395	2.283	0.881	0.610	0.624	3.899	2.121	1.929	1.966	4.349
F_z	A	0.138	0.123	0.096	0.322	0.152	0.133	0.101	0.373	0.245	0.233	0.136	0.583	0.270	0.251	0.143	0.676
F_z	B	0.152	0.133	0.103	0.451	0.475	0.407	0.216	0.805	0.294	0.263	0.145	0.973	0.846	0.770	0.304	1.457
F_z	C	0.234	0.178	0.137	0.612	0.882	0.836	0.568	0.844	0.441	0.330	0.212	1.166	1.569	1.466	0.863	1.527
F_z	D	0.386	0.307	0.225	0.676	1.171	1.069	0.886	0.934	0.865	0.684	0.397	1.515	2.084	2.163	1.250	1.690

Table 6.1: Mean and 95% Error Threshold for the three angles F_x, F_y, F_z for different segments, different segments and for use and no use of meme - Case for Accurate Gyroscope in Use.

6.7 Experiment 6. Attitude determination- Accurate Magnetometer - Moderate gyro

Exactly the same methodology was followed as in the previous experiment except for the gyro accuracy. The system was expected to experience a reduction of error as the error in the rotational velocity is not correlated with the error in the geomagnetic field and thus it can be identified in the cases which are not parallel to the error of the rotational velocity. The results are shown in Figures 6.32 to 6.37 and in Table 6.7.

These results show that the performance of the system was similar but with higher error. The main difference with the case of the accurate magnetometer is the increased values of mean and percentile threshold errors. In all three components the error remains significantly higher than in the case with the attitude magnetometer. The use of MEME offers a significant reduction in the error. The errors experienced when the MEME was not used were, as expected, higher than the ones experienced when the accurate gyroscope was used. This is translated into the fact that the error due to the inaccuracy of the gyroscope was also present in the experienced error. This is also shown in the fact that after the use of MEME the achieved accuracy is still low.

The accuracy of the system has a mean value of 1.356^o for category D and for segments 2 and 3. The percentile threshold for the same segments has a maximum value of 2.538^o. The equivalent values for the case when the MEME is not used are 2.141^o and 4.025^o respectively. These values show that, as expected, this system suffers from low accuracy and cannot be used for attitude determination. However, the most interesting observation is the fact that in all segments and in all categories the MEME resulted in a great reduction of the errors and that it can indeed provide a mechanism for reducing the error due to the activity of the ring current. Another important observation is the fact that the error in segment 6 is also decreased, although it still remains the highest from all the segments due to the presence of ionospheric currents.

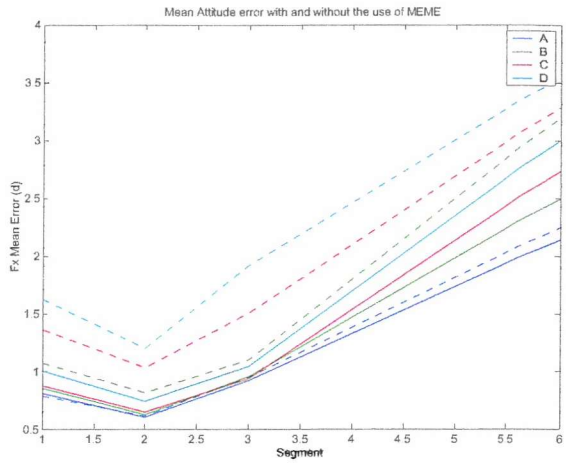

Figure 6.32: Mean attitude error F_x with and without (dotted lines) MEME for different categories and different segments with low accuracy gyroscope

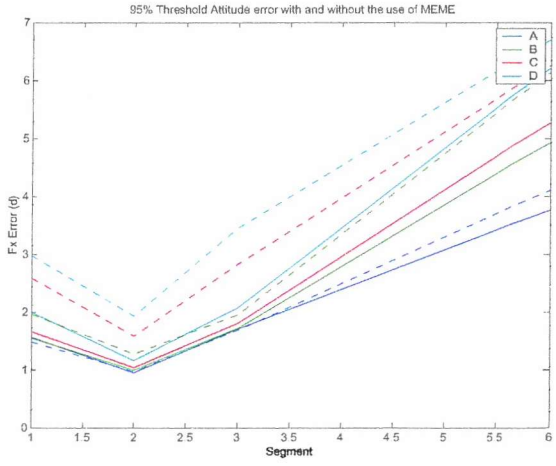

Figure 6.33: 95% Threshold attitude error F_x with and without (dotted lines) MEME for different categories and different segments with low accuracy gyroscope

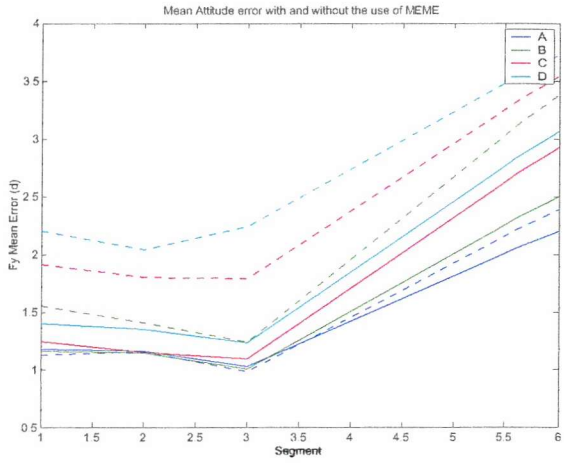

Figure 6.34: Mean attitude error F_y with and without (dotted lines) MEME for different categories and different segments with low accuracy gyroscope

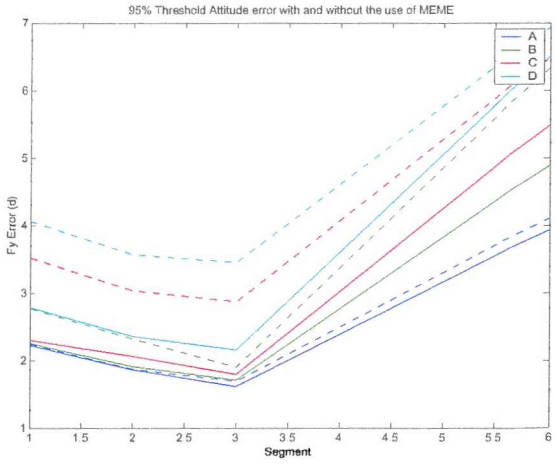

Figure 6.35: 95% Threshold attitude error F_y with and without (dotted lines) MEME for different categories and different segments with low accuracy gyroscope

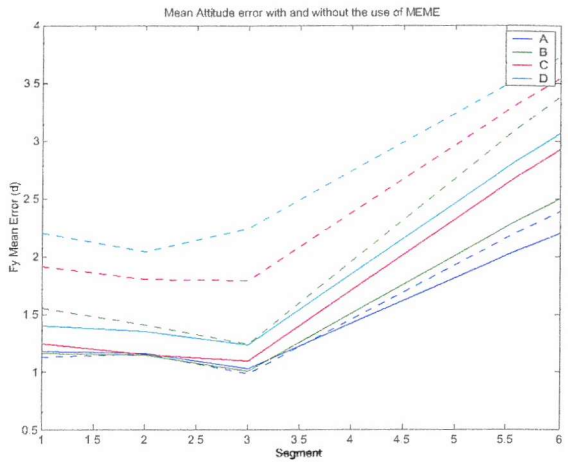

Figure 6.36: Mean attitude error F_z with and without (dotted lines) MEME for different categories and different segments with low accuracy gyroscope

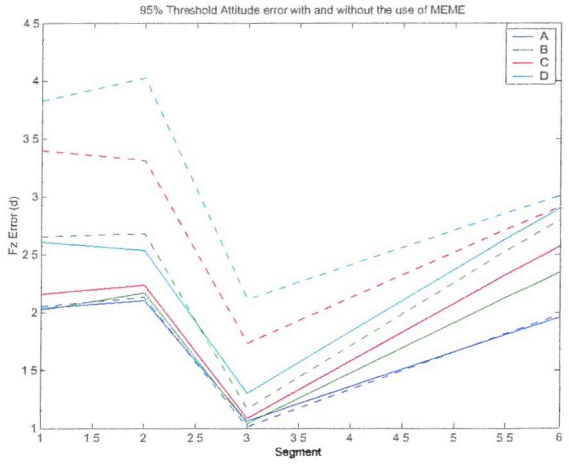

Figure 6.37: 95% Threshold attitude error F_z with and without (dotted lines) MEME for different categories and different segments with low accuracy gyroscope

		mean	mean	mean	mean	mean	mean	mean	mean	ptile	ptile	ptile	ptile	ptile	ptile	ptile	ptile
		meme	meme	meme	meme	no meme	no meme	no meme	no meme	meme	meme	meme	meme	no meme	no meme	no meme	no meme
seg		1.000	2.000	3.000	6.000	1.000	2.000	3.000	6.000	1.000	2.000	3.000	6.000	1.000	2.000	3.000	6.000
F_x	A	0.811	0.607	0.927	2.143	0.790	0.617	0.950	2.249	1.560	0.952	1.709	3.764	1.482	0.975	1.688	4.103
F_x	B	0.858	0.630	0.958	2.496	1.074	0.821	1.101	3.199	1.554	0.998	1.719	4.933	1.959	1.275	1.951	6.138
F_x	C	0.878	0.654	0.940	2.736	1.364	1.038	1.505	3.286	1.664	1.041	1.810	5.273	2.585	1.579	2.831	6.269
F_x	D	1.006	0.745	1.048	3.002	1.625	1.200	1.921	3.550	2.001	1.159	2.069	6.222	2.970	1.926	3.455	6.705
F_y	A	1.183	1.162	1.032	2.205	1.131	1.158	0.985	2.394	2.228	1.864	1.614	3.941	2.245	1.876	1.689	4.114
F_y	B	1.164	1.147	1.007	2.503	1.553	1.408	1.242	3.389	2.251	1.912	1.709	4.891	2.763	2.321	1.905	6.342
F_y	C	1.248	1.153	1.099	2.932	1.914	1.803	1.795	3.548	2.305	2.066	1.798	5.489	3.517	3.034	2.871	6.490
F_y	D	1.400	1.354	1.238	3.068	2.205	2.042	2.242	3.729	2.788	2.359	2.155	6.515	4.063	3.564	3.455	6.946
F_z	A	1.112	1.236	0.538	0.947	1.062	1.172	0.518	0.990	2.036	2.101	1.063	1.957	2.057	2.132	1.013	1.979
F_z	B	1.145	1.177	0.546	1.078	1.462	1.452	0.671	1.413	2.019	2.169	1.043	2.348	2.655	2.681	1.171	2.802
F_z	C	1.199	1.296	0.585	1.247	1.842	1.908	0.989	1.497	2.157	2.239	1.085	2.577	3.400	3.313	1.737	2.917
F_z	D	1.390	1.356	0.656	1.284	2.102	2.141	1.317	1.551	2.612	2.538	1.304	2.903	3.830	4.025	2.114	3.012

Table 6.2: Mean and 95% Error Threshold for the three angles F_x, F_y, F_z for different segments, different segments and for use and no use of meme - Case for Moderate Gyroscope in Use.

Chapter 7

Conclusions

7.1 Segmentation and MEME

7.1.1 Performance of Main Field Models in the Nightside

From the results presented in this work and the subsequent discussion, it can be concluded that the derived models are more appropriate for use on-board a satellite for attitude determination. The main improvements are as follows:

In segments 1, 2, 3, 4 and 5 the new models perform better than the refined IGRF2000. The following discussion refers to these segments. The first evaluation of the performance of the different models was based on the vector components. This was due to the fact that the models were developed only from vector measurements in order to adapt better to the orientation of the geomagnetic field vector rather than the magnitude. The mean and rms error of the three components treated as a whole, in the same way they were used in the modelling process, stay very close to zero for both the days used and those not used in the modelling process. This confirmed the mathematical validity of the model.

The rms error was smaller for lower latitudes. This resulted in lower values for segment 1, 2 and 3 progressively. The same was observed for segments 4 and 3 as their performance is the averaged of the above mentioned segments. When each of the components was treated individually, small shifts were observed in the mean error for the days not included in the modelling. These shifts did not result in degradation of the model.

This last conclusion was confirmed by the examination of the magnitude. The mean magnitude error stayed very close to zero for the days used in the modelling and for those that were not.

The rms error of the magnitude for days not included in the modelling stayed at the

same levels as for days not included in the modelling. For some models, a slight decrease was also observed, a fact which further reinforced the validity of the models.

An important observation here is that the rms error in segment 3 is higher than in segment 2, in contrast to the behavior of rms error of the vector components. This behavior is justified by the fact that at equatorial latitudes the magnitude of the geomagnetic field vector is significantly lower than in segment 2. As the vector components have only slightly different rms error values in these two segments, the effect in the vector with a smaller magnitude is greater. This is due to the fact that the vector experiences larger deviations (relative to the stronger vector) from its mean orientation and this, of course, is translated into higher magnitude variations around the mean.

The lowest magnitude rms error was observed for modelling and non modelling days in segment 2. In segment 1, the magnitude rms error was slightly higher than in segment 3. For the rest of the models it was higher. The phenomenon of the greater effect of the rms error of the vector components in segment 3 (relative to segment 2) was also observed, as expected, in the orientation error. The mean orientation error was higher in segment 2 than in segment 3 due to the higher effect of the variation of the vector components of the error on the low magnitude of the geomagnetic field in this segments. The lowest value was again observed in segment 2. An important observation here is that the mean angle error stayed well below 0.1^o for all segments and, of course, this was due to the low magnetic activity during the days used for the modelling and validation of the model.

However the mean error is not indicative of the most probable error that can be encountered. The rms value was used for this purpose in the examination of the error of the vector components and the magnitude. However the orientation error, due to the methodology used, is always positive as no information is available about its direction but only about the angle of deviation. This was also confirmed by plotting the histograms of the orientation error. As the distribution was not of a Gaussian, Laplacian or Huber form it was decided to use two different error measures. The first was the threshold angle value below which lies 95% of the error and the second was the percentage of error that lies below 0.1^o.

The threshold value was again lowest for segment 2. The reason is again the greater orientation errors caused by the lower magnitude of the field vector in segment 2. In higher latitudes the reason for the higher orientation error is the higher levels of disturbance. The most important fact by that in segments 2, 3 and 5 the threshold was lower than 0.1^o during the days used for the modelling and for those not used.

The examination of the percentage of error below 0.1^o also showed that the orientation error is least in segment 2. This was translated into the highest percentage over all the other segments. As expected from the threshold values, the percentage in segments 2, 3 and 5 exceeded the 95% value and for segment 2 by a significant amount. Segment 4 includes segments 1, 2 and 3. As in segment 1, the error was higher than in segments 2 and 3 and the resulting accuracy of segment 4 was deteriorated. Segment 5 includes segments 2 and 3 and as the error was lowest for these two segments its accuracy was also high, fact confirmed in the examination of the orientation error.

The error in segment 6 was always higher than any other segment. As this segment includes the geographical poles, where the most irregular magnetic activity is observed, this high error was expected. Segment 7 included all other models and due to the high disturbance in segment 6 the error in this segment was also high, and in particular higher than in segments 1, 2, 3, 4 and 5.

The above discussion refers to models 1, 2, 3, 4, 5, 6 and 7, when they valid for use in a segment. In each segment the model with the lowest error characteristics was the one developed for data only within this segment. This confirmed our hypothesis that a division of the field in segments and the derivation of a different model would result in a better representation of the regional anomalies.

The performance of the above models was compared to that of the refined IGRF, with the higher harmonics and D_{st} dependent part discarded (as it would be used on board a satellite). The IGRF performed significantly worse in all segments and compared to all models.

The examination of its vector components error via histograms revealed that it suffered from two sources of error, one strongest at the equator and one strongest at the poles. The equatorial error followed a Huber distribution and had a more spread lobe than for the other models. For higher latitudes, two additional symmetric lobes were added to distribution and intensified for higher latitudes. The central values of these lobes made clear that the source of error was not due to the exclusion of the D_{st} dependent part. The only reasonable explanation for this error was that the other models were better adapted to the quiet polar activity. During the derivation of this version of IGRF the maximum activity, as measured by the K_p index, was lower than 1+. In our example, the activity was chosen to be lower than 2 in order that the models could adapt to a wider range of quiet polar activity. Another reason for this is due to the effect of the exclusion of outliers during each iteration in the modelling

process for the IGRF. Finally a third cause is the exclusion of coefficients for degrees higher than 13. Although this explanation seems an obvious reason, doubts are caused by the fact that the lobes appear for all three vector components. As B_θ decreases with latitude the lobes should not intensify in higher latitudes for this component. The above discussion refers to both the sets of days used and not used in the modelling.

As IGRF performed worse than all the other models in all segments it was decided that in each segment the corresponding model, developed only from this segment, is more appropriate for use since it offers the highest accuracy according to all the statistical measures used.

The error statistics for the days used for the modelling and those not differ in values. Table 7.1 shows the worst case statistics in each segment for the corresponding model. By worst case statistics is meant that in some cases the performance was better for the days not used in the modelling and for some other cases the opposite was true. As it is important to have an indication of the overall worst performance, the highest error values were collected and presented in the Table 7.1.

7.1.2 Performance of Main Field Models in the Day side

The validation of the model accuracy in the dayside has not been presented in any paper on the development of a quantitative model for the geomagnetic field. This is due to the effect of the quiet solar field during the quiet days for which various models have been developed. However, the accuracy of the model must also be known in the day side if the model is to be used onboard a satellite.

The evaluation of the different models was performed separately for the set of days used for their derivation and for the set of days used for the validation of the models in the nightside. A deterioration of performance was observed in all segments.

The following discussion refers to segments 1, 2 and 3. Firstly, the mean error of the three vector components treated as a whole, as they were used for the derivation of the model, was again very close to zero and lower than 1 nT in absolute value. This again confirmed the numerical robustness of the model. The rms error was increased, where the most important feature was that the rms error was lower in segment 2 and not in segment 3 as in the case of the vector components error in the dayside. In segment 1 the rms error was higher than in segments 2 and 3. This phenomenon was observed in all three components treated together or individually.

The magnitude mean error was at identical levels in all segments. The main difference was that there was a negative shift of roughly $-5nT$, identically in all segments. This phenomenon was interpreted as the effect of the solar quiet field. This system of currents creates a field which reinforces the geomagnetic field lower than the ionosphere and opposes it above this region (Oersted orbit). This is shown in the negative dc levels of the magnitude mean error. The lowest mean magnitude error was observed in segment 2 and the reason for this is that again the effect of error is higher for the lower magnitude in segment 3. The magnitude rms error also increased and the lowest value was observed in segment 2.

The mean orientation error also increased. In segment 2 the lowest mean orientation error was observed. One significant fact was that in segments 1, 2 and 3 the mean orientation error stayed well below 0.1^o. The 95% threshold value was increased significantly and in all segments the threshold value was above 0.1^o. The lowest threshold value was observed in segment 2 in the nightside. The highest percentage of error below 0.1^o was observed in segment 2 at around 92%. In no other segment did the percentage exceed 90%.

The most important observation here is that the pattern of error remained the same. This means that the orientation error was lowest in segment 2, compared to segment 3 and segment 1. The fact that the accuracy has deteriorated comes from the introduction of the effect of the solar quiet day. Higher mean error creates a higher mean angle error and higher rms error creates larger deviation of the field vector from its modelled orientation. This discussion was refers to segments 1, 2 and 3.

In Segment 4, the performance level was intermediate between that in segments 1, 2 and 3. In segment 5 the performance was intermediate between that in segments 2 and 3. Consequently in segment 5 a lower error was observed than in segment 4. In segment 6 again the models showed the highest error all segments. In segment 7 the performance was worse than in segments 1, 2, 3, 4 and 5 as it included polar latitudes.

All the above models were tested against the IGRF in the nightside. Here the mean magnitude error of the IGRF experienced the same negative shift as all the other models in all components. This reinforced the suggestion that this shift is caused by the solar quiet field and not the model inaccuracy. If it was due to model magnitude misfit, this deviation would not be observed in the IGRF model.

The rms error of the IGRF did, however, increase by a small amount in segment 2 and very slightly in segment 3 compared to the nightside. As the rms error in segment 3 increased significantly over all other models, in some cases it was observed that IGRF had a slightly

lower error. This, of course, is caused by the higher error experienced in the other models and not the lower error in the IGRF. Additionally in segment 1 the increase in the rms error for IGRF was significant. By examining the histograms, it is observed the the rms error in segment 3 followed a Hubner distribution as in the nightside. However, in this case the lobes for the other models were as wide as for the IGRF. For higher latitudes in segment 2, the same lobes that were observed in the nightside appeared and in segment 1 they were clearly formed.

The only difference was that the lobes appeared clearly in higher latitudes than in the nightside. This is due to the fact that the increased disturbance in segment 3 was still present in higher latitudes and prevented the lobes from appearing. As there is no significant increase in the rms error of the IGRF in segment 3 compared to the nightside, this means that the new error is uncorrelated with the error of IGRF in the nightside. It is of similar level and that is why the rest of the models in segment 3 have similar rms error values. The very similar rms error values in segments 2 and 3 confirm this fact. Additionally the rms error in segment 1 is increased by a smaller amount and remains closer to the nightside values (already higher than the rms error in segments 2 and 3 in the dayside) which means that the noise is not correlated. This increase in segment 1 is probably enforced by higher polar activity in the dayside. The possible cause is reinforced by the disproportionably high rms error increase in segment 6. These conclusions are for both the sets of days used and not used in the derivation of the models.

Table 7.2 shows the worst cases statistics for both sets of days for each segment and the corresponding model.

Sg	Md	B_r Mean	B_θ Mean	B_ϕ Mean	|B| Mean	B_r rms	B_θ rms	B_ϕ rms	|B| rms	Mean (°)	95% Thrs.(°)	%below 0.1°
1	1	-0.702	0.285	0.107	0.315	11.926	23.855	28.599	10.623	0.034	0.116	93.970
2	2	1.083	1.297	-1.064	0.142	6.670	5.643	8.825	6.707	0.021	0.062	98.080
3	3	1.544	2.357	-2.144	-0.317	6.594	5.594	7.365	7.566	0.023	0.061	97.450
4	4	-0.616	0.863	-1.288	0.427	8.752	14.723	18.083	9.519	0.035	0.119	93.500
5	5	1.329	1.654	-1.712	0.073	6.812	6.044	8.277	7.442	0.028	0.094	95.530
6	6	-1.152	3.535	-3.313	-3.390	26.055	20.112	34.643	19.602	0.099	0.377	77.400
7	7	-1.764	2.657	2.224	-0.748	19.121	27.330	34.537	17.074	0.066	0.277	84.040

Table 7.1: Worst case statistics in each segment for the corresponding models - Night Side

Sg	Md	B_r Mean	B_θ Mean	B_ϕ Mean	|B| Mean	B_r rms	B_θ rms	B_ϕ rms	|B| rms	Mean (°)	95% Thrs.(°)	%below 0.1°
1	1	0.482	2.829	3.150	-8.524	18.035	20.153	22.120	13.744	0.053	0.178	88.880
2	2	-0.993	3.385	-3.481	-8.542	11.668	13.759	17.089	11.753	0.050	0.134	91.780
3	3	2.208	3.654	-4.616	-8.110	12.299	15.751	18.910	11.681	0.067	0.193	86.540
4	4	0.829	4.043	-2.767	-8.888	14.310	16.751	18.460	12.185	0.055	0.169	88.420
5	5	1.198	3.804	-3.931	-8.741	12.099	14.939	18.037	11.719	0.055	0.152	88.100
6	6	0.084	-0.671	2.455	-6.404	36.432	42.366	40.836	26.624	0.095	0.285	78.356
7	7	1.023	3.832	4.032	-9.935	28.735	36.221	40.888	32.443	0.079	0.235	84.640

Table 7.2: Worst case statistics in each model for the corresponding models

7.1.3 Consistency of MEME and the Performance of MEME Dependent Models

The mean equatorial magnitude error (MEME) index was first evaluated for a set of 35 days and in a first stage it was examined graphically. It was generally observed that there was an asymmetry to the measurements which consistently appeared especially when the D_{st} levels were in the negative axis (most of the time). The more negative the level of D_{st} was, the higher the asymmetry of MEME values appeared between succeeding passes in the nightside and the dayside. In the nightside the levels of MEME were generally stronger than in the dayside. For very low levels of D_{st} close to zero this asymmetry was violated in some cases. This was due to the inherent model errors and the dayside errors which were comparable to the ring current effect for such low levels.

In order to evaluate its performance, a large set of MEME equatorial measurements was quantified into 10 categories spanning positive to high negative values. For the same measurement the corresponding D_{st} values were collected, as published by the Kyoto World Data Cente for Geomagnetism. The data sets were further quantified according to the side that the measurements of MEME was taken (night or day). The mean of each subgroup was evaluated together with the corresponding mean of the D_{st} values. A plot of the means revealed that there is a persistent asymmetry of the ring current effect with the peak in the nightside. The asymmetry was measured by a similar indicator to the one used by Jorgensen et al. [56]. The values of the asymmetry and its variation with magnetic activity, as measured by D_{st}, was found to be similar to the one found by Jorgensen et al, for D_{st} values between -20 and -140 nT. Outside this range the asymmetry was found to be significantly different than Jorgensen, but in the lower case it was expected as other sources of error are comparable to the ring current. This was also mentioned by Jorgensen et al. in their work.

The difference for higher values, was probably due to the low number of measurements above this level due to the rare frequency of such phenomena. The asymmetry for the main range of magnetic activity revealed that MEME index can be used consistently within this range in order to produce an estimate for it. The first main advantage is the fact that MEME can be used onboard a satellite while D_{st} cannot. The second important advantage is that MEME identifies the asymmetry of ring current, a fact that can provide a better indication of the expected disturbance in the night and day sides. It was thus decided to develop a model dependent on the MEME index, in a similar way to the D_{st} dependent model included in the IGRF model, in order to compensate for the ring current effect on the real field.

Following the observation of asymmetry and its variation for different levels of magnetic activity, we decided to quantify the level of MEME measurements into four groups. Group A included disturbances up to $-20nT$ and represented quiet activity. Group B was for measurements between -20 and $-60nT$ and represented moderated activity. Group C was between $-60nT$ and -100nT and represented high activity and Group D was for measurements lower than -100nT and represented very high activity. This division was performed separately for night and dayside. Due to the asymmetry of the ring current it was generally expected that Group A category in the nightside will correspond to lower activity than group A in the dayside. This is due to the fact that when MEME is measured in the dayside the disturbance in the nightside is expected to be higher because of this effect. This was expected for all groups.

A large set of days from the entire range of magnetic activity were collected from Oersted measurements and MEME was evaluated over each equatorial pass and the corresponding index was stored for the next half orbit until the next equatorial pass. The main field model was then subtracted from all measurements and the corresponding groups were formed. The models used for the main field were 1, 2, 3 and 6 in the corresponding segments. Because of the asymmetry between day and night side it was decided to further quantify the data according to the side that MEME was measured and the side it was used. This led to four different cases. Night-Night, Night-Day,Day-Day-Day-Night. The resulting number of data sets was 16. From each of them a different model was developed and evaluated. Theese were validated further by a completely different set of days, outside the range of the days used for the modelling and for all 7 segments. In the validation phase in each segment the corresponding main field model was used and the MEME dependent models were added to it according to case and category. During the validation, the error after the use of MEME models was compared to that when these models are not used in order to quantify the level of improvement.

The results showed that there is a high error reduction for categories B, C and D in segments 2 and 3. In segment 1 the performance was variable. In some cases there was a significant improvement while in other cases there was not. This was caused by the close proximity of this segment to the polar regions. Especially for high magnetic activity the polar activity also intensifies and this creates errors that do not correspond to the morphology of the ring current effect. When the polar activity was smaller there was also a significant reduction in this segment. An important observation in terms of the mean magnitude error

was that, when MEME was not used, it progressively increased for categories B, C and D for all cases. This validated the suitability of the MEME index.

The only exception was in the Day-Night Case for Category D, for which the mean error was slightly lower than category C. This was probably caused by the small number of measurements available as the number of days in the validation set was much smaller than in the modelling set. As there was a small number of measurements for category D in such cases, it was suggested that these might have been contaminated by high peaks from ionospheric dayside phenomena. The mean magnitude error was always higher in segments 3 and 2 than in segment 1 as the effect of the ring current is stronger in equatorial latitudes. After the use of MEME models, a significant reduction of error was achieved in segments 2 and 3 for categories B, C and D. In category A in some cases there was a small reduction while in other cases there was even a small increase in the error. This was expected as the model errors are comparable to the disturbance for such low activity. Additionally for such low magnetic activity the effect of the ring current changes faster and this created inconsistency in the use of models in this category. The rms magnitude error was also significantly improved in segments 2 and 3 for categories B, C and D by the use of MEME models.

The same feature was observed for the mean orientation error and the percentage of orientation error below 0.1^o. The 95% threshold in most cases slightly reduced and in other cases slightly increased. This showed that, although a large number of high residuals caused by the ring current were removed, the highest errors persisted. This showed that most of these residuals did not follow the morphology of the ring current, even if they were associated with it. The most important observations are the significant decrease of the mean and rms magnitude error and the high increase of the orientation error percentage below 0.1^o.

Tables 7.3 to 7.4 show the worst case statistics for each case and the corresponding improvement compared to the values when MEME models were not used. By worst case statistics is meant that for each each set of days the lowest error was identified for each category. The lowest errors for the two sets of days were compared and the highest between them displayed in the table. This gives the "worst case" best performance. The values are accompanied by an index S showing in which segment these values were observed. The subscript denotes the number of the segment and the superscript shows whether values resulted from the use of MEME model or not. This was intended for category A, as in some cases the performance without the use of MEME was slightly better. From Tables 7.3 and 7.4 it can be seen that the reduction of magnitude mean and rms error was in all cases

very high for categories B, C and D.

The mean orientation error was significantly increased for these categories in all cases. The 94% threshold did not experience the same level of reduction. This means that the highest of the errors remained and this was probably caused by other sources that corrupted the field and created high errors. The percentage of error below 0.1^o was increased significantly especially for categories C and D.

For category A it can be seen that in certain cases there is a zero improvement. This is due to the fact that the use of MEME in these cases increased the error slightly and thus the initial values were better. This is observed especially for the mean and 95% threshold values for the orientation error in category A. Also in one case the mean magnitude error was not reduced in category A. The only case that this happened for another category was in case Night-Day. There for category C the 95% value was not improved. However as we already noted the threshold value had the least improvement through use of MEME and this was due to the presence of a small number of high errors.
The most important observations are summarized as follows:

1. The mean and rms magnitude errors are dramatically reduced consistently for categories B, C and D.

2. The mean orientation error is significantly reduced for categories B, C and D. For all cases the resulting mean orientation error is below 0.1^o.

3. The 95% threshold value was improved but not as much as the mean orientation error. This was due to the presence of high error not being represented by the MEME models.

4. The percentage of orientation error was consistently increased for categories B, C and D and was highest for categories C and D. The resulting values for all categories were above 80% for all cases except the Day-Night case where they were a bit lower for categories C and D.

5. From the index of the segments were the highest performance was observed we conclude that the highest performance was always in segments 2 and 3. This is due to the fact that the models have higher effect there. In all cases in these two segments the performance was comparable.

6. For category A the use of MEME created inconsistent results. In certain cases it reduced the error while in others it led to an increase. Thus the use of these models for this

category does not guarantee any improvement. This is not a significant problem since for this low level of disturbance the errors created are low and can be tolerated.

Category	$\|B\|_{mean}(nT)$		$\|B\|_{rmd}(nT)$		$A_{mean}(^o)$		$A_{95\%}(^o)$		$A_{0.1^o}(\%)$	
A	-1.033	S_3^M	10.477	S_3^M	0.037	S_2^M	0.122	S_2^M	93.630	S_2^M
B	-2.249	S_3^M	11.698	S_3^M	0.058	S_2^M	0.170	S_2	85.430	S_2^M
C	-1.113	S_3^M	14.132	S_3^M	0.060	S_2^M	0.153	S_2^M	80.060	S_2^M
D	2.703	S_3^M	11.797	S_3^M	0.080	S_3^M	0.222	S_3^M	80.290	S_3^M

Table 7.3: Worst case statistics for Night-Night Case

Category	$\|B\|_{mean}$		$\|B\|_{rmd}$		A_{mean}		$A_{95\%}$		$A_{0.1^o}$	
A	39.342	S_3^M	19.630	S_3	9.756	S_2^M	3.937	S_2^M	0.380	S_2^M
B	93.084	S_3^M	42.126	S_3^M	15.942	S_2^M	0.000	S_2^M	3.900	S_2^M
C	97.964	S_3^M	66.673	S_3^M	39.394	S_2^M	10.000	S_2^M	27.670	S_2^M
D	96.987	S_3^M	89.595	S_3^M	11.111	S_3^M	37.465	S_3^M	55.160	S_3^M

Table 7.4: Percentage of improvement from the values when MEME is not used - Night Night

Category	$\|B\|_{mean}$		$\|B\|_{rmd}$		A_{mean}		$A_{95\%}$		$A_{0.1^o}$	
A	0.891	S_2^M	16.431	S_1	0.044	S_2	0.083	S_2	96.520	S_2
B	-6.505	S_1^M	12.933	S_2^M	0.051	S_2^M	0.112	S_2^M	94.720	S_2^M
C	-4.530	S_3^M	16.329	S_2^M	0.062	S_2^M	0.141	S_2	87.770	S_2^M
D	-3.760	S_3^M	37.473	S_3^M	0.075	S_3^M	0.182	S_2^M	80.830	S_3^M

Table 7.5: Worst case statistics for Night-Day Case

Category	$\|B\|_{mean}$		$\|B\|_{rmd}$		A_{mean}		$A_{95\%}$		$A_{0.1^o}$	
A	8.802	S_2^M	0.000	S_1	0.000	S_2	0.000	S_2	0.000	S_2
B	24.069	S_1^M	35.039	S_2^M	19.048	S_2^M	4.274	S_2^M	1.610	S_2^M
C	87.264	S_3^M	49.748	S_2^M	13.889	S_2^M	0.000	S_2^M	2.990	S_2^M
D	94.839	S_3^M	51.882	S_3^M	17.582	S_3^M	6.186	S_2^M	40.740	S_3^M

Table 7.6: Percentage of improvement from the values when MEME is not used - Night Day

Category	$\|B\|_{mean}$		$\|B\|_{rmd}$		A_{mean}		$A_{95\%}$		$A_{0.1^o}$	
A	-2.142	S_3^M	15.594	S_2	0.045	S_3	0.150	S_3	91.190	S_1^M
B	-10.413	S_3^M	12.687	S_3^M	0.055	S_2^M	0.134	S_2^M	89.950	S_2^M
C	-10.581	S_3^M	12.979	S_3^M	0.065	S_2^M	0.151	S_2^M	82.590	S_3^M
D	-14.982	S_3^M	19.707	S_3^M	0.099	S_3^M	0.327	S_3^M	69.400	S_3^M

Table 7.7: Worst case statistics for Day-Day Case

Category	$\|B\|_{mean}$		$\|B\|_{rmd}$		A_{mean}		$A_{95\%}$		$A_{0.1^o}$	
A	63.872	S_3^M	0.000	S_2	0.000	S_3	0.000	S_3	0.050	S_1^M
B	67.749	S_3^M	33.635	S_2^M	6.780	S_2^M	10.067	S_2^M	3.200	S_2^M
C	81.865	S_3^M	66.587	S_2^M	30.851	S_2^M	14.689	S_2^M	13.030	S_3^M
D	86.817	S_3^M	77.669	S_3^M	36.129	S_3^M	8.914	S_3^M	34.410	S_3^M

Table 7.8: Percentage of improvement from the values when MEME is not used - Day Day

Category	$\|B\|_{mean}$		$\|B\|_{rmd}$		A_{mean}		$A_{95\%}$		$A_{0.1^o}$	
A	-3.696	S_1	17.671	S_2^M	0.042	S_2^M	0.138	S_3^M	91.940	S_3^M
B	-7.507	S_3^M	21.994	S_3^M	0.056	S_2^M	0.139	S_2^M	92.190	S_2^M
C	1.006	S_3^M	25.776	S_3^M	0.091	S_3^M	0.230	S_3^M	73.420	S_3^M
D	-13.020	S_3^M	29.585	S_3^M	0.074	S_2^M	0.192	S_2^M	77.540	S_3^M

Table 7.9: Worst case statistics for Day-Night Case

Category	$\|B\|_{mean}$		$\|B\|_{rmd}$		A_{mean}		$A_{95\%}$		$A_{0.1^o}$	
A	0.000	S_1	5.214	S_2^M	4.545	S_2^M	18.824	S_3^M	0.610	S_3^M
B	77.987	S_3^M	38.667	S_3^M	18.841	S_2^M	2.113	S_2^M	4.650	S_2^M
C	98.824	S_3^M	54.376	S_3^M	22.881	S_3^M	24.590	S_3^M	18.680	S_3^M
D	88.404	S_3^M	66.124	S_3^M	49.315	S_2^M	33.101	S_2^M	42.670	S_3^M

Table 7.10: Percentage of improvement from the values when MEME is not used - Day Night

7.2 Use of the model in an attitude determination system

The first conclusion from the results of the testing of the four different attitude determination systems was the importance of the sampling rate. A small sampling rate indeed creates a high error due to the fact that the difference vector due to the error in attitude knowledge is comparable to that due to the inertial geomagnetic field inertial vector, used for the determination of the attitude. Low sampling rates were disregarded. For higher sampling rates the error converged to lower values. The highest sampling rate considered was 30 Oersted data samples which corresponds roughly to 33-35 seconds on average. This interval was considered too high in order to preserve immunity to the effect of external disturbance torques. The optimal sampling rate was chosen as 15 Oersted data samples (approximately 16 seconds). Under this fixed sampling rate, the systems were tested for different rotational velocities and the results showed that above $1^o/sec$ the error increased while below this point it remained low. This effect was mainly due to the inaccuracy of the propagating integrator in the dynamics equation which transfers the initially measured field vector used in the attitude determination. Lower integration steps could lead to higher accuracies but here the one considered was 0.01 second which is considered acceptable in terms of number of calculations required. Under these conditions the system performed better under the $1^o/sec$ boundary. The last test was the evaluation for different segments. In the results it was seen that in segments 1, 2 and 3 showed the best performance, as expected.

The comparison of the different systems showed that the use of the accurate magnetometer with the accurate gyroscope could offer, during a quiet day, a mean accuracy of 0.15^o degree in segments 2 and 3 for a sampling rate of around 16 seconds (15 Oersted data samples) and rotational velocity of $0.5^o/sec$. The 95% percentile for the same conditions was close to $2.2^o/sec$. This accuracy is very high and approximates the accuracy of the geomagnetic field model. When the accurate magnetometer is used in conjunction with the moderate gyro with an error of $0.1^o/sec$ the accuracy deteriorates and for the same conditions mentioned above, the accuracy was deteriorated. The mean error was increased to values up to 1^o for all segments. The percentile was increased accordingly up to 1.9^o. This showed the importance of accurate angular velocity measurement for accurate attitude determination.

The next system considered was the moderate magnetometer combined with the accurate gyroscope, where the accuracy was deteriorated. The mean error for all segments increased to values as high as 2^o and the percentile error was increased to 3.5^o. This shows that magnetometers of this accuracy cannot offer a good accuracy even if they are used in

conjunction with an accurate gyro. The error due to the low resolution of such a sensor significantly corrupts the difference vector. As the corruption occurs in both the vector used for the derivation of the derivative the errors are high even with the use of a very accurate magnetometer. The combination of the moderate magnetometer and the moderate gyroscope showed the worst performance of all. The mean error reached a value of 2.4^o and the percentile a value of 4.1^o. This system characterizes the system than can be bought today off the self. The use of such an attitude determination methodology would not be beneficial for such a system.

The results from the second phase of experiments showed the suitability of the MEME model for reduction of the error due to the magnetic activity. Only the two systems with the high accurate magnetometer were investigated. This was due to the fact that the error in the moderate magnetometer would not allow correct identification of the MEME index. The two remaining systems were tested separately.

The system with the accurate magnetometer and the accurate gyroscope showed a high reduction of error after the use of MEME. The reduction was higher for categories C and D while the accuracy was higher for categories A and B. The mean errors were lower in segments 2 and 3 as expected. The highest mean error after the reduction was for category D in segments 2 and 3 and of value 0.333^o while without the use of MEME the corresponding high error is 1^o higher. This significant reduction showed the very important fact that the use of the MEME model offers a good adaptation to the ring current dipole. The dipolar nature of the ring current creates similar variations in the orientation of the geomagnetic field for the short time intervals considered in between sampling. The MEME model depicts the shape of the dipole and transforms the geomagnetic field model accordingly. This results in the high reduction of the errors in this methodology which uses the derivative of the geomagnetic field.

High error reductions were also observed for the system that uses the moderate gyroscope. Although the errors are higher due to the introduced rotation error, the use of MEME offers a significant error reduction. The errors experienced when MEME is not used are naturally higher than the corresponding errors in the case of the accuate gyroscope. After the use of MEME, segments 2 and 3 showed the lowest mean and percentile errors. The highest mean error in segments 2 and 3 without the use of MEME was 2.141^o, after the use of MEME this error was reduced to 1.356^o. This is significant reduction and the corresponding percentile values were 4.025^o and 2.538 respectively. The MEME again gave a significant reduction.

The overall evaluation of the 4 systems showed that if the angular velocity is known to an accuracy of $0.001^o/sec$ and a magnetometer with an accuracy of 1 nT is used then such a system can achieve high accuracy. No system that uses extended Kalman filtering with a magnetometer has produced such an accuracy even in the case of a highly accurate magnetometer. If the angular velocity is known to an accuracy of 0.01^o then the system can provide an accuracy of 2^o in the percentile sense for the worst case. This is an accuracy of an single frame measurement and indeed can be used for fast coarse attitude estimation.

7.3 Summary of the implementation of an on-board system using the MEME index

The MEME index is derived from equatorial measurements. The use of a geomagnetic field model including this new index is suitable for near-earth missions where the geomagnetic field can be consistently measured. Depending on the orbit of the spacecraft, and consequently the time between equatorial passes, the MEME index has a corresponding time resolution. For example for a typical polar LEO of a period of 90 minutes the spacecraft passes over the equator every 45 minutes. Thus the MEME index can also be calculated every 45 minutes. Once the MEME is evaluated from the equatorial measurements, it is used in the on-board geomagnetic field model for the rest of the orbit until the next equatorial pass. If the spacecraft is in an equatorial orbit, then MEME can be evaluated at any time instance as the satellite is always over the equatorial region. These two examples, of polar and equatorial orbits, are the extreme cases. For any other inclination the resolution of the MEME index takas intermediate values.

Due to the fact that MEME is evaluated only from magnitude measurements, it can always be derived irrespective of the attitude of the spacecraft. This provides robustness of this new index.

As it was established in Chapter 4, the MEME is the mean value of the error of the magnitude of the measurements in the equatorial region. This means that according to the orbital location, the value of the geomagnetic field model is calculated (without the MEME dependent part) and is the subtracted from the corresponding real magnitude measurement. As many measurements in the equatorial measurements are used, all the residuals are averaged and the mean value is used as the MEME index until the next equatorial pass. This requires a procedure for determining of the orbital location. GPS receivers are the most ac-

curate orbital location providers. One GPS receiver which has already been used successfully in space with high accuracy is the SSTL Mitel Chipset [69].

When an onboard system is using a MEME inclusive model, the main requirements for deriving this index are the passage over the equatorial region, the measurement of the magnitude of the geomagnetic field and accurate orbital location knowledge for use in the geomagnetic field model.

7.4 Future Work

There are a number of areas to which further work based on the results in this thesis should be very profitable which are summarized in general terms as follows.

- The first general area for such work is in terms of the geometric field model where segmentation has been established as a key area of research. Due to the high volume of data collected by satellites in polar orbits, the use of alternative segmentation techniques/algorithms should be investigated. The objective here would be to obtain an even better fit of the model to the real field.

- Another general area for further work relates to the index MEME and, in particular, the selection of the sampling rate to reduce the error magnitude. This is based on the premise that a lower mean error will result in higher accuracy in the MEME model. Another area here is an investigation into the variation of the MEME coefficients with time as per the D_{st} dependent model.

- The application of the modelling approach developed here to attitude determination is a very wide area indeed and there are a great many sub-problems which require further work. Chief among these is the preservation of the model accuracy in the presence of magnetic activity.

Appendix A

Coefficients of the Models for Different Segments

A.1 Main Field Coefficients of Models for Different Segments

In this Appendix are given the coefficients of the derived models for the 7 different segments. First are given the Internal Field Coefficients and then the External Field Coefficients. Finally the coefficients of the MEME dependent model are given.

n-m	0	1	2	3	4	5	6	7	8	9	10	11	12	13
1	-29679.769	-1729.613	0.000	0.000	0.000	0.000	0.000	0.000	0.000	0.000	0.000	0.000	0.000	0.000
2	-2270.913	3070.334	1670.837	0.000	0.000	0.000	0.000	0.000	0.000	0.000	0.000	0.000	0.000	0.000
3	1401.877	-2285.913	1253.427	713.584	0.000	0.000	0.000	0.000	0.000	0.000	0.000	0.000	0.000	0.000
4	928.913	784.203	249.745	-404.014	98.533	0.000	0.000	0.000	0.000	0.000	0.000	0.000	0.000	0.000
5	-294.537	353.710	224.608	-128.921	-177.426	0.443	0.000	0.000	0.000	0.000	0.000	0.000	0.000	0.000
6	75.218	71.588	74.647	-160.216	1.893	14.059	-30.508	0.000	0.000	0.000	0.000	0.000	0.000	0.000
7	153.420	-72.444	3.555	32.203	22.061	-3.180	-10.668	-8.868	0.000	0.000	0.000	0.000	0.000	0.000
8	17.895	1.995	-12.681	-9.813	-20.281	11.729	-26.357	-0.478	14.759	0.000	0.000	0.000	0.000	0.000
9	-51.279	13.593	8.922	-8.230	-8.429	-2.137	15.730	10.880	-3.922	22.937	0.000	0.000	0.000	0.000
10	-0.128	-3.295	2.041	-1.958	0.341	1.792	17.881	-3.174	-5.172	5.850	-29.871	0.000	0.000	0.000
11	35.519	-1.195	0.659	1.090	9.732	-2.877	-11.845	1.419	2.142	-8.826	8.520	1.122	0.000	0.000
12	-5.600	-2.467	-1.966	-0.632	0.699	2.072	-5.806	2.646	2.467	-3.045	8.504	-0.029	0.378	0.000
13	-12.598	1.903	4.826	0.071	-7.885	2.479	4.331	-0.654	-0.485	1.904	-3.474	2.728	-4.392	-19.452
14	0.000	0.000	0.000	0.000	0.000	0.000	0.000	0.000	0.000	0.000	0.000	0.000	0.000	0.000

Table A.1: g coefficients for segment 1

n-m	0	1	2	3	4	5	6	7	8	9	10	11	12	13
1	0.000	5193.835	0.000	0.000	0.000	0.000	0.000	0.000	0.000	0.000	0.000	0.000	0.000	0.000
2	0.000	-2480.275	-448.821	0.000	0.000	0.000	0.000	0.000	0.000	0.000	0.000	0.000	0.000	0.000
3	0.000	-230.180	289.983	-469.443	0.000	0.000	0.000	0.000	0.000	0.000	0.000	0.000	0.000	0.000
4	0.000	269.170	-240.031	120.935	-276.267	0.000	0.000	0.000	0.000	0.000	0.000	0.000	0.000	0.000
5	0.000	53.191	175.319	-156.091	-37.384	105.829	0.000	0.000	0.000	0.000	0.000	0.000	0.000	0.000
6	0.000	-18.035	70.916	62.680	-84.251	11.772	49.639	0.000	0.000	0.000	0.000	0.000	0.000	0.000
7	0.000	-65.372	-28.005	28.969	21.006	9.827	-20.655	74.268	0.000	0.000	0.000	0.000	0.000	0.000
8	0.000	7.680	-26.590	13.376	-2.261	4.765	6.141	-13.175	-14.970	0.000	0.000	0.000	0.000	0.000
9	0.000	-11.330	13.837	-12.536	-3.213	-0.747	3.909	-38.216	0.714	26.824	0.000	0.000	0.000	0.000
10	0.000	1.078	3.213	0.972	-7.000	1.533	-0.060	-5.009	4.311	-4.880	-23.637	0.000	0.000	0.000
11	0.000	-0.426	0.852	11.137	-4.307	-5.536	2.365	16.933	-6.743	-10.191	6.533	-2.681	0.000	0.000
12	0.000	-1.941	-0.856	6.443	3.394	-2.447	0.494	1.131	-0.873	2.498	3.417	-1.377	6.078	0.000
13	0.000	1.396	-1.296	-9.535	0.072	3.394	-1.780	-5.014	2.532	2.761	-2.352	0.547	-5.530	10.139
14	0.000	0.000	0.000	0.000	0.000	0.000	0.000	0.000	0.000	0.000	0.000	0.000	0.000	0.000

Table A.2: h coefficients for segment 1

n-m	0	1	2	3	4	5	6	7	8	9	10	11	12	13
1	-29573.194	-1732.221	0.000	0.000	0.000	0.000	0.000	0.000	0.000	0.000	0.000	0.000	0.000	0.000
2	-2280.357	3069.353	1671.210	0.000	0.000	0.000	0.000	0.000	0.000	0.000	0.000	0.000	0.000	0.000
3	1510.315	-2296.492	1252.311	715.790	0.000	0.000	0.000	0.000	0.000	0.000	0.000	0.000	0.000	0.000
4	944.123	788.425	252.714	-402.679	111.606	0.000	0.000	0.000	0.000	0.000	0.000	0.000	0.000	0.000
5	32.445	333.599	222.805	-128.275	-168.779	-12.340	0.000	0.000	0.000	0.000	0.000	0.000	0.000	0.000
6	90.309	69.378	76.470	-159.538	-5.496	17.087	-90.458	0.000	0.000	0.000	0.000	0.000	0.000	0.000
7	352.211	-97.673	-0.445	37.232	8.880	6.693	7.544	-1.401	0.000	0.000	0.000	0.000	0.000	0.000
8	48.324	9.009	-5.472	-3.939	-15.824	8.822	6.992	-7.749	-7.291	0.000	0.000	0.000	0.000	0.000
9	211.668	-13.064	2.225	-3.883	6.016	-7.548	-0.854	9.310	-4.426	-8.649	0.000	0.000	0.000	0.000
10	13.036	-5.205	3.907	0.105	0.194	3.748	0.993	1.969	4.356	0.089	-2.160	0.000	0.000	0.000
11	108.553	-15.645	-2.685	4.704	0.095	0.460	-0.025	0.667	1.832	0.391	1.219	3.188	0.000	0.000
12	6.125	0.699	1.882	3.699	0.587	0.760	-0.347	0.640	-0.629	-0.121	0.614	-0.049	0.136	0.000
13	26.955	-5.790	-0.172	0.870	-0.341	2.047	0.743	1.001	-0.646	0.024	-0.413	1.128	0.267	0.146
14	0.000	0.000	0.000	0.000	0.000	0.000	0.000	0.000	0.000	0.000	0.000	0.000	0.000	0.000

Table A.3: g coefficients for segment 2(in nanoTesla)

n-m	0	1	2	3	4	5	6	7	8	9	10	11	12	13
1	0.000	5187.934	0.000	0.000	0.000	0.000	0.000	0.000	0.000	0.000	0.000	0.000	0.000	0.000
2	0.000	-2478.668	-456.821	0.000	0.000	0.000	0.000	0.000	0.000	0.000	0.000	0.000	0.000	0.000
3	0.000	-230.535	296.242	-490.143	0.000	0.000	0.000	0.000	0.000	0.000	0.000	0.000	0.000	0.000
4	0.000	276.466	-229.759	119.243	-303.980	0.000	0.000	0.000	0.000	0.000	0.000	0.000	0.000	0.000
5	0.000	36.213	181.419	-133.709	-39.809	106.786	0.000	0.000	0.000	0.000	0.000	0.000	0.000	0.000
6	0.000	-9.766	68.318	65.172	-60.776	0.460	43.257	0.000	0.000	0.000	0.000	0.000	0.000	0.000
7	0.000	-75.950	-9.666	4.850	24.682	14.738	-25.286	-5.848	0.000	0.000	0.000	0.000	0.000	0.000
8	0.000	20.523	-14.484	7.359	-21.786	15.037	9.446	-14.257	-2.544	0.000	0.000	0.000	0.000	0.000
9	0.000	-33.208	32.421	11.067	-5.671	-7.761	8.106	3.766	-8.212	4.213	0.000	0.000	0.000	0.000
10	0.000	7.754	6.060	3.191	4.894	-6.413	-1.405	-3.572	0.435	-2.423	-7.461	0.000	0.000	0.000
11	0.000	-9.234	13.967	-2.154	-2.070	0.993	-0.934	-2.889	-0.850	-1.156	-2.270	0.330	0.000	0.000
12	0.000	2.196	4.392	1.168	-3.146	0.127	0.531	0.568	-0.157	0.425	-0.680	-0.679	1.428	0.000
13	0.000	-5.880	7.519	1.223	-0.016	-0.431	-0.438	0.766	0.190	0.566	0.715	-0.774	-0.426	0.185
14	0.000	0.000	0.000	0.000	0.000	0.000	0.000	0.000	0.000	0.000	0.000	0.000	0.000	0.000

Table A.4: h coefficients for segment 2 (in nanoTesla)

n-m	0	1	2	3	4	5	6	7	8	9	10	11	12	13
1	-29141.612	-1723.683	0.000	0.000	0.000	0.000	0.000	0.000	0.000	0.000	0.000	0.000	0.000	0.000
2	-2279.751	3174.811	1669.267	0.000	0.000	0.000	0.000	0.000	0.000	0.000	0.000	0.000	0.000	0.000
3	2703.408	-2243.681	1275.628	724.439	0.000	0.000	0.000	0.000	0.000	0.000	0.000	0.000	0.000	0.000
4	893.364	1116.771	243.573	-406.116	114.517	0.000	0.000	0.000	0.000	0.000	0.000	0.000	0.000	0.000
5	2182.348	469.860	310.115	-70.187	-170.338	-12.498	0.000	0.000	0.000	0.000	0.000	0.000	0.000	0.000
6	-35.862	604.135	63.920	-165.735	8.743	12.337	-90.900	0.000	0.000	0.000	0.000	0.000	0.000	0.000
7	2780.436	98.900	163.355	175.528	7.489	8.505	7.808	-2.144	0.000	0.000	0.000	0.000	0.000	0.000
8	-117.471	512.214	-14.145	-12.050	9.768	-2.375	4.268	-7.926	-7.291	0.000	0.000	0.000	0.000	0.000
9	1924.422	156.372	178.787	166.948	9.740	-5.300	-1.912	5.253	-4.373	-8.183	0.000	0.000	0.000	0.000
10	-97.704	259.914	1.408	-4.878	21.514	-7.057	-2.469	1.819	4.061	0.020	-0.913	0.000	0.000	0.000
11	793.562	66.889	104.444	115.838	6.608	3.669	-1.506	-4.900	2.074	0.201	1.130	4.242	0.000	0.000
12	-28.444	60.740	0.294	0.697	7.243	-3.060	-2.175	0.207	-0.724	-0.467	-0.716	0.493	-0.263	0.000
13	144.735	12.221	28.914	32.025	3.107	2.713	-0.883	-1.971	-0.363	0.764	0.111	0.152	0.498	0.181
14	0.000	0.000	0.000	0.000	0.000	0.000	0.000	0.000	0.000	0.000	0.000	0.000	0.000	0.000

Table A.5: g coefficients for segment 3(in nanoTesla)

n-m	0	1	2	3	4	5	6	7	8	9	10	11	12	13
1	0.000	5198.341	0.000	0.000	0.000	0.000	0.000	0.000	0.000	0.000	0.000	0.000	0.000	0.000
2	0.000	-2563.295	-448.703	0.000	0.000	0.000	0.000	0.000	0.000	0.000	0.000	0.000	0.000	0.000
3	0.000	-166.394	331.073	-495.256	0.000	0.000	0.000	0.000	0.000	0.000	0.000	0.000	0.000	0.000
4	0.000	31.007	-184.814	133.855	-303.297	0.000	0.000	0.000	0.000	0.000	0.000	0.000	0.000	0.000
5	0.000	204.835	296.891	-170.319	-28.061	108.774	0.000	0.000	0.000	0.000	0.000	0.000	0.000	0.000
6	0.000	-377.549	170.692	107.793	-61.240	-0.910	44.260	0.000	0.000	0.000	0.000	0.000	0.000	0.000
7	0.000	170.090	190.000	-83.145	64.706	28.420	-27.723	-5.579	0.000	0.000	0.000	0.000	0.000	0.000
8	0.000	-300.743	106.460	65.933	-26.344	13.117	11.226	-16.122	-2.168	0.000	0.000	0.000	0.000	0.000
9	0.000	180.927	220.438	-95.028	56.212	17.051	2.606	4.854	-7.985	4.552	0.000	0.000	0.000	0.000
10	0.000	-149.979	83.528	42.606	-3.521	-7.440	1.321	-5.731	0.345	-2.399	-7.846	0.000	0.000	0.000
11	0.000	93.949	110.225	-67.254	44.953	22.792	-6.471	-1.559	-0.455	-1.094	-2.370	-0.735	0.000	0.000
12	0.000	-33.098	24.673	12.941	-7.805	0.515	0.844	-2.047	-0.210	-0.054	-1.125	-0.607	0.839	0.000
13	0.000	16.916	24.414	-15.321	14.142	6.462	-2.087	0.681	0.637	0.438	0.244	-0.100	0.072	-0.882
14	0.000	0.000	0.000	0.000	0.000	0.000	0.000	0.000	0.000	0.000	0.000	0.000	0.000	0.000

Table A.6: h coefficients for segment 3(in nanoTesla)

n-m	0	1	2	3	4	5	6	7	8	9	10	11	12	13
1	-29694.317	-1729.241	0.000	0.000	0.000	0.000	0.000	0.000	0.000	0.000	0.000	0.000	0.000	0.000
2	-2271.993	3069.560	1670.930	0.000	0.000	0.000	0.000	0.000	0.000	0.000	0.000	0.000	0.000	0.000
3	1331.826	-2287.127	1252.964	715.282	0.000	0.000	0.000	0.000	0.000	0.000	0.000	0.000	0.000	0.000
4	931.791	786.920	250.790	-403.702	111.705	0.000	0.000	0.000	0.000	0.000	0.000	0.000	0.000	0.000
5	-225.593	352.433	224.545	-130.072	-168.597	-12.858	0.000	0.000	0.000	0.000	0.000	0.000	0.000	0.000
6	70.612	68.270	73.339	-161.164	-5.908	16.972	-90.323	0.000	0.000	0.000	0.000	0.000	0.000	0.000
7	72.498	-72.841	3.195	33.183	8.996	6.794	7.632	-1.317	0.000	0.000	0.000	0.000	0.000	0.000
8	22.995	6.682	-10.012	-8.125	-16.530	8.858	6.974	-7.814	-7.241	0.000	0.000	0.000	0.000	0.000
9	0.869	10.458	6.746	-8.525	6.056	-8.708	-1.702	9.151	-4.393	-8.169	0.000	0.000	0.000	0.000
10	-3.636	-6.068	0.793	-3.390	-0.479	3.864	1.250	2.047	4.316	0.142	-0.773	0.000	0.000	0.000
11	0.314	-0.895	1.402	1.402	-0.749	0.215	-0.609	0.523	1.958	0.083	0.920	4.338	0.000	0.000
12	-2.483	-0.419	-0.210	0.743	0.192	1.086	-0.429	0.556	-0.467	-0.385	0.037	0.218	-0.178	0.000
13	-1.170	-0.437	1.974	0.023	-1.419	1.302	-0.127	0.560	-0.448	0.289	-0.268	0.509	0.404	0.294
14	0.000	0.000	0.000	0.000	0.000	0.000	0.000	0.000	0.000	0.000	0.000	0.000	0.000	0.000

Table A.7: g coefficients for segment 4

n-m	0	1	2	3	4	5	6	7	8	9	10	11	12	13
1	0.000	5189.590	0.000	0.000	0.000	0.000	0.000	0.000	0.000	0.000	0.000	0.000	0.000	0.000
2	0.000	-2480.723	-456.829	0.000	0.000	0.000	0.000	0.000	0.000	0.000	0.000	0.000	0.000	0.000
3	0.000	-226.081	293.946	-489.901	0.000	0.000	0.000	0.000	0.000	0.000	0.000	0.000	0.000	0.000
4	0.000	270.547	-232.243	119.595	-303.666	0.000	0.000	0.000	0.000	0.000	0.000	0.000	0.000	0.000
5	0.000	46.993	171.614	-133.437	-39.859	106.401	0.000	0.000	0.000	0.000	0.000	0.000	0.000	0.000
6	0.000	-19.365	64.262	65.398	-60.964	0.566	43.734	0.000	0.000	0.000	0.000	0.000	0.000	0.000
7	0.000	-61.181	-23.756	5.108	24.197	14.838	-25.354	-5.848	0.000	0.000	0.000	0.000	0.000	0.000
8	0.000	9.669	-21.125	8.894	-21.521	15.795	9.104	-14.846	-2.248	0.000	0.000	0.000	0.000	0.000
9	0.000	-16.996	13.715	10.577	-6.229	-8.428	8.493	3.780	-8.213	4.427	0.000	0.000	0.000	0.000
10	0.000	0.156	0.717	4.569	5.081	-5.778	-1.020	-3.141	0.329	-2.231	-7.711	0.000	0.000	0.000
11	0.000	1.305	1.745	-3.160	-2.687	1.048	-0.757	-2.697	-0.818	-1.274	-2.208	-0.769	0.000	0.000
12	0.000	-1.100	0.838	3.005	-2.501	0.631	0.443	0.038	-0.155	0.489	-0.633	-0.621	0.974	0.000
13	0.000	-0.993	0.657	-0.084	-0.590	-0.447	-0.133	0.775	0.410	0.513	0.511	-0.280	-0.225	-0.968
14	0.000	0.000	0.000	0.000	0.000	0.000	0.000	0.000	0.000	0.000	0.000	0.000	0.000	0.000

Table A.8: h coefficients for segment 4

n-m	0	1	2	3	4	5	6	7	8	9	10	11	12	13
1	-29627.047	-1731.534	0.000	0.000	0.000	0.000	0.000	0.000	0.000	0.000	0.000	0.000	0.000	0.000
2	-2272.063	3067.892	1671.067	0.000	0.000	0.000	0.000	0.000	0.000	0.000	0.000	0.000	0.000	0.000
3	1446.884	-2294.382	1252.904	715.686	0.000	0.000	0.000	0.000	0.000	0.000	0.000	0.000	0.000	0.000
4	934.003	782.405	250.852	-403.642	111.736	0.000	0.000	0.000	0.000	0.000	0.000	0.000	0.000	0.000
5	-48.799	338.634	224.306	-128.020	-168.719	-12.786	0.000	0.000	0.000	0.000	0.000	0.000	0.000	0.000
6	74.205	61.076	72.841	-160.921	-5.520	17.003	-90.322	0.000	0.000	0.000	0.000	0.000	0.000	0.000
7	267.093	-91.204	2.512	37.427	8.876	7.005	7.770	-1.352	0.000	0.000	0.000	0.000	0.000	0.000
8	26.605	-0.898	-11.056	-7.521	-15.914	8.857	6.867	-7.842	-7.225	0.000	0.000	0.000	0.000	0.000
9	152.296	-6.918	5.533	-3.390	6.263	-8.390	-1.271	9.154	-4.436	-8.214	0.000	0.000	0.000	0.000
10	-1.109	-11.219	-0.318	-2.485	0.172	3.799	1.115	2.079	4.351	0.181	-0.780	0.000	0.000	0.000
11	77.650	-12.129	-0.214	5.008	0.112	0.269	0.043	0.657	1.857	0.081	0.967	4.283	0.000	0.000
12	-1.328	-2.357	-0.738	1.484	0.372	0.842	-0.419	0.516	-0.514	-0.235	-0.125	0.226	-0.176	0.000
13	19.338	-4.691	0.773	1.084	-0.133	1.123	0.263	0.795	-0.610	0.376	-0.165	0.482	0.400	0.204
14	0.000	0.000	0.000	0.000	0.000	0.000	0.000	0.000	0.000	0.000	0.000	0.000	0.000	0.000

Table A.9: g coefficients for segment 5

n-m	0	1	2	3	4	5	6	7	8	9	10	11	12	13
1	0.000	5189.624	0.000	0.000	0.000	0.000	0.000	0.000	0.000	0.000	0.000	0.000	0.000	0.000
2	0.000	-2480.292	-456.209	0.000	0.000	0.000	0.000	0.000	0.000	0.000	0.000	0.000	0.000	0.000
3	0.000	-224.732	298.337	-489.907	0.000	0.000	0.000	0.000	0.000	0.000	0.000	0.000	0.000	0.000
4	0.000	271.519	-229.634	119.620	-303.687	0.000	0.000	0.000	0.000	0.000	0.000	0.000	0.000	0.000
5	0.000	50.514	182.977	-133.325	-39.864	106.378	0.000	0.000	0.000	0.000	0.000	0.000	0.000	0.000
6	0.000	-17.960	69.364	65.350	-60.979	0.305	43.753	0.000	0.000	0.000	0.000	0.000	0.000	0.000
7	0.000	-56.305	-6.689	5.776	24.057	14.922	-25.407	-5.851	0.000	0.000	0.000	0.000	0.000	0.000
8	0.000	11.070	-14.826	8.630	-21.596	15.183	9.047	-14.864	-2.199	0.000	0.000	0.000	0.000	0.000
9	0.000	-12.856	30.150	11.942	-6.701	-8.430	8.307	3.658	-8.189	4.461	0.000	0.000	0.000	0.000
10	0.000	1.173	5.743	4.014	4.739	-6.541	-1.211	-3.132	0.203	-2.287	-7.695	0.000	0.000	0.000
11	0.000	3.322	11.614	-1.481	-3.244	0.742	-0.942	-2.843	-0.850	-1.225	-2.184	-0.773	0.000	0.000
12	0.000	-0.737	3.192	2.278	-3.145	0.258	0.067	-0.184	-0.254	0.240	-0.715	-0.654	0.888	0.000
13	0.000	-0.670	3.457	1.282	-0.857	-0.994	-0.076	0.514	0.302	0.546	0.549	-0.252	-0.178	-0.853
14	0.000	0.000	0.000	0.000	0.000	0.000	0.000	0.000	0.000	0.000	0.000	0.000	0.000	0.000

Table A.10: h coefficients for segment 5

n-m	0	1	2	3	4	5	6	7	8	9	10	11	12	13
1	-29742.533	-660.936	0.000	0.000	0.000	0.000	0.000	0.000	0.000	0.000	0.000	0.000	0.000	0.000
2	-2334.126	2858.013	950.114	0.000	0.000	0.000	0.000	0.000	0.000	0.000	0.000	0.000	0.000	0.000
3	1587.115	-3941.110	1146.221	-1780.814	0.000	0.000	0.000	0.000	0.000	0.000	0.000	0.000	0.000	0.000
4	1140.596	1264.309	764.827	68.869	4058.813	0.000	0.000	0.000	0.000	0.000	0.000	0.000	0.000	0.000
5	-485.171	2488.553	391.022	2212.358	-947.087	-4434.342	0.000	0.000	0.000	0.000	0.000	0.000	0.000	0.000
6	-170.949	-599.335	-155.127	-748.291	-3003.078	318.066	-4804.375	0.000	0.000	0.000	0.000	0.000	0.000	0.000
7	306.537	-2094.006	-148.947	-1748.626	843.604	3115.680	-405.322	-18358.191	0.000	0.000	0.000	0.000	0.000	0.000
8	196.896	610.277	-21.515	432.443	1863.990	-209.932	2563.240	-625.676	2528.820	0.000	0.000	0.000	0.000	0.000
9	-159.439	1344.310	67.243	891.480	-534.463	-1783.727	586.344	8207.035	3607.908	-9609.024	0.000	0.000	0.000	0.000
10	-72.431	-341.882	76.482	-196.588	-770.274	91.252	-1014.281	473.458	-93.104	2115.368	8563.393	0.000	0.000	0.000
11	94.583	-568.014	-1.339	-249.610	204.504	655.311	-351.359	-2674.678	-1283.697	2574.602	-1258.061	31562.185	0.000	0.000
12	8.001	90.790	-28.566	41.075	153.612	-15.364	196.679	-142.149	-73.798	-403.194	-1115.481	-911.344	3431.359	0.000
13	-31.712	118.076	-9.545	21.477	-36.143	-117.538	83.656	417.797	190.120	-391.589	258.196	-2924.192	-886.156	-27826.337
14	0.000	0.000	0.000	0.000	0.000	0.000	0.000	0.000	0.000	0.000	0.000	0.000	0.000	0.000

Table A.11: g coefficients for segment 6 (in nanoTesla)

n-m	0	1	2	3	4	5	6	7	8	9	10	11	12	13
1	0.000	5157.962	0.000	0.000	0.000	0.000	0.000	0.000	0.000	0.000	0.000	0.000	0.000	0.000
2	0.000	-2172.719	4924.143	0.000	0.000	0.000	0.000	0.000	0.000	0.000	0.000	0.000	0.000	0.000
3	0.000	-477.175	444.207	-2588.032	0.000	0.000	0.000	0.000	0.000	0.000	0.000	0.000	0.000	0.000
4	0.000	-400.408	-6133.610	-127.900	-2854.162	0.000	0.000	0.000	0.000	0.000	0.000	0.000	0.000	0.000
5	0.000	711.137	-165.897	2523.086	1584.679	1248.075	0.000	0.000	0.000	0.000	0.000	0.000	0.000	0.000
6	0.000	889.908	5555.685	389.221	1767.675	-1456.340	-11285.973	0.000	0.000	0.000	0.000	0.000	0.000	0.000
7	0.000	-983.173	423.524	-2741.357	-1675.370	-453.091	-4873.771	-6038.145	0.000	0.000	0.000	0.000	0.000	0.000
8	0.000	-785.883	-3664.497	-255.120	-1092.604	1284.616	5230.074	-1265.068	895.462	0.000	0.000	0.000	0.000	0.000
9	0.000	747.293	-354.704	2001.459	1098.965	185.001	3655.790	1882.187	-1282.122	30564.469	0.000	0.000	0.000	0.000
10	0.000	431.383	1535.912	133.606	406.778	-628.780	-1826.724	596.341	-487.798	-504.100	1526.063	0.000	0.000	0.000
11	0.000	-370.587	174.778	-909.076	-437.173	-81.446	-1582.383	-438.499	241.513	-7760.919	2692.605	35792.671	0.000	0.000
12	0.000	-112.088	-316.622	-29.892	-74.243	139.737	317.379	-129.990	108.333	92.636	-148.130	1341.538	3998.376	0.000
13	0.000	82.029	-30.679	204.677	83.783	23.113	317.173	47.120	8.536	1153.740	-575.644	-3976.006	-4077.786	7975.338
14	0.000	0.000	0.000	0.000	0.000	0.000	0.000	0.000	0.000	0.000	0.000	0.000	0.000	0.000

Table A.12: h coefficients for segment 6

n-m	0	1	2	3	4	5	6	7	8	9	10	11	12	13
1	-29677.643	-1730.288	0.000	0.000	0.000	0.000	0.000	0.000	0.000	0.000	0.000	0.000	0.000	0.000
2	-2262.274	3070.121	1671.148	0.000	0.000	0.000	0.000	0.000	0.000	0.000	0.000	0.000	0.000	0.000
3	1337.838	-2288.824	1251.999	715.318	0.000	0.000	0.000	0.000	0.000	0.000	0.000	0.000	0.000	0.000
4	933.072	787.571	250.903	-403.420	111.570	0.000	0.000	0.000	0.000	0.000	0.000	0.000	0.000	0.000
5	-219.624	350.615	222.379	-130.178	-168.449	-12.938	0.000	0.000	0.000	0.000	0.000	0.000	0.000	0.000
6	72.015	68.675	73.881	-161.324	-6.043	16.763	-90.284	0.000	0.000	0.000	0.000	0.000	0.000	0.000
7	77.712	-74.657	0.229	33.316	9.191	6.797	7.443	-1.277	0.000	0.000	0.000	0.000	0.000	0.000
8	24.014	6.966	-9.458	-8.191	-16.618	8.859	7.076	-7.846	-7.117	0.000	0.000	0.000	0.000	0.000
9	4.357	8.951	3.354	-8.565	6.355	-8.887	-1.584	9.125	-4.245	-8.145	0.000	0.000	0.000	0.000
10	-3.245	-5.835	1.323	-3.529	-0.582	3.673	1.140	1.991	4.185	0.382	-0.805	0.000	0.000	0.000
11	1.709	-2.064	-1.734	1.393	-0.406	0.165	-0.668	0.590	1.956	0.075	1.019	4.039	0.000	0.000
12	-3.050	-0.038	-0.069	0.546	0.061	0.745	-0.628	0.292	-0.362	-0.400	0.187	0.017	-0.347	0.000
13	-2.122	-1.043	-0.401	-0.284	-1.214	1.097	-0.399	0.487	-0.400	0.368	-0.205	0.638	-0.017	0.170
14	0.000	0.000	0.000	0.000	0.000	0.000	0.000	0.000	0.000	0.000	0.000	0.000	0.000	0.000

Table A.13: g coefficients for segment 7 (in nanoTesla)

n-m	0	1	2	3	4	5	6	7	8	9	10	11	12	13
1	0.000	5188.442	0.000	0.000	0.000	0.000	0.000	0.000	0.000	0.000	0.000	0.000	0.000	0.000
2	0.000	-2479.663	-457.278	0.000	0.000	0.000	0.000	0.000	0.000	0.000	0.000	0.000	0.000	0.000
3	0.000	-227.455	293.912	-489.864	0.000	0.000	0.000	0.000	0.000	0.000	0.000	0.000	0.000	0.000
4	0.000	272.718	-232.465	119.397	-303.782	0.000	0.000	0.000	0.000	0.000	0.000	0.000	0.000	0.000
5	0.000	44.673	172.237	-132.740	-39.646	106.322	0.000	0.000	0.000	0.000	0.000	0.000	0.000	0.000
6	0.000	-17.294	63.629	65.214	-61.125	0.725	43.754	0.000	0.000	0.000	0.000	0.000	0.000	0.000
7	0.000	-63.475	-23.461	6.454	24.096	14.690	-25.344	-5.832	0.000	0.000	0.000	0.000	0.000	0.000
8	0.000	11.901	-21.789	8.630	-21.467	15.645	9.042	-14.952	-2.154	0.000	0.000	0.000	0.000	0.000
9	0.000	-19.151	13.933	12.384	-6.179	-8.498	8.424	3.851	-8.321	4.592	0.000	0.000	0.000	0.000
10	0.000	1.844	-0.184	4.316	5.049	-5.817	-1.091	-3.056	0.335	-2.181	-7.622	0.000	0.000	0.000
11	0.000	0.089	1.764	-1.350	-2.603	0.915	-0.791	-2.775	-0.742	-1.243	-2.104	-0.864	0.000	0.000
12	0.000	-0.398	-0.023	2.766	-2.401	0.685	0.437	-0.027	0.044	0.462	-0.765	-0.596	0.805	0.000
13	0.000	-1.195	0.236	1.425	-0.596	-0.542	-0.043	0.617	0.328	0.745	0.390	-0.342	-0.365	-1.127
14	0.000	0.000	0.000	0.000	0.000	0.000	0.000	0.000	0.000	0.000	0.000	0.000	0.000	0.000

Table A.14: h coefficients for segment 7 (in nanoTesla)

A.2 External Coefficients of Models for Different Segments

$q_{1,0}$	$q_{1,1}$	$s_{1,1}$	$q_{2,0}$	$s_{2,1}$	$q_{2,1}$	$q_{2,2}$	$s_{2,2}$
14.326	3.075	-3.317	3.556	0.084	-0.344	0.015	-1.034

Table A.15: external coefficients for segment 1

$q_{1,0}$	$q_{1,1}$	$s_{1,1}$	$q_{2,0}$	$s_{2,1}$	$q_{2,1}$	$q_{2,2}$	$s_{2,2}$
32.392	1.447	-2.841	9.310	0.066	-0.358	-0.139	0.045

Table A.16: external coefficients for segment 2(in nanoTesla)

$q_{1,0}$	$q_{1,1}$	$s_{1,1}$	$q_{2,0}$	$s_{2,1}$	$q_{2,1}$	$q_{2,2}$	$s_{2,2}$
-5.439	0.578	-4.094	5.825	-1.831	2.063	0.105	-0.402

Table A.17: external coefficients for segment 3(in nanoTesla)

$q_{1,0}$	$q_{1,1}$	$s_{1,1}$	$q_{2,0}$	$s_{2,1}$	$q_{2,1}$	$q_{2,2}$	$s_{2,2}$
73.166	1.577	-3.031	2.945	0.389	-0.174	-0.094	-0.197

Table A.18: external coefficients for segment 4

$q_{1,0}$	$q_{1,1}$	$s_{1,1}$	$q_{2,0}$	$s_{2,1}$	$q_{2,1}$	$q_{2,2}$	$s_{2,2}$
56.701	1.149	-3.412	3.369	0.625	-0.152	-0.023	-0.142

Table A.19: external coefficients for segment 5

$q_{1,0}$	$q_{1,1}$	$s_{1,1}$	$q_{2,0}$	$s_{2,1}$	$q_{2,1}$	$q_{2,2}$	$s_{2,2}$
-51.413	-73.638	29.650	-20.268	5.286	-13.510	37.698	-151.101

Table A.20: external coefficients for segment 6

$q_{1,0}$	$q_{1,1}$	$s_{1,1}$	$q_{2,0}$	$s_{2,1}$	$q_{2,1}$	$q_{2,2}$	$s_{2,2}$
60.817	0.041	-2.890	-3.149	1.093	0.324	-0.091	-0.208

Table A.21: external coefficients for segment 6 (in nanoTesla)

A.3 MEME Coefficients

Disturbance category	$\tilde{q}_1^0$	$\tilde{q}_1^1$	$\tilde{s}_1^1$	Case
A	-0.837	0.048	0.106	NN
B	-0.867	-0.024	0.132	NN
C	-0.874	-0.023	0.110	NN
D	-0.877	-0.016	0.137	NN
A	-0.022	0.178	0.180	ND
B	-0.486	0.013	0.084	ND
C	-0.590	-0.020	0.131	ND
D	-0.664	0.015	0.113	ND
A	-1.014	-0.054	0.201	DN
B	-0.999	-0.258	0.354	DN
C	-1.124	-0.156	0.240	DN
D	-0.692	-0.128	0.095	DN
A	-0.816	-0.213	-0.424	DD
B	-0.663	-0.166	0.027	DD
C	-0.758	-0.153	0.027	DD
D	-0.845	0.004	0.033	DD

Table A.22: MEME Coefficients

Appendix B

Histograms

In this Appendix are presented the error histograms for the testing of the various models in the 7 segments, First are presented the histograms for the night side experiments and then for the day side experiments.

B.1 Night

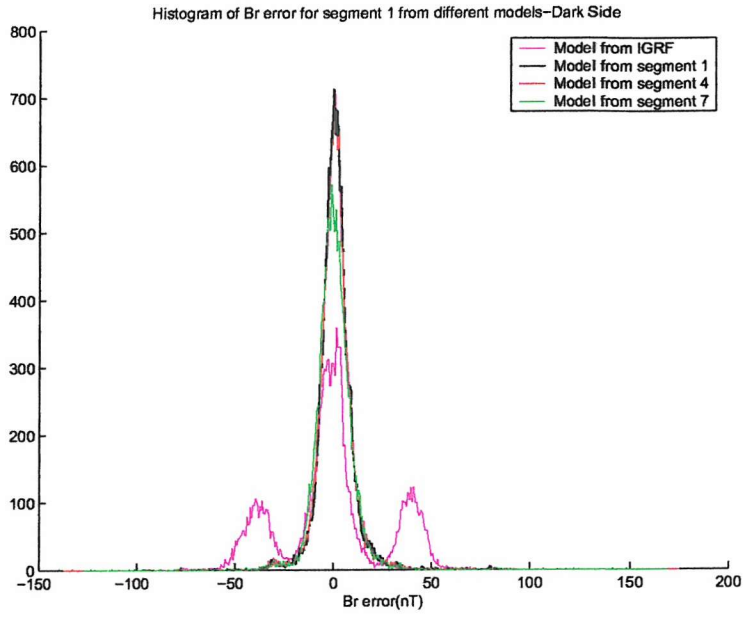

(a) Segment1

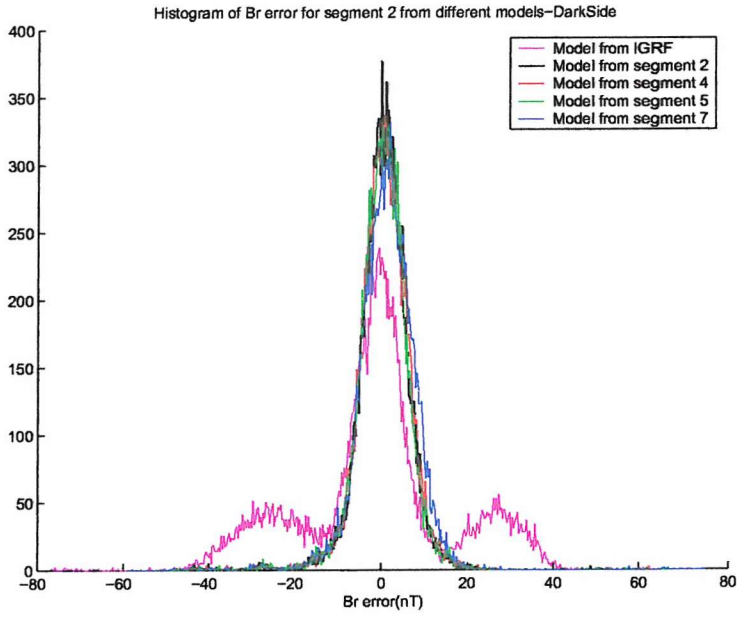

(b) Segment2

Figure B.1: Histogram of B_r error for (a)segment 1 (b)segment 2

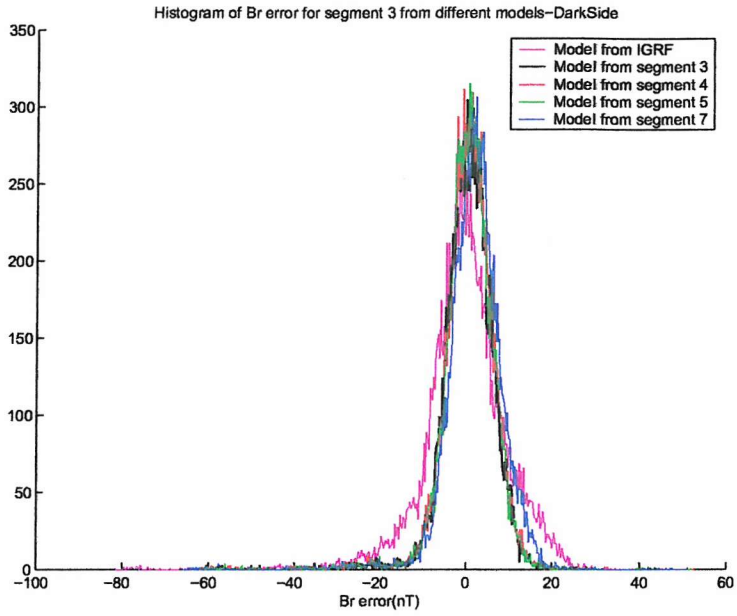

(a) Segment3

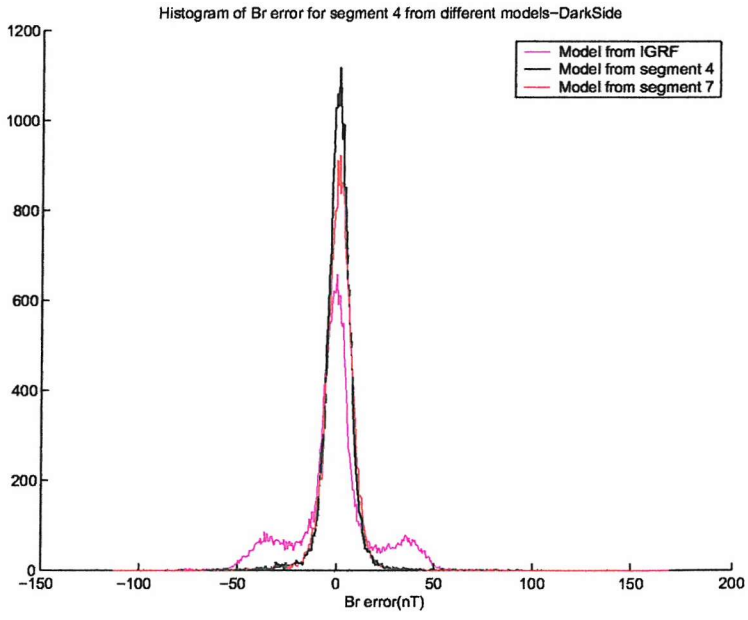

(b) Segment4

Figure B.2: Histogram of B_r error for (a)segment 3 (b)segment 4

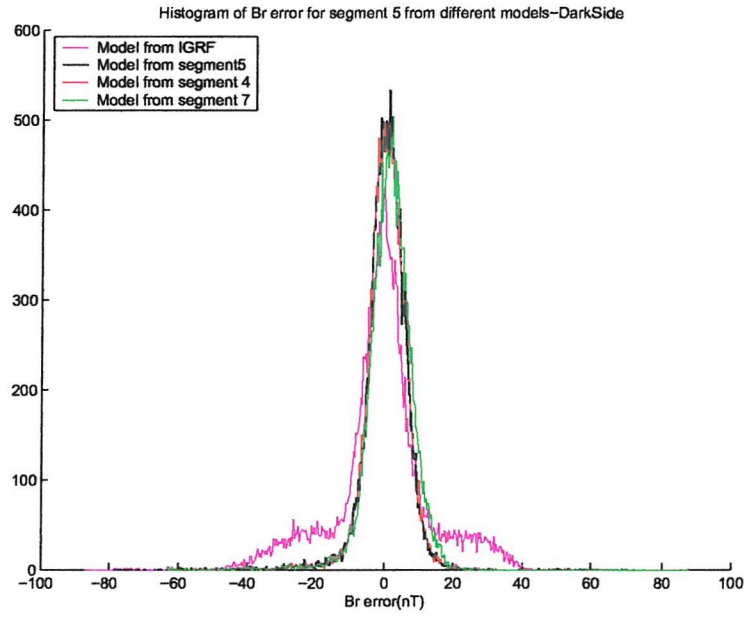

(a) Segment5

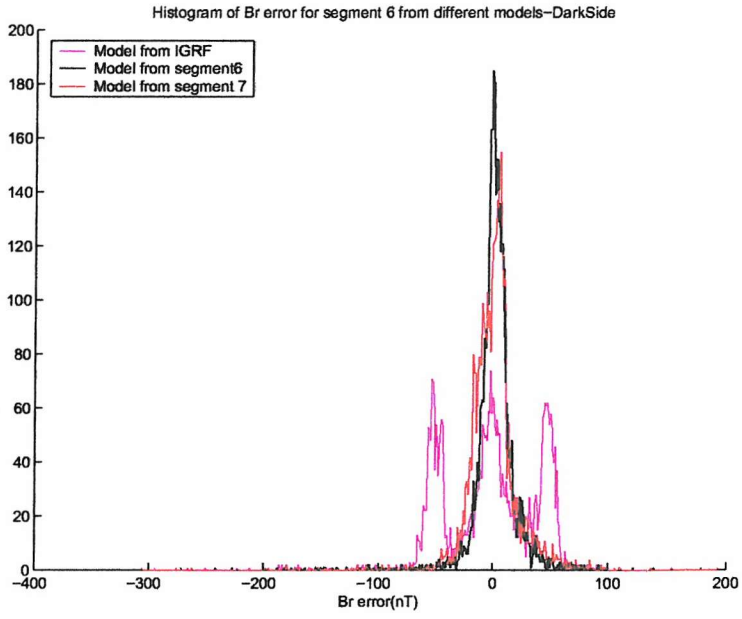

(b) Segment6

Figure B.3: Histogram of B_r error for (a)segment 5 (b)segment 6

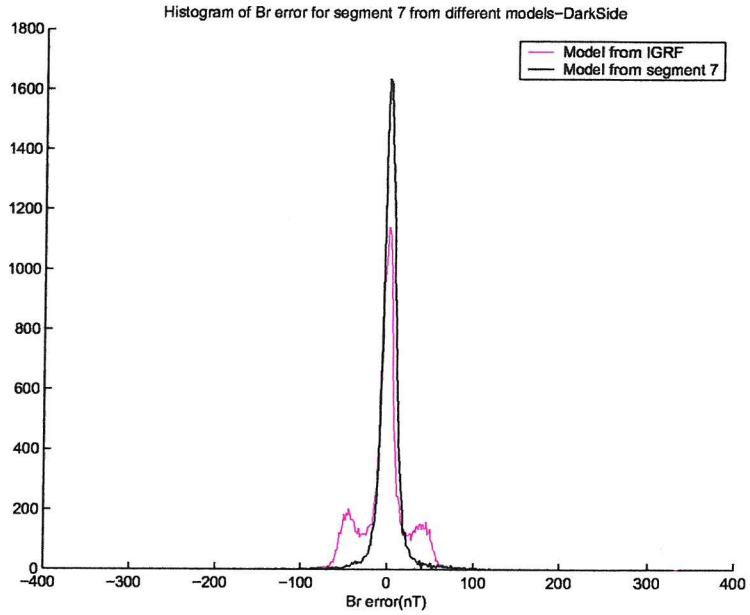

(a) Segment7

Figure B.4: Histogram of B_r error for (a)segment 7 (b)segment

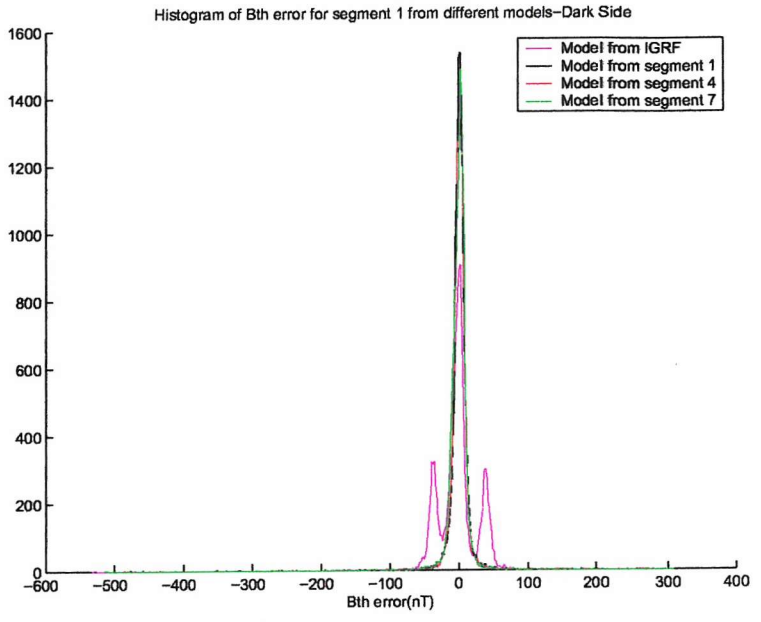

(a) Segment1

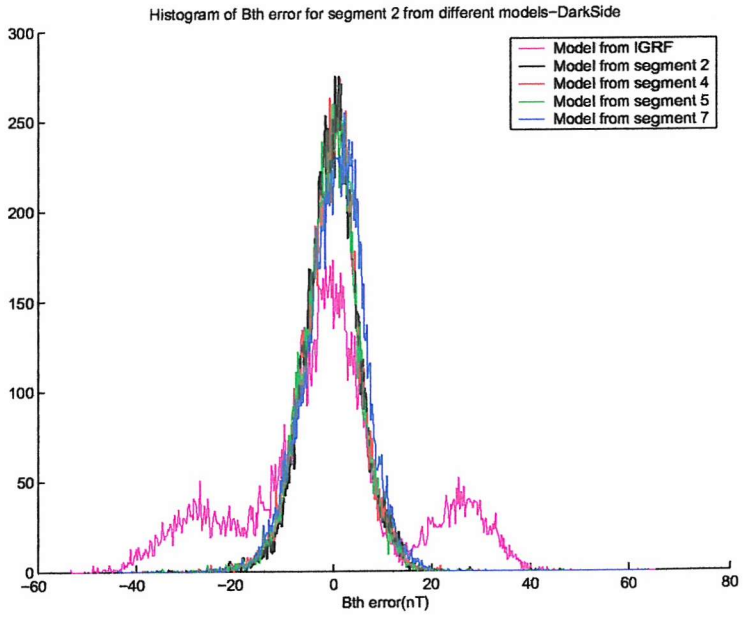

(b) Segment2

Figure B.5: Histogram of B_ϕ error for (a)segment 1 (b)segment 2

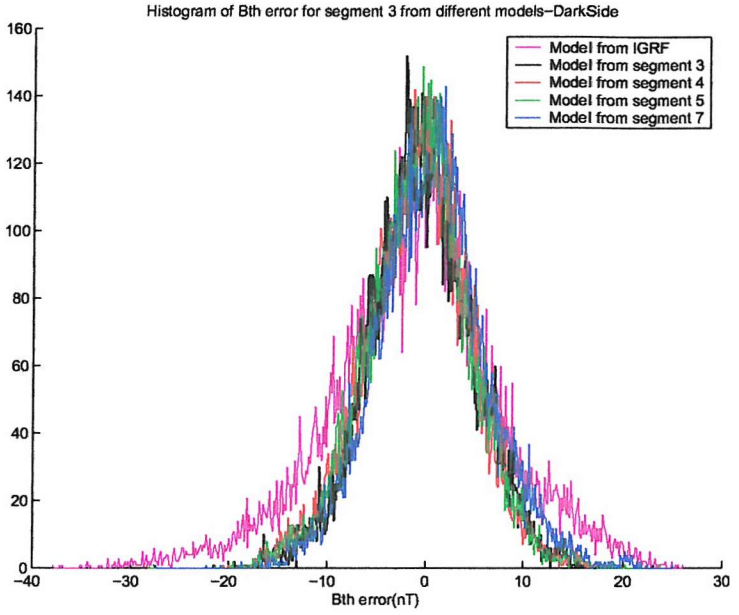

(a) Segment3

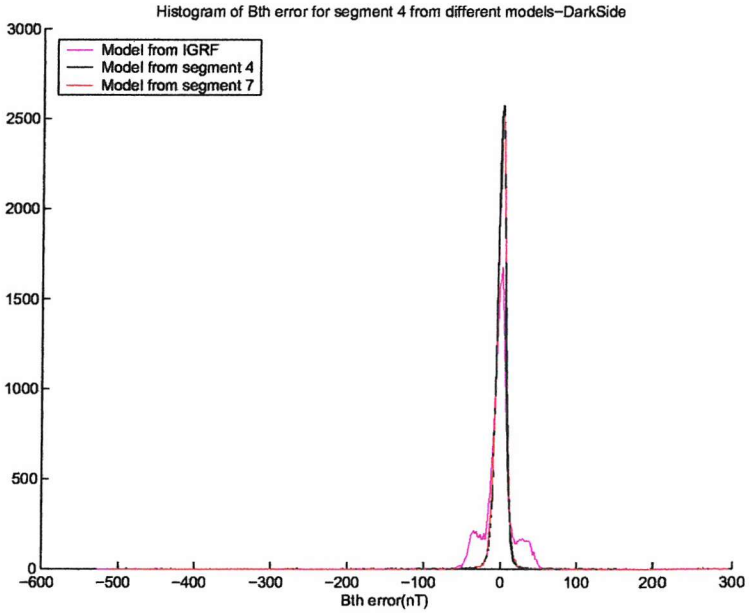

(b) Segment4

Figure B.6: Histogram of B_ϕ error for (a)segment 3 (b)segment 4

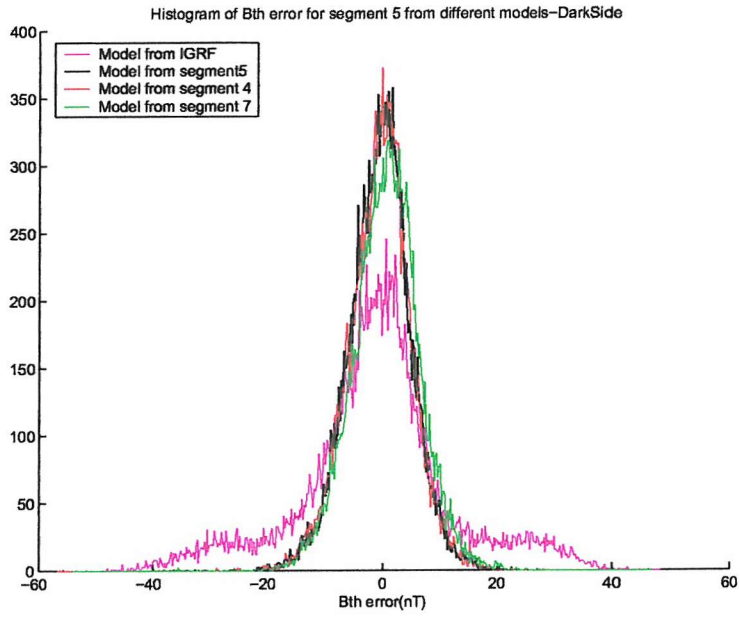

(a) Segment5

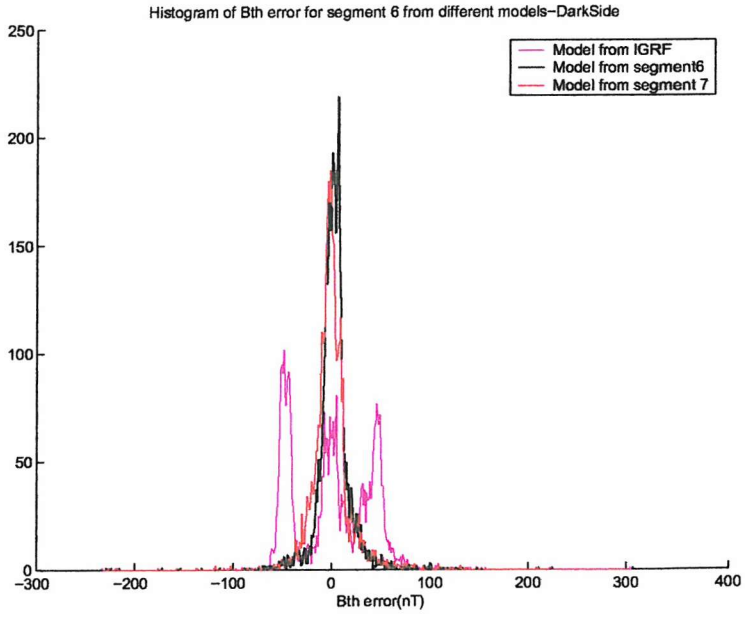

(b) Segment6

Figure B.7: Histogram of B_ϕ error for (a)segment 5 (b)segment 6

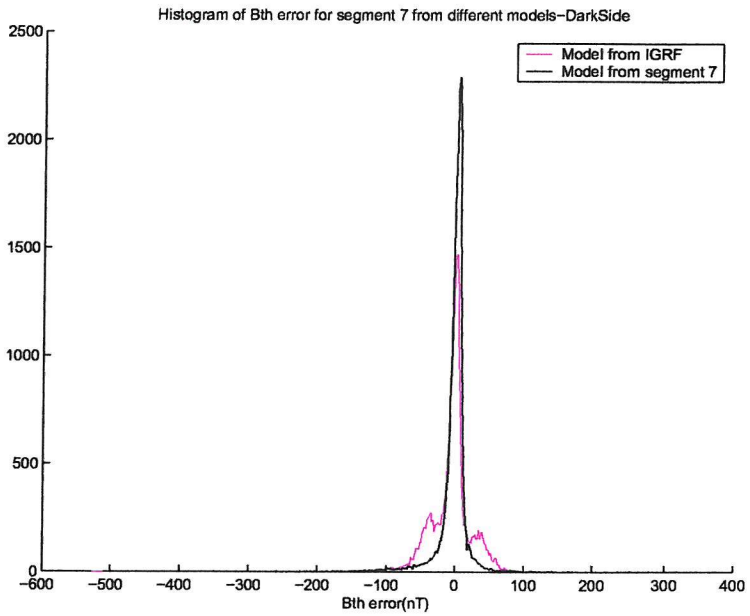

(a) Segment7

Figure B.8: Histogram of B_ϕ error for (a)segment 7

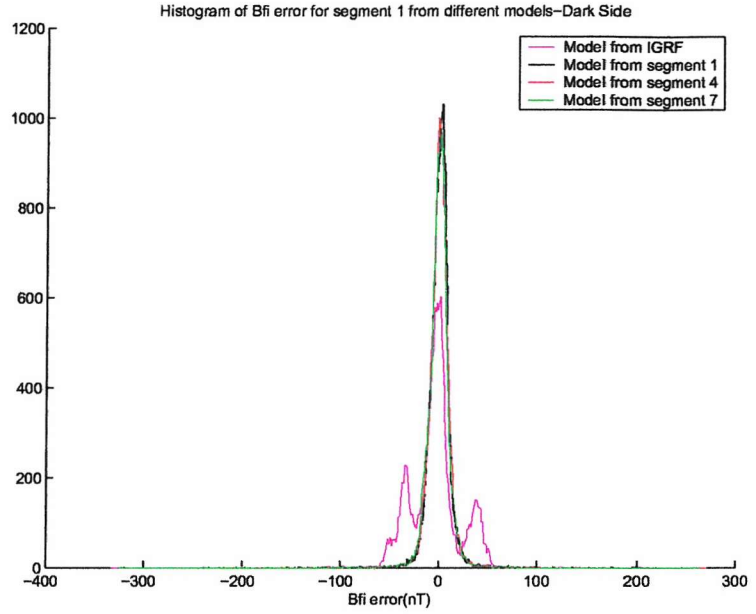

(a) Segment1

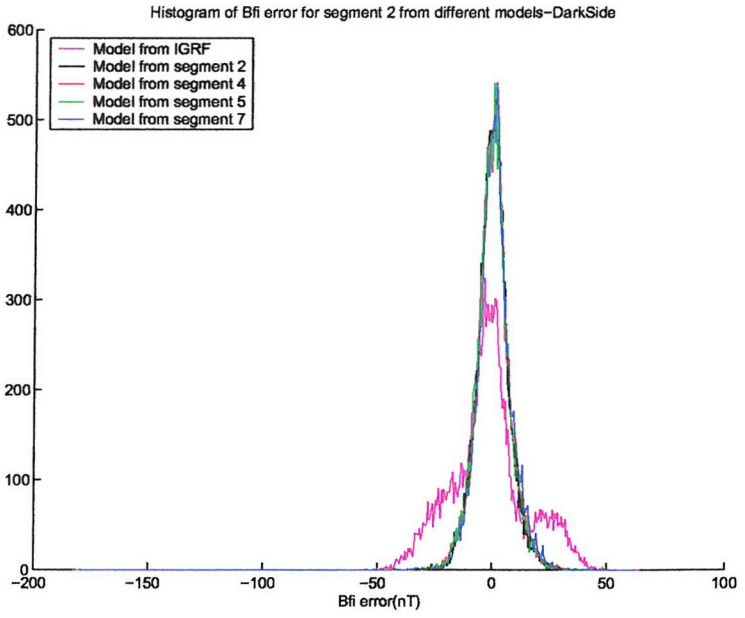

(b) Segment2

Figure B.9: Histogram of B_θ error for (a)segment 1 (b)segment 2

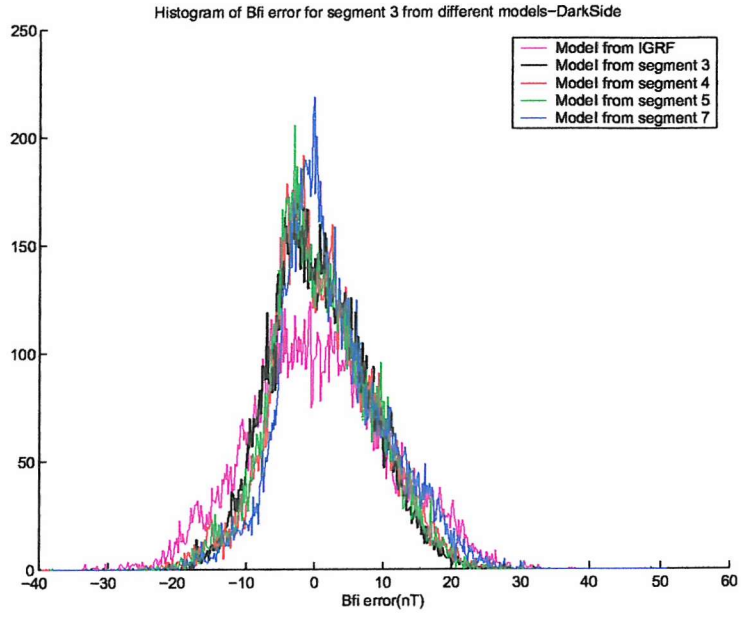

(a) Segment3

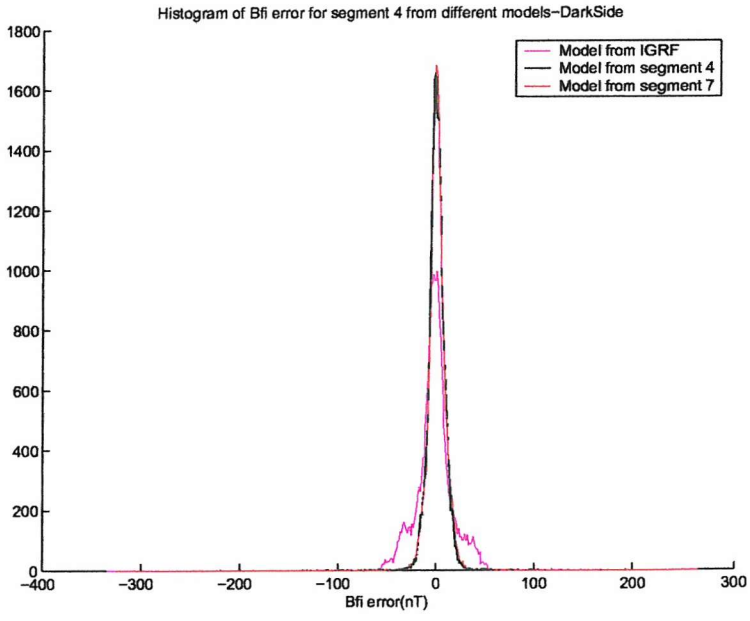

(b) Segment4

Figure B.10: Histogram of B_θ error for (a)segment 3 (b)segment 4

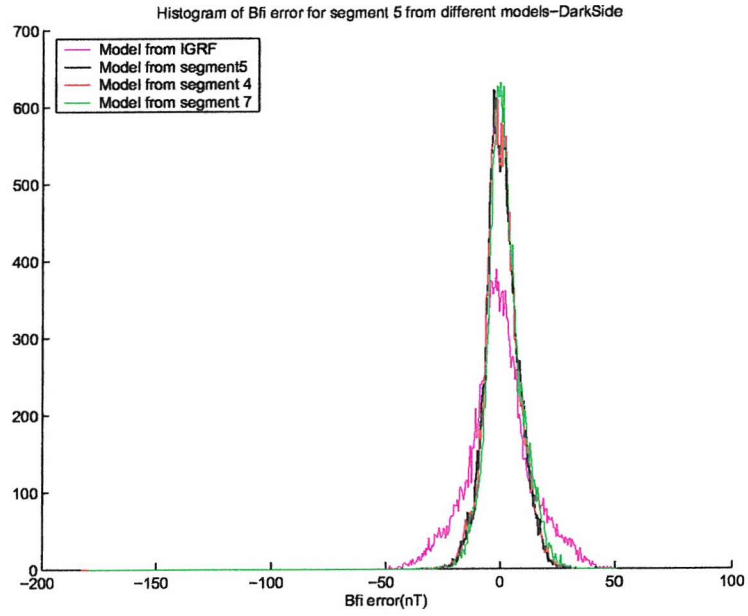

(a) Segment5

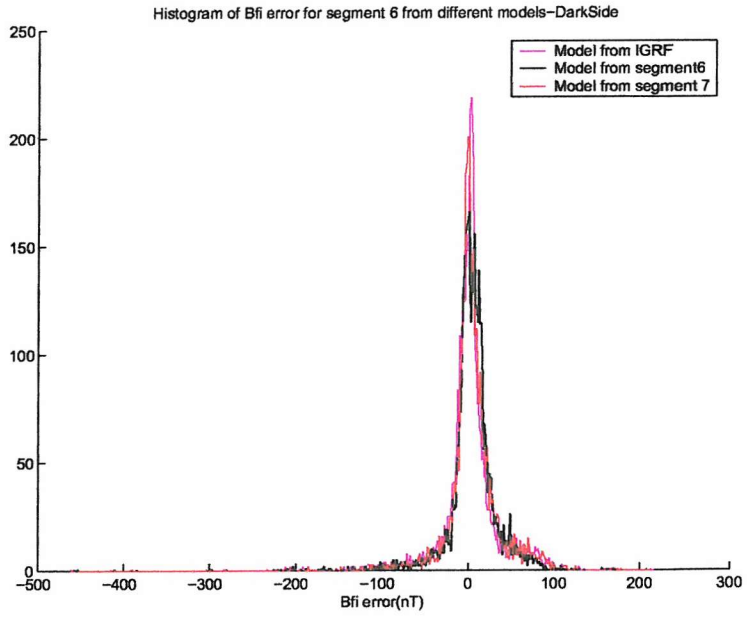

(b) Segment6

Figure B.11: Histogram of B_θ error for (a)segment 5 (b)segment 6

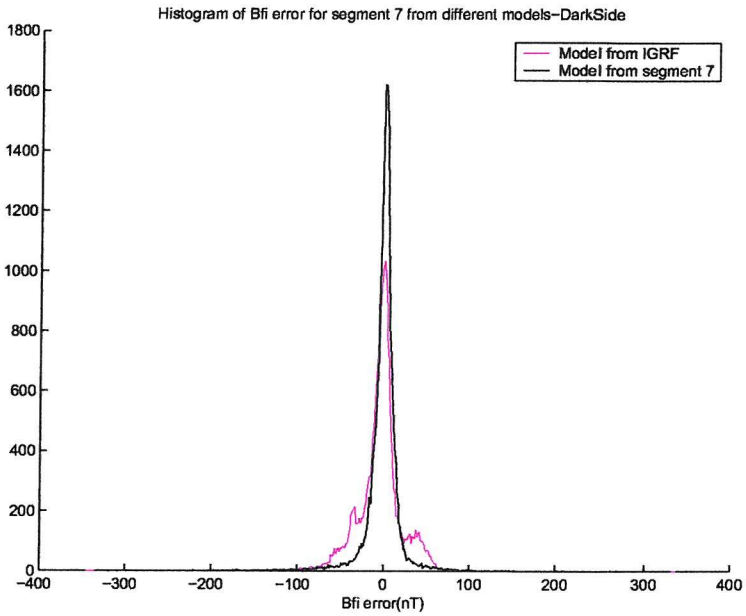

(a) Segment7

Figure B.12: Histogram of B_θ error for (a)segment 7

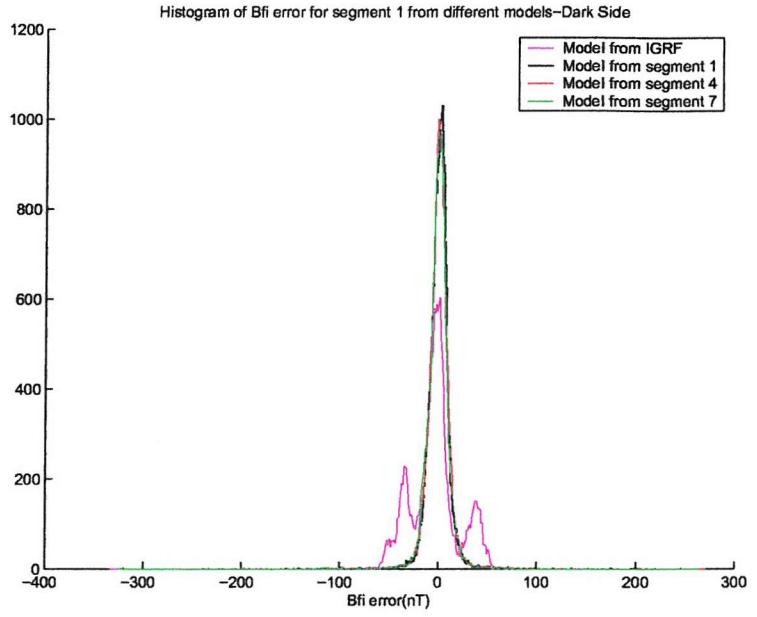

(a) Segment1

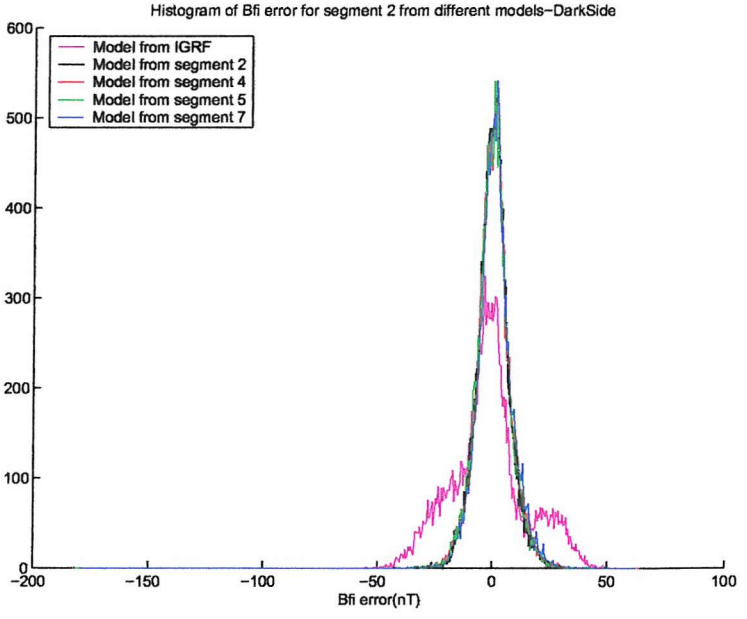

(b) Segment2

Figure B.13: Histogram of B_θ error for (a)segment 1 (b)segment 2

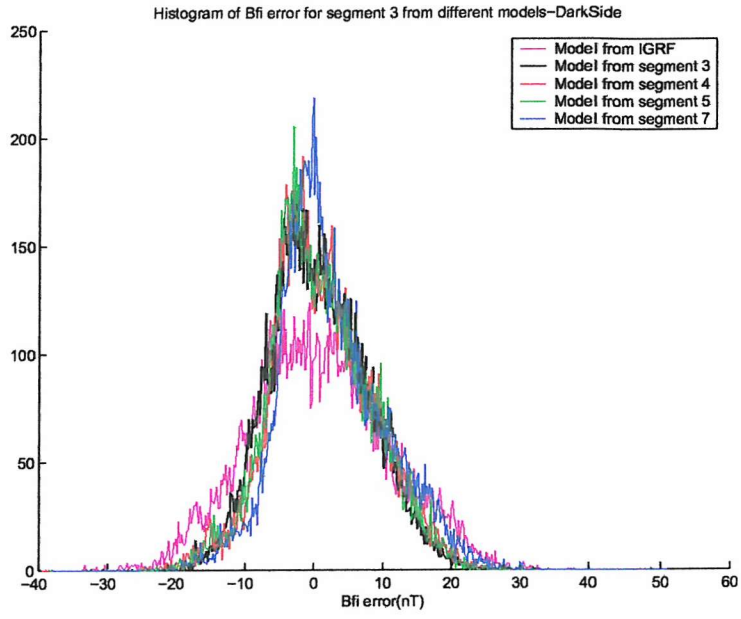

(a) Segment3

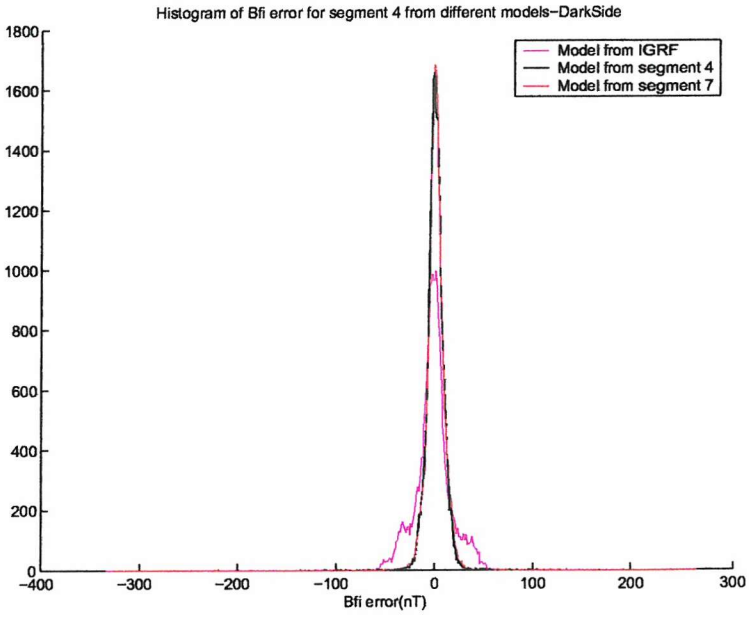

(b) Segment4

Figure B.14: Histogram of B_θ error for (a)segment 3 (b)segment 4

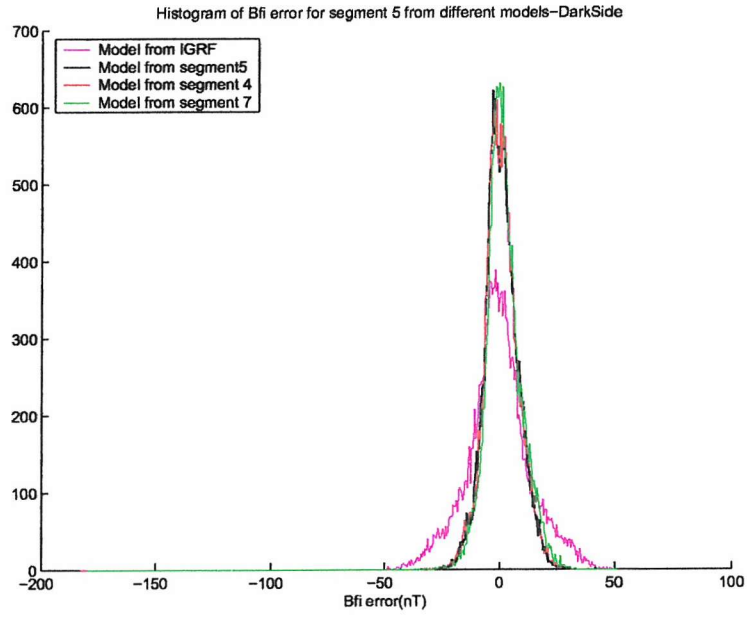

(a) Segment5

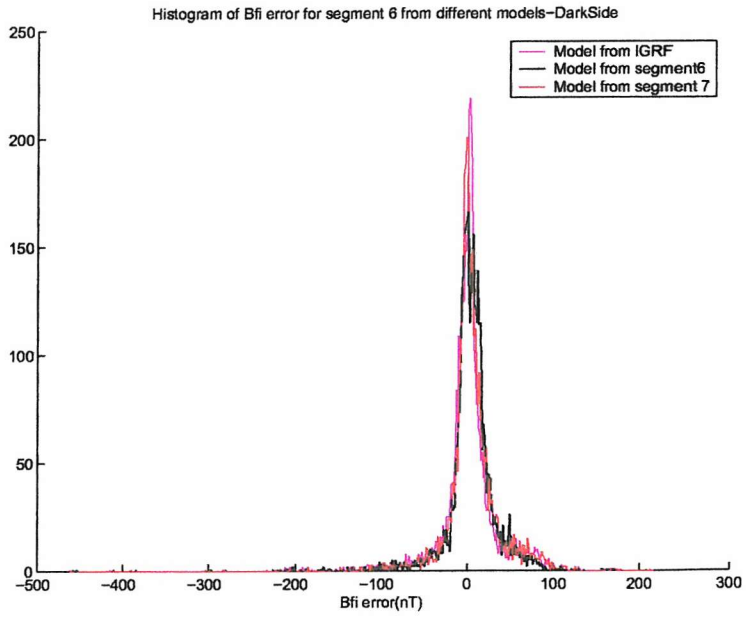

(b) Segment6

Figure B.15: Histogram of B_θ error for (a)segment 5 (b)segment 6

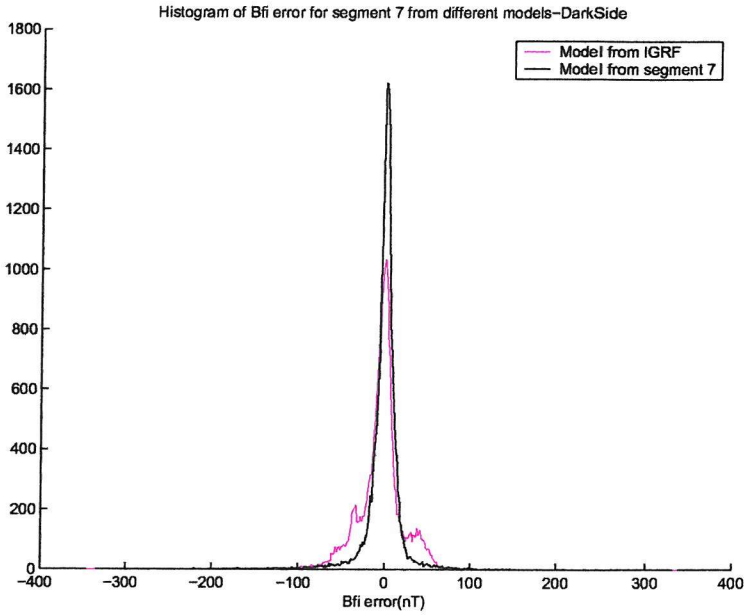

(a) Segment7

Figure B.16: Histogram of B_θ error for (a)segment 7

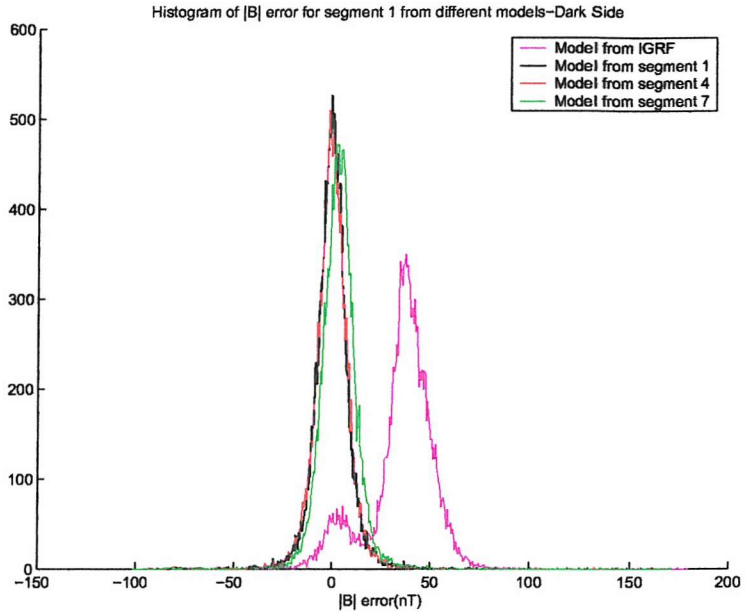

(a) Segment1

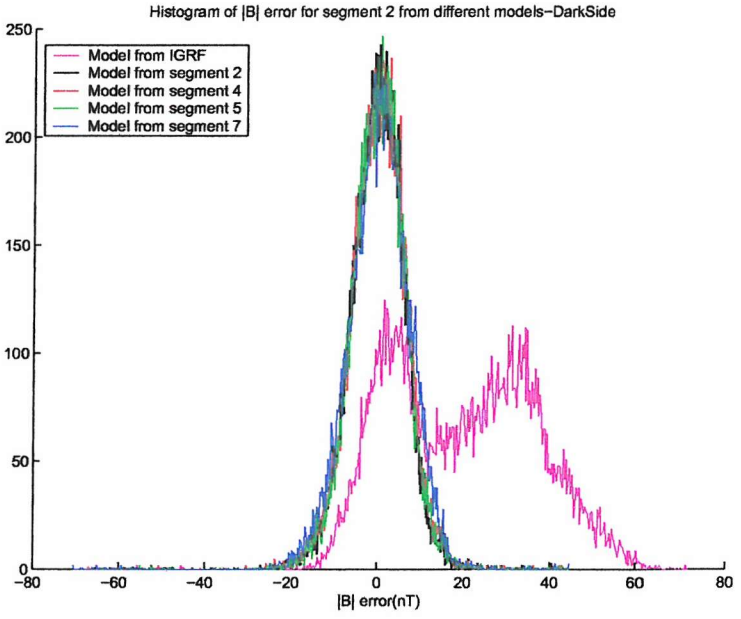

(b) Segment2

Figure B.17: Histogram of $|B|$ error for (a)segment 1 (b)segment 2

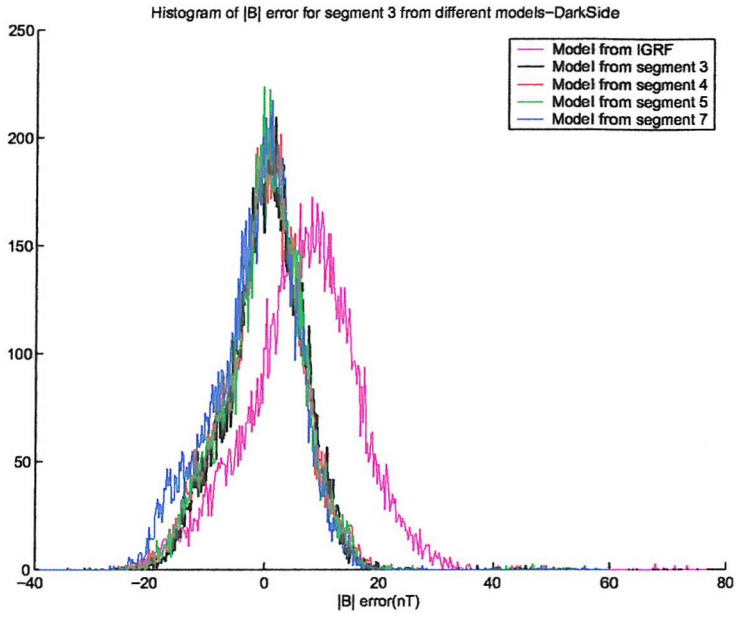

(a) Segment3

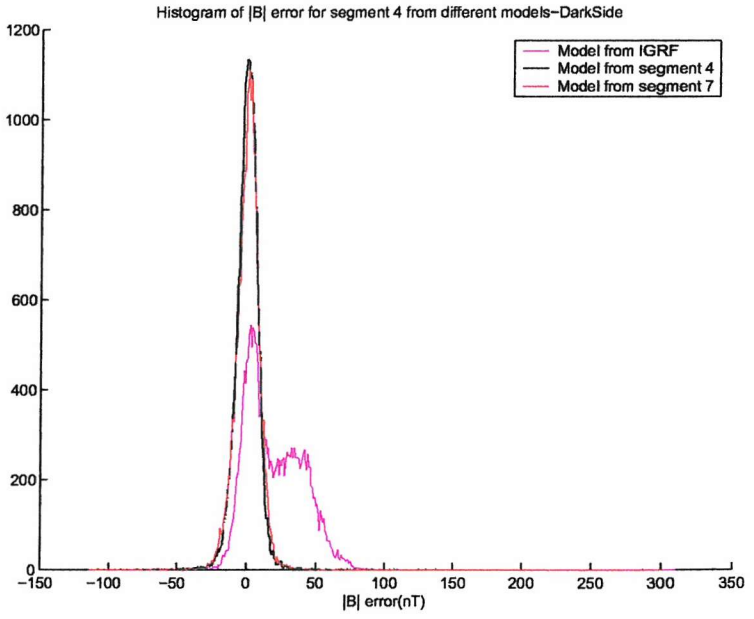

(b) Segment4

Figure B.18: Histogram of $|B|$ error for (a)segment 3 (b)segment 4

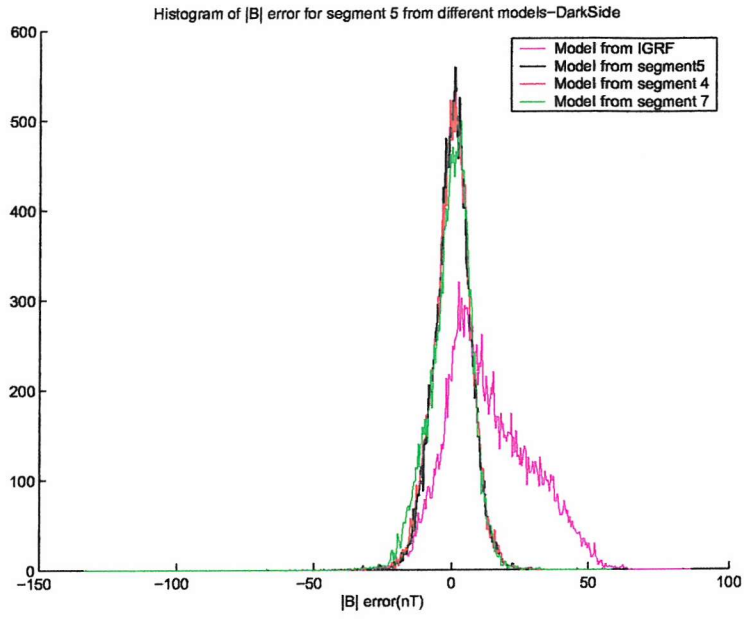

(a) Segment5

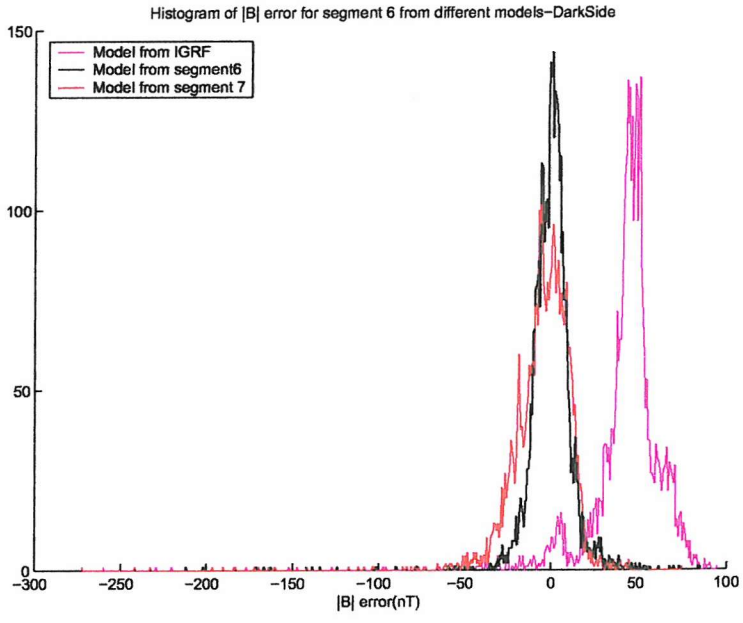

(b) Segment6

Figure B.19: Histogram of $|B|$ error for (a)segment 5 (b)segment 6

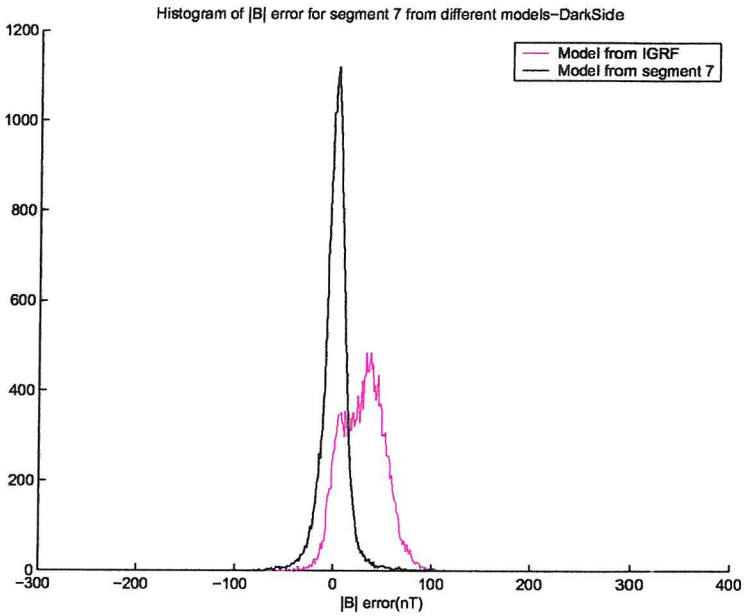

(a) Segment7

Figure B.20: Histogram of $|B|$ error for (a)segment 7

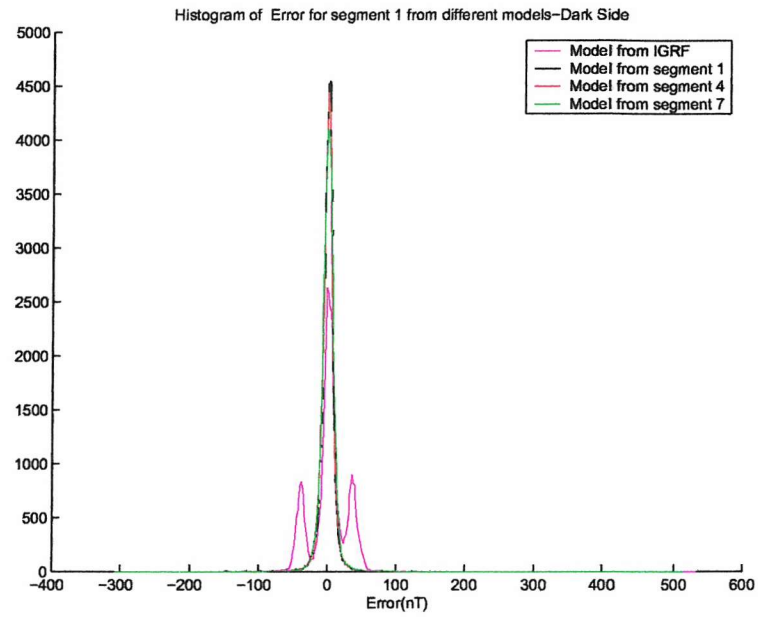

(a) Segment1

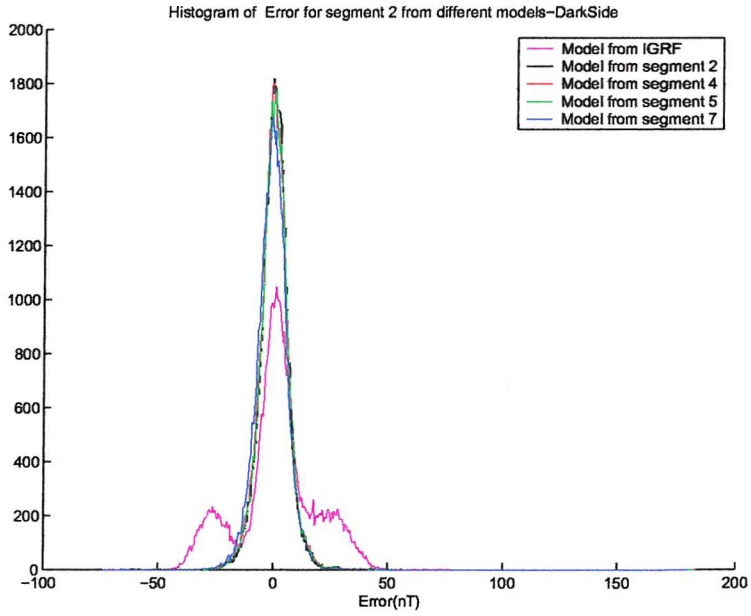

(b) Segment2

Figure B.21: Histogram of Error for (a)segment 1 (b)segment 2

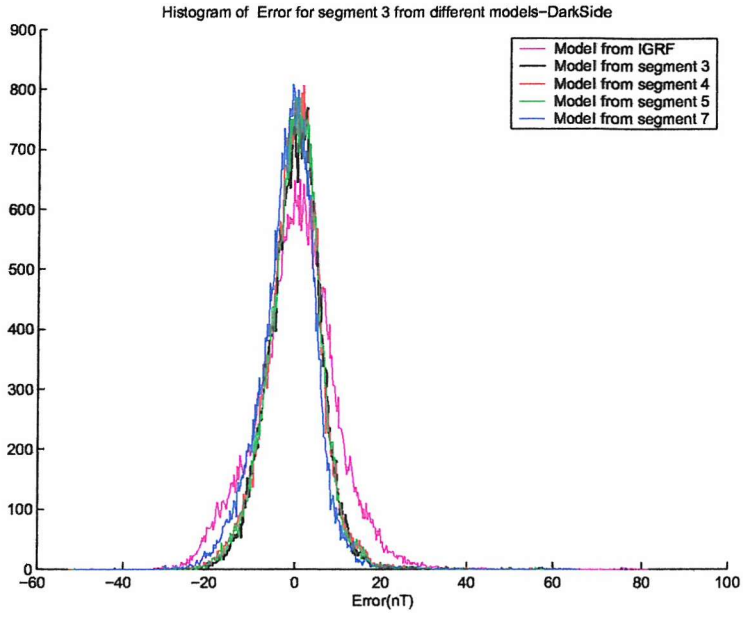

(a) Segment3

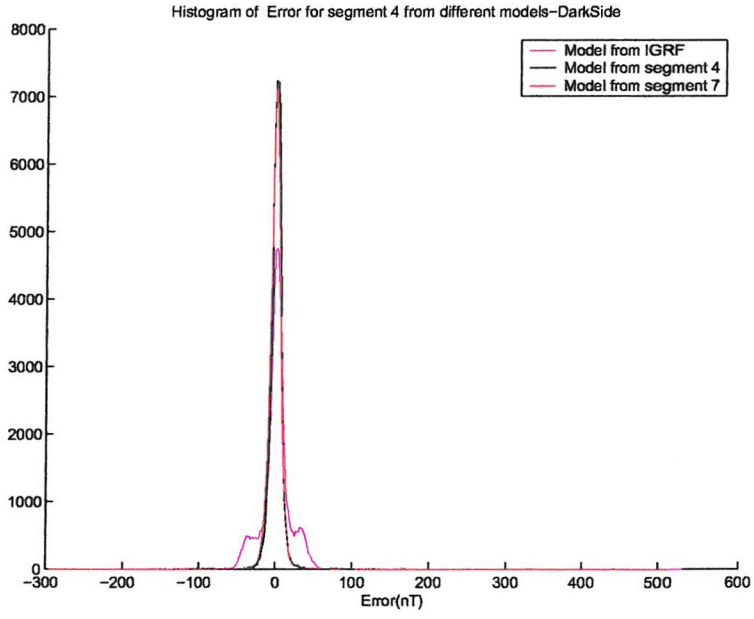

(b) Segment4

Figure B.22: Histogram of Error for (a)segment 3 (b)segment 4

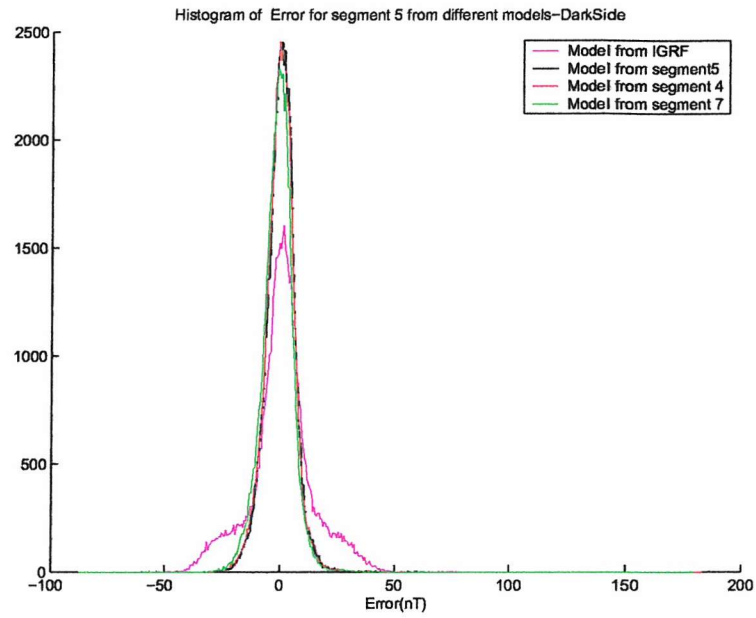

(a) Segment5

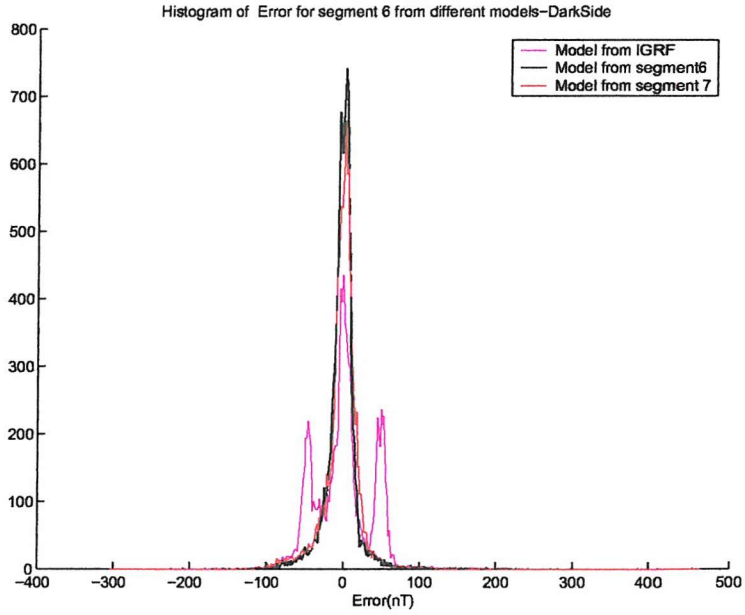

(b) Segment6

Figure B.23: Histogram of Error for (a)segment 5 (b)segment 6

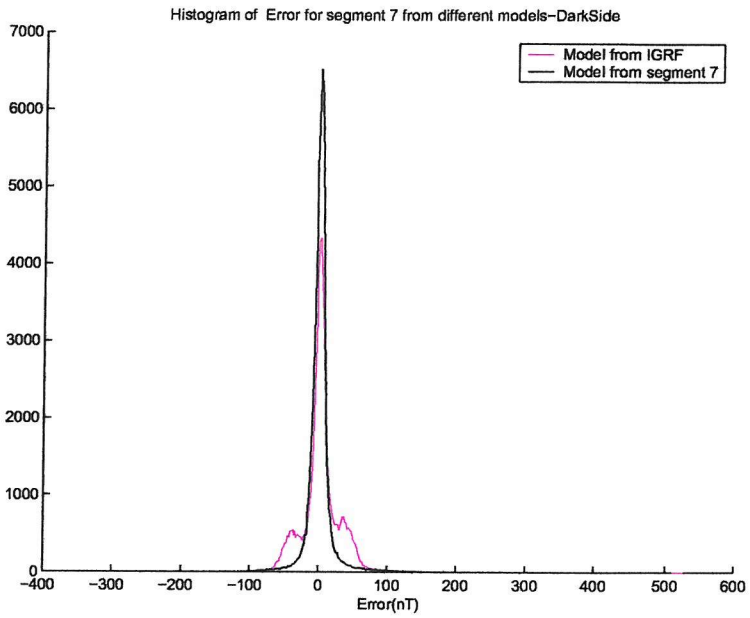

(a) Segment7

Figure B.24: Histogram of Error for (a)segment 7

B.2 Day

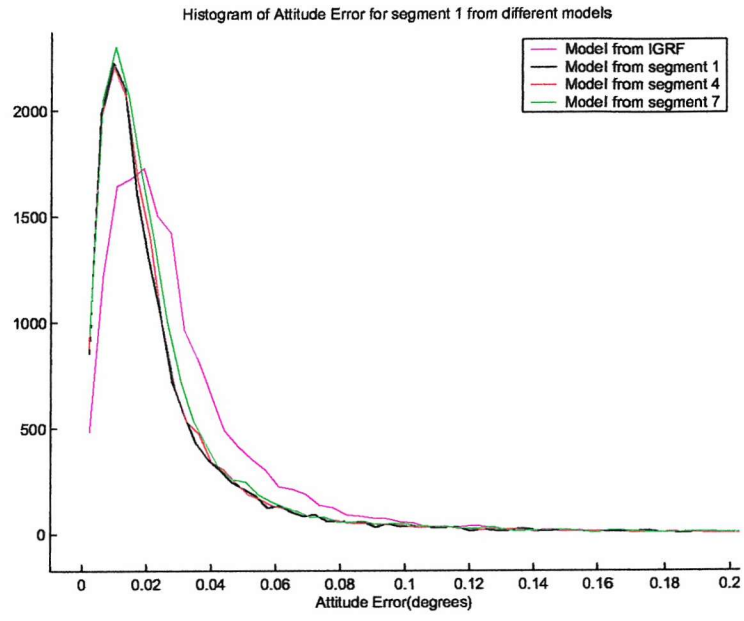

(a) Segment1

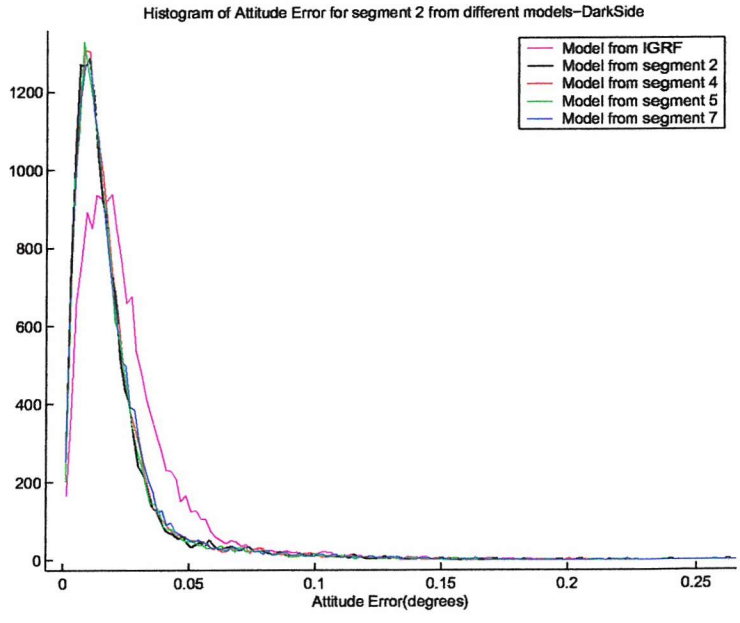

(b) Segment2

Figure B.25: Histogram of Attitude error for (a)segment 1 (b)segment 2

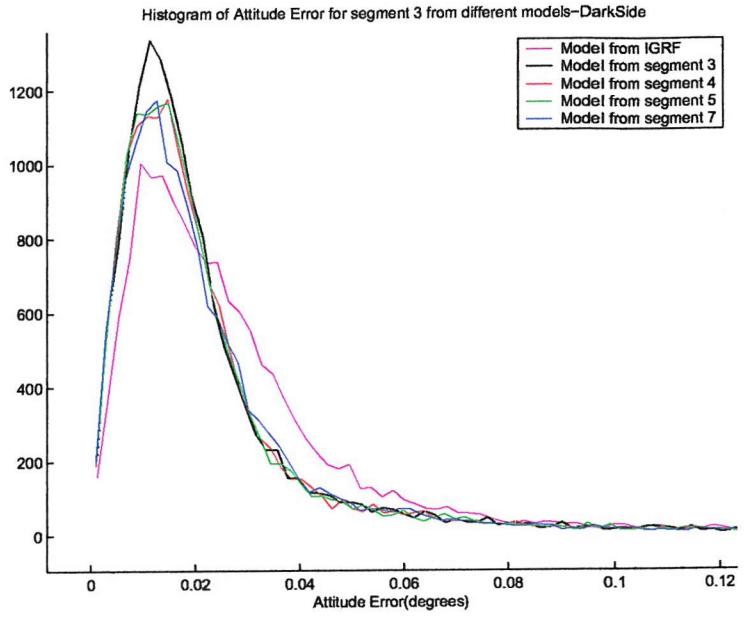

(a) Segment3

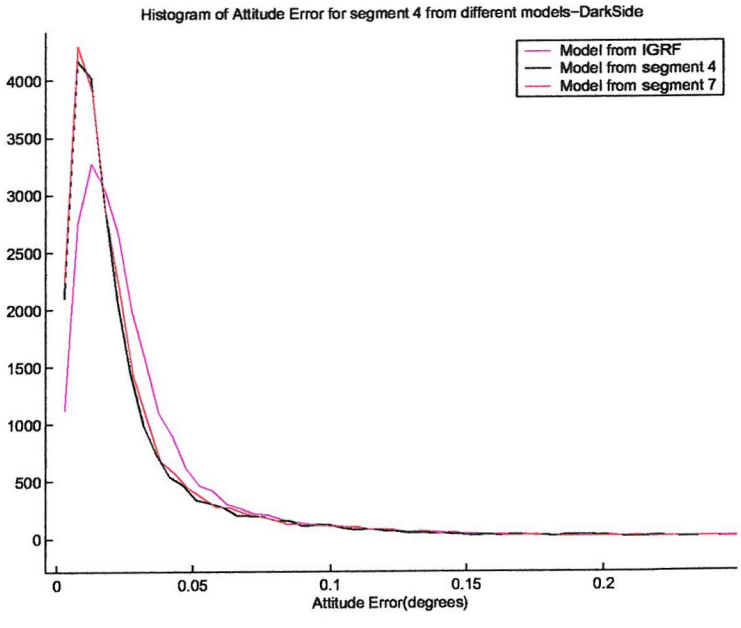

(b) Segment4

Figure B.26: Histogram of Attitude error for (a)segment 3 (b)segment 4

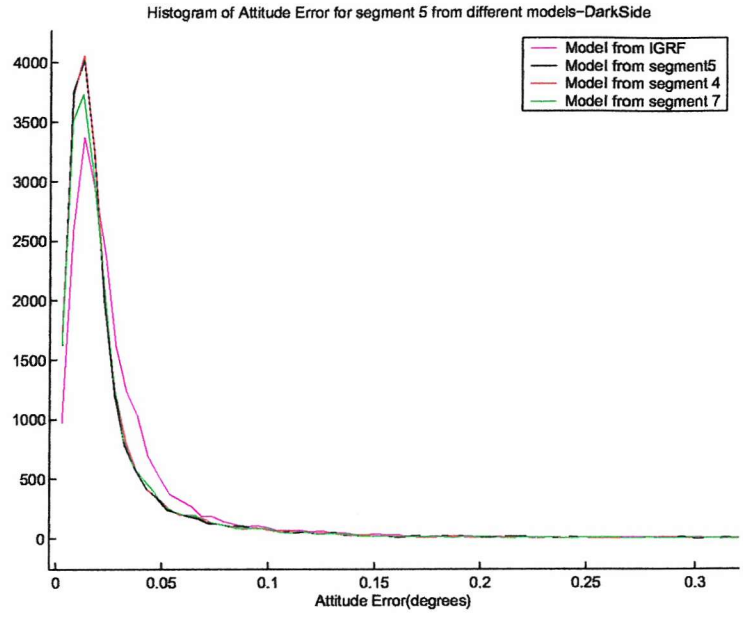

(a) Segment5

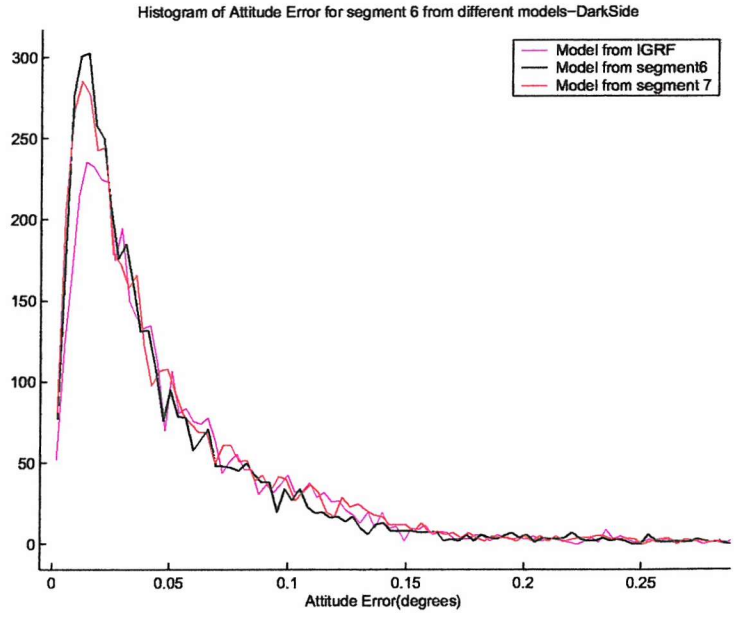

(b) Segment6

Figure B.27: Histogram of Attitude error for (a)segment 5 (b)segment 6

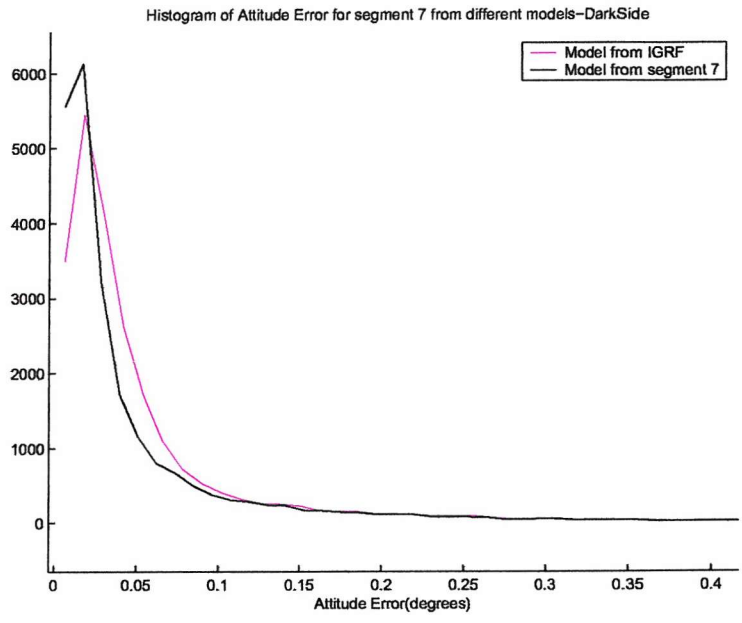

(a) Segment7

Figure B.28: Histogram of Attitude error for (a)segment 7

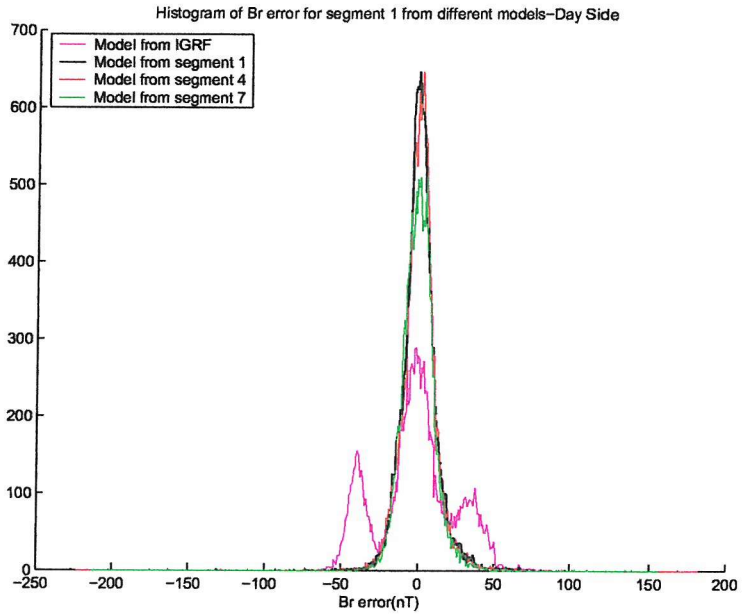

(a) Segment1

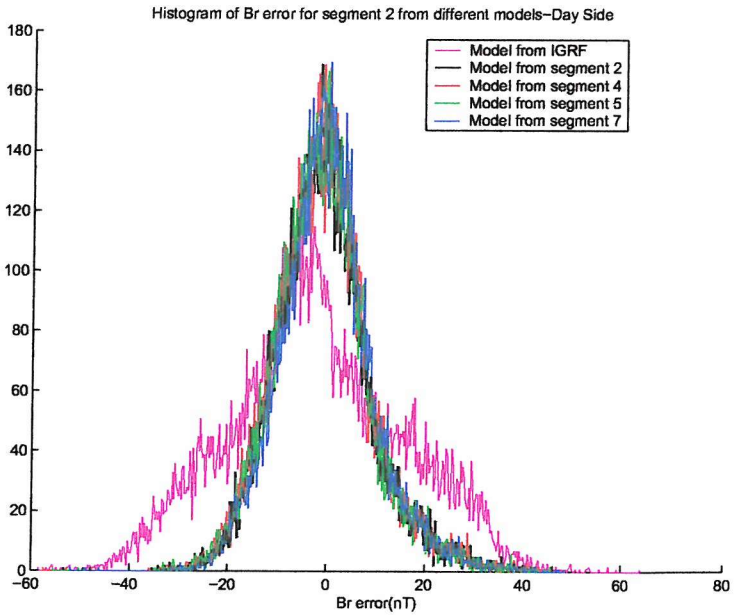

(b) Segment2

Figure B.29: Histogram of B_r error for (a)segment 1 (b)segment 2

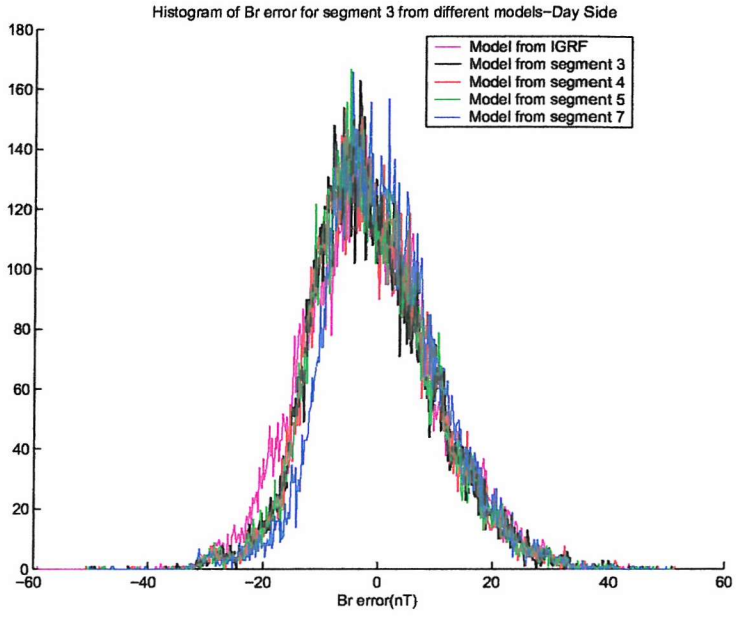

(a) Segment3

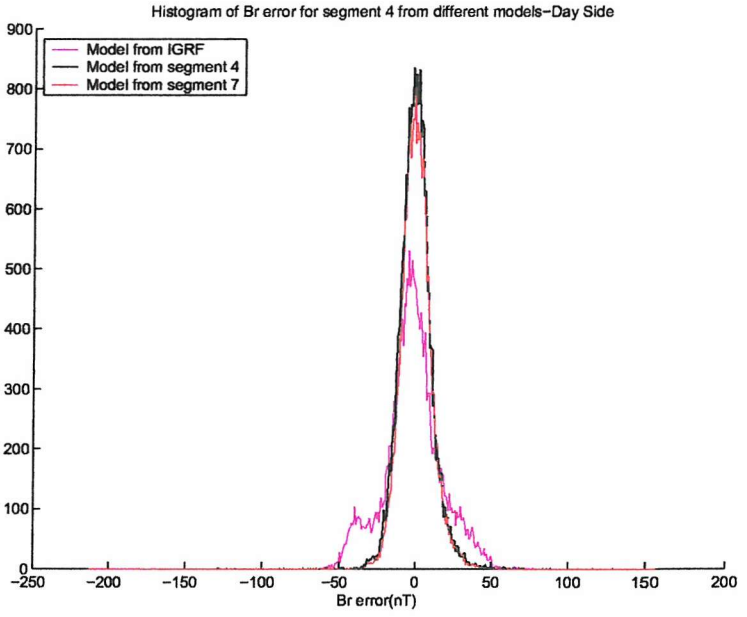

(b) Segment4

Figure B.30: Histogram of B_r error for (a)segment 3 (b)segment 4

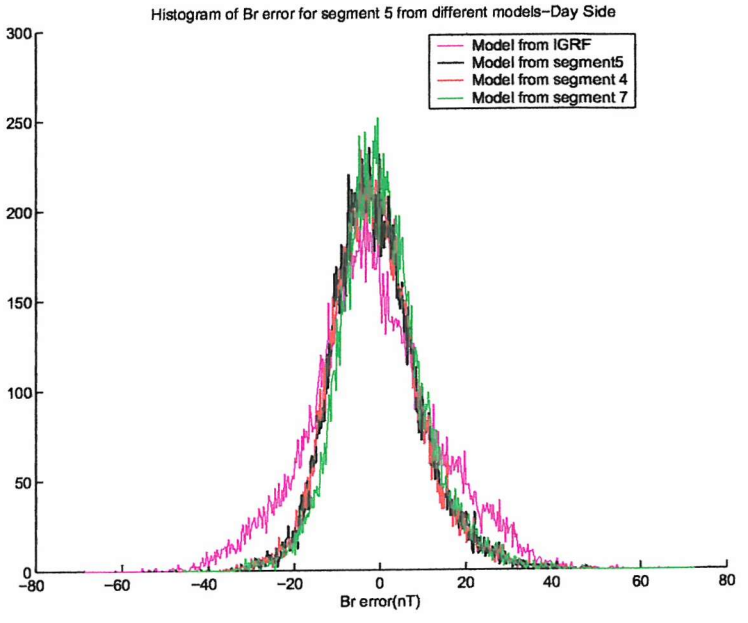

(a) Segment5

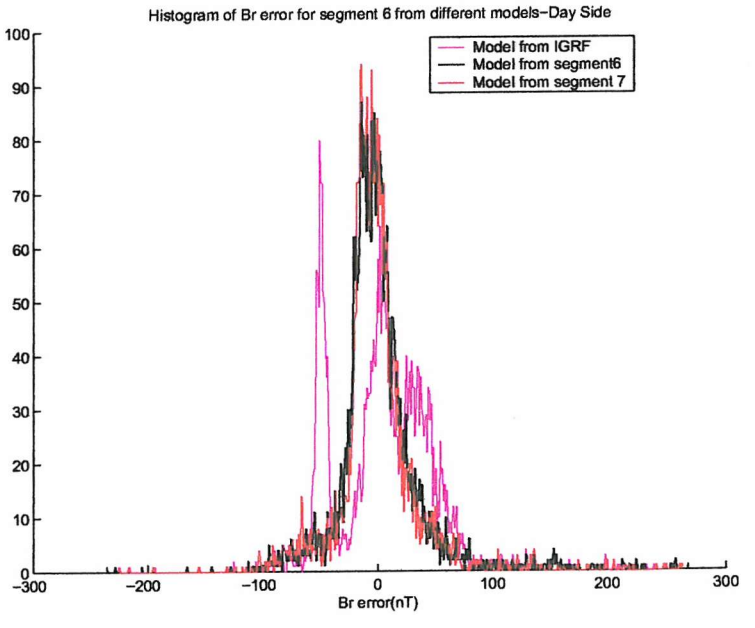

(b) Segment6

Figure B.31: Histogram of B_r error for (a)segment 5 (b)segment 6

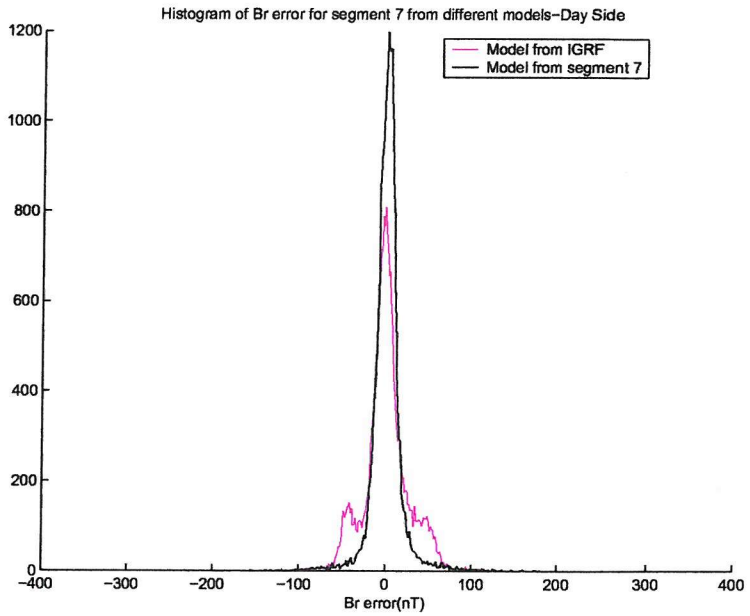

(a) Segment7

Figure B.32: Histogram of B_r error for (a)segment 7

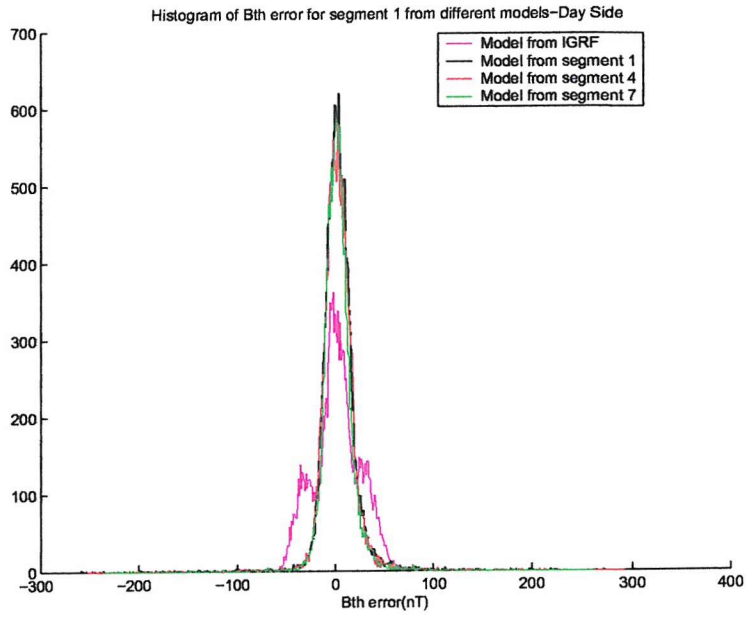

(a) Segment1

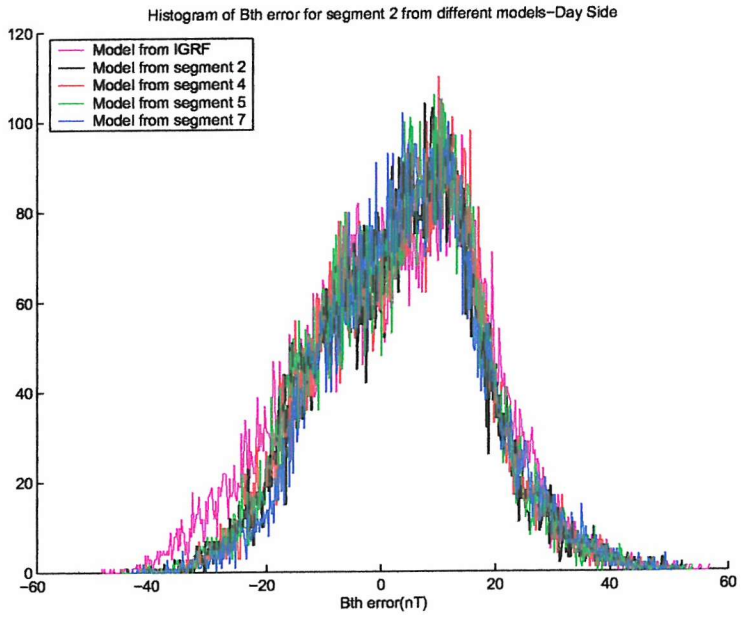

(b) Segment2

Figure B.33: Histogram of B_ϕ error for (a)segment 1 (b)segment 2

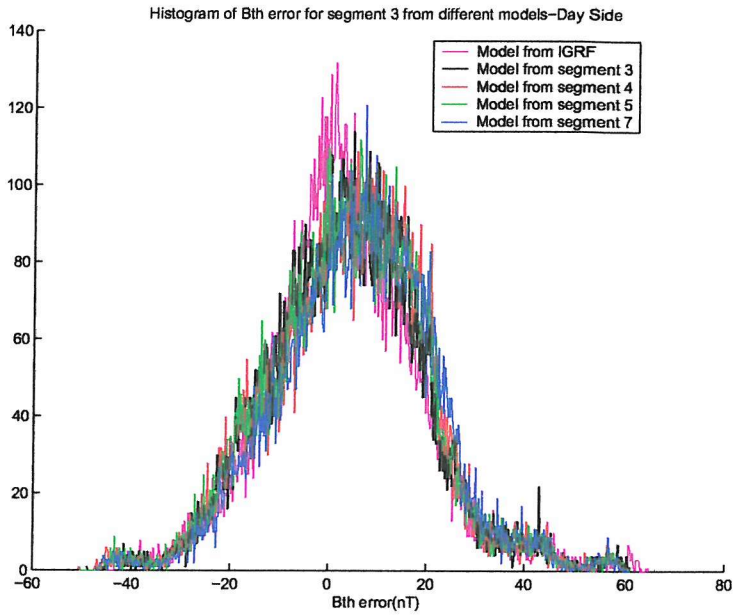

(a) Segment3

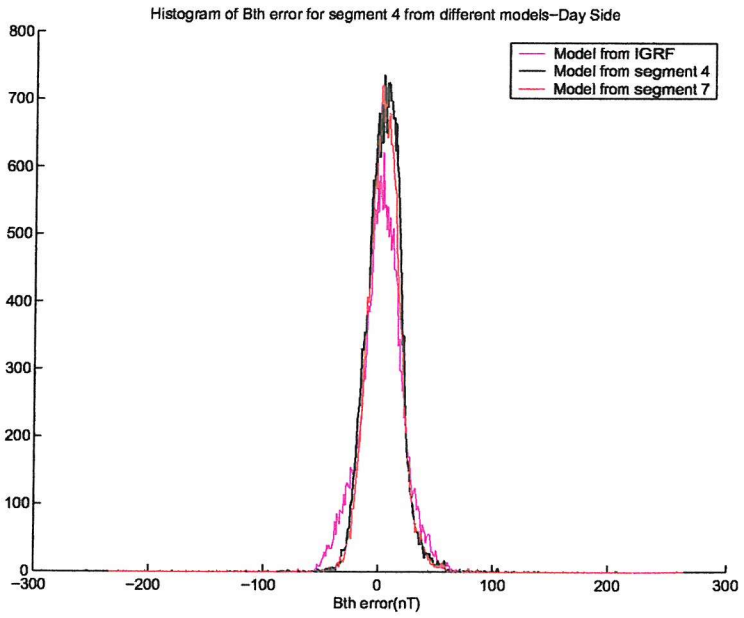

(b) Segment4

Figure B.34: Histogram of B_ϕ error for (a)segment 3 (b)segment 4

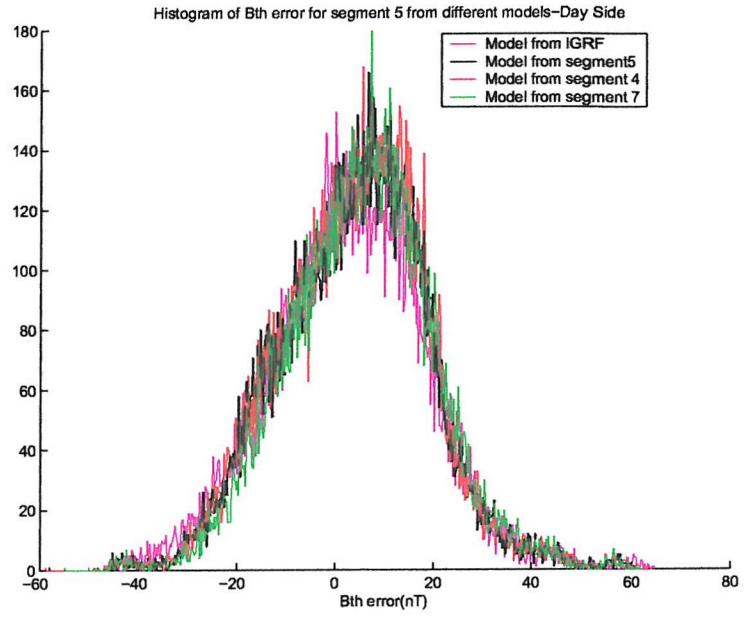

(a) Segment5

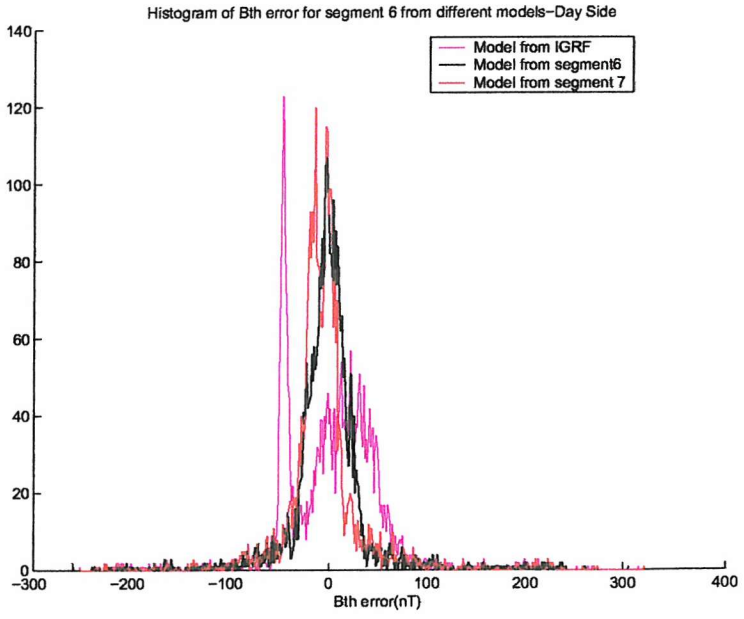

(b) Segment6

Figure B.35: Histogram of B_ϕ error for (a)segment 5 (b)segment 6

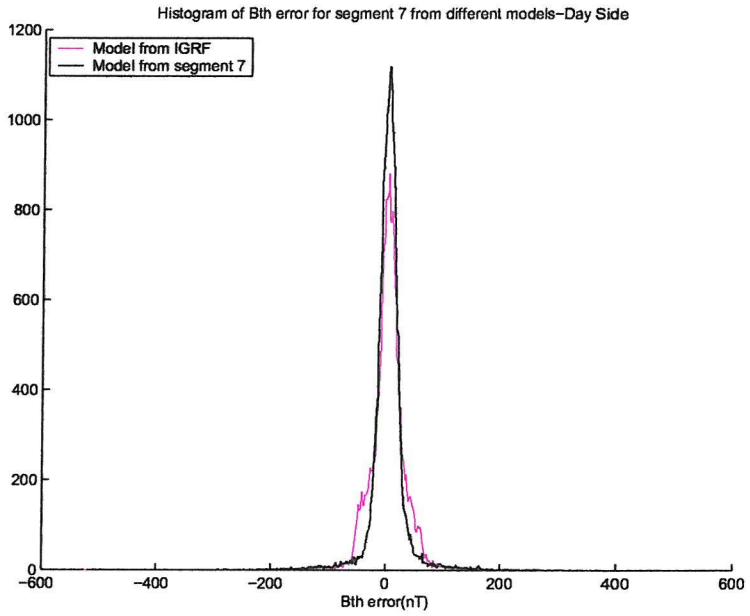

(a) Segment7

Figure B.36: Histogram of B_ϕ error for (a)segment 7

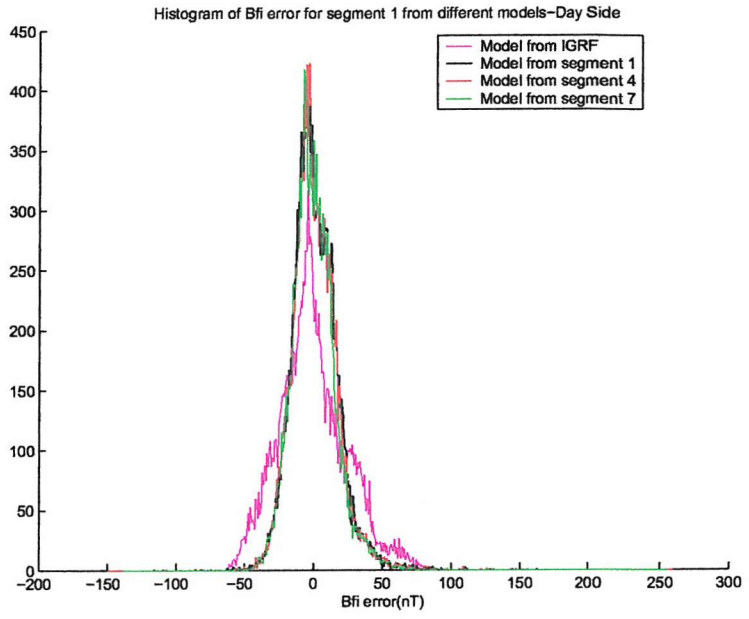

(a) Segment1

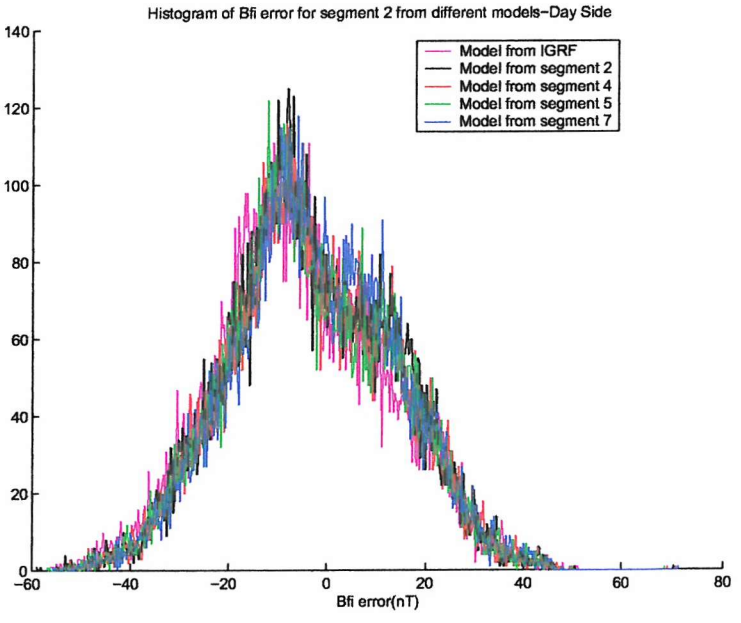

(b) Segment2

Figure B.37: Histogram of B_θ error for (a)segment 1 (b)segment 2

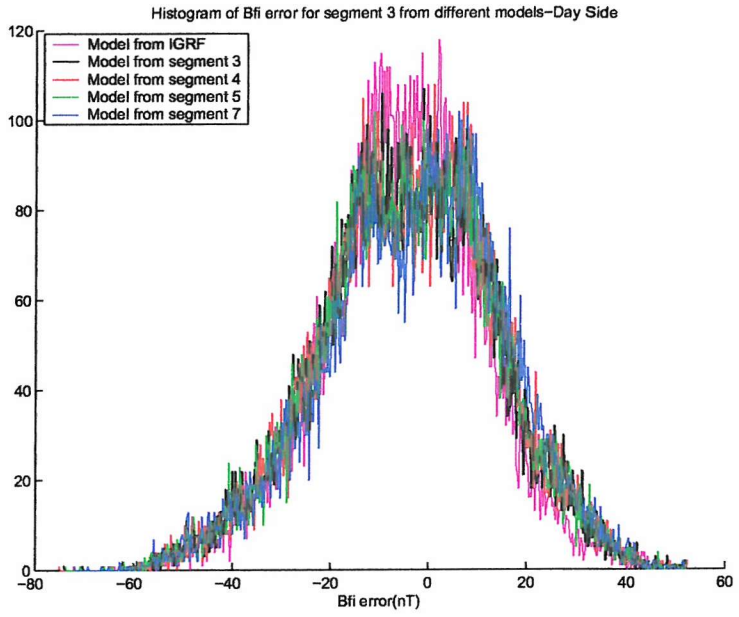

(a) Segment3

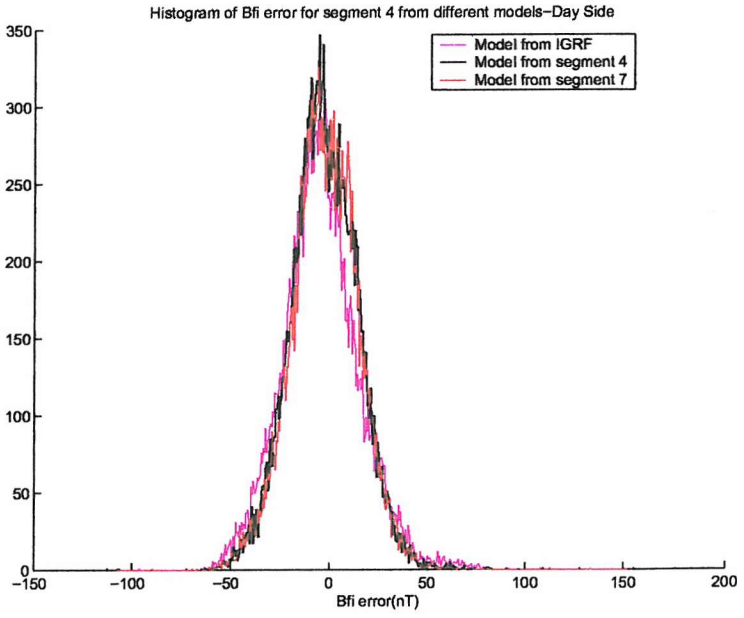

(b) Segment4

Figure B.38: Histogram of B_θ error for (a)segment 3 (b)segment 4

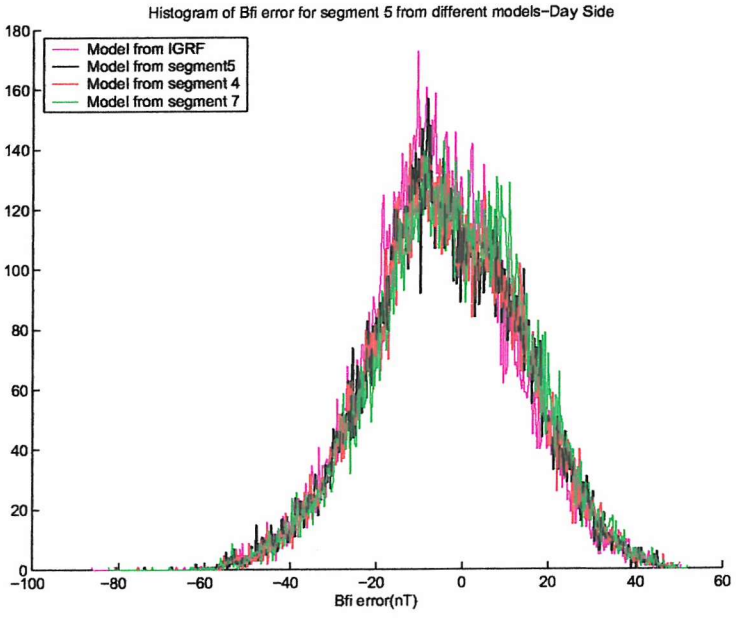

(a) Segment5

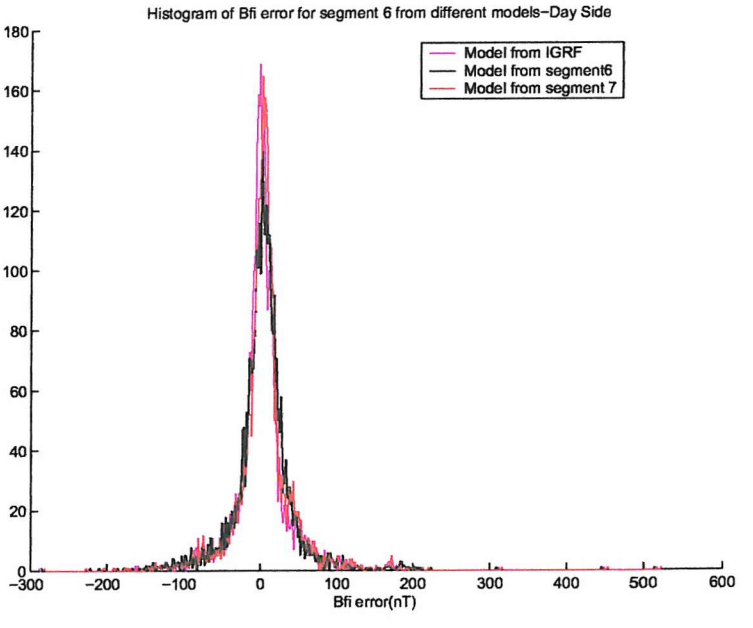

(b) Segment6

Figure B.39: Histogram of B_θ error for (a)segment 5 (b)segment 6

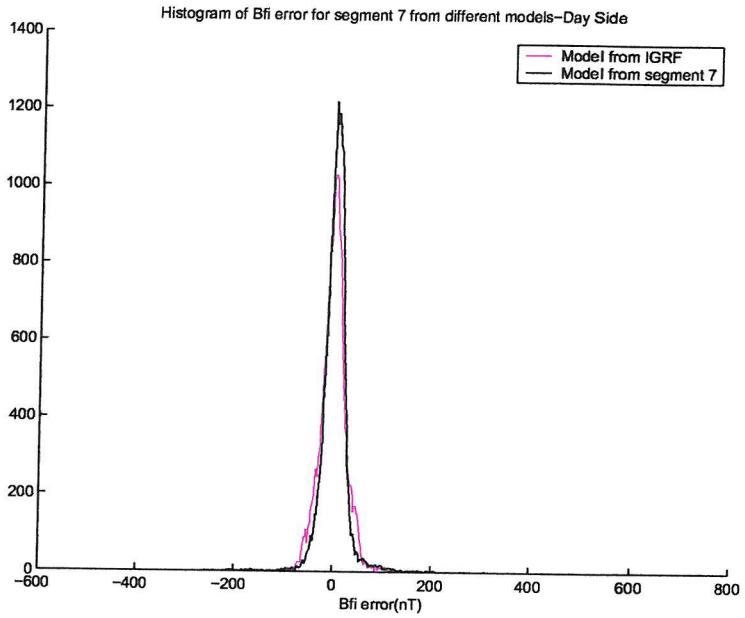

(a) Segment7

Figure B.40: Histogram of B_θ error for (a)segment 7 2

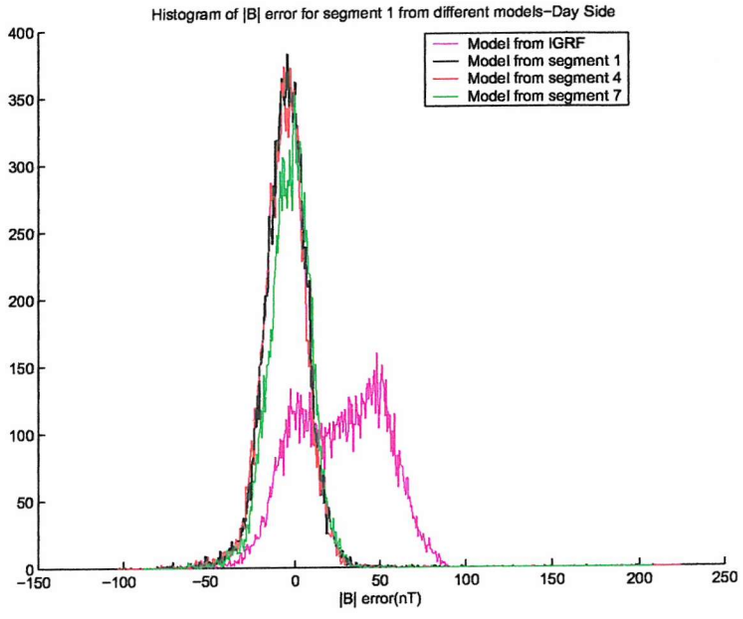

(a) Segment1

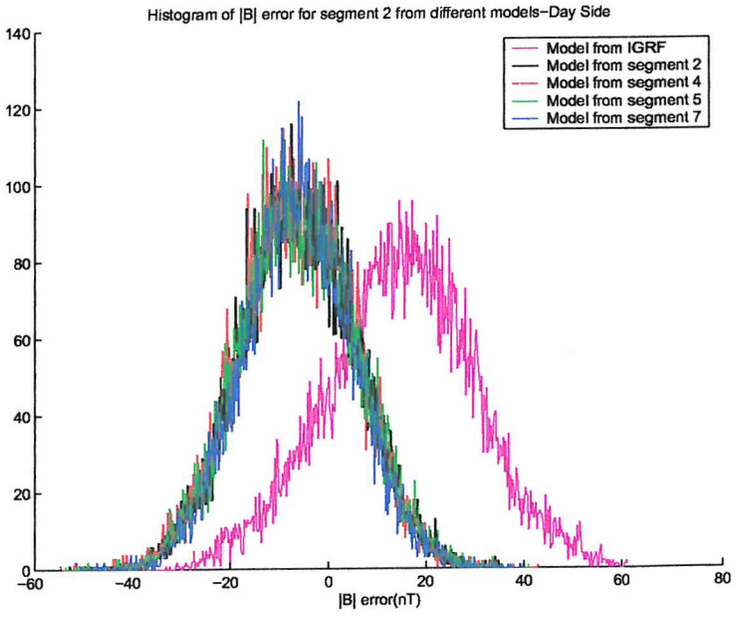

(b) Segment2

Figure B.41: Histogram of $|B|$ error for (a)segment 1 (b)segment 2

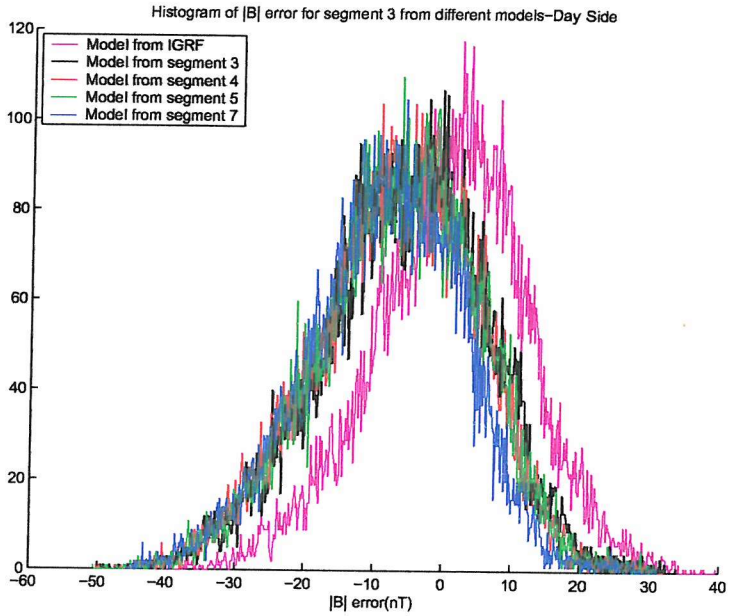

(a) Segment3

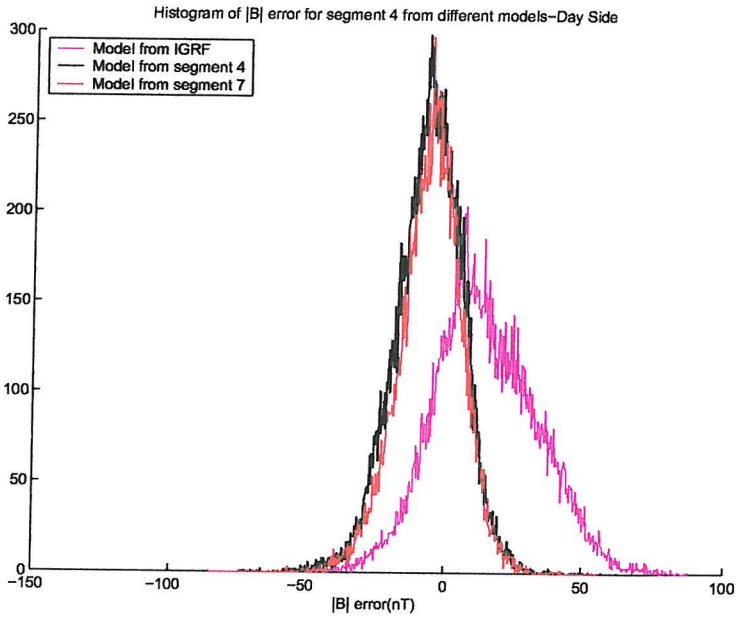

(b) Segment4

Figure B.42: Histogram of $|B|$ error for (a)segment 3 (b)segment 4

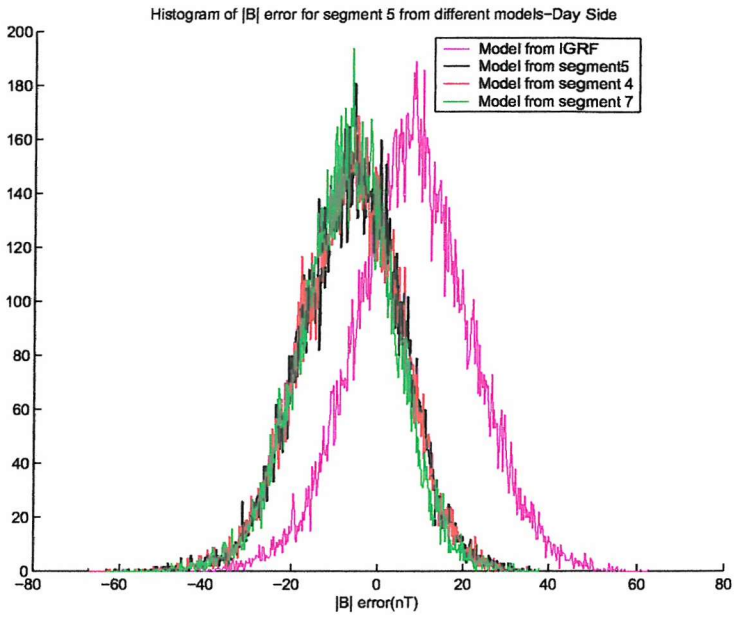

(a) Segment5

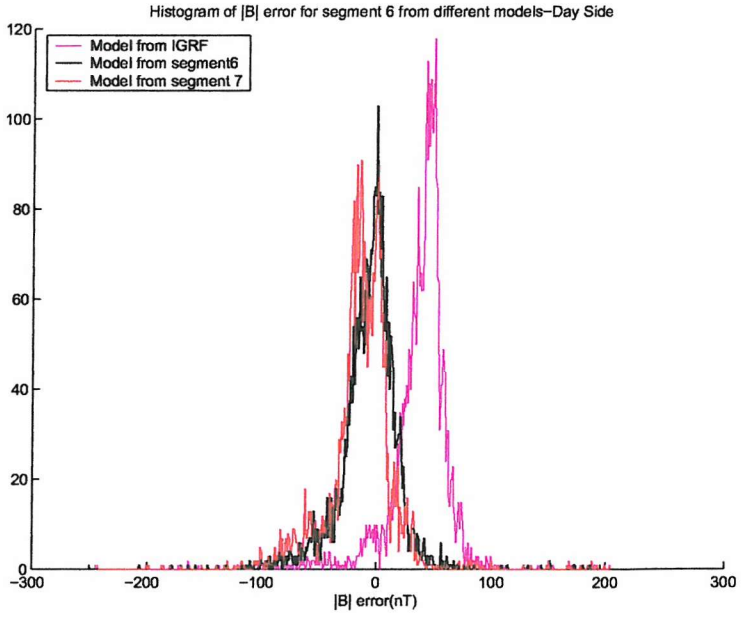

(b) Segment6

Figure B.43: Histogram of $|B|$ error for (a)segment 5 (b)segment 6

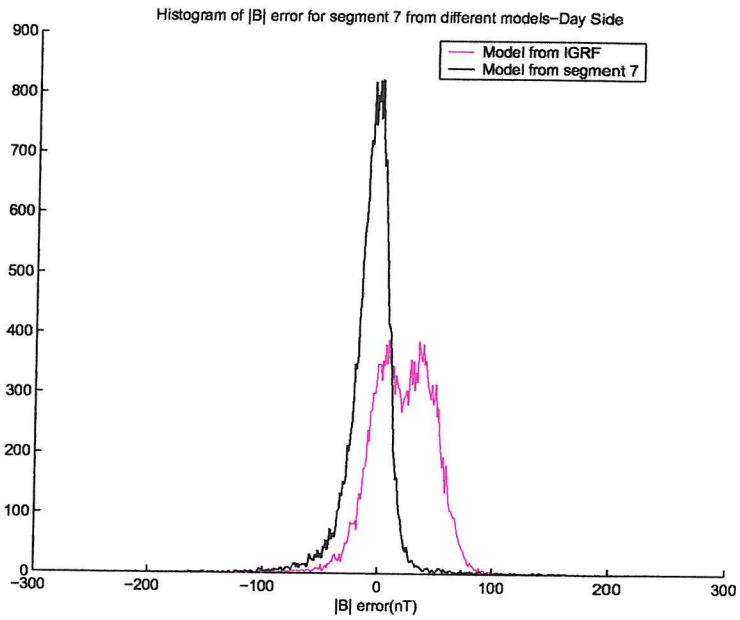

(a) Segment7

Figure B.44: Histogram of $|B|$ error for (a)segment 7

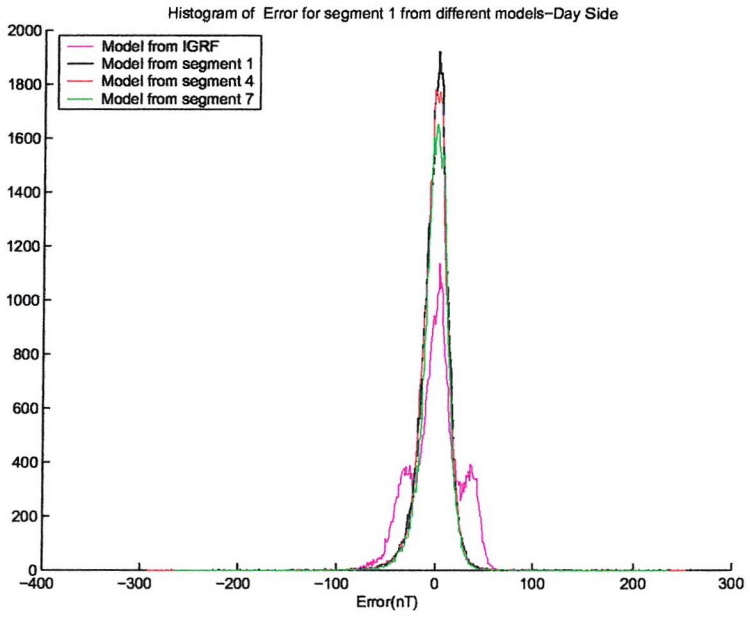

(a) Segment1

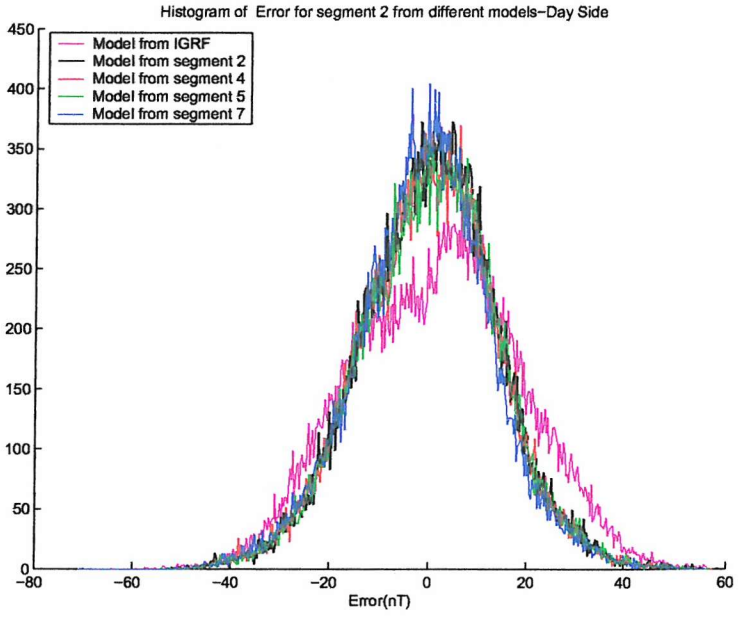

(b) Segment2

Figure B.45: Histogram of Error for (a)segment 1 (b)segment 2

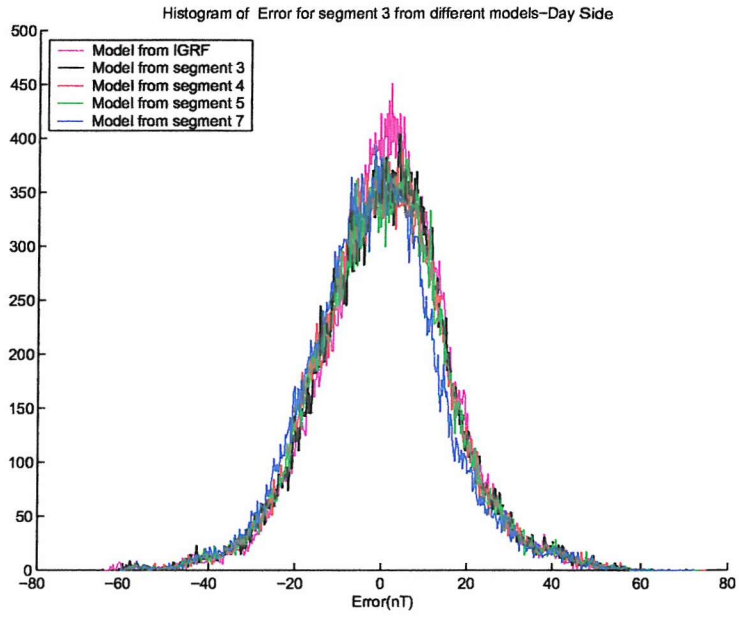

(a) Segment3

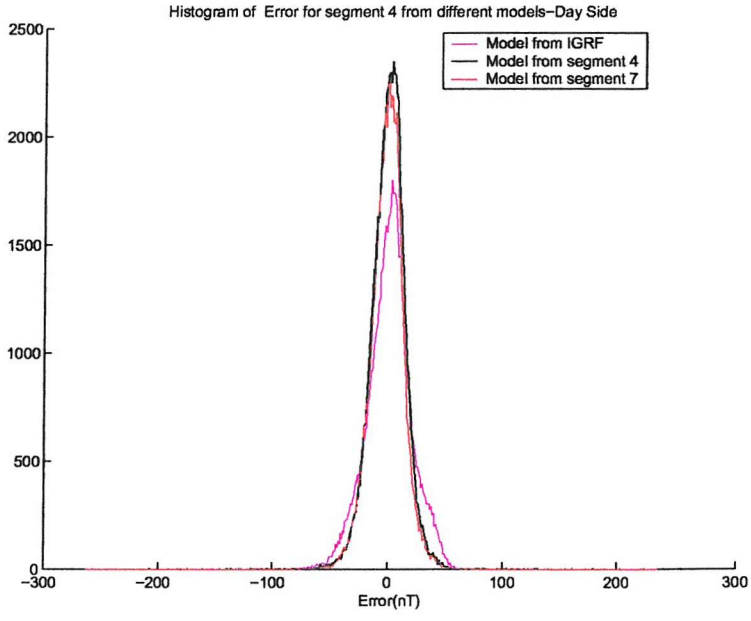

(b) Segment4

Figure B.46: Histogram of Error for (a)segment 3 (b)segment 4

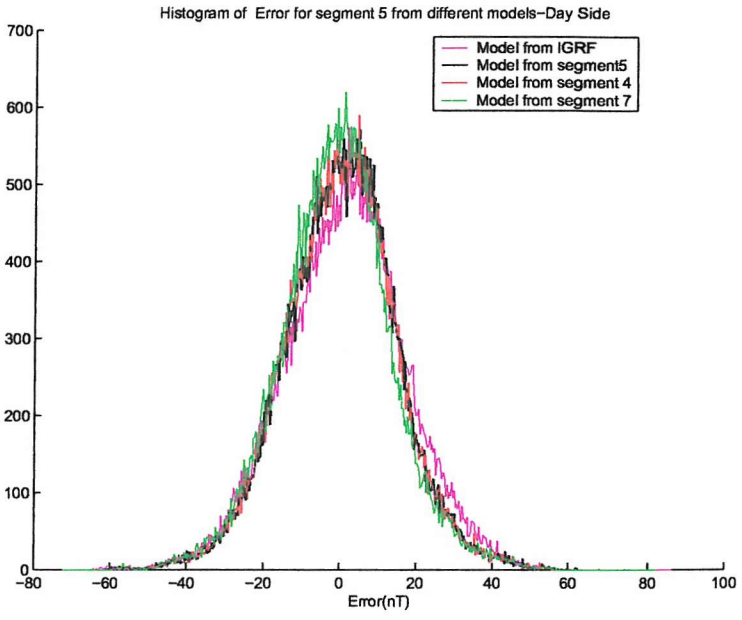

(a) Segment5

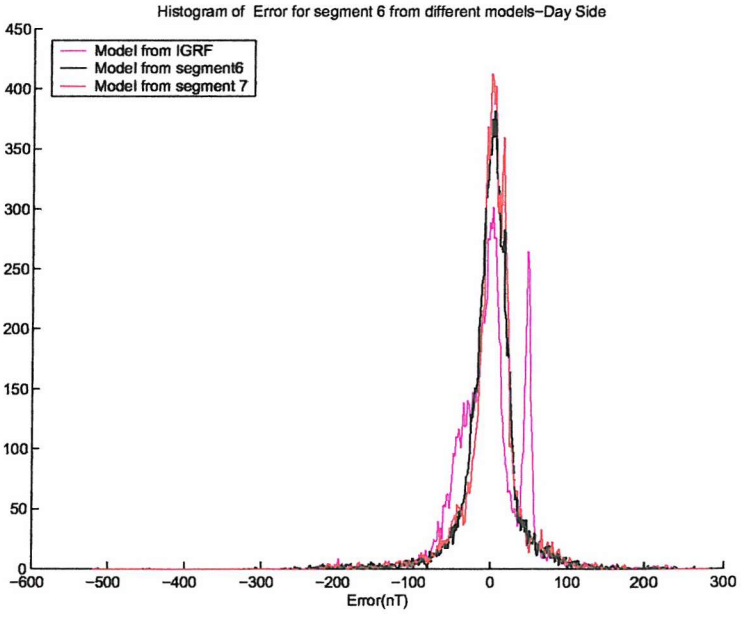

(b) Segment6

Figure B.47: Histogram of Error for (a)segment 5 (b)segment 6

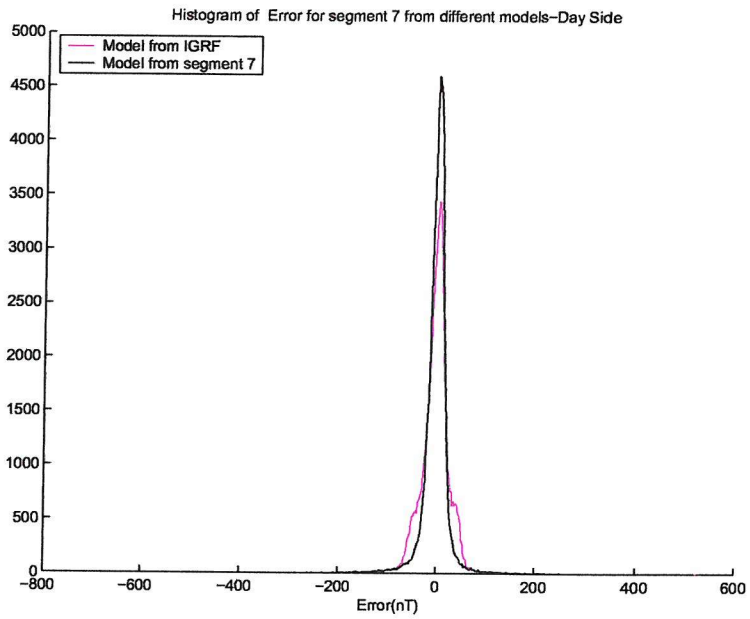

(a) Segment7

Figure B.48: Histogram of Error for (a)segment 7

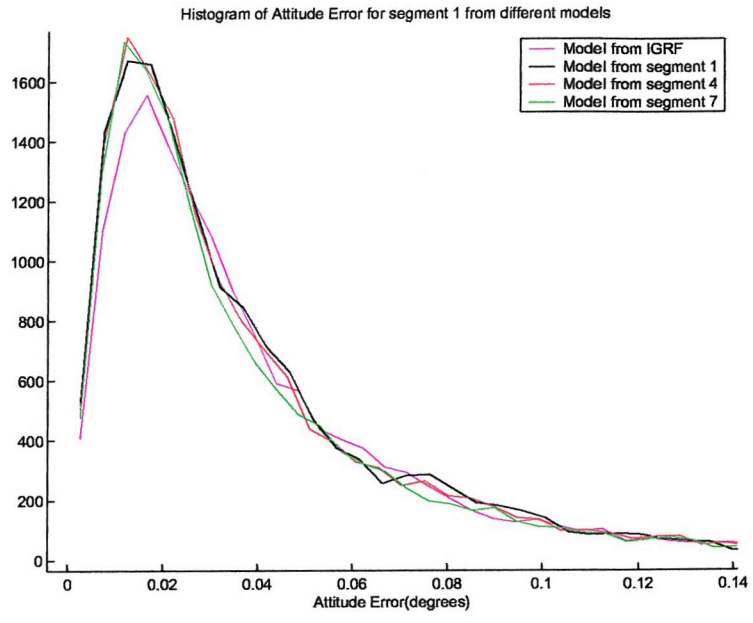

(a) Segment1

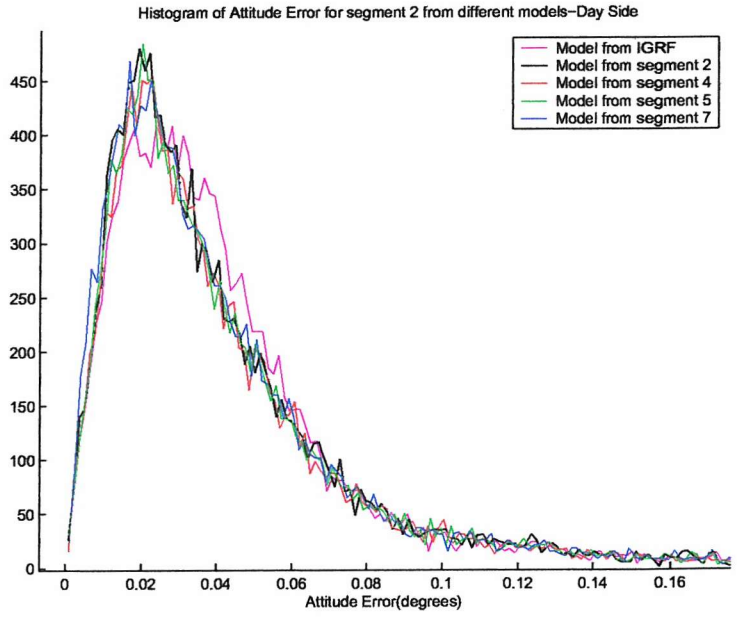

(b) Segment2

Figure B.49: Histogram of Attitude error for (a)segment 1 (b)segment 2 (c)segment

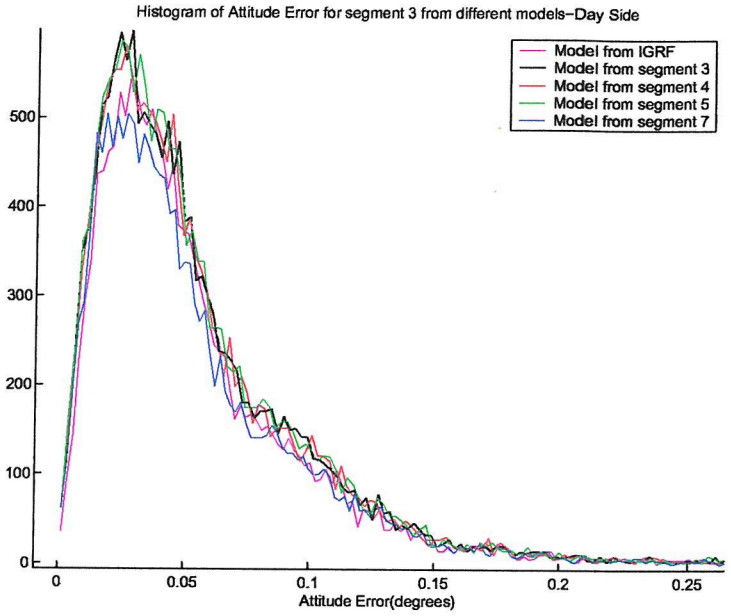

(a) Segment3

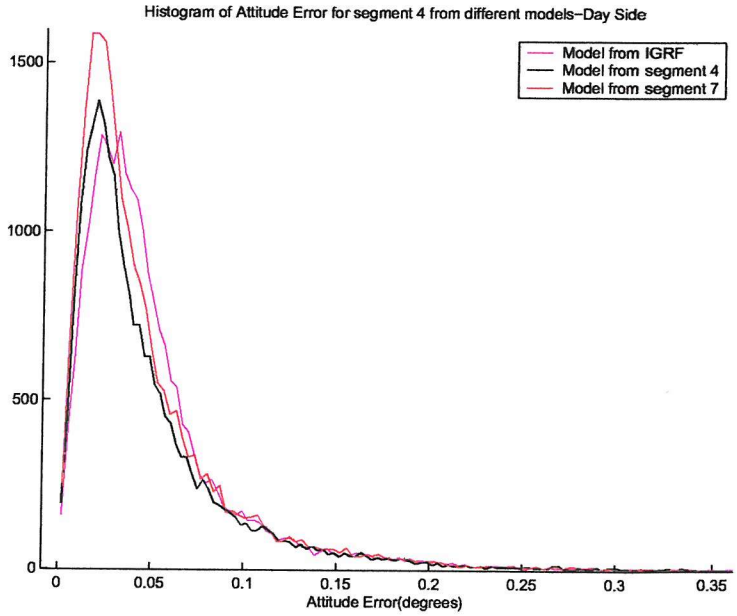

(b) Segment4

Figure B.50: Histogram of Attitude error for (a)segment 3 (b)segment 4 (c)segment

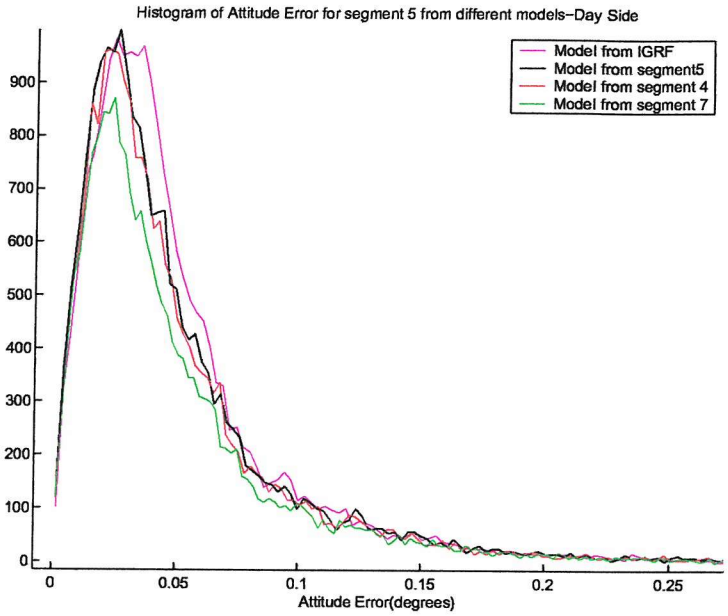

(a) Segment5

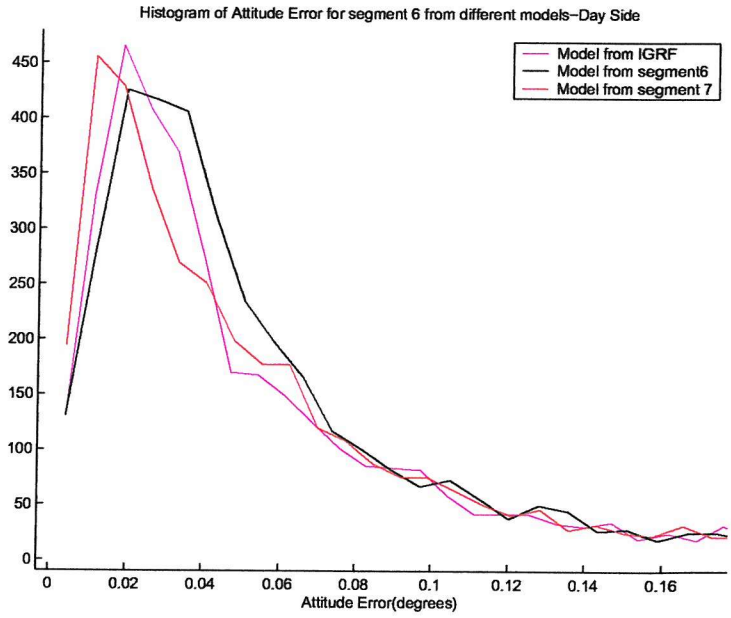

(b) Segment6

Figure B.51: Histogram of Attitude error for (a)segment 5 (b)segment 6 (c)segment

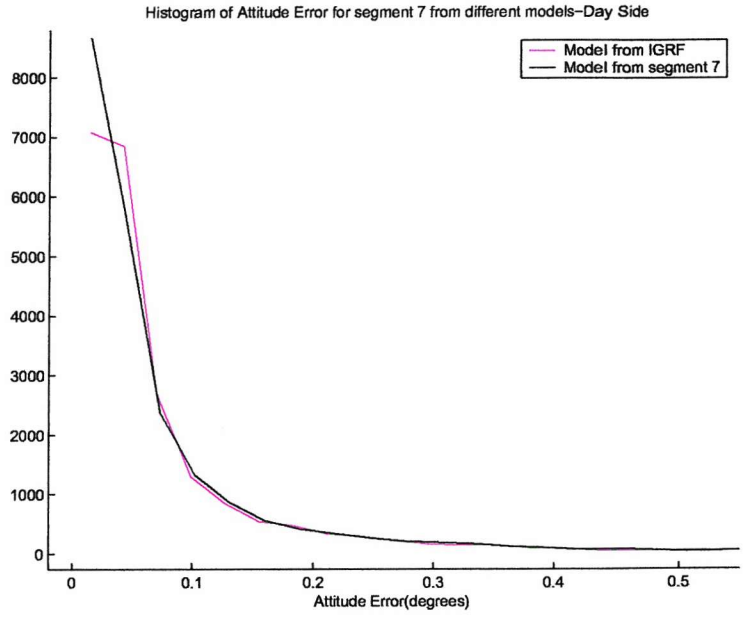

(a) Segment7

Figure B.52: Histogram of Attitude error for (a)segment 7

Appendix C

Figures and tables from testing Segmentation for days not included in the modelling - Day and night side

C.1 Night-side

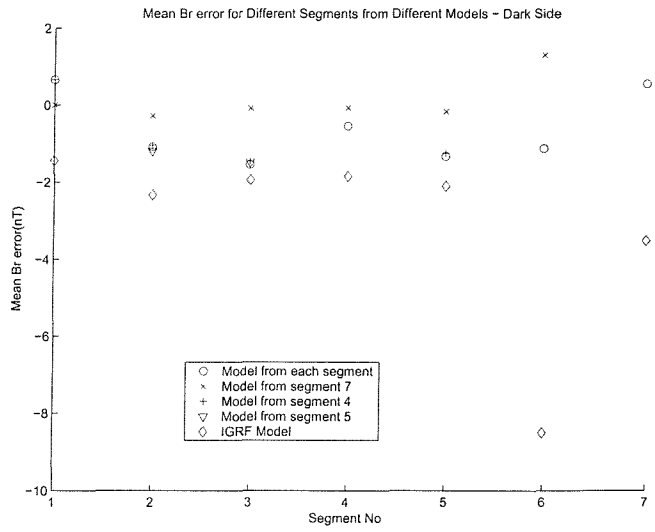

Figure C.1: Mean B_r error for Different Segments from Different Models - Dark Side

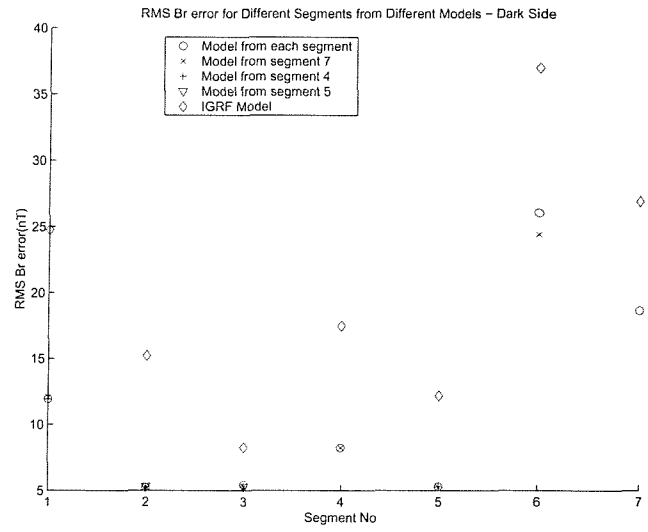

Figure C.2: rms B_r error for Different Segments from Different Models - Dark Side

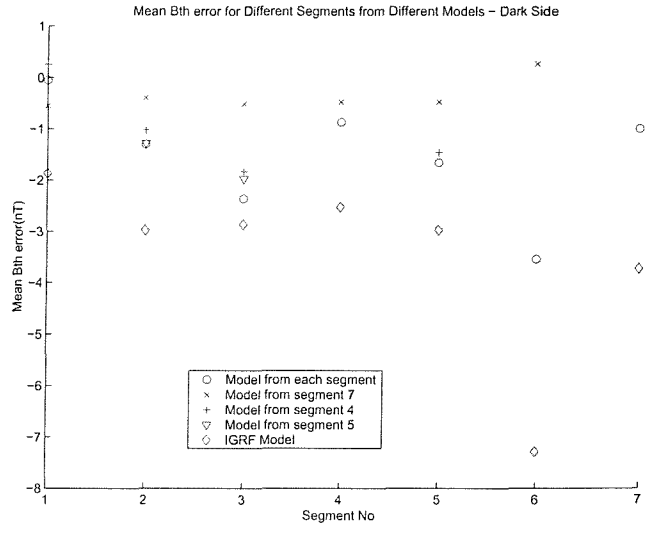

Figure C.3: Mean B_ϕ error for Different Segments from Different Models - Dark Side

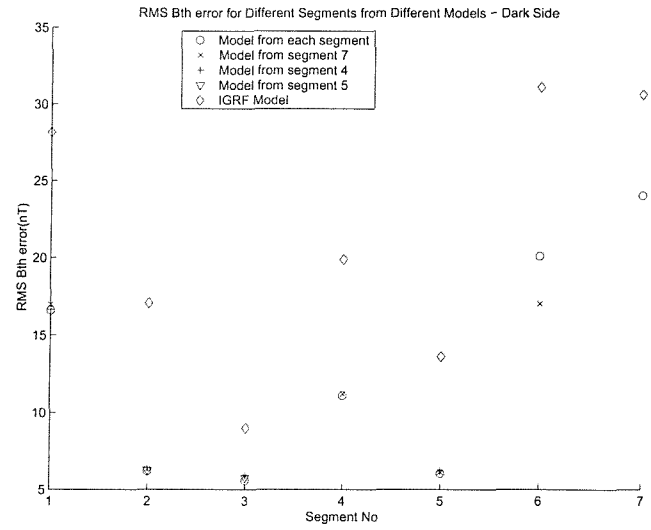

Figure C.4: rms B_ϕ error for Different Segments from Different Models - Dark Side

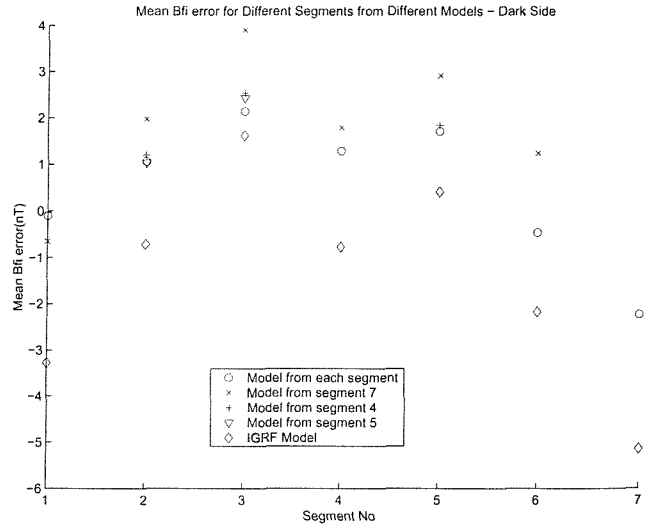

Figure C.5: Mean B_θ error for Different Segments from Different Models - Dark Side

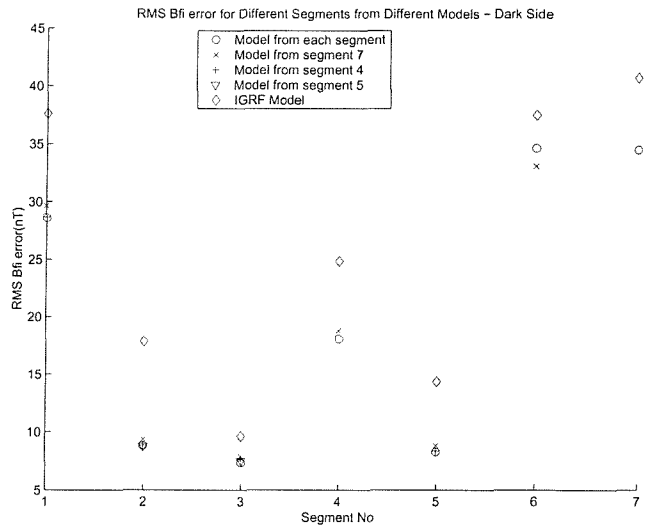

Figure C.6: rms B_θ error for Different Segments from Different Models - Dark Side

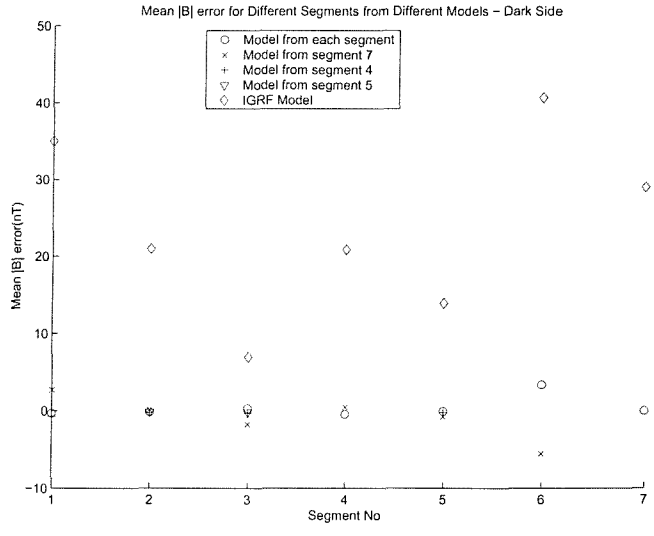

Figure C.7: Mean $|B|$ error for Different Segments from Different Models - Dark Side

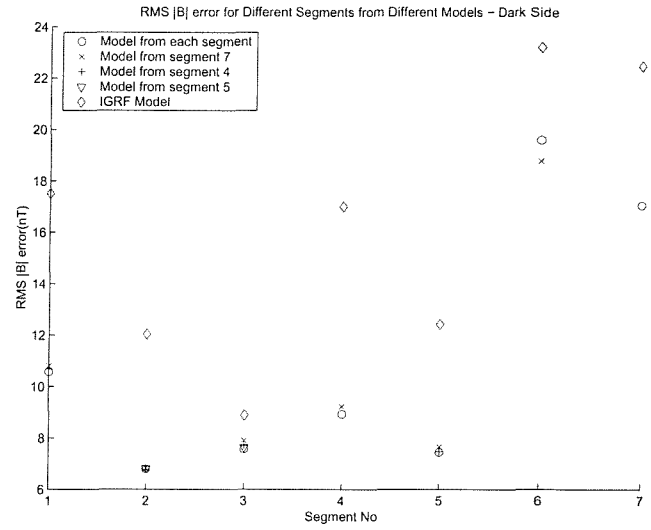

Figure C.8: rms $|B|$ error for Different Segments from Different Models - Dark Side

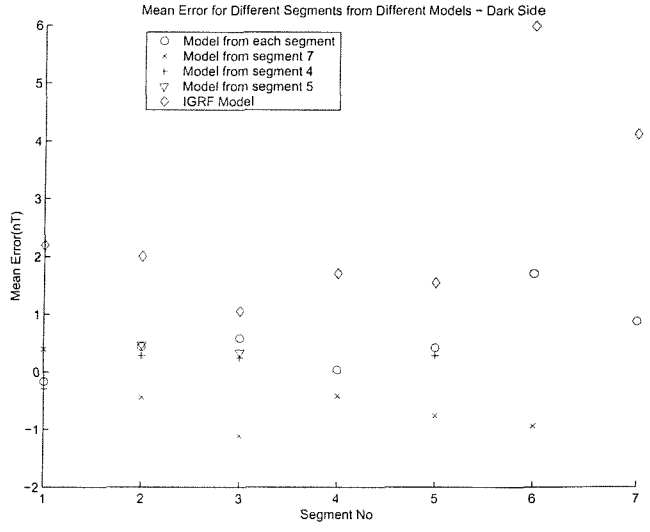

Figure C.9: Mean error for Different Segments from Different Models - Dark Side

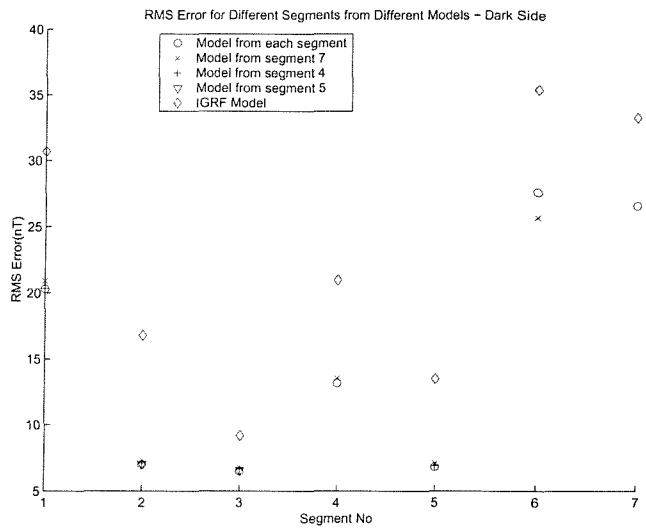

Figure C.10: rms error for Different Segments from Different Models - Dark Side

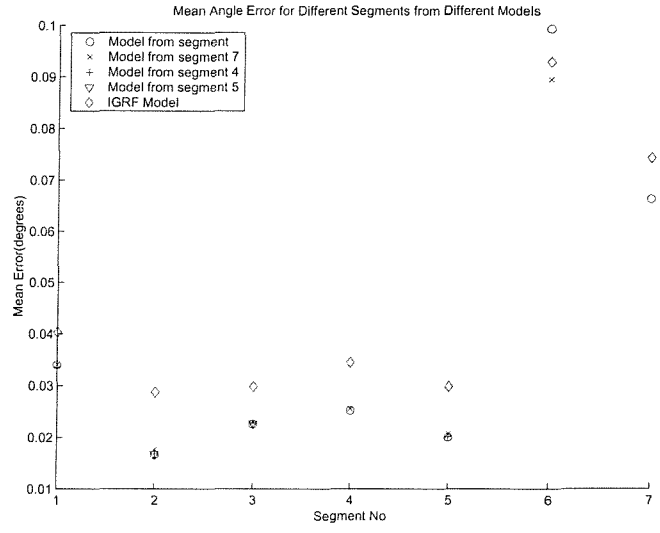

Figure C.11: Mean Angle Error for Different Segments from Different Models-Dark Side

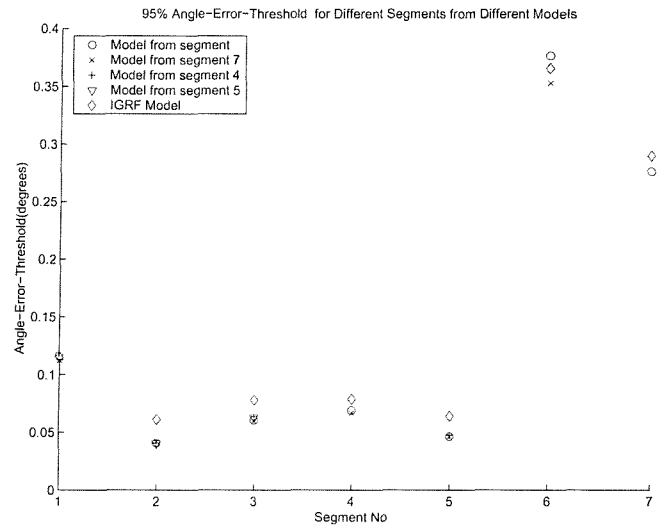

Figure C.12: '95 % Angle-Error-Threshold for Different Segments from Different Models'

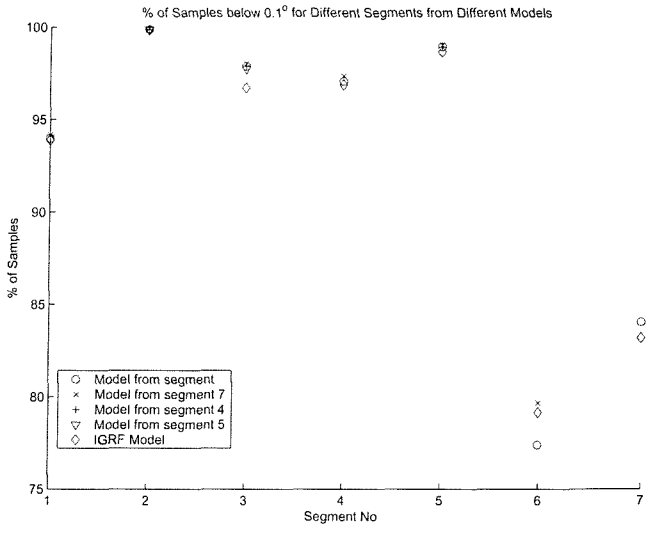

Figure C.13: % of Samples below 0.1^o for Different Segments from Different Models

Segment	Model	B_r Mean	B_θ Mean	B_ϕ Mean	|B| Mean	B_r&B_θ&B_ϕ Mean	B_r rms	B_θ rms	B_ϕ rms	|B| rms	B_r&B_θ&B_ϕ rms
1	1	0.658	-0.051	-0.107	-0.315	0.167	11.926	16.588	28.599	10.569	20.294
1	IGRF	-1.445	-1.867	-3.276	35.013	-2.196	24.758	28.162	37.609	17.506	30.671
1	7	0.003	-0.549	-0.651	2.705	-0.399	12.056	16.989	29.642	10.804	20.919
1	4	0.658	0.260	-0.028	-0.692	0.297	11.908	16.656	28.655	10.677	20.335
2	2	-1.083	-1.297	1.064	-0.142	-0.439	5.240	6.195	8.825	6.793	7.002
2	IGRF	-2.329	-2.970	-0.715	20.994	-2.005	15.227	17.084	17.867	12.038	16.789
2	7	-0.276	-0.390	1.973	0.132	0.436	5.263	6.336	9.397	6.823	7.296
2	4	-1.044	-1.015	1.201	-0.243	-0.286	5.271	6.440	8.859	6.762	7.096
2	5	-1.194	-1.272	1.038	-0.139	-0.476	5.350	6.276	8.767	6.818	7.031
3	3	-1.544	-2.357	2.144	0.317	-0.586	5.421	5.594	7.365	7.566	6.492
3	IGRF	-1.934	-2.860	1.623	6.970	-1.057	8.246	9.004	9.643	8.888	9.187
3	7	-0.080	-0.509	3.910	-1.717	1.107	5.297	5.929	7.934	7.903	6.783
3	4	-1.452	-1.829	2.536	-0.310	-0.249	5.318	5.911	7.592	7.705	6.647
3	5	-1.483	-1.969	2.432	-0.177	-0.340	5.284	5.781	7.530	7.631	6.575
4	4	-0.543	-0.863	1.288	-0.427	-0.039	8.226	11.111	18.083	8.930	13.175
4	IGRF	-1.843	-2.519	-0.770	20.893	-1.711	17.475	19.894	24.857	17.009	20.980
4	7	-0.064	-0.469	1.791	0.493	0.419	8.234	11.213	18.812	9.229	13.544
5	5	-1.329	-1.654	1.712	-0.073	-0.424	5.293	6.044	8.277	7.442	6.830
5	IGRF	-2.100	-2.970	0.413	13.927	-1.552	12.181	13.623	14.371	12.427	13.499
5	7	-0.166	-0.470	2.914	-0.760	0.759	5.269	6.147	8.820	7.649	7.079
5	4	-1.242	-1.453	1.842	-0.209	-0.284	5.279	6.200	8.351	7.469	6.900
6	6	-1.129	-3.535	-0.463	3.390	-1.709	26.055	20.112	34.643	19.602	27.620
6	IGRF	-8.504	-7.287	-2.167	40.698	-5.986	36.989	31.116	37.495	23.215	35.424
6	7	1.303	0.270	1.241	-5.539	0.938	24.421	17.037	33.104	18.792	25.711
7	7	0.560	-0.993	-2.224	-0.011	-0.886	18.680	24.077	34.537	17.074	26.616
7	IGRF	-3.517	-3.719	-5.138	29.021	-4.125	26.948	30.673	40.783	22.494	33.325

Table C.1: Mean and rms error statistics for Different Segments and Different Models for Dark Side and days not included in the modelling

Segment	Model	Mean(°)	95%Threshold(°)	%below0.1°	Maximum(°)
1	1	0.034	0.116	93.970	1.002
1	IGRF	0.040	0.115	93.870	0.976
1	7	0.034	0.112	94.160	0.994
1	4	0.033	0.113	94.150	1.010
2	2	0.017	0.041	99.880	0.017
2	IGRF	0.029	0.061	99.850	0.177
2	7	0.018	0.042	99.900	0.168
2	4	0.017	0.041	99.880	0.167
2	5	0.017	0.041	99.880	0.177
3	3	0.023	0.061	97.890	0.490
3	IGRF	0.030	0.078	96.730	0.628
3	7	0.023	0.060	98.020	0.537
3	4	0.023	0.064	97.890	0.479
3	5	0.023	0.063	97.750	0.500
4	4	0.025	0.069	97.070	1.050
4	IGRF	0.034	0.079	96.890	0.954
4	7	0.026	0.067	97.360	0.968
5	5	0.020	0.046	98.950	0.483
5	IGRF	0.030	0.064	98.670	0.613
5	7	0.021	0.046	99.050	0.501
5	4	0.020	0.048	98.940	0.438
6	6	0.099	0.377	77.400	5.052
6	IGRF	0.093	0.366	79.160	7.047
6	7	0.090	0.353	79.680	7.909
7	7	0.066	0.277	84.040	7.866
7	IGRF	0.074	0.290	83.180	7.478

Table C.2: Mean,95%percentile and % below 0.1^o angle error statistics for Different Segments and Different Models for Dark Side and days not included in the modelling

C.2 Day-Side

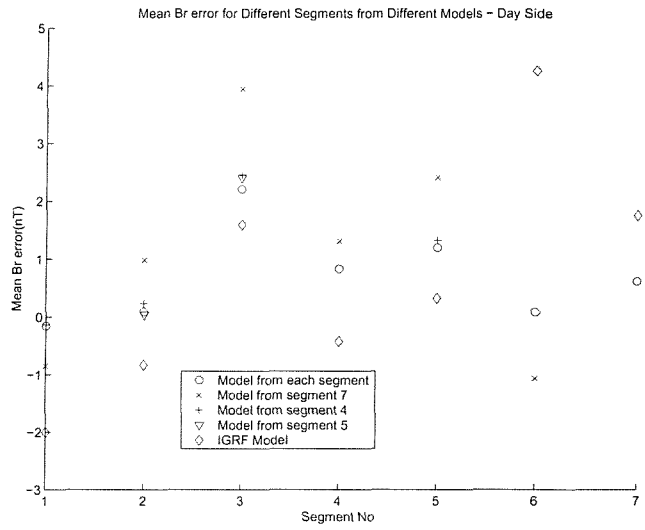

Figure C.14: Mean B_r error for Different Segments from Different Models - Day Side

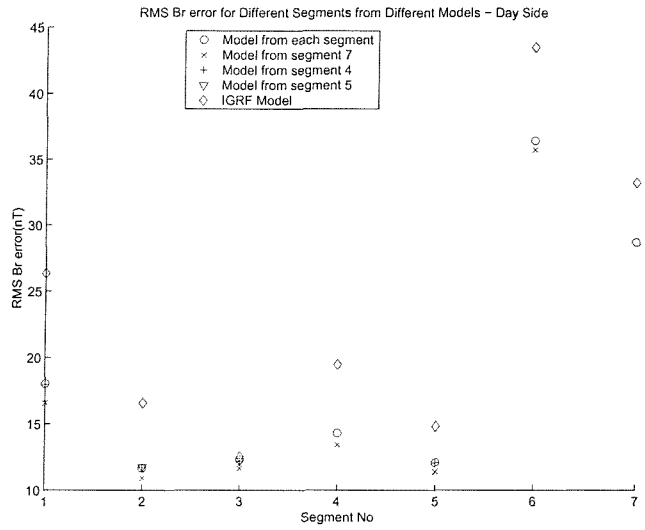

Figure C.15: rms B_r error for Different Segments from Different Models - Day Side

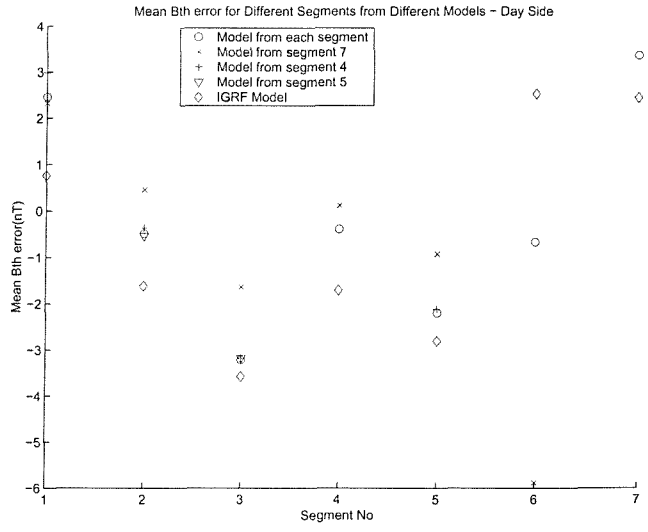

Figure C.16: Mean B_ϕ error for Different Segments from Different Models - Day Side

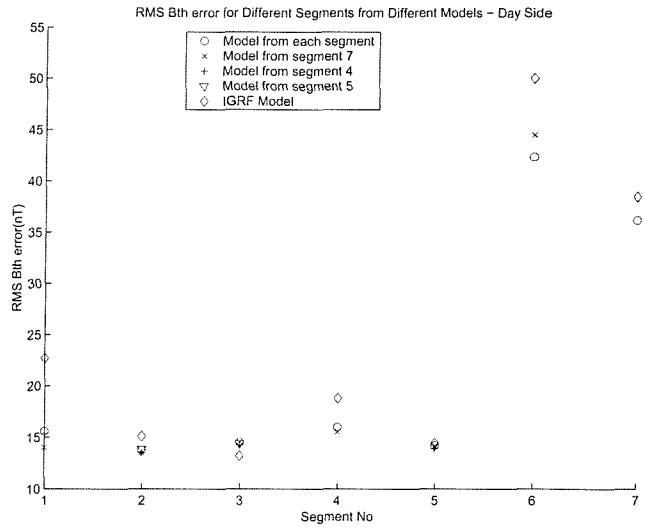

Figure C.17: rms B_ϕ error for Different Segments from Different Models - Day Side

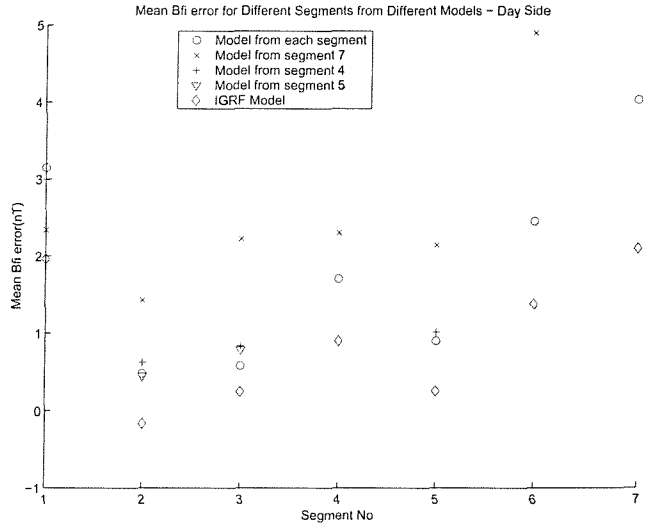

Figure C.18: Mean B_θ error for Different Segments from Different Models - Day Side

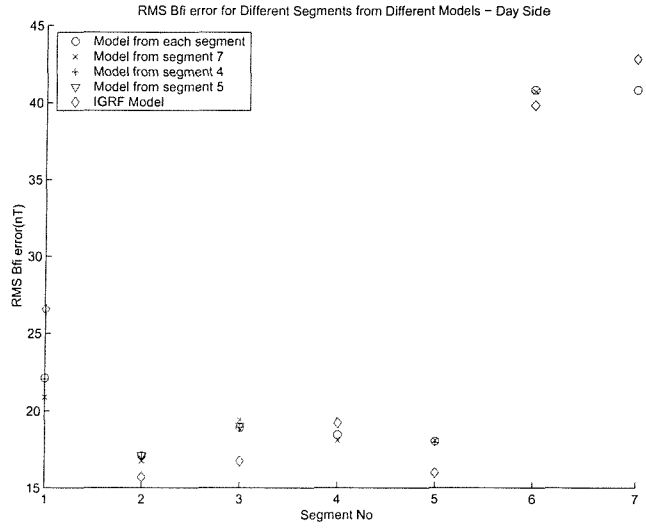

Figure C.19: rms B_θ error for Different Segments from Different Models - Day Side

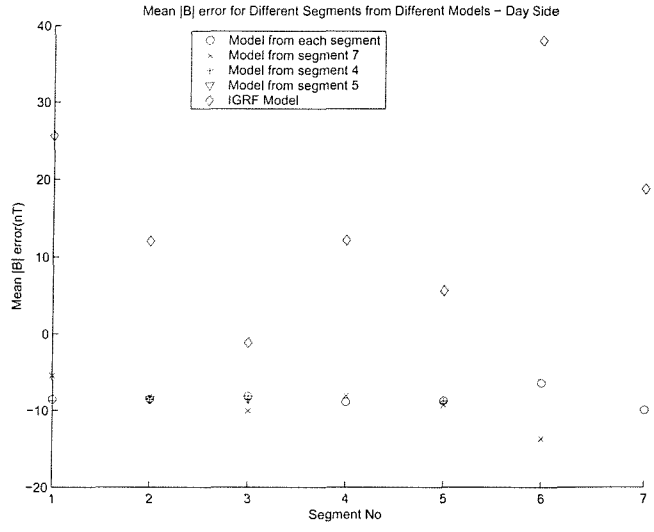

Figure C.20: Mean $|B|$ error for Different Segments from Different Models - Day Side

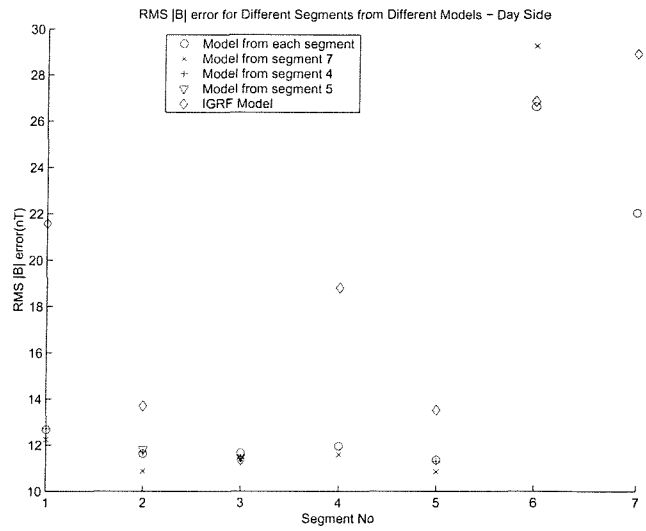

Figure C.21: rms $|B|$ error for Different Segments from Different Models - Day Side

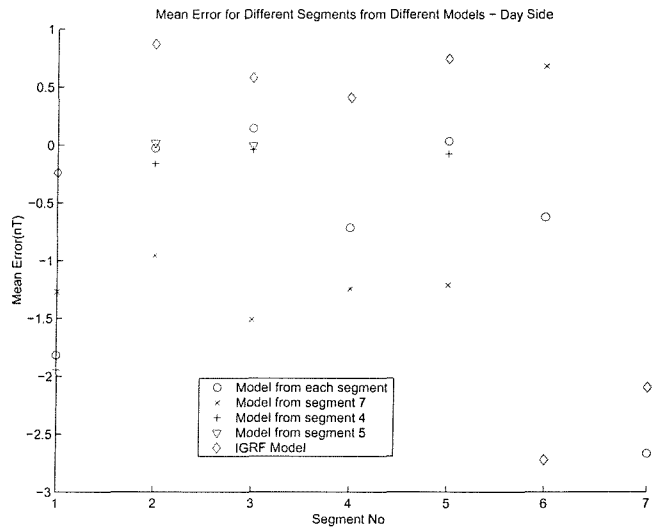

Figure C.22: Mean error for Different Segments from Different Models - Day Side

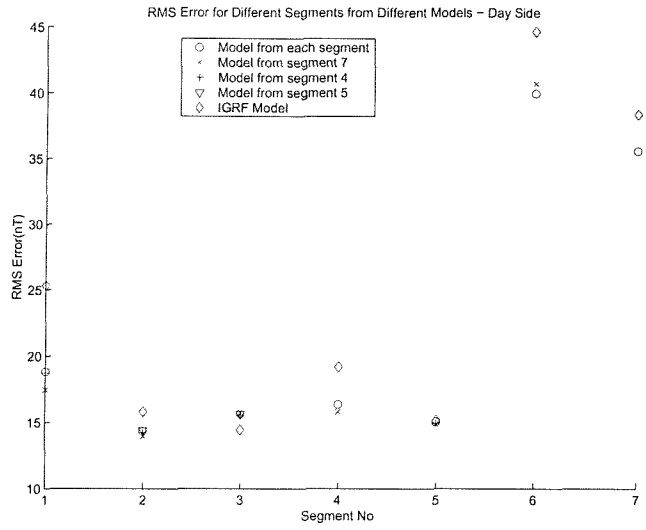

Figure C.23: rms error for Different Segments from Different Models - Day Side

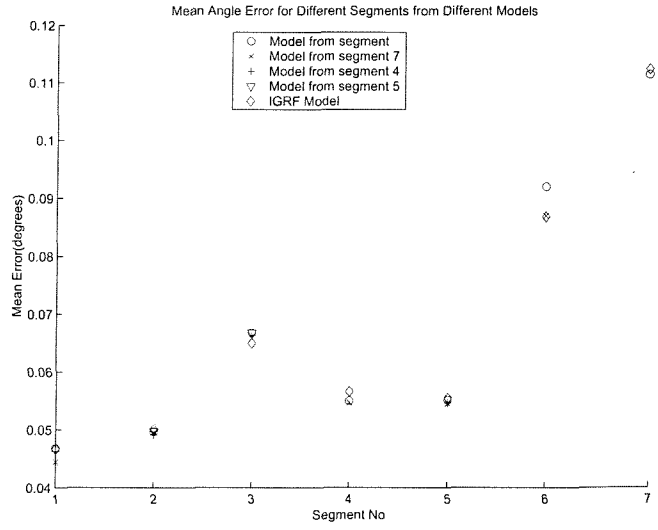

Figure C.24: Mean Angle Error for Different Segments from Different Models-Day Side

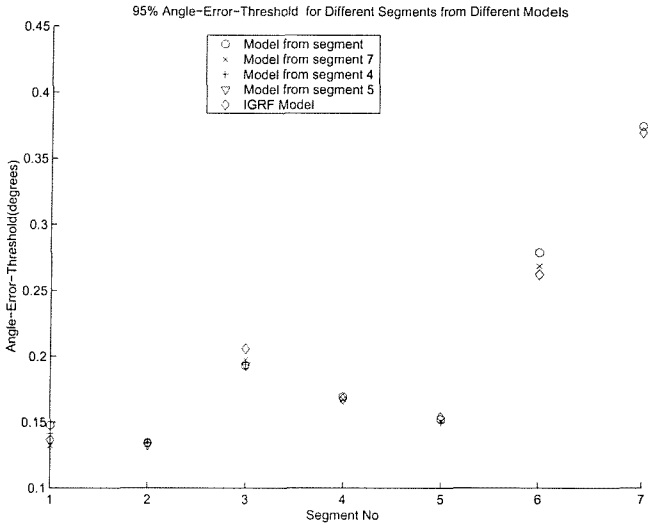

Figure C.25: '95 % Angle-Error-Threshold for Different Segments from Different Models'

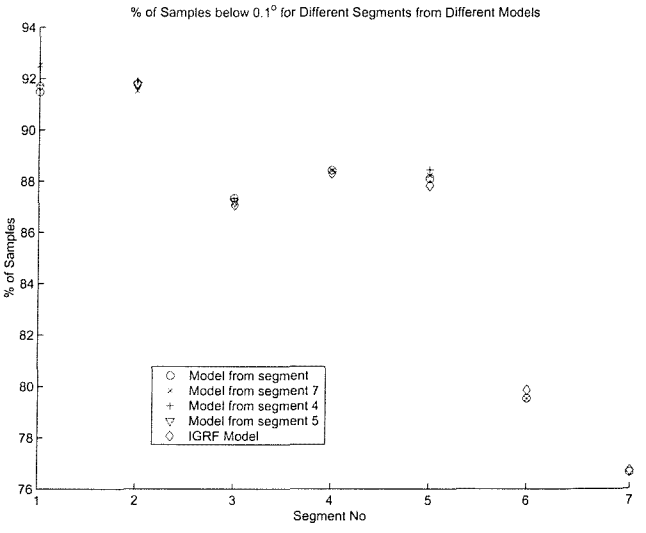

Figure C.26: % of Samples below 0.1^o for Different Segments from Different Models

Segment	Model	B_r Mean	B_θ Mean	B_ϕ Mean	|B| Mean	B_r&B_θ&B_ϕ Mean	B_r rms	B_θ rms	B_ϕ rms	|B| rms	B_r&B_θ&B_ϕ rms
1	1	-0.155	2.459	3.150	-8.524	1.818	18.035	15.574	22.120	12.670	18.825
1	IGRF	-2.004	0.758	1.961	25.628	0.238	26.336	22.703	26.566	21.583	25.317
1	7	-0.850	2.319	2.339	-5.437	1.269	16.588	14.025	20.893	12.240	17.465
1	4	-0.139	2.982	2.995	-8.723	1.946	17.967	15.366	22.070	12.708	18.730
2	2	0.091	-0.490	0.480	-8.542	0.027	11.668	13.759	17.089	11.623	14.352
2	IGRF	-0.832	-1.615	-0.162	12.050	-0.870	16.588	15.114	15.699	13.702	15.822
2	7	0.984	0.454	1.431	-8.150	0.956	10.926	13.523	16.755	10.881	13.945
2	4	0.231	-0.375	0.624	-8.574	0.160	11.735	13.542	17.006	11.700	14.268
2	5	0.039	-0.541	0.449	-8.515	-0.018	11.752	13.864	17.117	11.818	14.419
3	3	2.208	-3.216	0.581	-8.110	-0.142	12.299	14.528	18.910	11.669	15.656
3	IGRF	1.591	-3.578	0.249	-1.136	-0.579	12.530	13.215	16.740	11.348	14.447
3	7	3.944	-1.637	2.228	-10.064	1.511	11.640	14.569	19.416	11.390	15.716
3	4	2.458	-3.176	0.837	-8.501	0.040	12.161	14.261	18.930	11.422	15.560
3	5	2.402	-3.177	0.787	-8.442	0.004	12.200	14.406	19.033	11.465	15.653
4	4	0.829	-0.390	1.705	-8.888	0.715	14.310	16.001	18.460	11.960	16.368
4	IGRF	-0.424	-1.703	0.903	12.160	-0.408	19.479	18.834	19.234	18.808	19.213
4	7	1.308	0.118	2.305	-8.066	1.243	13.431	15.548	18.091	11.598	15.830
5	5	1.198	-2.197	0.901	-8.741	-0.033	12.099	14.189	18.037	11.355	15.056
5	IGRF	0.320	-2.809	0.255	5.591	-0.745	14.833	14.432	15.985	13.523	15.168
5	7	2.411	-0.923	2.147	-9.280	1.212	11.406	14.128	18.080	10.853	14.871
5	4	1.324	-2.111	1.013	-8.816	0.075	12.071	13.944	17.947	11.285	14.938
6	6	0.086	-0.683	2.499	-6.421	0.633	36.476	42.312	40.901	26.531	39.912
6	IGRF	4.331	2.512	1.312	38.197	2.812	43.642	50.145	39.755	26.719	44.222
6	7	-1.101	-5.900	4.113	-13.786	-0.615	35.689	44.444	40.153	29.361	41.004
7	7	0.620	3.354	4.032	-9.935	2.669	28.735	36.221	40.888	22.066	35.665
7	IGRF	1.755	2.434	2.101	18.753	2.097	33.276	38.528	42.897	28.962	38.436

Table C.3: Mean and rms error statistics for Different Segments and Different Models for Day Side and days not included in the modelling

Segment	Model	Mean(^{o})	95%Threshold(^{o})	%below0.1^o	Maximum(^{o})
1	1	0.047	0.148	91.480	1.626
1	IGRF	0.047	0.136	91.710	1.307
1	7	0.044	0.132	92.530	1.420
1	4	0.046	0.141	91.740	1.587
2	2	0.050	0.134	91.780	0.050
2	IGRF	0.050	0.134	91.820	1.267
2	7	0.050	0.136	91.530	1.336
2	4	0.049	0.134	91.910	1.391
2	5	0.050	0.132	91.750	1.260
3	3	0.067	0.193	87.340	4.071
3	IGRF	0.065	0.206	87.070	2.712
3	7	0.066	0.198	87.170	3.792
3	4	0.066	0.194	87.340	3.861
3	5	0.067	0.193	87.200	3.940
4	4	0.055	0.169	88.420	2.689
4	IGRF	0.057	0.168	88.300	2.650
4	7	0.055	0.167	88.410	2.663
5	5	0.055	0.152	88.100	3.011
5	IGRF	0.055	0.154	87.830	3.999
5	7	0.055	0.151	88.230	3.659
5	4	0.055	0.150	88.440	2.958
6	6	0.092	0.279	79.530	3.873
6	IGRF	0.087	0.262	79.850	3.574
6	7	0.087	0.269	79.520	3.661
7	7	0.111	0.375	76.640	14.072
7	IGRF	0.112	0.370	76.710	14.547

Table C.4: Mean,95%percentile and % below 0.1^o angle error statistics for Different Segments and Different Models for Day Side and days not included in the modelling

Appendix D

Figures and tables from testing MEME dependent models for days not included in the modelling

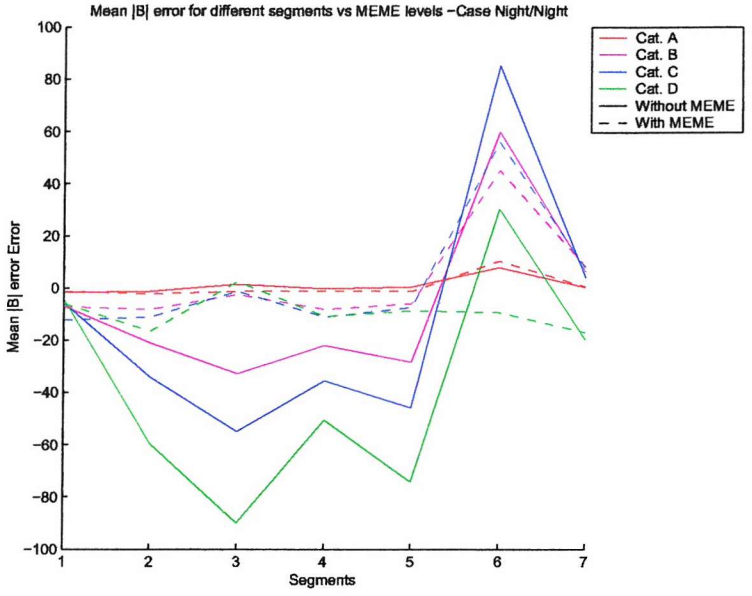

Figure D.1: Mean $|B|$ error for Different Segments and Categories - NN

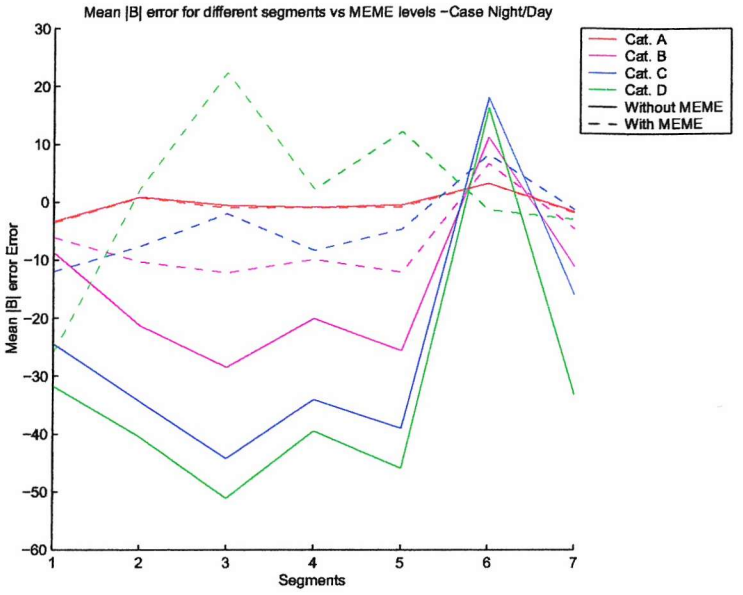

Figure D.2: Mean $|B|$ error for Different Segments and Categories - ND

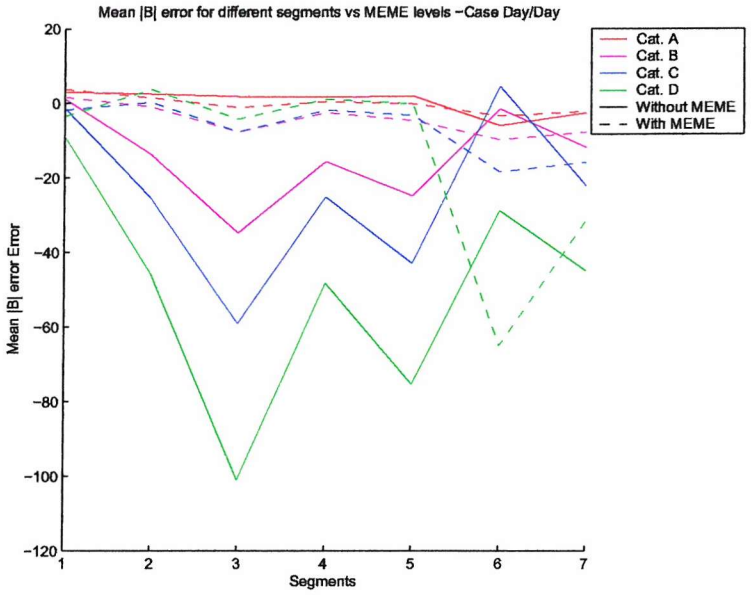

Figure D.3: Mean $|B|$ error for Different Segments and Categories - DD

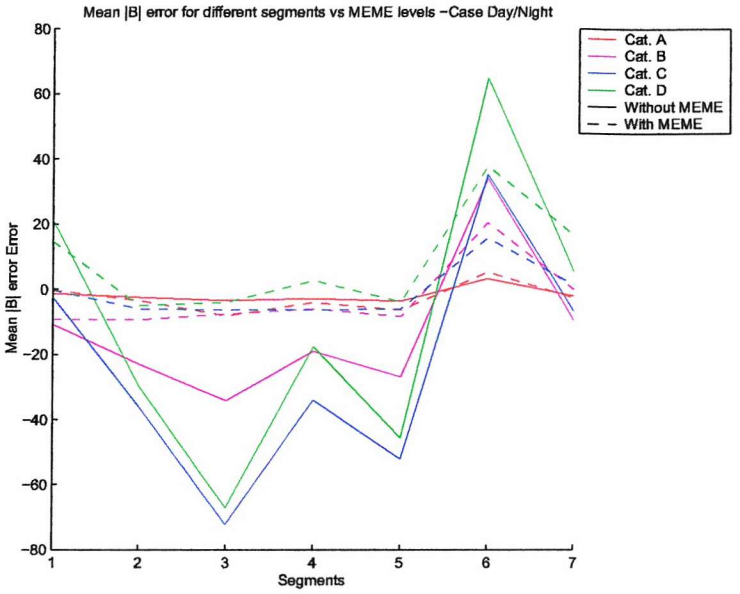

Figure D.4: Mean $|B|$ error for Different Segments and Categories - DN

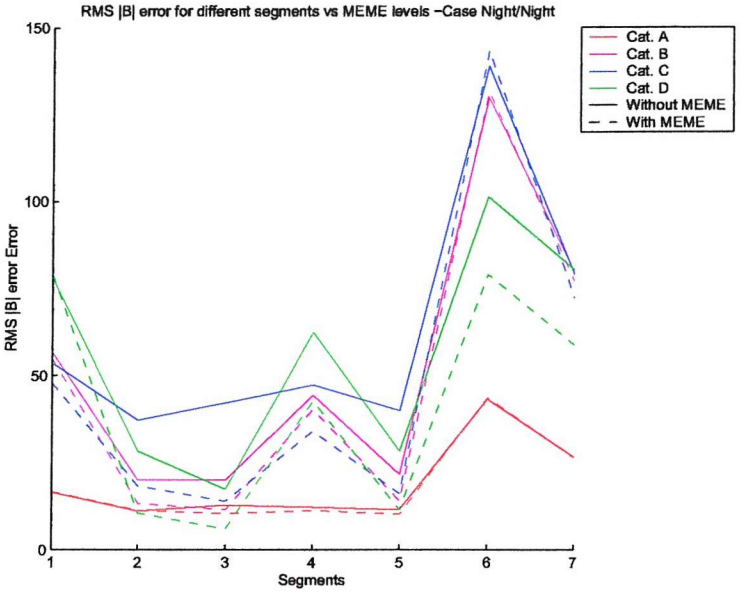

Figure D.5: rms $|B|$ error for Different Segments and Categories - NN

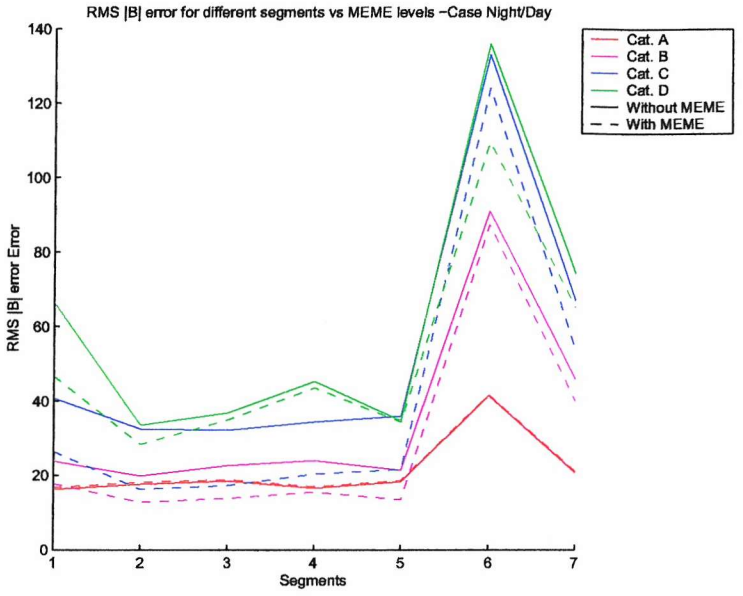

Figure D.6: rms $|B|$ error for Different Segments and Categories - ND

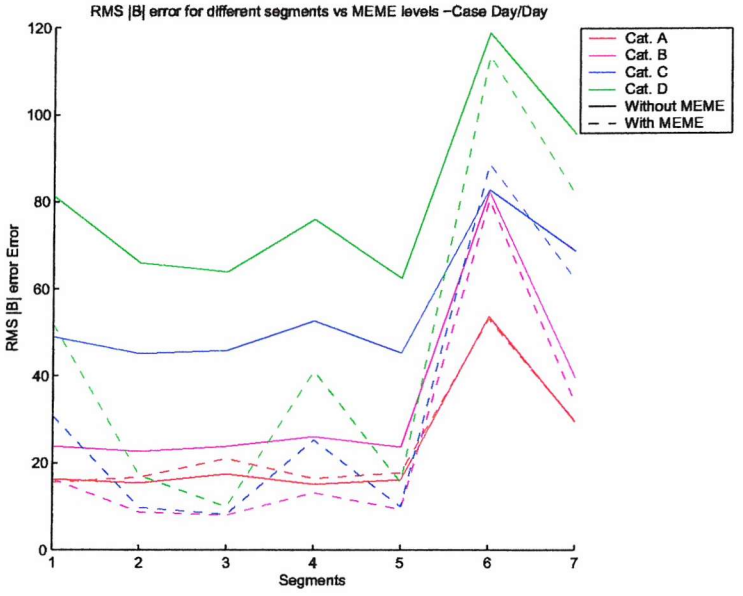

Figure D.7: rms $|B|$ error for Different Segments and Categories - DD

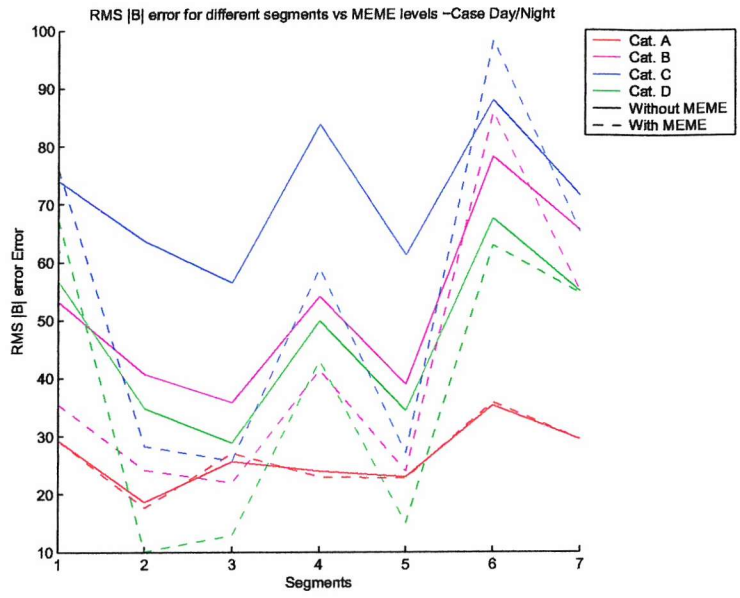

Figure D.8: rms $|B|$ error for Different Segments and Categories - DN

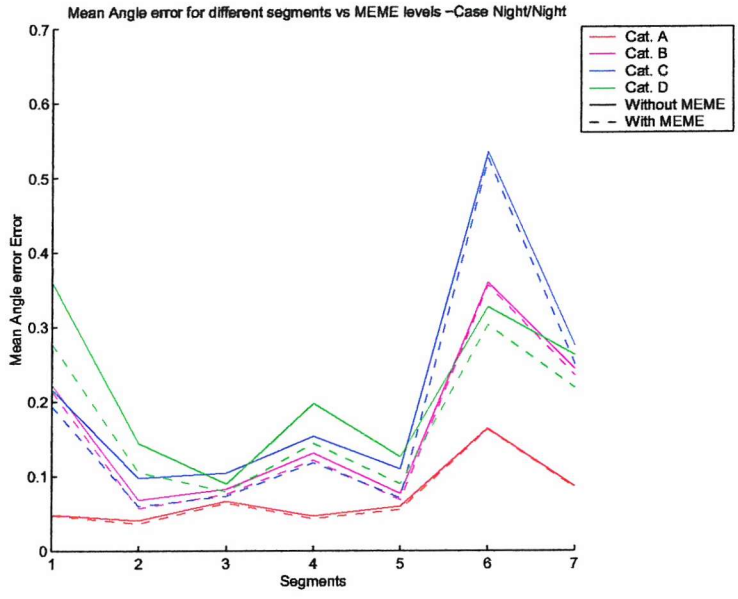

Figure D.9: Mean Angle Error for Different Segments and Categories - NN

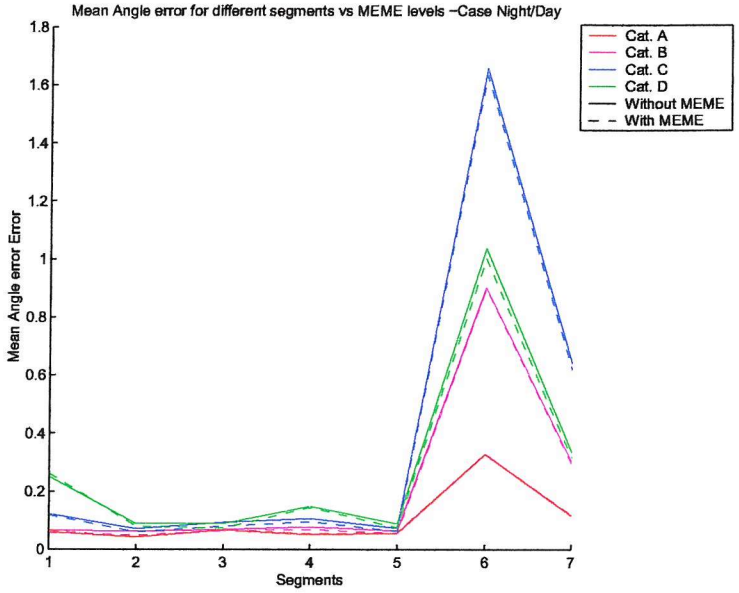

Figure D.10: Mean Angle Error for Different Segments and Categories - ND

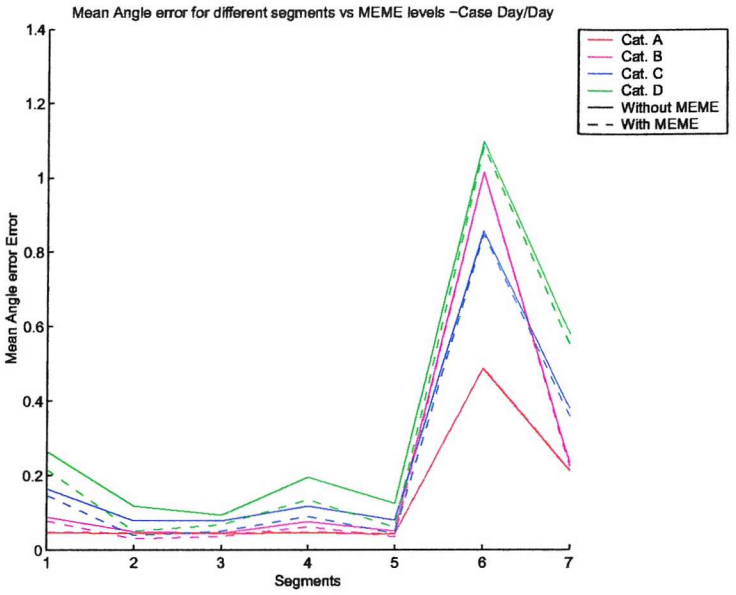

Figure D.11: Mean Angle Error for Different Segments and Categories - DD

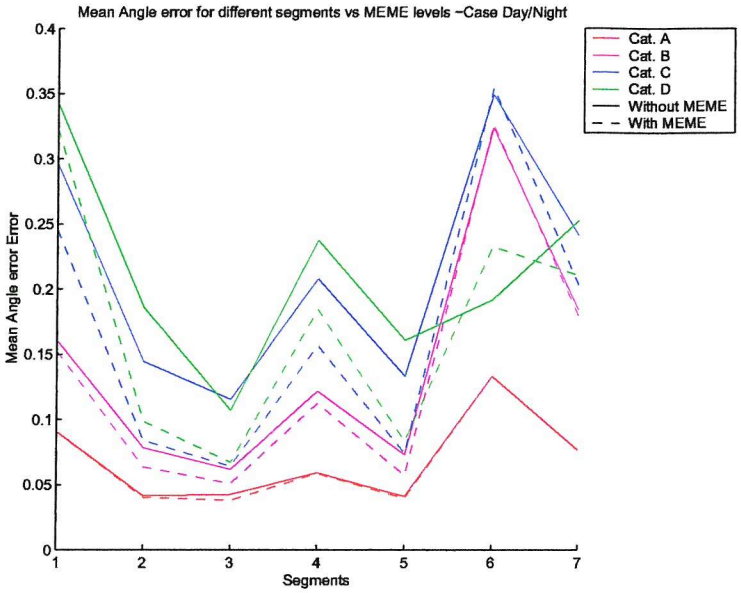

Figure D.12: Mean Angle Error for Different Segments and Categories - DN

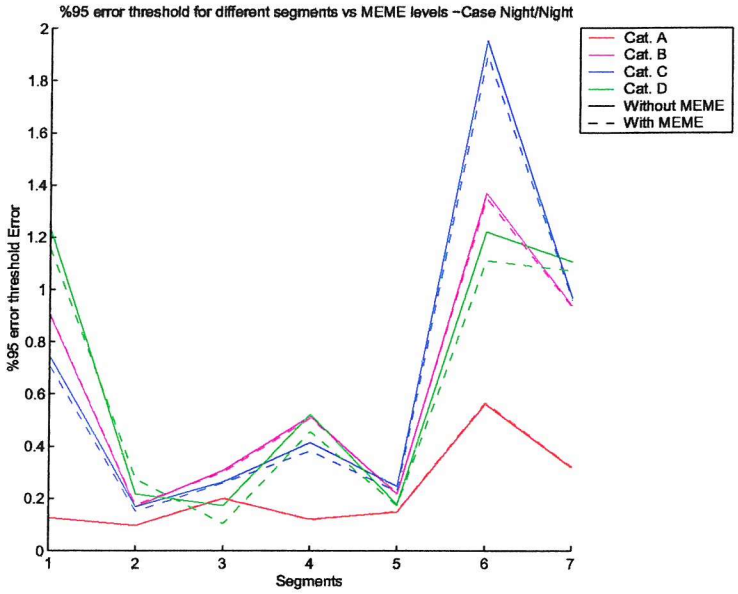

Figure D.13: 95 % Angle-Error-Threshold for Different Segments and Categories - NN

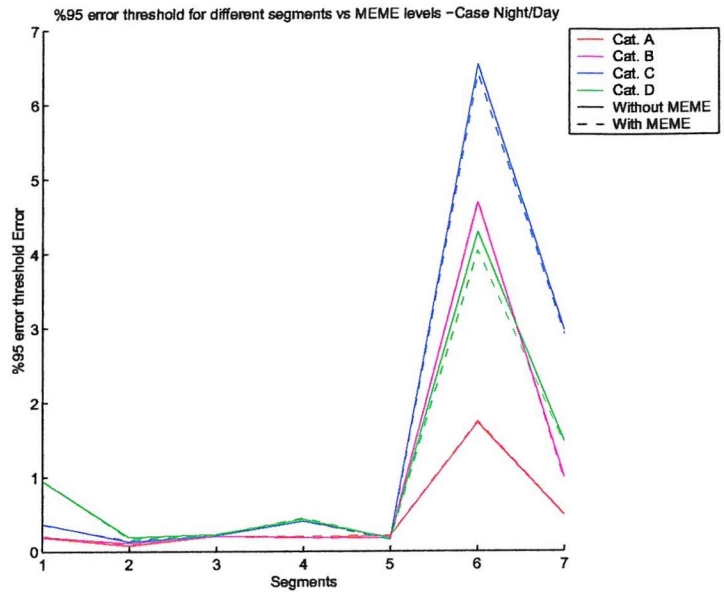

Figure D.14: 95 % Angle-Error-Threshold for Different Segments and Categories - ND

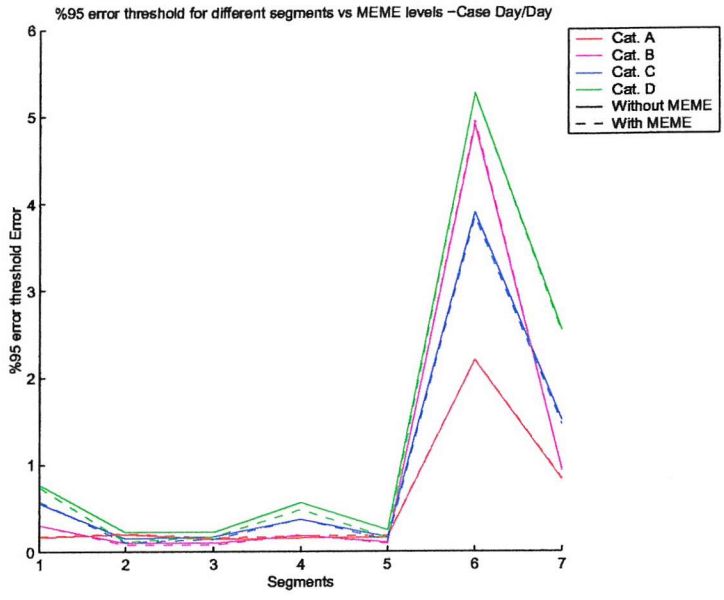

Figure D.15: 95 % Angle-Error-Threshold for Different Segments and Categories - DD

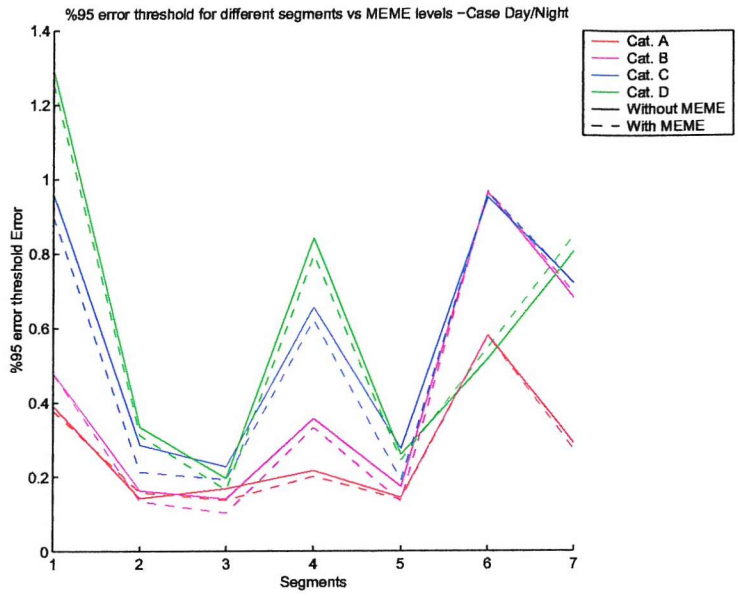

Figure D.16: 95 % Angle-Error-Threshold for Different Segments and Categories - DN

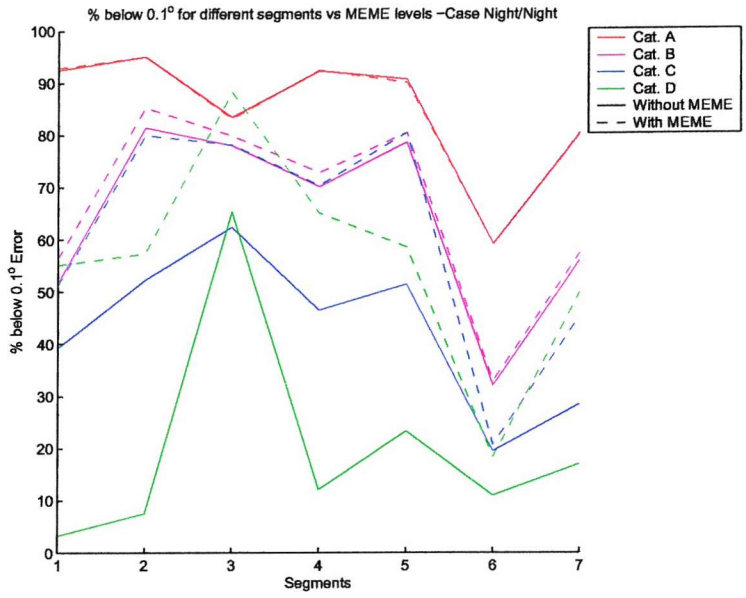

Figure D.17: % of Samples below 0.1^o for Different Segments and Categories - NN

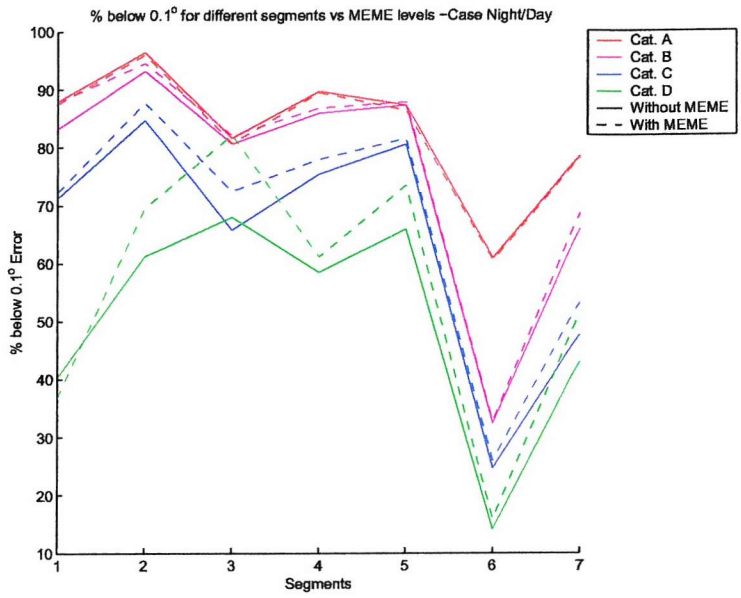

Figure D.18: % of Samples below 0.1^o for Different Segments and Categories - ND

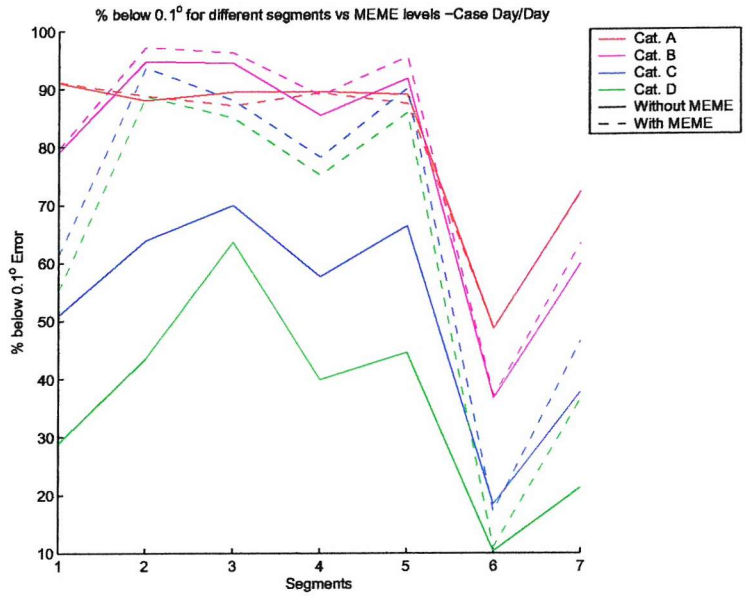

Figure D.19: % of Samples below 0.1^o for Different Segments and Categories - DD

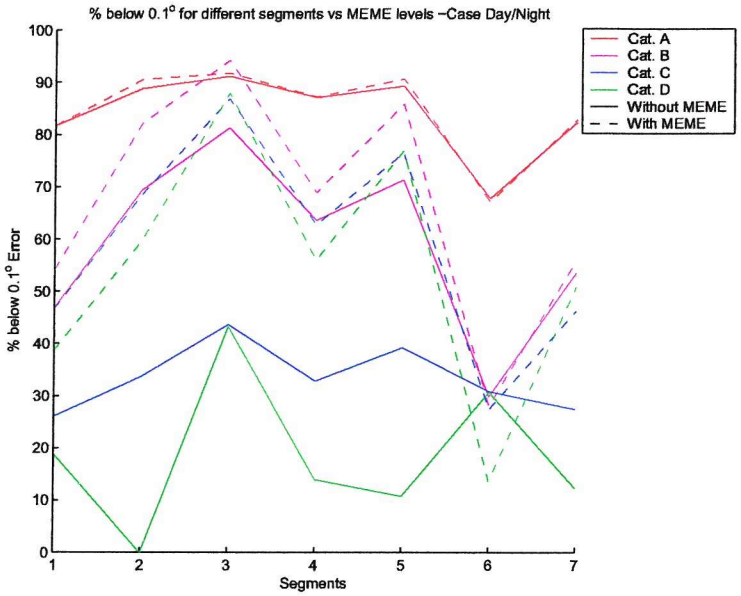

Figure D.20: % of Samples below 0.1^o for Different Segments and Categories - DN

Case	Category	meme s1	meme s2	meme s3	meme s4	meme s5	meme s6	meme s7	- s1	- s2	- s3	- s4	- s5	- s6	s7
NN	A	1.069	-1.008	-0.788	-1.055	-0.918	17.843	1.595	-1.096	-1.582	-1.506	-1.479	-1.529	18.024	1.467
NN	B	2.169	1.548	0.937	0.630	1.004	26.760	5.036	-1.854	-16.859	-26.883	-17.715	-23.477	33.644	-6.156
NN	C	5.074	1.882	1.260	3.082	0.893	82.422	15.834	-7.794	-36.482	-66.820	-35.853	-52.782	101.133	-7.866
NN	D	13.938	3.598	3.395	5.250	2.291	67.811	14.202	-12.004	-70.574	-140.347	-80.581	-111.567	96.643	-42.530
ND	A	-1.915	0.303	2.443	-0.443	0.840	6.470	0.434	-1.425	0.705	2.829	0.022	1.236	7.187	0.984
ND	B	0.729	-0.822	-1.648	1.099	-1.025	11.035	2.516	1.111	-7.748	-16.722	-4.128	-11.046	18.752	2.193
ND	C	-3.574	-6.089	-4.530	-3.652	-5.878	20.060	2.993	1.062	-22.850	-35.569	-15.436	-29.218	37.108	0.499
ND	D	14.184	-5.590	-3.760	3.731	-5.003	9.697	5.372	13.209	-40.253	-72.852	-23.536	-50.738	47.367	0.936
DD	A	-8.260	-6.295	-2.142	-5.101	-3.859	-7.249	-8.259	-8.859	-8.719	-5.927	-7.316	-7.088	-6.348	-9.462
DD	B	-10.463	-12.821	-10.413	-12.383	-12.065	-13.571	-13.714	-10.651	-23.974	-32.287	-24.921	-29.144	-4.673	-21.172
DD	C	-16.188	-16.383	-10.581	-14.005	-13.996	-4.359	-15.191	-16.076	-39.489	-58.345	-38.892	-50.383	12.880	-30.816
DD	D	-37.908	-32.785	-14.982	-23.045	-21.236	-75.138	-39.461	-37.226	-74.163	-113.647	-74.105	-93.142	-26.270	-71.681
DN	A	-3.851	-7.626	-12.449	-8.196	-9.742	0.170	-8.483	-3.696	-8.055	-13.498	-8.646	-10.549	0.216	-8.703
DN	B	0.689	-3.598	-5.385	-3.256	-4.376	8.279	-2.815	-7.625	-27.057	-41.614	-24.324	-33.373	13.036	-13.012
DN	C	-7.481	-4.387	1.006	-6.381	-2.343	-12.955	-14.055	-15.533	-50.927	-85.571	-48.755	-65.291	7.116	-34.620
DN	D	-27.314	-16.068	-13.020	-18.284	-15.616	5.421	-23.853	-47.522	-79.292	-112.279	-70.281	-91.270	31.047	-42.524

Table D.1: Mean Magnitude Error(in nanoTesla) Comparison in Different Segments for Different Cases(NN/ND/DD/DN) and different Categories(A/B/C/D)

		meme	meme	meme	meme	meme	meme	meme	-	-	-	-	-	-	
Case	Category	s1	s2	s3	s4	s5	s6	s7	s1	s2	s3	s4	s5	s6	s7
NN	A	11.000	7.826	6.995	8.833	7.020	41.213	23.275	11.848	9.792	9.625	10.315	9.020	41.252	23.942
NN	B	13.912	8.642	6.869	9.385	7.775	48.867	22.518	26.685	25.961	25.875	27.909	25.940	52.016	36.099
NN	C	51.732	11.427	8.526	25.481	11.647	159.288	64.405	60.667	36.393	36.441	48.589	38.565	147.656	80.481
NN	D	65.321	16.987	11.797	50.009	15.985	107.976	67.721	103.625	101.536	113.382	116.296	114.879	105.536	115.029
ND	A	15.389	7.588	8.793	11.421	8.377	38.943	26.519	15.317	7.498	8.801	11.361	8.325	39.157	26.625
ND	B	29.915	11.259	13.685	22.675	12.459	63.849	37.639	32.533	16.039	18.424	25.471	17.431	63.691	38.967
ND	C	34.404	14.572	15.851	21.444	15.250	63.748	34.214	42.612	35.287	36.177	38.314	32.124	62.714	44.795
ND	D	87.644	43.005	37.473	76.279	42.129	156.145	115.444	94.760	80.608	77.877	100.767	91.651	164.660	132.533
DD	A	12.327	9.173	7.361	10.872	8.431	44.833	29.870	13.465	9.416	9.670	12.006	9.654	44.897	30.080
DD	B	24.047	16.692	12.687	20.762	15.131	73.477	38.915	27.552	17.619	19.117	25.975	18.816	74.845	41.829
DD	C	28.499	16.566	12.979	18.586	15.826	86.870	40.747	42.113	29.698	38.844	37.205	33.521	86.055	52.898
DD	D	62.284	34.121	19.707	57.225	28.410	130.099	77.739	82.107	69.443	88.251	101.055	81.340	149.692	119.635
DN	A	14.892	14.583	17.134	17.627	15.897	41.689	27.828	15.083	15.104	18.160	18.416	16.686	41.285	27.915
DN	B	30.726	16.918	14.632	19.576	15.415	51.515	35.691	38.716	27.617	30.516	34.497	30.035	53.868	41.750
DN	C	35.050	38.599	44.146	41.193	41.892	94.581	71.692	58.797	59.543	61.712	62.077	57.892	101.076	92.860
DN	D	62.266	36.786	29.585	43.319	32.149	127.586	78.436	108.233	89.931	87.333	99.605	87.869	136.018	115.968

Table D.2: Magnitude rms Error(in nanoTesla) Comparison in Different Segments for Different Cases(NN/ND/DD/DN) and different Categories(A/B/C/D)

		meme	meme	meme	meme	meme	meme	meme	-	-	-	-	-	-	
Case	Category	s1	s2	s3	s4	s5	s6	s7	s1	s2	s3	s4	s5	s6	s7
NN	A	0.054	0.033	0.039	0.043	0.035	0.292	0.135	0.055	0.035	0.042	0.045	0.038	0.292	0.136
NN	B	0.057	0.025	0.045	0.043	0.035	0.375	0.124	0.068	0.044	0.058	0.056	0.051	0.372	0.137
NN	C	0.210	0.043	0.045	0.088	0.049	0.608	0.243	0.224	0.098	0.079	0.126	0.097	0.602	0.269
NN	D	0.258	0.079	0.064	0.164	0.062	2.135	0.274	0.301	0.221	0.175	0.276	0.173	2.039	0.371
ND	A	0.056	0.027	0.030	0.038	0.028	0.138	0.079	0.056	0.028	0.030	0.038	0.028	0.139	0.079
ND	B	0.124	0.038	0.032	0.069	0.036	0.261	0.136	0.129	0.047	0.046	0.079	0.047	0.264	0.143
ND	C	0.137	0.046	0.044	0.080	0.043	0.243	0.128	0.163	0.083	0.068	0.110	0.077	0.249	0.150
ND	D	0.341	0.101	0.067	0.213	0.089	0.651	0.356	0.343	0.156	0.137	0.252	0.145	0.644	0.376
DD	A	0.054	0.028	0.050	0.044	0.039	0.226	0.108	0.056	0.031	0.052	0.045	0.042	0.229	0.111
DD	B	0.096	0.055	0.066	0.076	0.059	0.331	0.152	0.103	0.059	0.073	0.083	0.066	0.335	0.160
DD	C	0.104	0.065	0.070	0.070	0.062	0.599	0.177	0.134	0.094	0.096	0.110	0.099	0.612	0.206
DD	D	0.365	0.151	0.099	0.261	0.106	0.474	0.325	0.441	0.238	0.155	0.330	0.174	0.506	0.374
DN	A	0.043	0.042	0.068	0.051	0.056	0.298	0.147	0.045	0.044	0.069	0.053	0.058	0.298	0.148
DN	B	0.106	0.056	0.067	0.076	0.061	0.411	0.197	0.129	0.069	0.079	0.097	0.075	0.414	0.213
DN	C	0.136	0.145	0.091	0.128	0.095	0.732	0.309	0.183	0.179	0.118	0.173	0.149	0.757	0.333
DN	D	0.339	0.074	0.084	0.168	0.079	0.904	0.598	0.405	0.146	0.151	0.233	0.155	0.921	0.643

Table D.3: Mean Angle Error (in °) Comparison in Different Segments for Different Cases(NN/ND/DD/DN) and different Categories(A/B/C/D)

		meme	meme	meme	meme	meme	meme	meme	-	-	-	-	-	-	
Case	Category	s1	s2	s3	s4	s5	s6	s7	s1	s2	s3	s4	s5	s6	s7
NN	A	0.206	0.122	0.141	0.158	0.142	1.309	0.553	0.208	0.127	0.141	0.157	0.144	1.301	0.551
NN	B	0.243	0.059	0.156	0.130	0.093	1.794	0.501	0.239	0.092	0.176	0.145	0.106	1.796	0.504
NN	C	0.709	0.116	0.121	0.345	0.157	2.454	1.089	0.726	0.184	0.166	0.331	0.172	2.470	1.075
NN	D	1.020	0.327	0.222	0.578	0.207	10.495	1.123	1.047	0.531	0.355	0.690	0.414	10.242	1.128
ND	A	0.173	0.070	0.076	0.105	0.071	0.501	0.307	0.178	0.071	0.078	0.106	0.073	0.502	0.305
ND	B	0.506	0.112	0.092	0.233	0.104	0.936	0.572	0.515	0.117	0.102	0.241	0.117	0.941	0.572
ND	C	0.628	0.136	0.103	0.224	0.122	0.838	0.515	0.611	0.182	0.124	0.268	0.177	0.865	0.531
ND	D	1.173	0.223	0.159	0.801	0.234	2.204	1.278	1.112	0.384	0.343	0.779	0.368	2.161	1.256
DD	A	0.181	0.067	0.159	0.130	0.110	0.869	0.451	0.196	0.074	0.166	0.133	0.111	0.886	0.462
DD	B	0.349	0.134	0.220	0.267	0.171	1.234	0.586	0.351	0.149	0.236	0.279	0.190	1.244	0.597
DD	C	0.332	0.151	0.211	0.204	0.163	2.213	0.810	0.322	0.177	0.260	0.275	0.195	2.232	0.869
DD	D	1.266	0.433	0.327	0.851	0.317	1.380	1.218	1.408	0.567	0.359	0.963	0.393	1.523	1.272
DN	A	0.133	0.112	0.192	0.143	0.173	1.335	0.547	0.135	0.116	0.190	0.149	0.172	1.327	0.551
DN	B	0.340	0.139	0.211	0.261	0.179	2.196	0.865	0.453	0.142	0.240	0.356	0.215	2.204	0.891
DN	C	0.445	0.278	0.230	0.481	0.241	3.067	1.344	0.503	0.334	0.305	0.565	0.347	3.247	1.303
DN	D	1.399	0.192	0.197	0.615	0.191	4.196	2.931	1.535	0.287	0.374	0.736	0.283	4.113	2.876

Table D.4: %95 Angle Error Threshold (in °) Comparison in Different Segments for Different Cases(NN/ND/DD/DN) and different Categories(A/B/C/D)

		meme	meme	meme	meme	meme	meme	meme	-	-	-	-	-	-	
Case	Category	s1	s2	s3	s4	s5	s6	s7	s1	s2	s3	s4	s5	s6	s7
NN	A	89.210	93.630	90.540	90.990	91.760	56.000	76.940	88.900	93.250	90.630	90.850	91.710	55.790	76.810
NN	B	88.750	97.730	89.840	92.850	95.610	48.570	77.650	87.390	96.090	88.130	91.910	94.540	49.810	76.500
NN	C	54.260	91.530	92.120	79.930	89.990	27.080	62.300	49.110	44.190	67.280	50.170	50.200	29.140	42.610
NN	D	52.900	81.140	80.290	71.170	83.060	19.520	56.210	29.930	21.360	25.130	24.080	34.020	27.320	21.750
ND	A	89.390	97.660	97.260	94.480	97.620	61.740	80.990	89.230	97.610	97.080	94.350	97.520	61.200	80.990
ND	B	73.090	93.180	96.240	86.560	94.440	42.180	70.600	72.610	91.360	94.560	83.990	91.740	41.390	68.710
ND	C	75.910	90.200	94.710	81.610	90.990	43.560	68.460	56.520	67.140	85.410	65.710	75.630	40.660	53.520
ND	D	32.760	56.890	81.830	52.010	70.200	14.120	35.720	24.550	36.600	41.090	33.330	44.740	11.030	26.720
DD	A	89.110	97.600	88.910	92.560	94.060	52.420	76.860	88.580	97.280	88.050	91.720	93.730	52.460	76.420
DD	B	77.600	89.950	86.400	83.460	86.220	35.460	69.000	74.420	86.750	83.840	81.190	84.270	33.930	67.320
DD	C	76.600	76.490	82.590	82.920	86.260	31.000	65.640	51.490	63.410	69.560	56.140	61.080	28.740	51.350
DD	D	38.540	63.440	69.400	56.530	67.490	14.230	46.170	20.500	35.010	34.990	26.300	33.920	11.820	26.770
DN	A	92.190	94.050	81.730	90.780	88.610	53.850	74.230	92.080	93.440	81.830	90.470	88.790	53.770	74.100
DN	B	77.980	92.190	81.950	83.390	87.240	50.810	65.360	74.760	87.540	76.610	81.470	84.050	50.210	62.380
DN	C	60.270	67.510	73.420	68.940	68.620	24.900	50.390	43.490	47.870	54.740	46.190	43.270	24.540	39.590
DN	D	42.490	76.760	77.540	58.400	76.320	18.010	37.910	16.930	33.930	34.870	26.610	32.850	17.260	19.280

Table D.5: Percentage of Angle Error below 0.1^o Comparison in Different Segments for Different Cases(NN/ND/DD/DN) and different Categories(A/B/C/D)

Bibliography

[1] N. Olsen, "A model of the geomagnetic field and its secular variation for epoch 2000 estimated from oersted data," *Geophys.J.Int.*, vol. 149, pp. 454–462, 2002.

[2] I. Bar-Itzhack, "Classification of algorithms for angular velocity estimation," *Journal of Guidance, Control, and Dynamics*, vol. 24, no. 2, pp. 214–218, 2001.

[3] T. Bak, "Spacecraft attitude determination - a magnetometer approach," Ph.D. dissertation, Department of Control Engineering, Aalborg University, 2001.

[4] R. Walker, *Quantitative modeling of planetary magnetospheric magnetic fields, in Quantitative Modelling of Magnetospheric Processes*, 1979.

[5] N. Tsyganenko and V. Usmanov, "Determination of the magnetospheric current system parameters and development of experimental geomagnetic field models based on data from imp and heos satellites," *Planet. Space Sci.*, vol. 30, pp. 985–998, 1982.

[6] N. Tsyganenko, "Global quantitative models of the geomagnetic field in the cislunar magneto- sphere for different disturbance levels," *Planet. Space Sci.*, vol. 35, pp. 1347–1358, 1987.

[7] ——, "Magnetospheric magnetic field model with a warped tail current sheet," *Planet. Space Sci.*, vol. 37, pp. 5–20, 1989.

[8] M. Sugiura, B. Ledley, T. Skillman, and J. Heppner, "Magnetospheric-field distortions observed by ogo 3 and 5," *J.Geophys. Res.*, vol. 76, p. 7552, 1971.

[9] A. Lui, R. McEntire, and S. Krimgis, "Evolution of the ring current during two gemagnetic storms," *J. Geophys. Res.*, vol. 92, p. 7459, 1987.

[10] T. Ijima, T., A. Potemra, and L. J. Zaneti, "Large-scale characteristics of magnetospheric equatorial currents," *J. Geophys.Res.*, vol. 95, p. 991, 1990.

[11] A. Lui and D. Hamilton, "Radial profiles of quiet time magnetospheric parameters," *J. Geophys. Res.*, vol. 97, p. 325, 1992.

[12] P. De Michelis, I. Daglis, and G. Consolini, "Average terrestrial ring current derived from ampte/cce-chem measurements," *J. Geophys. Res.*, vol. 102, p. 103, 1997.

[13] S. Nakabe, T. Iyemori, M. Sugiura, and J. Slavin, "A statistical study of the magnetic field structure in the inner magnetosphere," *J. Geophys. Res.*, vol. 102, p. 571, 1997.

[14] H. Nakai, Y. Kamide, and C. Russell, "Statistical nature of the magnetotail current in the near-earth region," *J. Geophys. Res.*, vol. 102, p. 9573, 1987.

[15] P. Mayaud, *Derivation, Meaning, and Use of Geomagnetic Indices.* American Geophysical Union, 1980.

[16] S. Chapman and V. C. A. Ferraro, "A new theory of magnetic storms," *Nature*, vol. 126, p. 129, 1930.

[17] S. Chapman and V. Ferraro, "A new theory of magnetic storms," *Terr. Magn. Atmosph. Elec.*, vol. 36, pp. 171–186, 1931.

[18] ——, "A new theory of magnetic storms," *Terr. Magn. Atmosph. Elec*, vol. 37, pp. 147–156, 1932.

[19] S. Akasofu, "The development of the auroral substorm," *J.Geophys.Res.*, vol. 12, pp. 273–282, 1964.

[20] C. Russell and R. McPherron, "The magnetotail and substorms," *Space Sci. Rev.*, pp. 111–122, 1973.

[21] R. McPherron, "Magnetospheric substorms," *Rev. Geophys. Space Phys.*, vol. 17, pp. 657–681, 1979.

[22] J. Jacobs, *Geomagnetism.* Academic Press, 1991.

[23] W. Duffin, *Electricity and Magnetism.* McGraw-Hill, 1990.

[24] S. Chapman and J. Bartels, *Geomagnetism.* Oxford University Press, 1962.

[25] J. Wertz, *Spacecraft Attitude Determination and Control.* D.Reidel Publishing Company, 1984.

[26] J. Cain, S. Hendricks, R. Langel, and H. W.V., "A proposed model for the international geomagnetic reference field-1965," *J.Geomag.Geoelectr.*, vol. 19, pp. 335–355, 1967.

[27] R. Langel and R. Estes, "Some new methods in geomagnetic field modelling applied to the 1960-1980 epoch," *J.Geomag.Geoelectr.*, vol. 34, pp. 327–349, 1982.

[28] J. A. Walker, M.R., "Robust modelling of the earth's magnetic field," *Geophys.J.Int.*, vol. 143, pp. 799–808, 2000.

[29] K. Whaler and D. Gubbins, "Spherical harmonic analysis of the geomagnetic field:an example of a linear inverse problem," *Geophys.J.R.astr.Soc.*, vol. 65, pp. 645–693, 1981.

[30] P. Huber, "Robust estimation of a location parameter," *Ann.Math.Statist.*, vol. 35, pp. 73–101, 1964.

[31] D. Freedman, R. Pisani, R. Purves, and A. Adhikari, *Statistics.* Norton International, 1991.

[32] Y. Linnik, *Method of Least Squares and Principles of the Theory of Observations.* Pergamon Press, 1961.

[33] R. Kashyap and A. Rao, *Dynamic Stochastic Models from Empirical Data.* Academic Press, 1987.

[34] F. Hildebrand, *Introduction to Numerical Analysis.* Dover, 1987.

[35] F. Lowes and J. Martin, "Optimum use of satellite intensity and vector data in modelling the main geomagnetic field," *Physics of the Earth and Planetary Interiors*, vol. 48, pp. 183–192, 1987.

[36] A. Bjorck, *Numerical Methods for Least Squares problems.* Society for Industrial and Applied Mathematics, 1996.

[37] J. Dennis and R. Schnabel, *Numerical Methods for Unconstrained Optimization and Nonlinear Equations.* Society for Industrial and Applied Mathematics, 1996.

[38] R. Langel and R. Estes, "The near-earth magnetic field at 1980 determined from magsat data," *J.Geophys.Res.*, vol. 90, pp. 2495–2509, 2000.

[39] J. Quinn, R. Coleman, S. Macmillan, and D. Barraglough, "The 1995 revision of the joint us/uk geomagnetic field models.ii-main field," *Earth Planets Space*, vol. 52, pp. 1137–1148, 1997.

[40] M. Mandea and B. Langlais, "Use of oersted scalar data in evaluating the pre-oersted main field candidate models for the igrf 2000," *Earth Planets Space*, vol. 52, pp. 1167–1170, 2000.

[41] B. Langlais and M. Mandea, "An igrf candidate main geomagnetic field model for epoch 2000 and a secular variation model for 2000-2005," *Earth Planets Space*, vol. 52, pp. 1137–1148, 2000.

[42] V. Golovkov, T. Bondar, and I. Burdelnaya, "Spatial-temporal modeling of the geomagnetic field for 1980-2000 period and a candidate igrf secular-variation model for 2000-2005," *Earth Planets Space*, vol. 52, pp. 1125–1135, 2000.

[43] F. Lowes, "The working of the igrf 2000 task force," *Earth Planets Space*, vol. 52, pp. 1171–1174, 2000.

[44] S. Macmillan, "An evaluation of of candidate geomagnetic field models for igrf 2000," *Earth Planets Space*, vol. 52, pp. 1163–1165, 2000.

[45] N. Olsen, T. Sabaka, and T.-C. L., "Determination of the igrf 2000 model," *Earth Planets Space*, vol. 52, pp. 1175–1182, 2000.

[46] J. Bloxham, D. Gubbins, and A. Jackson, "Geomagnetic secular variation," *Phil.Trans.R.Soc.Lond.*, vol. 329, pp. 415–502, 1989.

[47] C. Constable, "Parameter estimation in non gaussian noise," *Geophys.J.*, vol. 94, pp. 131–142, 1989.

[48] R. Holme, "Modelling the attitude error in vector magnetic data:application to oersted data," *Earth Planets Space*, vol. 52, pp. 1187–1197, 2000.

[49] A. Thomson, S. McMillan, and D. Barraclough, "Geomagnetic main-field modelling with pogs satellite data," *Geophys.J.*, vol. 49, pp. 417–440, 1997.

[50] A. Lui, H. Spence, and D. Stern, "Empirical modeling of the quite time nightside magnetosphere," *J.Geophys.Res.*, vol. 99, pp. 151–157, 1994.

[51] F. Lowes, "Vector errors in spherical harmonic analysis," *Geophys.J.*, vol. 42, pp. 637–651, 1975.

[52] T. Sabaka, R. Langel, R. Baldwin, and J. Conrad, "The geomagnetic field 1900-1995, including the large-scale field from magnetospheric sources and the nasa candidate models for the 1995 revision of the igrf," *Journal of Geomag. Geoelec.*, vol. 49, pp. 157–206, 1997.

[53] S. Chapman, "An outline of theory of magnetic storms," *Proc. R. Soc. London*, vol. 95, pp. 61–83, 1918.

[54] C. Kirkpatrick, "On currentsystems proposed for s_d in the theory of magnetic storms," *J.Geophys.Res.*, vol. 57, pp. 511–526, 1952.

[55] S.-I. Akasofu and S. Chapman, "On the assymetric developement of magnetic storm fields in low and middle latitudes," *Planet. Space Sci.*, vol. 12, pp. 607–626, 1964.

[56] A. Jorgensen, H. Spence, Hughes, and H. Singer, "A statistical study of the global structure of the ring current," *J. Geophys. Res.*, vol. ?, p. ?, 1999.

[57] R. Bate, D. Mueller, and J. White, *Fundamentals of Astrodynamics.* New York: Dover Publications, 1986.

[58] J. Kuipers, *Quaternions and Rotation Sequences.* Princeston: Princeston University Press, 1999.

[59] E. Neville, *Jacobian Elliptic Functions.* Oxford University Press, 1951.

[60] P. Byrd and Friedman, *Handbook of Elliptic Functions.* Berlin: Springer-Verlag, 1971.

[61] G. Wahba, "A least squares estimate of spacecraft attitude," *SIAM Review*, vol. Vol. 7, no. No. 3, p. 409, July 1965.

[62] F. Markley, "Attitude determination from vector observations: A fast optimal matrix algorithm," *The Journal of the Astronautical Sciences*, vol. Vol. 41, no. No. 2, pp. 261–280, April 1993.

[63] M. Shuster and S. Oh, "Three-axis attitude determination from vector observations," *Journal of Guidance and Control*, vol. Vol. 4, no. No. 1, pp. 70–77, Jan 1981.

[64] P. Hughes, *Spacecraft Attitude Dynamics.* New York: John Wiley and Sons, 1986.

[65] H. F. Z. John S. Eterno, Robert O. Zermuehlen, *Attitude Determination and Control. SPACE MISSION ANALYSIS AND DESIGN.* Space Technology Series, Microcosm, Inc. and Kluwer Academic Publishers, 1992.

[66] E. BARNES, "Model 13-500wide-angle, miniature, solid-sate horizon sensor," Weblink, January 2002.

[67] M. Challa, G. Natanson, J. 0Deutschmann, and K. Galal, "A pc-based magnetometer-only attitude and rate determination system for gyroless spacecraft," *GSFC FDD Flight Mechanics Symposium Proceedings*, pp. 83–96, 1995.

[68] A. P. Systems, "Model 533 miniature 3-axis fluxgate magnetometer," Weblink, 2002.

[69] W. Steyn and Y. Hashida, "In-orbit attitude performance of the 3-axis stabilised snap-1 nanosatellite," *Proceedings of the 15 AIAA/USU Conference on small Satellites*, no. SSC01-V-1, 2001.

[70] W. Steyn, Y. Hashida, and V. Lappas, "An attitude control system and commissioning results of the snap-1 nanosatellite," *Proceedings of the 14th Annual AIAA Conference on Small Satellites/USU*, no. SSC00-VIII-8, SlRy02.

[71] R. Slocum and L. Ryan, "Self-calibrating vector magnetometer for space," *Proceedings of Eart Science Technology Conference 2002- NASA*, no. B3P4(Slocum), 2002.

[72] Y. Navid, A. Farrokh, and N. Khalil, "Michromachined inertial sensors," *Proceeding of the IEEE*, vol. 86, no. NOV 8, pp. 1640–1659, 1998.

[73] S. Donner, "Bei gyrochip tm micromachined angular rate sensor," Weblink, 2002.

[74] B. S. Systems, "Silicon gyroscope," Weblink, 2002.

[75] G. Natanson, "A deterministic method for estimating attitude from magnetometer data only," *Proceedings of the World Space Congress*, no. 1AF-92-0036, 1992.

[76] J. Forden, T. Flatley, D. Henretty, and E. Lightsey, "On-board attitude determination and control algorithms for sampex," *Flight Mechanics and Estimation Theory Symposium*, no. NASA Conference Publication 3102, 1990.

[77] M. Psiaki, F. Martel, and P. Pal, "Three-axis attitude determination via kalman filtering of magnetometerdata," *Journal of Guidance, Control, and Dynamics*, vol. 13, no. 3, pp. 506–514, 1989.

[78] E. Lefferts, F. Markley, and M. Shuster, "Kalman filtering for spacecraft attitude estimation," *Journal of Guidance, Control, and Dynamics*, vol. 5, no. 5, pp. 417–429, 1982.

[79] P. Landiech, "Extensive use of magnetometers and magnetotorquers for small satellites attitude estimation and control," *AIAA Paper*, no. AAS 95-012, 1995.

[80] R. Azor, I. Bar-Itzhack, and R. Harman, "Satellite angular rate estimation from vector measurements," *Journal of Guidance, Control, and Dynamics*, vol. 21, no. 3, pp. 450–457, 1998.

[81] R. Harman and I. Bar-Itzhack, "Pseudolinear and state-dependent riccati equation filters for angular rate estimation," *Journal of Guidance, Control, and Dynamics*, vol. 22, no. 5, pp. 723–725, 1999.

[82] R. Azor, z. D. J. Bar-Itzhack, I.Y., and R. Harman, "Angular rate estimation using delayed quaternion measurements," *Journal of Guidance, Control, and Dynamics*, vol. 24, no. 3, pp. 436–443, 2001.

[83] Y. Oshman and F. Dellus, "Fast estimation of spacecraft angular velocity from sequential geomagnetic field observations," *Proceedings of the AIAA/AAS Astrodynamics Specialists Conf., American Institute of Aeronautics and Astronautics, Reston*, pp. 322–330, 2000.

[84] C. Researchers and Participants, "University nanosatellite program," *Proceedings of Symosium on Novel Concepts for smaller,faster and Better Space Mission*, April 1999.

[85] T. E. Humphreys, "Attitude determination for small satellites with modest pointing constraints," *16 Annual AIAA/USU Conference on Small Satellites*, 2002, available at http://www.aria.cec.wustl.edu/SSC02/scheduleframe.htm.

[86] L. Team, "Lunarsat website," http://www.lunarsat.de/.

[87] H. Goldstein, C. Poole, P. Charles, and J. Safko, *Classical Mechanics (3rd Edition)*. Prentice Hall, 2002.

[88] N. P. R. PRACTICES, "Magnetic design control for science instruments," NASA, Tech. Rep. PRACTICE NO. PD-ED-1207.

[89] J. Oden and E. Ripperger, *Mechanics of Elastic Structures*, 1981.

[90] N. Alfutov, *Stability of Elastic Structures*, 2000.